

INAUGURAL-DISSERTATION
zur
Erlangung der Doktorwürde
der
Naturwissenschaftlich-Mathematischen
Gesamtfakultät
der
Ruprecht-Karls-Universität
Heidelberg

vorgelegt von
Dipl.-Phys. Wolfgang Gradl
aus Heidelberg

Tag der mündlichen Prüfung: 18. Juli 2001

**Das Auslesesystem des Inneren Spurkammersystems
des HERA-*B* Detektors
und
Drell-Yan Physik mit dem HERA-*B* Detektor**

Gutachter: Prof. Dr. Franz Eisele
Prof. Dr. Johanna Stachel

Dissertation
submitted to the
Combined Faculties for the Natural Sciences and for Mathematics
of the Rupertus Carola University of
Heidelberg, Germany
for the degree of
Doctor of Natural Sciences

**The Readout System of the HERA-*B* Inner Tracker
and
Prospects of HERA-*B* in the Field of Drell-Yan
Physics**

presented by
Diplom-Physicist Wolfgang Gradl
Born in Heidelberg

Heidelberg, July 18th, 2001

Referees: Prof. Dr. Franz Eisele
Prof. Dr. Johanna Stachel

Abstract

The HERA- B experiment at the HERA accelerator at DESY is designed and built to measure \mathcal{CP} violation in the system of neutral B mesons. One sub-detector is the Inner Tracker, which is built of Micro-Strip Gas Chambers with Gas Electron Multiplier (GEM-MSGC) with about 120 000 readout channels.

Using results of test beam experiments, the readout system of the Inner Tracker was finalised in its design. At HERA- B , it was extended from small test installations to the full system during the installation 1999/2000. The software needed for the processing of the raw data was developed. This thesis describes the readout hardware and software in use at HERA- B and the steps needed for commissioning. Results from the first year of running at HERA- B are reported.

In a second part of this thesis, the prospects of HERA- B to contribute to the field of Drell-Yan physics are evaluated, where significant deviations from the predictions of perturbative QCD were observed. Starting from an analysis of the di-muon triggered data of the run period 2000, the expected number of high-mass muon pairs produced by the Drell-Yan process is extrapolated. With a conservative estimate of the outcome of the detector and trigger improvements, about 26 000 high-mass Drell-Yan pairs are expected for the run period 2002. Although the measurement will be difficult due to the low number of events at higher transverse momentum, this will allow a first measurement of the angular distributions of Drell-Yan pairs produced in pN collisions.

Zusammenfassung

Das Experiment HERA- B am Speicherring HERA ist geplant worden, um die Verletzung der \mathcal{CP} Symmetrie im System der neutralen B -Mesonen zu messen. Eine der Hauptkomponenten des Detektors ist das Innere Spurkammersystem, das aus Mikrostreifen-Gaszählern mit einer GEM-Folie (GEM-MSGC) aufgebaut ist. Das Innere Spurkammersystem hat ungefähr 120 000 analoge Auslesekanäle.

Das Design des Auslesesystems für die Inneren Spurkammern wurde nach ausführlichen Systemtests festgelegt. Bei HERA- B wurde das Auslesesystem im Laufe der Jahre 1999/2000 von kleinen Testinstallationen zum vollständigen System für die gesamten Inneren Spurkammern ausgebaut und erfolgreich in Betrieb genommen. Ebenso wurde die zum Aufbereiten der Rohdaten benötigte Software entwickelt. Diese Arbeit beschreibt Hard- und Software des bei HERA- B eingesetzten Auslesesystems und die zur Inbetriebnahme nötigen Tests. Ergebnisse aus dem ersten Betriebsjahr werden berichtet.

In einem zweiten Teil werden die Aussichten von HERA- B untersucht, einen Beitrag zum Feld der Drell-Yan Physik zu leisten. Hier wurden in früheren Experimenten signifikante Abweichungen von den Vorhersagen der perturbativen QCD festgestellt. Ausgehend von einer Analyse der im Jahr 2000 aufgenommenen Di-Myon Daten wird die erwartete Zahl von Drell-Yan Myon-Paaren für das Betriebsjahr 2002 abgeschätzt; mit konservativen Annahmen über den Zustand des Detektors nach dem Luminositäts-Upgrade von HERA werden etwa 26 000 Myon-Paare mit hohen invarianten Massen erwartet. Nur eine geringe Zahl von Ereignissen in diesem Massenbereich wird auch einen großen Transversalimpuls haben. Dennoch wird eine erste signifikante Messung der Winkelverteilung der in pN -Kollisionen erzeugten Drell-Yan Paare möglich sein.

Contents

| | |
|--|-----------|
| Introduction | 1 |
| 1 The Experiment HERA-<i>B</i> | 3 |
| 1.1 The HERA Storage Ring | 3 |
| 1.2 Physics Goals of HERA- <i>B</i> | 4 |
| 1.2.1 Generation of \mathcal{CP} Violation in the Standard Model | 5 |
| 1.2.2 Physics with <i>B</i> Mesons and \mathcal{CP} Violation in <i>B</i> Decays | 8 |
| 1.2.3 Proposed Physics Programme for 2002 | 9 |
| 1.3 Overview over the Detector | 10 |
| 1.4 Trigger | 15 |
| 1.4.1 Pretriggers | 15 |
| 1.4.2 First Level Trigger | 15 |
| 1.4.3 Second and Third Level Trigger | 17 |
| 1.4.4 Fourth Level Trigger | 17 |
| 1.5 Data Acquisition System | 18 |
| I Readout for the Inner Tracker of HERA-<i>B</i> | 21 |
| 2 The Inner Tracker of HERA-<i>B</i> | 23 |
| 2.1 Requirements | 23 |
| 2.2 Detector Technology | 24 |
| 2.2.1 Operation Principle | 25 |
| 2.2.2 Construction of the HERA- <i>B</i> GEM-MSGC | 26 |
| 2.3 Building a Tracking Device with GEM-MSGCs | 29 |
| 2.4 Chamber Operation and Infrastructure | 32 |
| 3 Readout for the Inner Tracker | 35 |
| 3.1 Readout Chain and Data Flow | 35 |
| 3.2 Front End Chip: Helix128S | 36 |
| 3.2.1 Input Stage | 36 |
| 3.2.2 Comparators | 37 |
| 3.2.3 Pipeline | 39 |
| 3.2.4 Readout Cycle | 39 |
| 3.2.5 Multi-Event Buffer and Dead Time | 39 |
| 3.2.6 Testpulse Circuit | 40 |
| 3.2.7 Programmable Parameters | 41 |
| 3.2.8 Helix PCB | 42 |
| 3.2.9 Helix Versions Used | 45 |

| | | |
|-----------|--|------------|
| 3.3 | FED System | 46 |
| 3.4 | Additional Electronics | 48 |
| 3.4.1 | Data Valid Board | 49 |
| 3.4.2 | Digital Control Signals | 50 |
| 3.4.3 | Helix Register Loading | 50 |
| 3.4.4 | Signal Distribution Board | 51 |
| 3.4.5 | Analogue Data Transmission | 51 |
| 3.4.6 | Setup in the Electronics Trailer | 52 |
| 3.5 | Grounding Scheme | 53 |
| 3.6 | Readout Software | 55 |
| 3.6.1 | Data Format | 55 |
| 3.6.2 | Pedestal and Noise Following | 55 |
| 3.6.3 | Cluster Finder | 59 |
| 3.6.4 | Online Sparsification | 61 |
| 3.6.5 | Configuration and Setup Database | 63 |
| 3.6.6 | Online Monitoring | 64 |
| 4 | Commissioning of the ITR Readout System | 67 |
| 4.1 | Preparatory Beam Tests | 67 |
| 4.2 | Installation in HERA- <i>B</i> | 68 |
| 4.2.1 | Cabling Cross-checks | 68 |
| 4.3 | Timing and Synchronisation | 69 |
| 4.4 | Optimisation of Pulse Shaping | 70 |
| 4.5 | Operation Experience and Performance | 77 |
| 4.5.1 | Variation of Analogue Gain | 77 |
| 4.5.2 | Time Stability of Noise and Pedestal Estimates | 79 |
| 4.5.3 | Stability of Readout System | 79 |
| 4.5.4 | Noise Behaviour | 82 |
| 4.5.5 | Chamber Occupancies | 84 |
| 4.5.6 | Chamber Performance | 87 |
| 4.5.7 | Chamber Efficiency | 91 |
| 4.6 | Simulation of Pulse Shapes | 98 |
| 4.6.1 | Time Evolution of the Chamber Signals | 98 |
| 4.6.2 | Results of the Simulation | 101 |
| 4.7 | Summary and Outlook | 104 |
| II | Drell-Yan Physics at HERA-<i>B</i>: A Feasibility Study | 105 |
| 5 | The Drell-Yan Process | 107 |
| 5.1 | Perturbative QCD Predictions | 107 |
| 5.2 | Angular Distributions and the Lam-Tung Relation | 110 |
| 5.2.1 | Violation of the Lam-Tung Relation | 110 |
| 5.2.2 | Theoretical Models | 111 |
| 5.2.3 | Concluding Remarks | 114 |
| 5.3 | DY as Surrogate for Prompt Photon Production | 114 |

| | | |
|----------|--|------------|
| 6 | Prospects of doing Drell-Yan Physics at HERA-<i>B</i> | 119 |
| 6.1 | Geometrical Acceptance | 119 |
| 6.1.1 | Detector Resolution and Acceptance Correction | 124 |
| 6.2 | Background | 124 |
| 6.2.1 | Sources of Background | 125 |
| 6.2.2 | Reducing the Background | 128 |
| 6.3 | Expected Event Rate | 130 |
| 6.3.1 | J/ψ Search in 2000 Data | 130 |
| 6.3.2 | Expected Improvements and Impact on J/ψ Rate | 137 |
| 6.3.3 | Expected Drell-Yan Rate in 2002 | 139 |
| 6.4 | Measuring the Angular Distribution | 139 |
| 6.4.1 | Expected Shape of the Angular Distributions | 140 |
| 6.4.2 | Direct Fit | 140 |
| 6.4.3 | Method of Moments | 142 |
| 6.5 | Summary | 144 |
| 7 | Summary and Conclusions | 147 |
| A | Readout Setup | 149 |
| A.1 | Location of Readout Electronics | 149 |
| A.2 | Configuration of the FED Controller | 151 |
| B | Organisation of the ITR Software | 153 |
| B.1 | Software Packages for Data Processing | 153 |
| B.2 | Organisation on Disk | 154 |
| B.3 | Programs running online | 154 |
| C | Total Gain of the Analogue Readout Chain | 157 |
| D | Kinematics of the Drell-Yan Process | 159 |
| D.1 | Kinematical Variables | 159 |
| D.2 | Reference Frames | 160 |
| | Bibliography | 168 |
| | Acknowledgements | 169 |

Introduction

Symmetries are one of the fundamental principles of nature. By identifying the symmetries of a system, many of its physical properties can be discovered. Continuous symmetries are always linked to conserved currents of a certain quantity (Noether's theorem); for example, symmetry under time and space translation is linked with the conservation of energy and momentum.

A different kind of symmetries are the *discrete* symmetries time reversal \mathcal{T} , charge conjugation \mathcal{C} , and parity (space inversion) \mathcal{P} . It was long believed that the physical laws governing the interaction of elementary particles are also symmetric under each of these three operations. In 1957, it was experimentally shown that the weak interaction violates both \mathcal{C} and \mathcal{P} maximally [WAH⁺57]. The combined symmetry \mathcal{CP} was then thought to be a good symmetry for the weak interaction, until \mathcal{CP} violation was found in the system of neutral K mesons in 1964 [CCFT64]. In the K system, the effect of \mathcal{CP} violation is very small; the asymmetry of decay probabilities which shows \mathcal{CP} violation is of the order $\mathcal{O}(10^{-3})$. In analogy to the K system, the standard model predicts \mathcal{CP} violation in the system of neutral B_d mesons; the expected asymmetry is large.

To search for the violation of \mathcal{CP} symmetry in the system of neutral B -mesons, a number of new, dedicated experiments for B physics have been planned and built: BaBar (SLAC) and Belle (KEK) are situated at asymmetric electron-positron colliders, where the B^0 mesons are produced by the decay of the $\Upsilon(4S)$ resonance. They reported first measurements in 2000. HERA- B , which is currently being commissioned at DESY in Hamburg, is a fixed-targeted experiment using the proton beam of the HERA storage ring impinging on thin wire targets. Here, also B_s -mesons are produced and accessible for measurements. The experiment of the next generation is planned at the Large Hadron Collider (LHC) at CERN, which will start operation in the middle of this decade. There, LHCb is dedicated to study \mathcal{CP} violation in the B_d and the B_s systems; it will allow high precision measurements of the \mathcal{CP} violating parameters.

To produce enough B^0 s at HERA- B to measure the \mathcal{CP} violation within about one year, a large interaction rate of up to 40 MHz is needed, which results in very high particle fluxes and track densities. The high radiation load poses strict requirements on the radiation tolerance of the detectors and readout electronics used. One of the main components of HERA- B is the Inner Tracker, which was developed and built by the Universities of Heidelberg, Siegen, and Zürich. The Inner Tracker measures tracks 6 – 25 cm away from the beam centre. It consists of 184 Micro-Strip Gas Chambers with Gas Electron Multipliers (GEM-MSGC) and contains in total about 120 000 analogue readout channels.

The first part of this thesis describes the readout system of the Inner Tracker. The design of the readout system was finalised based on the experience gained during several test beam experiments in 1998. In parallel to the installation of tracking chambers in HERA- B during autumn 1999 and spring 2000, the readout system was extended from a small test installation to the full system. The steps necessary to commission the readout system are described, and an overview over the software packages processing the raw data is given. Results of the first year of running at HERA- B are presented.

In the second part, the results of a feasibility study concerning the prospects of HERA-*B* to contribute to the field of Drell-Yan physics are presented. Drell-Yan production is considered as one of the possible topics of the physics programme for HERA-*B* besides \mathcal{CP} violation. The number of expected Drell-Yan events is estimated based on a measurement using the data of the run 2000 and an extrapolation about the detector performance after the upgrade during 2000/2001.

Chapter 1

The Experiment HERA-*B*

This chapter presents a brief overview over the experiment HERA-*B*. The original physics goal—measuring the \mathcal{CP} violating parameter $\sin 2\beta$ in the system of neutral B mesons—for which the experiment was proposed and designed is outlined, as well as the modified physics programme intended for the run period 2001/2002. Finally, the components of the HERA-*B* detector are explained.

1.1 The HERA Storage Ring

HERA-*B* is one of four high energy experiments which are located at the storage ring HERA¹ at DESY² in Hamburg. HERA is the world's only lepton-proton collider. The electrons³ have an energy of 27.5 GeV, and the protons an energy of 920 GeV. The storage ring has a circumference of 6.3 km and is located in the North-West of Hamburg, partly beneath the Volkspark. It is depicted schematically in Fig. 1.1, together with the cascade of pre-accelerators.

The two beams are brought to collision in two interaction zones (Hall North and Hall South), where the experiments H1 and ZEUS are situated. Their physics programme comprises the measurement of the proton structure with a resolution varying over more than five orders of magnitude, reaching partons with momentum fractions down to 10^{-6} . Studies of the hadronic final state include jet physics, diffractive scattering in deep inelastic scattering, and the photo-production of jets.

The experiment HERMES, which is located in the East experimental area, uses only the electron beam, which is longitudinally polarised for the experiment by means of spin rotators. Using an internal polarised gas target, HERMES investigates the spin structure of the nucleon.

Finally, HERA-*B* is located in the West experimental area. It uses the protons in the outer regions of the proton beam, which are brought to collision with thin wires. With this target in the halo of the proton beam, high interaction rates are possible without disturbing the operation of the other experiments. The physics programme of HERA-*B* and the detector are described in more detail below.

¹Hadron-Elektron-Ring-Anlage

²Deutsches Elektronen-Synchrotron

³or positron; both options were used several times so far. However, with positrons the lepton beam is much more stable and can reach higher currents, providing better running conditions and higher luminosities for the collider experiments. In the following, 'electron beam' and 'positron beam' are used interchangeably.

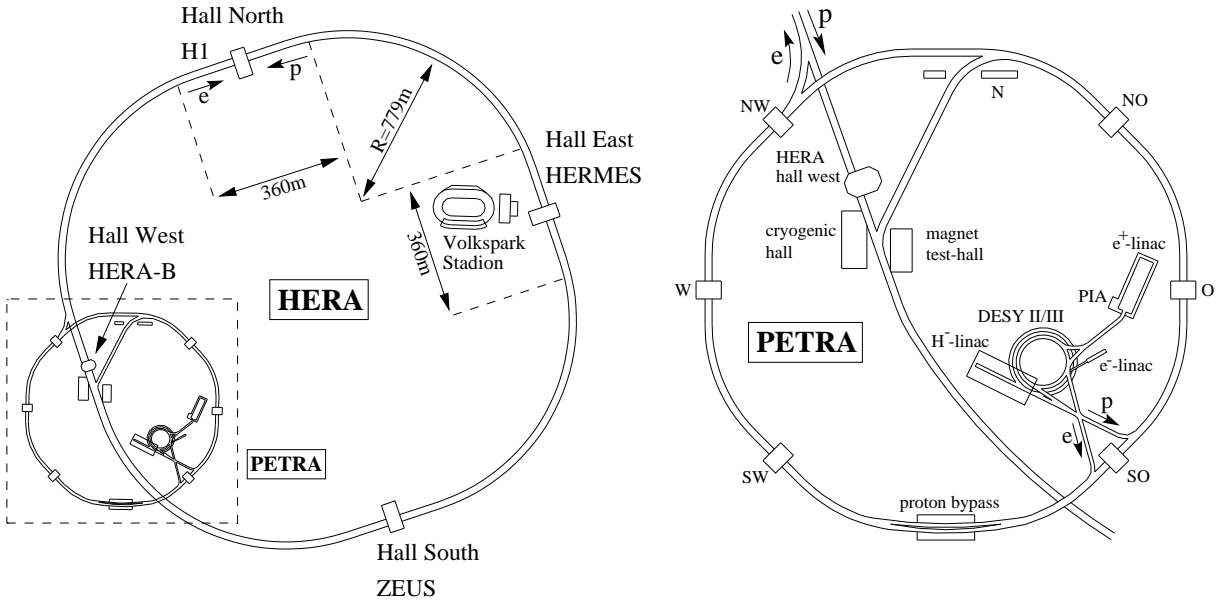


Figure 1.1: The HERA storage ring at DESY in Hamburg. *Left:* overview over the complete facility, which extends below the Volkspark. *Right:* the pre-accelerators DESY-II and PETRA which are situated on the DESY site, and the experimental area Hall West, where HERA-B is installed.

1.2 Physics Goals of HERA-B

The experiment HERA-B was proposed and designed to measure the violation of the \mathcal{CP} symmetry in the system of B^0/\bar{B}^0 -mesons. The violation of \mathcal{CP} symmetry was first observed in the system of $K^0-\bar{K}^0$ mesons [CCFT64], and the standard model of high-energy physics offers a mechanism which can explain the violation. Also the system of neutral B mesons should show \mathcal{CP} violation, caused by the same mechanism. While the effect is exceedingly small in the kaon system, it is predicted to be large in the B -system.

A series of experiments was planned and built in the past few years to measure \mathcal{CP} violation in the B -system: the first generation of ‘ B -factories’ BELLE ([BEL01], at KEK, Japan) and BaBar ([BAB01], at PEP-II, SLAC, USA) are built at asymmetric e^+e^- colliders whose centre-of-mass energy is near the $\Upsilon(4S)$ resonance. The small production cross section ($\sigma_{e^+e^- \rightarrow \Upsilon(4S)} \approx 1$ nb) is offset by luminosities of $\mathcal{L} \approx 3 \times 10^{33} \text{ cm}^{-2} \text{ s}^{-1}$. Both BaBar and BELLE reported first measurements on \mathcal{CP} violation in the B -system in summer 2000 (see below).

A different approach to produce the needed B mesons to measure \mathcal{CP} violation is pursued by HERA-B. Here the $b\bar{b}$ are produced in proton-nucleon collisions at a centre-of-mass energy of about $\sqrt{s} = 41.6$ GeV. Due to many problems during the development and commissioning of the detector, the start of HERA-B data taking was delayed by several years. Most of the detector problems could be solved in the meantime. Nevertheless, a significant contribution to this field cannot be expected from HERA-B at least during the run period 2001/2002. However, the intended physics programme imposed stringent demands on the detector design; it is therefore briefly explained in this section. An alternative physics programme for the run period 2001/2002 was proposed in December 2000. Its aim is to prove that the complete detector, including the First Level Trigger, is capable of doing valuable physics, while only setting goals which are realistically achievable.

1.2.1 Generation of \mathcal{CP} Violation in the Standard Model

The three fundamental discrete symmetries in the standard model are *Charge Conjugation* (\mathcal{C} , particles are replaced by their antiparticles) *Parity* (\mathcal{P} , *Space Inversion*), and *Time Reversal* (\mathcal{T}). The \mathcal{CPT} theorem [Lue57] states that any local, causal, relativistic field theory is invariant under the combined application of \mathcal{C} , \mathcal{P} , and \mathcal{T} . The weak interaction violates both \mathcal{C} and \mathcal{P} maximally. \mathcal{CP} violation is another special feature of the weak interaction; both the electromagnetic and the strong interaction conserve each of the two symmetries separately. The generation of \mathcal{CP} violation in the standard model is described in great detail *e.g.* in [har98] and [G⁺00].

CKM Matrix. The eigenstates of the weak interaction of quarks do not coincide with the mass eigenstates; the transition between the two bases is described by the Cabibbo-Kobayashi-Maskawa matrix V_{CKM} :

$$V_{\text{CKM}} = \begin{pmatrix} V_{ud} & V_{us} & V_{ub} \\ V_{cd} & V_{cs} & V_{cb} \\ V_{td} & V_{ts} & V_{tb} \end{pmatrix} \quad (1.1)$$

This mixing between the quarks implies that *e.g.* the decay of an s quark into an u quark involves the matrix element V_{us} (see Fig. 1.2). To conserve probability, V_{CKM} must be unitary if only three generations of quarks exist.

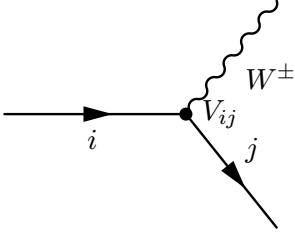


Figure 1.2: Weak interaction of two quarks i and j , taking into account the quark mixing described by the CKM matrix

The constraint of unitarity implies that the CKM matrix can be described using only four parameters; these could be three angles θ_i and one complex phase δ . However, nature exhibits a hierarchy in the mixing between the quark families, and most of the mixing angles are small; this is used to parametrise V_{CKM} using the real parameters λ , A , ρ , and η (Wolfenstein parametrisation, [Wol83]):

$$V_{\text{CKM}} \approx \begin{pmatrix} 1 - \lambda^2/2 & \lambda & A\lambda^3(\rho - i\eta) \\ -\lambda & 1 - \lambda^2/2 & A\lambda^2 \\ A\lambda^3(1 - \rho - i\eta) & -A\lambda^2 & 1 \end{pmatrix} \quad (1.2)$$

where $\lambda = \sin \theta_{\text{Cabibbo}} \approx 0.22$. Using the unitarity condition, relations between the parameters can be obtained, for example

$$V_{ud}V_{ub}^* + V_{cd}V_{cb}^* + V_{td}V_{tb}^* = 0 \quad (1.3)$$

or approximately

$$V_{ub}^* + V_{td} = \lambda V_{cb}^* . \quad (1.4)$$

Using the Wolfenstein parametrisation, this relation can be visualised in the complex (ρ, η) -plane as a triangle (the ‘unitarity triangle’, see Fig. 1.3). The angle β is connected to the CKM matrix elements by

$$\sin 2\beta = \text{Im} \left(\frac{V_{td} V_{tb}^*}{V_{ud}^* V_{ub}} \right) . \quad (1.5)$$

The current knowledge (as of end of 2000) about the parameters $\bar{\rho} = \rho(1 - \lambda^2/2)$ and $\bar{\eta} = \eta(1 - \lambda^2/2)$ is shown in Fig. 1.4 (from [CDF⁺00]).

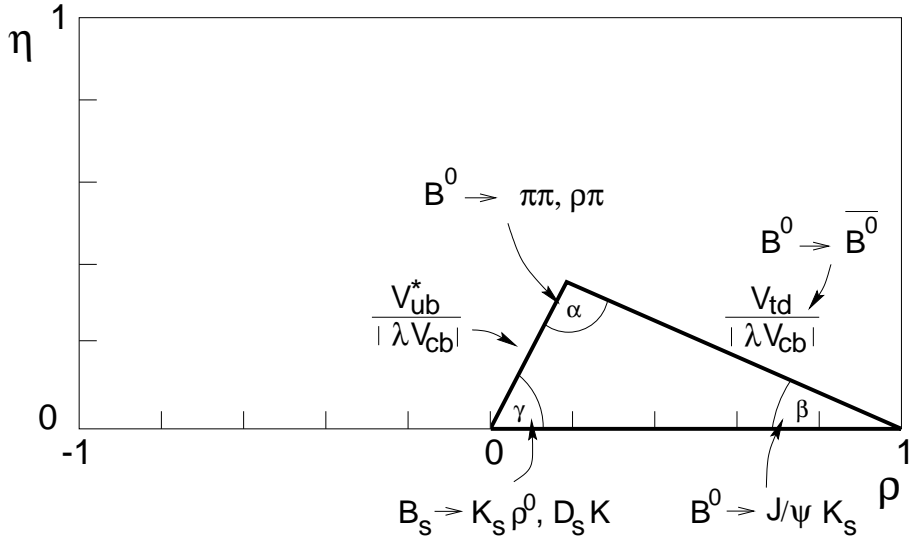


Figure 1.3: Unitarity triangle in the complex (ρ, η) -plane. It is a visualisation of one of the unitarity relations; if its area is non-zero, \mathcal{CP} is violated. Also indicated in the figure are different physics channels which can be used to measure constraints for the angles or sides of the triangle (figure from [Hau98]).

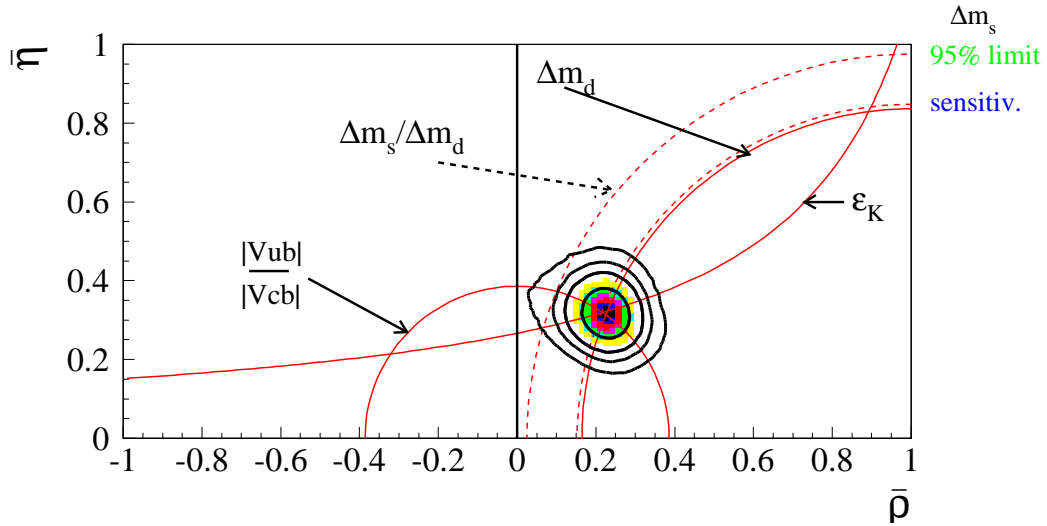


Figure 1.4: Knowledge as of end of 2000 about the unitarity triangle (from [CDF⁺00]): the contours show the allowed regions for $\bar{\rho}$ and $\bar{\eta}$ at 68 %, 95 %, 99 %, and 99.5 %.

Mixing in the B System. Like in the K system, the neutral B mesons can mix via diagrams like the box diagrams depicted in Fig. 1.5. Therefore, the two weak eigenstates $|B^0\rangle$ and $|\bar{B}^0\rangle$ will mix to give two states $B_{H,L}^0$:

$$|B_{H,L}^0\rangle \equiv p |B^0\rangle \mp q |\bar{B}^0\rangle \quad (1.6)$$

where p and q satisfy the normalisation condition $|p|^2 + |q|^2 = 1$. The two states B_H and B_L are those which travel through the detector. They are no longer degenerate, but have slightly different masses by $\Delta m_B \equiv m_H - m_L$ and decay widths Γ_H, Γ_L . The mass difference has been measured for the neutral B_d mesons to be [G⁺00]

$$x_d \equiv \frac{\Delta m_{B_d}}{\Gamma_{B_d}} = 0.73 \pm 0.03 ;$$

the lifetime difference $\Delta\Gamma_{B_d}$ is expected to very small.

An initially pure $|B^0\rangle$ state which is created at time $t = 0$ *e.g.* by a strong interaction propagates through the vacuum as a physical state $|B_{\text{phys}}^0\rangle$ which has the time evolution

$$|B_{\text{phys}}^0(t)\rangle = e^{-iMt} e^{-\Gamma t/2} \cos(\Delta m_B t/2) |B^0\rangle + \frac{q}{p} e^{-iMt} e^{-\Gamma t/2} i \sin(\Delta m_B t/2) |\bar{B}^0\rangle , \quad (1.7)$$

at a time $t > 0$ it therefore has a non-zero probability to be a $|\bar{B}^0\rangle$.

\mathcal{CP} Violation by Interference. With a complex phase present in the CKM matrix, \mathcal{CP} violation can be generated if two decay amplitudes interfere which contain complex conjugates of the same CKM matrix element. This condition is fulfilled in the mixing of B^0 with \bar{B}^0 mesons, which is mediated by intermediate weak reaction (see Fig. 1.5). If both B^0 and \bar{B}^0 can decay into the same final state f_{CP} which is a \mathcal{CP} eigenstate, the decay of a B^0 can therefore either take place directly, $B^0 \rightarrow f_{CP}$, or the B^0 can first oscillate into a \bar{B}^0 , $B^0 \rightarrow \bar{B}^0 \rightarrow f_{CP}$. The amplitudes for the two processes interfere. If a complex matrix element of V_{CKM} occurs in the mixing, the two decay rates are not the same, and \mathcal{CP} is violated. This type of \mathcal{CP} violation is called *\mathcal{CP} violation in the interference between decays with and without mixing* [har98].

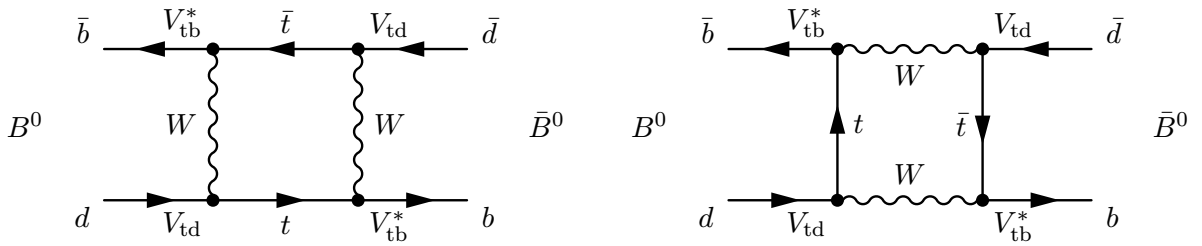


Figure 1.5: Lowest order Feynman diagrams describing the mixing of $B^0 \leftrightarrow \bar{B}^0$. The main contribution to the loops comes from t, \bar{t} quarks.

This can be observed by comparing the decay rates into final \mathcal{CP} eigenstates of a time-evolving B state that begins at time $t = 0$ as a B^0 to those of the state that begin as a \bar{B}^0 :

$$\begin{aligned} a_{f_{CP}} &= \frac{\Gamma(B_{\text{phys}}^0(t) \rightarrow f_{CP}) - \Gamma(\bar{B}_{\text{phys}}^0(t) \rightarrow f_{CP})}{\Gamma(B_{\text{phys}}^0(t) \rightarrow f_{CP}) + \Gamma(\bar{B}_{\text{phys}}^0(t) \rightarrow f_{CP})} \\ &= \frac{(1 - |\lambda_{f_{CP}}|^2) \cos \Delta m_B t - 2 \text{Im} \lambda_{f_{CP}} \sin \Delta m_B t}{1 + |\lambda_{f_{CP}}|^2} . \end{aligned} \quad (1.8)$$

Here, $\lambda_{f_{CP}}$ is the parameter which decided if \mathcal{CP} is violated. It is defined as the ratio of the decay amplitudes into the final state f_{CP} ,

$$\lambda_{f_{CP}} \equiv \frac{q}{p} \frac{\langle f_{CP} | H | \bar{B}^0 \rangle}{\langle f_{CP} | H | B^0 \rangle}. \quad (1.9)$$

The ‘cleanest’ decay modes are those where one \mathcal{CP} violating phase dominates; for these modes, the hadronic uncertainties in λ cancel.

1.2.2 Physics with B Mesons and \mathcal{CP} Violation in B Decays

The Gold-Plated Decay. The favoured decay mode of the B^0/\bar{B}^0 in which \mathcal{CP} violation can be measured is the so-called *gold-plated decay*

$$B^0 \rightarrow J/\psi K_s^0.$$

It has the advantage that the decay proceeds dominantly through the tree diagram shown in Fig. 1.6. Other diagrams involving W -loops (‘penguin’ diagrams) are very difficult to calculate; they are however doubly suppressed and can be neglected for this decay mode. Besides being ‘gold-plated’ theoretically, this decay channel has a clean experimental signature.

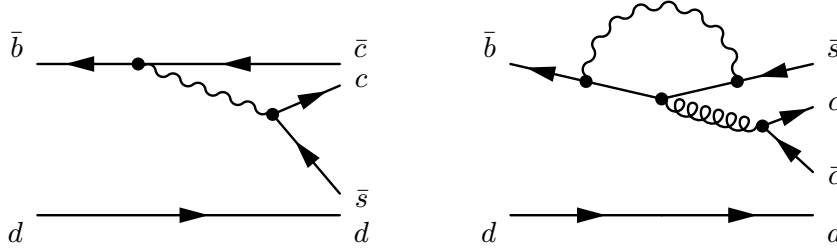


Figure 1.6: Tree level (*left*) and ‘QCD penguin’ diagram (*right*) for the ‘gold-plated’ decay $B^0 \rightarrow J/\psi K_s^0$. Compared to the tree level diagram, the QCD and electroweak penguin diagrams are strongly suppressed for this special decay mode.

The measurement consists in counting how many B^0 and how many \bar{B}^0 decay into the \mathcal{CP} eigenstate $J/\psi K_s^0$. The resulting asymmetry $a(t)$ is connected to the angle β of the unitarity triangle like this:

$$a(t) \equiv \frac{N(\bar{B}^0 \rightarrow J/\psi K_s^0) - N(B^0 \rightarrow J/\psi K_s^0)}{N(\bar{B}^0 \rightarrow J/\psi K_s^0) + N(B^0 \rightarrow J/\psi K_s^0)} = \sin 2\beta \sin \Delta m_b t. \quad (1.10)$$

Besides reconstructing the decay of the B , it is also needed to determine whether a B^0 or a \bar{B}^0 has decayed. This can be done by *tagging* the other B meson which contains the other produced b quark. Its flavour is determined by the charge of a lepton or kaon produced in its decay (see Fig. 1.7).

Recently, both BaBar and Belle reported first measurements of $\sin 2\beta$ using the gold-plated decay. Their results are

$$\begin{aligned} \sin 2\beta &= 0.34 \pm 0.20 \text{ (stat)} \pm 0.05 \text{ (syst)} && \text{BaBar, [A}^+01\text{b]} \\ \sin 2\beta &= 0.58^{+0.32}_{-0.34} \text{ (stat)}^{+0.09}_{-0.10} \text{ (syst)} && \text{Belle, [A}^+01\text{a]} \end{aligned}$$

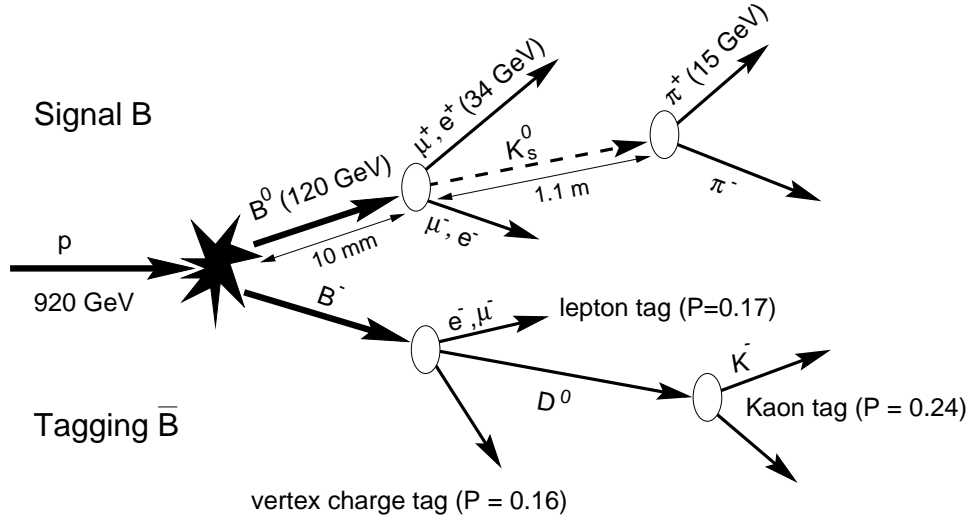


Figure 1.7: The ‘gold-plated’ decay mode $B^0 \rightarrow J/\psi K_s^0 \rightarrow \mu^+ \mu^- \pi^+ \pi^-$. The flavour of the B meson decaying into $J/\psi K_s^0$ (*top*) is measured by tagging the other B (*bottom*), using its decay into a lepton (*lepton tag*) or a kaon (*Kaon tag*). The decay lengths and momenta indicated in the figure are valid for the conditions at HERA-B.

The experimental challenge to measure $\sin 2\beta$ in the gold-plated decay at HERA-B consists in the vast difference between the expected rate of events with $B \rightarrow J/\psi K_s^0$ to all produced events. With a beam momentum of 920 GeV, the total inelastic cross section for proton-nucleon scattering is of the order of 13 mb/nucleon, while the production cross section of a $b\bar{b}$ pair is only about 10–20 nb/nucleon. Additionally, the produced B mesons have many decay channels; the branching ratio into the gold-plated decay mode is only $\text{BR}(B^0 \rightarrow J/\psi K_s^0) = 8.9 \times 10^{-4}$ [G⁺00]. Together with the branching ratio $\text{BR}(J/\psi \rightarrow \mu\mu) = 0.059$ and trigger and reconstruction efficiencies, about 10^{11} interactions result in one triggered, reconstructed gold-plated decay written to tape. For a significant measurement of $\sin 2\beta$, about 2000 events are needed; if these are to be collected within one year of running, this implies a mean interaction rate of about 40 MHz.

B_s mixing and Rare Decays. Other possible topics for HERA-B in the field of B physics are the measurement of mixing in the B_s system, and rare decays of b -flavoured mesons.

1.2.3 Proposed Physics Programme for 2002

The proposed physics programme for the run 2002 is documented in an [HER01]. It concentrates on the physics feasible with an experiment which is optimised for the detection of lepton pairs with high transverse momentum, but where the expected trigger rates are not high enough to be competitive in the field of B physics.

The physics programme comprises the measurement of nuclear effects in charmonium suppression and the determination of the $b\bar{b}$ production cross section in proton-nucleon collisions at $\sqrt{s} \approx 41$ GeV.

Other topics which were investigated for inclusion into the physics programme were open charm production, prompt photon production and measurements in the field of Drell-Yan physics. The prospects of HERA-B in the latter field were investigated during the work on this thesis. The results of this study are presented in Part II of this thesis.

Charmonium Suppression. The A -dependent suppression of charmonium production is of considerable interest. In heavy ion collisions, the relative suppression of J/ψ production relative to the production of Drell-Yan pairs or open charm is generally believed to be a tell-tale sign of the formation of a quark-gluon plasma. Such a suppression has been observed by NA50 in central lead-lead collisions (see for example [A⁺00]). However, charmonium production in heavy-ion collisions is far from being well understood; the different theoretical models lack basic experimental input and give vastly differing predictions.

The existing measurements mainly cover the phase space region with $x_F > 0$, while HERA- B covers the range of $-0.4 < x_F < 0.3$, extending the range where model predictions can be tested. The possibility to measure simultaneously the production of J/ψ , ψ' , $\chi_{c1,2}$, and even Υ allows the determination of *relative* suppression factors which are almost completely free of systematic effects.

Measurement of the $b\bar{b}$ Cross Section. The production cross section $\sigma_{b\bar{b}}$ at $\sqrt{s} = 41$ GeV is known only to about one order of magnitude. The measurement of $\sigma_{b\bar{b}}$ at HERA- B will most likely proceed using the inclusive decay $B \rightarrow J/\psi X$, identifying the J/ψ from B decays with a detached secondary vertex. The cross section can then be obtained by scaling the ratio $N_{B \rightarrow J/\psi X} / N_{\text{prompt } J/\psi}$ with the cross section for prompt J/ψ production. This is expected to give a measurement which is accurate to about 20 %, the error being dominated by the uncertainty on $\sigma_{J/\psi}$.

Apart from being an interesting measurement in itself, constraining perturbative QCD calculations for the production of heavy quarks, knowledge about $\sigma_{b\bar{b}}$ is essential to assess the prospects of HERA- B to pursue a programme in B physics after 2002.

1.3 Overview over the Detector

A schematic overview of HERA- B is shown in Fig. 1.8. The experiment is a typical forward spectrometer with a multi-wire target followed by a Vertex Detector. The spectrometer consists of a warm dipole magnet with a field integral of $\int B dl \approx 2.2$ Tm and a series of tracking stations in front, behind and inside the magnet. Particle identification is provided by a Ring Imaging Čerenkov Counter (RICH), an Electromagnetic Calorimeter (ECAL) and a Muon Detector System. The complete detector had to fit into the existing West hall of HERA, posing a length limit of about 20 m to the experiment.

The coordinate system used throughout this thesis has its origin at the target system. The z axis is along the direction of the proton beam, the y axis points upwards, and the x axis points to the centre of the HERA ring.

Target. The internal wire target consists of two stations with four wires each. The wires can be moved into the halo or the outmost regions of HERA's proton beam. This allows to choose the desired interaction rate within a wide range. The interaction rate is measured by a set of scintillator hodoscopes which are mounted at the exit window of the RICH. The target position relative to the beam is actively controlled to obtain a fixed interaction rate.

The measurement of \mathcal{CP} violation within a reasonable time requires interaction rates as high as 40 MHz. To achieve this rate with the bunch structure of HERA's proton beam which has a bunch spacing of 96 ns, multiple interactions have to occur during one bunch crossing. The reconstruction program should be able to separate the different interactions. This is achieved by using several (eventually all eight) target wires simultaneously. Charge integrators which monitor the interactions produced by each wire help to distribute the interaction rate evenly among the wires. During the run period 2000, the first target station was equipped with titanium wires,

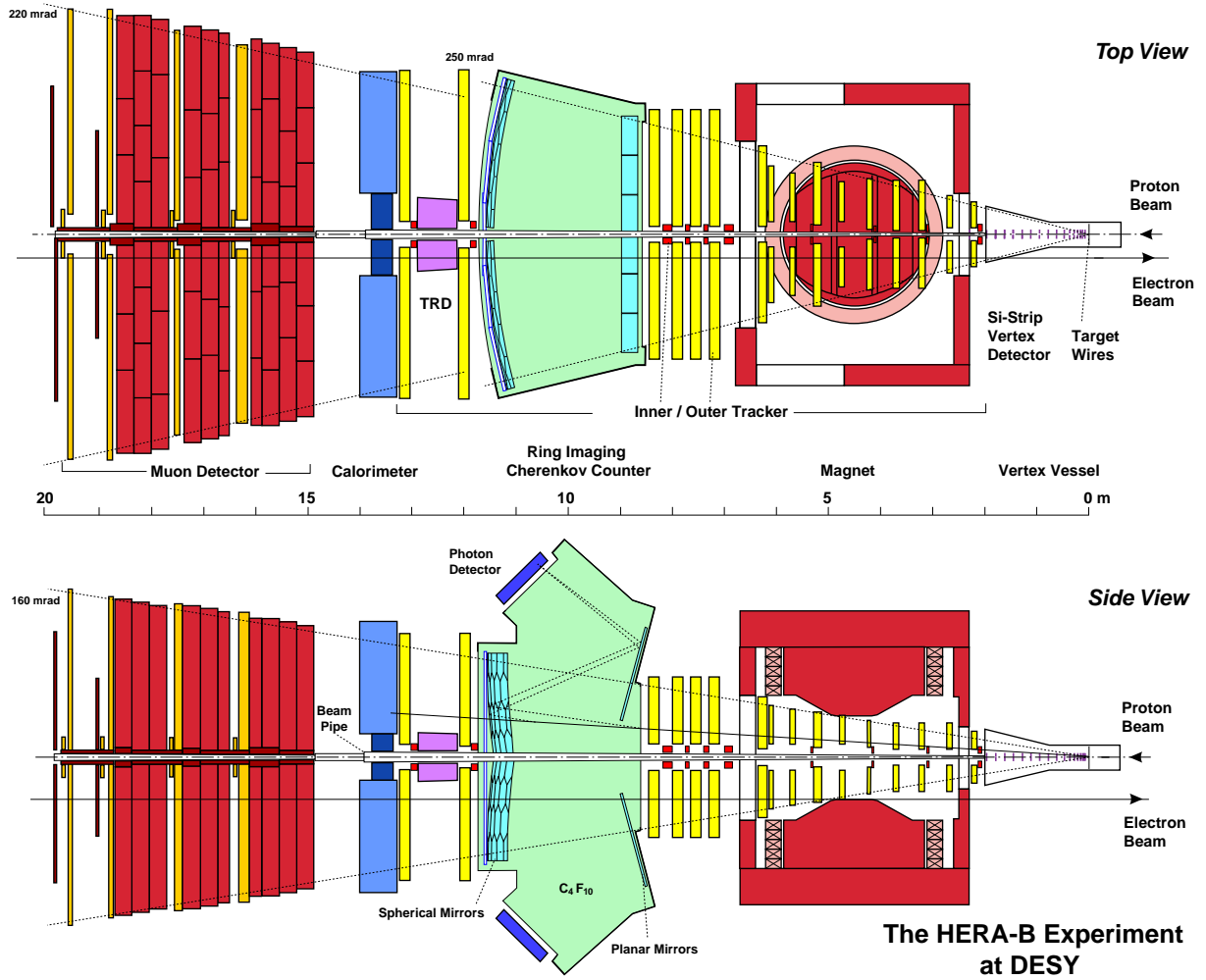


Figure 1.8: Schematic overview of the HERA-B experiment. The protons enter from the right. From right to left visible are the vertex vessel with the target wires and the Vertex Detector System, the spectrometer magnet with tracking chambers, and four layers of tracking chambers between the exit of the magnet and the RICH. Between RICH and the electromagnetic calorimeter, another two tracking layers are installed. The Muon System is located downstream of the ECAL, behind a shielding of iron and armoured concrete.

while the second station also contained wires made from aluminium, carbon, and tungsten. For the run period 2002 a similar setup is planned. The different target materials allow to measure nuclear effects in the production of *e.g.* charmonium. These measurements can be performed using two wires at the same time, drastically reducing the impact a possible change of the detector configuration has on the systematic error.

The target mechanics is mounted together with the Vertex Detector System into one vacuum vessel which is part of the primary vacuum of the proton beam.

Spectrometer

Vertex Detector System. The Vertex Detector System (VDS) is built of 64 double-sided silicon micro-strip detectors which are arranged in eight super-layers. The detectors have a readout pitch of $50\ \mu\text{m}$. A system of manipulators and vacuum bellows (*roman pots*) allows to retract the detectors while the beam is injected, and to move the detectors in their measuring position once stable beam conditions have been reached. In its nominal position, about 10 mm away from the beam core, the detector can measure tracks with polar angles from 10–250 mrad.

The track information measured in the VDS is used to reconstruct the primary interaction vertices as well as detached secondary vertices from decays like $B \rightarrow J/\psi K_s^0$ or $K_s^0 \rightarrow \pi\pi$. The secondary vertex resolution obtained during the run 2000 are $\sigma_x \approx 70\ \mu\text{m}$ perpendicular to the beam and $\sigma_z \approx 700\ \mu\text{m}$ along the beam direction.

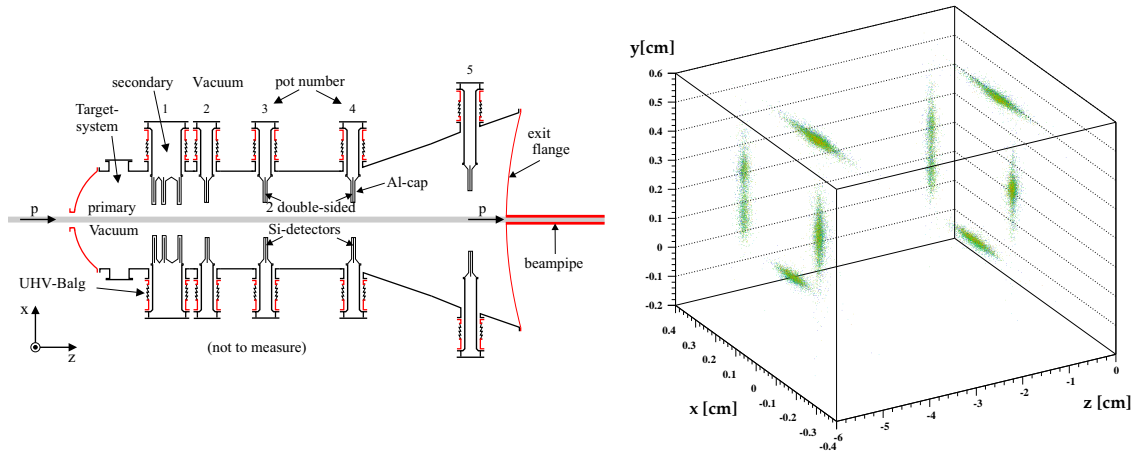


Figure 1.9: *Left:* Schematic view of the Vertex Vessel. *Right:* Primary vertices reconstructed with the VDS during a multi-wire run which used all eight target wires. Dimensions in cm (figures from [Mas00]).

Spectrometer Magnet. The spectrometer magnet is a warm (non-superconducting) dipole magnet with a field integral of 2.2 Tm. The magnetic field is parallel to the y axis, deflecting charged particles crossing the magnet in the (xz) plane.

A system of three magnets upstream of HERA-B compensates the deflection the proton beam experiences while travelling through the spectrometer magnet; the electron beam which has also to pass through the magnet is protected by a specifically shaped pole face of the spectrometer magnet, a compensating coil and a series of shielding cylinders around the beam pipe.

Tracking System. Along the beam axis, the stations of the tracking system are installed. The track density is highest near the beam pipe and falls off approximately like $1/r_{\perp}^2$ with transverse distance from the beam. To cope with the vastly different particle fluxes and the ensuing different requirements on spatial resolution, the tracking system is divided into two parts, the Inner and the Outer Tracker. The Inner Tracker uses GEM-MSGCs with an intrinsic resolution of about $100\ \mu\text{m}$; it covers the area up to $r_{\perp} \approx 25\ \text{cm}$. It is described in detail in Chapter 2.

With a small overlap to the Inner Tracker, the Outer Tracker covers the remaining acceptance up to polar angles of $\theta_x \approx 250\ \text{mrad}$. It is built of honeycomb drift chambers with a cell size of $5\ \text{mm}$ in the inner and $10\ \text{mm}$ in the outer part. In both tracking systems, each tracking station is equipped with several layers of detectors; the counting wires are oriented perpendicular to the bending plane of the magnet. Some of these layers are additionally rotated by a *stereo angle* of $\pm 5^\circ$, so that also the coordinate along the counting wire of a passing particle can be measured. The hit resolution which was reached during the run 2000 is about $350\ \mu\text{m}$ perpendicular to the wire [HER00b].

High- p_T System. The high- p_T system consists of three super-layers of tracking chambers which are placed inside the spectrometer magnet. In its inner part, it is made of gas pixel chambers, while the outer part consists of straw tube drift chambers with cathode pad readout. Using the segmentation in x and y , the high- p_T system looks for tracks with a high transverse momentum and signals them to the First Level Trigger.

Particle Identification

A series of detectors serves to identify particles. This is needed for most of the physics studies intended for HERA- B ; for example, tagging the second B in the golden decay with high efficiency requires an excellent separation of π and K .

Ring Imaging Čerenkov Counter. The Ring Imaging Čerenkov Counter (RICH) exploits the Čerenkov radiation to distinguish between different particle types: a particle passing through a medium with refractive index n emits photons if its velocity βc is larger than the speed of light c/n . The photons are emitted on a cone around the path of the particle; the opening angle θ_C of the cone depends on n and β :

$$\cos \theta_C = 1/(\beta n) .$$

The photons are focused by a spherical mirror to a ring whose radius depends on θ_C . If the particle's momentum $p = m\beta/\sqrt{1-\beta^2}$ is known, *e.g.* measured by the tracking system, the information about the Čerenkov angle allows to distinguish between particles of different masses m . To a good approximation, for each particle type the relation between θ_C^2 and $1/p^2$ is linear.

The HERA- B RICH uses perfluoro-butane (C_4F_{10}) as a radiator; this gas has a refractive index of $n - 1 \approx 3 \times 10^{-3}$, leading to a Čerenkov angle of $\theta_C = 51.5\ \text{mrad}$ for particles with the velocity $\beta = 1$. The Čerenkov light is read out by photomultiplier tubes.

Electromagnetic Calorimeter. The Electromagnetic Calorimeter (ECAL) is a sampling calorimeter of the ‘shashlik’ type: each cell consists of a sandwich of absorber and scintillator plates; the light output of the scintillator is collected by wavelength shifting fibres and guided parallel to the beam direction to photo-multipliers. The ECAL is segmented into an inner, a middle and an outer part, with cell sizes of $2.23 \times 2.23\ \text{cm}^2$, $5.58 \times 5.58\ \text{cm}^2$, and $11.15 \times 11.15\ \text{cm}^2$,

respectively. In the inner part, the absorber consists of a tungsten-nickel-iron alloy, while the middle and outer parts use lead. The total radiation length is about $20 - 22 X_0$.

The ECAL measures the deposited energy and the position of electrons and photons with a fine granularity, providing information for many interesting physics channels, *e.g.* decays of $J/\psi \rightarrow e^+e^-$. Information about clusters with high energy (and transverse energy) deposition is very quickly available and is used as one of the pretriggers. Additionally, the ECAL is used to distinguish electrons and photons from hadrons, providing particle identification for e and γ .

Muon System. To identify muons *e.g.* from decays $J/\psi \rightarrow \mu\mu$, a system of hadron absorbers and tracking chambers is installed downstream of the ECAL. The absorber consists of iron and armoured concrete; it is instrumented with four tracking super-layers of the Muon System. In total, the absorber has a thickness of about 20 interaction lengths. The innermost part of the Muon System is made of Gas Pixel Chambers with a cell size of about 9×9 mm²; they cover radial distances from 14 to 30 – 40 cm around the beam axis.

In the first two super-layers MU1 and MU2, the outer part consists of proportional wire chambers which are arranged in three stereo views of 0° and $\pm 20^\circ$. The last two super-layers, MU3 and MU4, are built of single layers of drift chambers (stereo angle 0°) with cathode pad readout. The readout pads have a size of about $12 \times 10 \text{ cm}^2$. Since very little absorber material is placed between these two layers, pad coincidences can be used as a pretrigger signal.

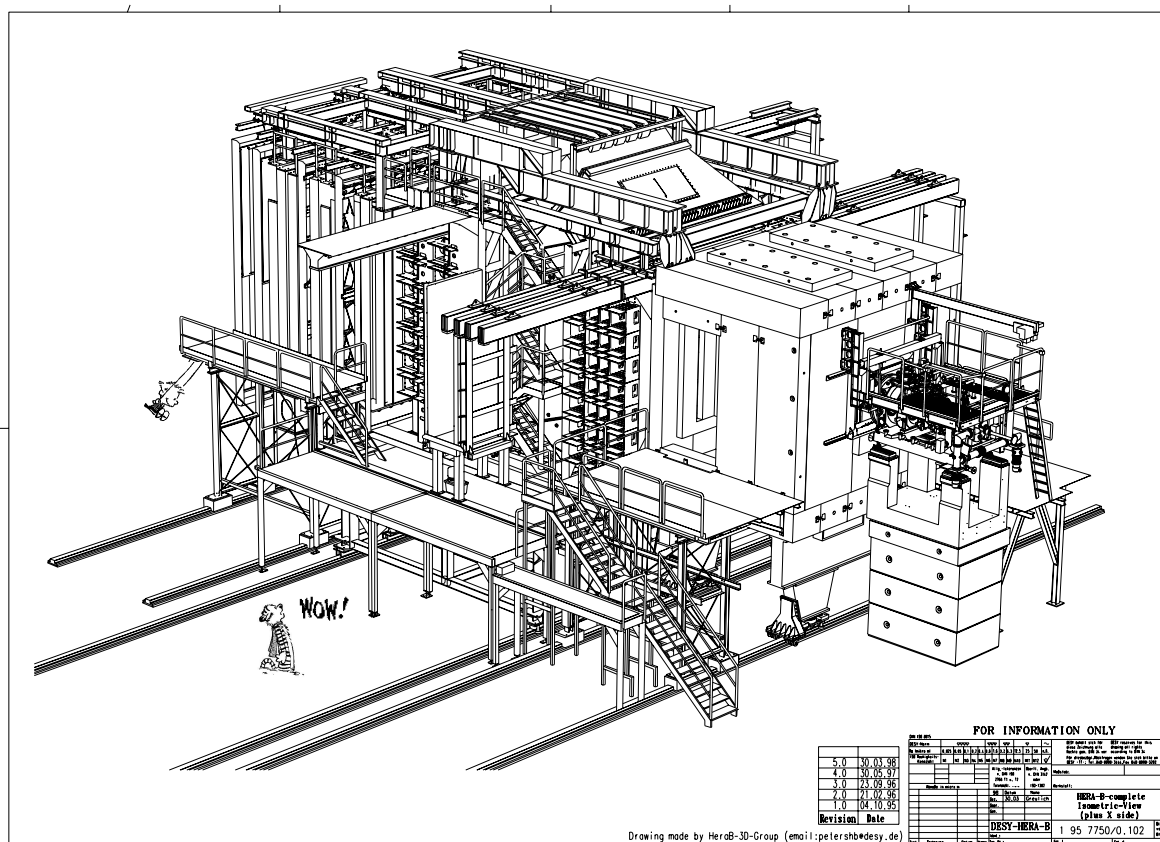


Figure 1.10: Isometric drawing of the HERA-B detector.

1.4 Trigger

It is not feasible to read out and record the complete detector data for every event; with 600 000 detector channels and a bunch crossing rate of 10 MHz this would amount to more than 6 Tbit/s. The tiny ratio of interesting events (*e.g.* from B production) to all produced interactions precludes a simple down-scaling of the trigger rate. Therefore, a highly selective event filter has to be used which suppresses most of the background events and keeps the interesting ones with high efficiency. Rejection factors of the order $\mathcal{O}(10^5)$ have to be reached. This is the task of the trigger system.

The trigger design of HERA- B foresees a multi-stage trigger scheme. According to the main physics goal at the time of design, already at the first trigger level a pair of lepton candidates is searched which point back to the target region. The description given here reflects the intended mode of operation for the run period 2002; during the run 2000, not all components of the trigger chain could be used as designed.

1.4.1 Pretriggers

Three pretrigger systems provide fast information on track candidates, which is then passed to the FLT:

- The ECAL pretrigger searches for clusters of 3×3 calorimeter cells where a local maximum of deposited energy can be found. Programmable thresholds can be applied to the cluster energy and the ratio of the energies deposited in the centre cell and its neighbours. The resulting centre-of-gravity of the cluster is then converted into a Region of Interest (RoI) for the First Level Trigger.
- The high- p_T pretrigger searches for coincidences in projective segments in the pad and pixel chambers of the three super-layers of the high- p_T system. This pretrigger offers the possibility to trigger on non-leptonic decay modes of B mesons, *e.g.* $B^0 \rightarrow \pi^+ \pi^-$, making a wide field of rare B decays and other \mathcal{CP} violating channels available.
- The muon pretrigger uses the data from the cathode pads in the super-layers MU3 and MU4 of the Muon System. It requires coincident hits which form a track segment pointing back to the target region.

1.4.2 First Level Trigger

The First Level Trigger is a hardware trigger. It implements a discrete Kalman-filter algorithm to trace tracks through the detector. Starting from the pretrigger seeds given by the Muon System or the ECAL, the FLT extrapolates a *region of interest* (RoI) into the next super-layer of the tracking system, using the assumption that the track originates from the target. If a coincidence of hits in all stereo-layers of the tracking station can be found within the RoI, a refined RoI is determined for the next tracking chamber. This procedure is shown schematically in Fig. 1.11.

If the FLT was able to successfully trace a track from the pretrigger seed to the exit of the spectrometer magnet, the Track Parameter Unit (TPU) computes an estimate for the momentum of the track. For each pair of trigger tracks, the invariant mass of the track pair is calculated. If the mass exceeds a threshold, the event is triggered. The decision whether to keep an event has to come within $12.2 \mu\text{s} \hat{=} 128\text{BX}$ cycles, otherwise the event is discarded. The maximal FLT output rate which can be digested by the following trigger stages is about 50 kHz.

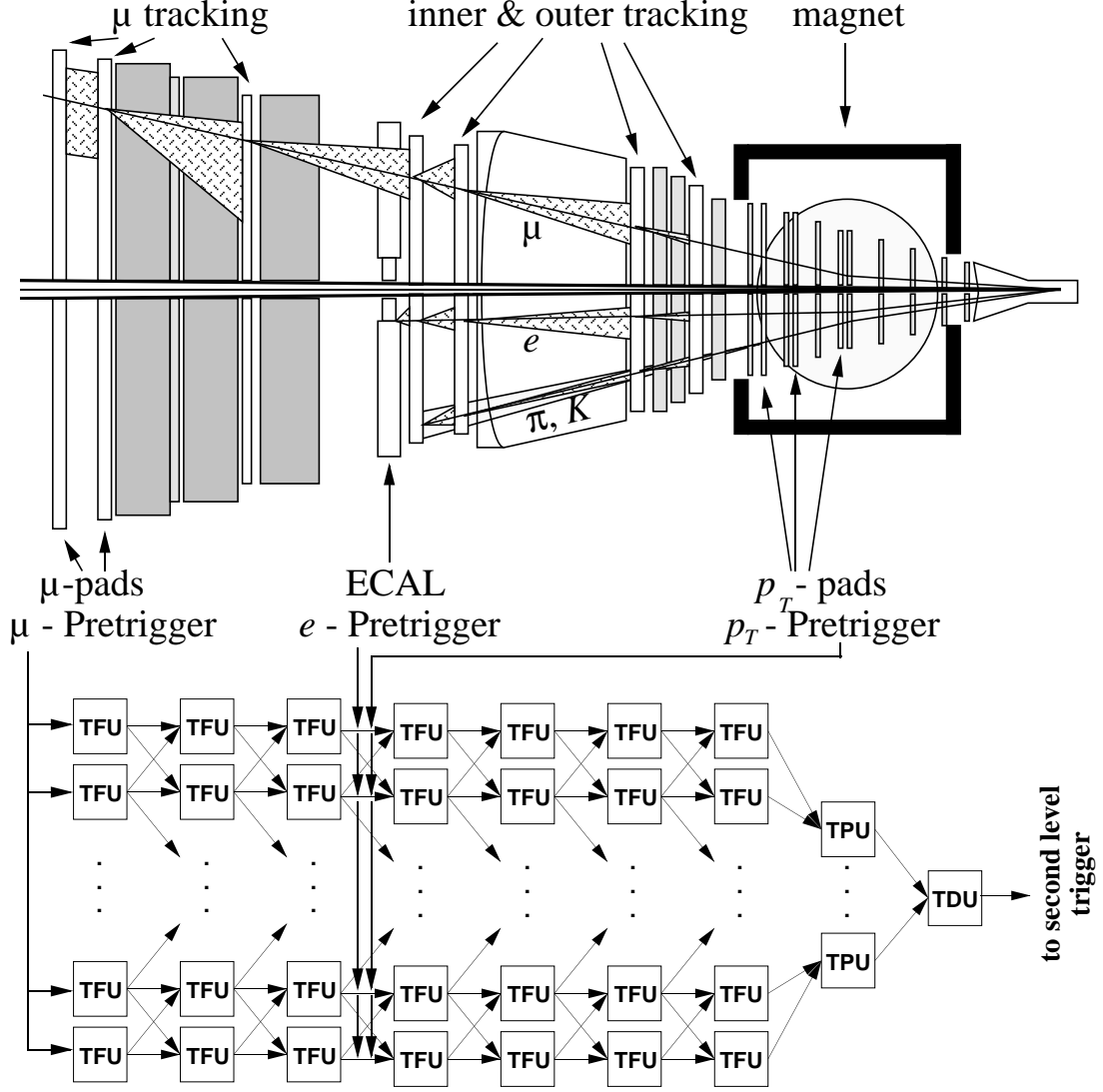


Figure 1.11: Sketch of the FLT implementation [HER00b]. The hit information of four tracking super-layers is transferred into Track Finding Units (TFU). Starting from seeds given by the three pretrigger sources, the TFUs extrapolate Regions of Interest (RoIs) into the next trigger layer upstream and search for coincident hits in these regions. If a coincidence was found, the RoI is refined and projected into the next super-layer. Tracks which were successfully traced through the complete detector behind the magnet are passed to the Track Parameter Units (TPUs), which computes an estimate for the momenta. This information is then passed to the Track Decision Unit (TDU) which decides whether to keep or discard the event. In case of a positive decision, the regions of interest and the found track parameters are passed to the Second Level Trigger.

To limit the amount of data which has to be transferred from the detector readout electronics to the FLT processors, the FLT uses only four of all installed tracking super-layers, and the information from these layers is reduced to digital information ‘hit’/‘no hit.’ The trigger electronics of the Inner Tracker combines the hit information of four neighbouring channels, resulting in a much coarser resolution which is available to the FLT.

During the run period 1999/2000, the FLT was still in the commissioning phase. At the end, a reliable trigger requiring one track found by the FLT could be used routinely, but the results of runs triggered with a two-track mode are not yet understood.

1.4.3 Second and Third Level Trigger

The following trigger levels are implemented as software triggers; the trigger programs run on a farm of about 240 industry-standard PCs (they are called *second level processors*, SLP). After the FLT decided to keep an event, the complete event information is transferred from the sub-detector specific front-end electronics into the Second Level Buffers (SLB). These are digital signal processors which are used to buffer the detector data for a longer time ($\mathcal{O}(100\text{ ms})$). A dedicated custom network using the same type of signal processors as an active *switch* allows each of the SLPs to access the event data from every sub-detector.

Each triggered event is assigned to one node of the SLT farm for processing. The SLT algorithm starts with the RoIs defined by the FLT and refines the tracks, using the drift-time information of the OTR, and the full resolution of the Inner Tracker, adding hits from more layers if necessary. The search is however still restricted to the RoIs, so that only a limited amount of data has to be transferred from the SLBs to the SLPs. The successfully confirmed tracks are then propagated through the spectrometer magnet using a look-up table for the magnetic field. Finally, track segments in the Vertex Detector are reconstructed. The event is accepted if the trigger tracks can be matched to VDS track segments which form a common vertex.

Only at this point the complete event data are transferred from the SLBs into the SLP which processes the event. The *event builder* assembles the data to form one complete event record. The option to call a Third Level Trigger routine at this stage exists, but was not used during the run 2000. The event data is then transferred to the Fourth Level Trigger Farm via a Fast-Ethernet network.

1.4.4 Fourth Level Trigger

The Fourth Level Trigger farm consists of another about 200 processors. Here, the complete event is reconstructed, making full use of all detector information and the best known calibration and alignment constants. The possibility to reject events also at this stage is foreseen, although it was not used in the run period 2000. An event classification routine searches for signatures of interesting physics processes; the result of this search is also stored with the event data, providing a fast pre-selection for analysis jobs. The software performing this online reconstruction is exactly the same which also used for the offline data analysis.

Finally, the event data, containing the raw detector information and the output of the reconstruction, is transferred to the DESY computing centre, where it is archived (*logged*) on tape. Including all information, about 150 kB per event **check** are needed; since the logging rate is restricted to about 10 MB/s, the output rate of the Fourth Level Trigger farm should not exceed about 30 events per second.

1.5 Data Acquisition System

The Data Acquisition System is depicted schematically in Fig. 1.12. It is closely connected to the trigger system. Its main components are

- The Fast Control System [Ful99]. It is the interface between the DAQ system, the front-end electronics of all sub-detectors and the trigger system. It distributes the bunch crossing clock (*BX clock*) and trigger information (trigger number, BX number of the trigger, trigger type) to the front-ends to synchronise the readout. The FCS also provides a means for the later trigger stages to reduce (*throttle*) the FLT trigger rate in case the network gets congested; throttling the FLT produces dead time.
- The system of Second Level Buffers (SLBs) and the switch connecting the SLBs with the processors of the Second Level Trigger farm [Wag00]. This is done using about 1 200 digital signal processors (SHARCs, ADSP-21060 from Analog Devices), which buffer the detector data.
- The Second Level Trigger (SLT) Farm. It consists of 240 off-the-shelf PCs (with Intel Pentium II processors running at 350 MHz), which are equipped with a custom-made interface to the SHARC network.
- The Fourth Level Trigger (4LT) Farm consists of another group of single- and dual-processor PCs, with altogether 200 CPUs. The connection between the SLT and the 4LT farm is done using a switched Fast-Ethernet network; the up-link to the computing centre where the data is archived centrally is a Gigabit-Ethernet line.

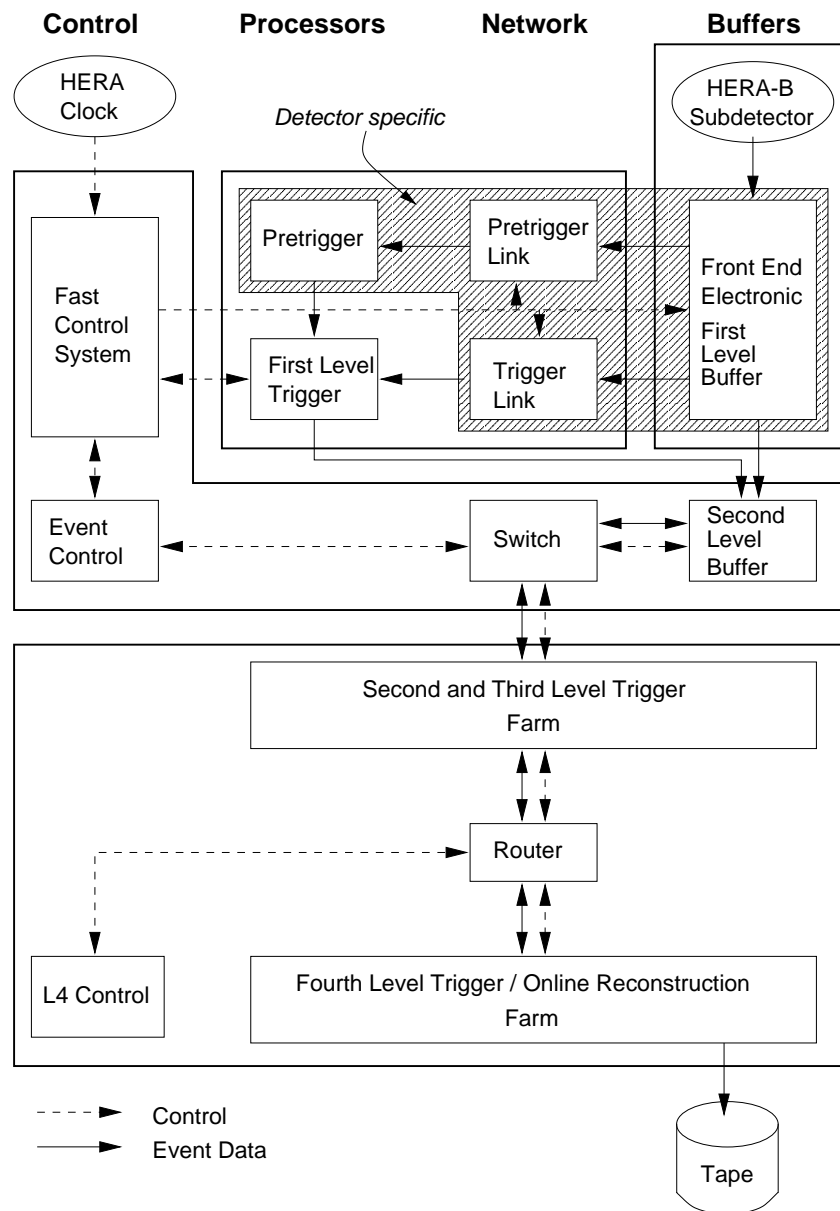


Figure 1.12: The HERA-B Data Acquisition System (from [Med97]).

Part I

Readout for the Inner Tracker of **HERA-*B***

Chapter 2

The Inner Tracker of HERA-*B*

As explained in the previous chapter, HERA-*B* is a high rate experiment. In order to cope with the high particle flux and the ensuing high occupancies, the HERA-*B* tracking system is divided in two main parts, which are using different geometries and detector technologies. In the centre-of-mass system of the proton-nucleon system, the backwards hemisphere ($\eta^* < 0$ in the proton-nucleon centre-of-mass system) is covered by the Outer Tracker, while the Inner Tracker covers most of the forward hemisphere. The Outer Tracker covers distances perpendicular to the beam from about 20 cm up to 290 cm, corresponding to track angles up to 250 mrad. It consists of honeycomb drift chambers with cell sizes of 5 mm in the inner part and 10 mm in the outer part. The Inner Tracker covers the region from the inner border of the Outer Tracker down to about 6 cm around the beam, measuring tracks with slopes from 10 – 100 mrad. In both tracking systems the counting wires are oriented vertically, perpendicular to the bending plane of the spectrometer magnet. The Inner Tracking system was developed and built by the Universities of Heidelberg, Siegen, and Zürich. In this chapter, the detectors developed for the Inner Tracker and the configuration at HERA-*B* are presented.

2.1 Requirements

From the physics programme intended for HERA-*B*, the following requirements on the Inner Tracking system are derived:

Radiation tolerance and rate capability. The Inner Tracker covers the region from 6 – 25 cm around the beam pipe, where the track density is highest. The particle flux varies from $2 \times 10^4 \text{ mm}^{-2} \text{ sec}^{-1}$ in the innermost region to $2 \times 10^3 \text{ mm}^{-2} \text{ sec}^{-1}$ at the outer edge of the Inner Tracker at a nominal interaction rate of 40 MHz, which was foreseen at the time of HERA-*B*'s design [L⁺95]. This translates to a radiation dose of up to 1 Mrad/year, which the detectors have to withstand for several years without a serious degradation in performance. Also, the detectors must be capable of operating at such high counting rates without loss in detection efficiency. Operation experience showed that the presence of heavily ionising particles (HIPs) in hadronic beams poses a very severe constraint because they can induce fatal discharges in the chambers.

Granularity. The granularity of the detector has to be chosen such that the maximal occupancy (the percentage of readout channels which are hit on average in each event) does not exceed 5–10%. If the occupancy is significantly higher, the trigger and the pattern recognition and track reconstruction software have a much harder job to find the correct tracks. This requirement poses a constraint on the maximal length of a readout strip, given a certain readout

pitch: to obtain the needed resolution, the Inner Tracker chambers should have a readout pitch of 300 μm (see below), and therefore have strips which are not longer than about 25 cm.

Spatial Resolution. The requirements on the spatial resolution of the Inner Tracker are moderate, since the resolution of the HERA-*B* spectrometer is limited by multiple scattering. For the Inner Tracker, a resolution of $\sigma_x \approx 100 \mu\text{m}$ in the bending plane of the spectrometer magnet, $\sigma_y \approx 1 \text{ mm}$ perpendicular to it, and $\sigma_z \approx 3 \text{ mm}$ along the beam axis is sufficient. Together with the granularity requirement, the pitch of the readout strips was chosen to be 300 μm for the chambers in front of the RICH, and 350 μm for the chambers between RICH and ECAL, which gives the required resolution perpendicular to the strips (measuring coordinate, x). The other coordinate, y , is measured by using three stereo views (rotated by 0° , $+5^\circ$ and -5°). The stereo angle was determined by a Monte Carlo study in such a way that the resolution in y is optimised while the number of random coincidences between two stereo layers is kept at a tolerable level.

Signal Speed. At HERA-*B*, interactions can occur with each bunch crossing, *i.e.* every 96 ns. Both the chamber signal and the readout electronics must be fast enough to be able to distinguish signals from adjacent bunch crossings.

Trigger Information. A part of the Inner Tracker chambers have to deliver fast hit information to the First Level Trigger (FLT), which has to decide within about 10 μs whether the event is to be kept or discarded. Therefore the front-end electronics must be able to derive a fast decision which channels show a signal from the passage of a particle, and this information must be transferred to the FLT as fast as possible.

Magnetic Field. A part of the chambers of the Inner Tracking system are operated inside the spectrometer magnet of HERA-*B*, where the magnetic field strength is about 0.85 T. The chambers are not tilted to compensate for the Lorentz angle in order to keep the option to reverse the polarity of the magnetic field. Resolution and detection efficiency must still be acceptable under these conditions, and no magnetic components may be used in the construction of the Inner Tracker chambers and their support structure.

Radiation Length. Any material which is put in the active area of the detector gives rise to multiple scattering, bremsstrahlung, and photon conversion. The momentum resolution of the spectrometer is limited by the effects of multiple scattering. Therefore, detectors, support structure, and all other infrastructure like cables and gas pipes should be as thin as possible, measured in radiation lengths X_0 .

2.2 Detector Technology

The detector technology chosen for the Inner Tracker is the GEM-MSGC. These detectors were specially developed for the requirements of HERA-*B*; the development is documented in a number of PhD theses [Hot97, Zeu98, Hil99, Ric00, Wal01]. They combine a Micro-Strip Gas Counter (MSGC) [Oed88] with a Gas-Electron Multiplier (GEM) [Sau97]. In this section, the operation principle of these devices is explained, and the actual construction as it is used for the main series chambers employed at HERA-*B* is described.

2.2.1 Operation Principle

MSGC. The operation principle of a Micro Strip Gas Counter (MSGC) is the same as that of the Multi-wire Proportional Chamber (MWPC). In an MSGC, however, the wires are replaced by an electrode structure which is produced on a solid substrate, usually some kind of glass. This prevents mechanical and electrostatic instabilities and allows to choose a much smaller distance between the counting and field wires, resulting in an overall small readout pitch. Using a device with a small readout pitch, a high granularity and an intrinsically high spatial resolution is obtained.

The electrode structure consists of thin anodes ($\approx 10 \mu\text{m}$), which are kept at ground potential, and much broader cathodes, which play the role of the field wires found in an MWPC. A negative high voltage ($\approx 500 \text{ V}^1$) is applied to the cathodes. Opposite the MSGC structure, a drift cathode is kept at a negative high voltage, creating an electrical field of several kV/cm which forces the electrons deposited by the passage of an ionising particle to drift towards the MSGC plate. Fig. 2.1 depicts a simulation of the field configuration near the MSGC structure. In the region of high field strength close to the anode, gas amplification occurs. Amplification factors of several thousands can be reached. Since the field cathodes are close to the anodes, the ions produced in the avalanche near the anodes are removed quickly, avoiding the build-up of space charge. Due to high field strength, the ion drift velocity is high, resulting in fast chamber signals.

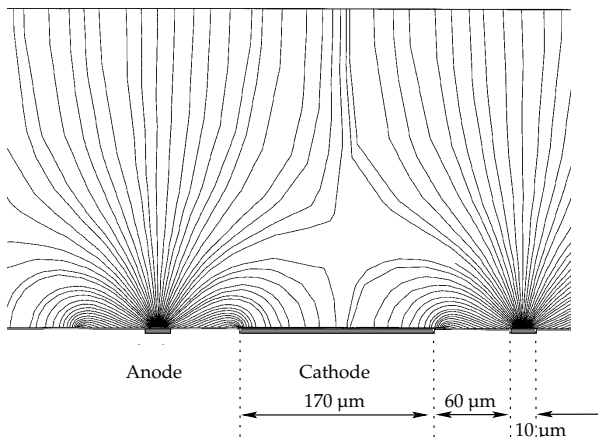


Figure 2.1: Simulation of the electrical field near the MSGC surface (from [Bre97]). Gas amplification occurs in the region of high field strength near the anodes. The dimensions of the actual detector used for the HERA-*B* Inner Tracker are indicated.

During the detector development it turned out that an MSGC alone is unsuitable to detect MIPs² with high efficiency in a hadronic environment: Heavily ionising particles ('HIPs') which are always present in a hadronic environment induce discharges between the anodes and the cathodes on the MSGC. At the gas gains necessary to detect MIPs with sufficient efficiency, these discharges proved fatal to the electrode structure, destroying the anodes within a short time of operation. This phenomenon was first observed during a beam test at the PSI³ and subsequently reproduced in the laboratory using a gaseous source of α -particles and also with a test installation at HERA-*B* (see [Vis96], [Bre97], and [Hau98]). The occurrence of these fatal discharges precluded the use of a pure MSGC in the HERA-*B* environment.

GEM. The Gas Electron Multiplier (GEM) is a thin insulating foil which is cladded with copper on both sides. A regular pattern of holes is produced in the foil (usually by chemical etching). The GEM is placed in a homogeneous drift field of several kV/cm , and another high

¹Since all voltages which are used to operate a GEM-MSGC are negative, the sign is omitted for convenience.

²Minimum Ionising Particles

³Paul-Scherrer-Institut, Villigen, Switzerland

voltage (typically ≈ 400 V) is applied across the device. The field lines are forced through the holes of the GEM. Close to a hole in the GEM, the field strength is high and gas amplification can occur. A simulation of the resulting electrical field is shown in Fig. 2.2. The gas gain also depends on the geometry of the holes; typically, values from 20–100 can be reached with the geometry and fields chosen for the Inner Tracker chambers. The probability that electrons produced above the GEM are transmitted through the GEM is called *transparency*. Like the gas gain, the transparency depends on the geometry of the holes, and also on the field strength below the GEM (the ‘transfer field’).

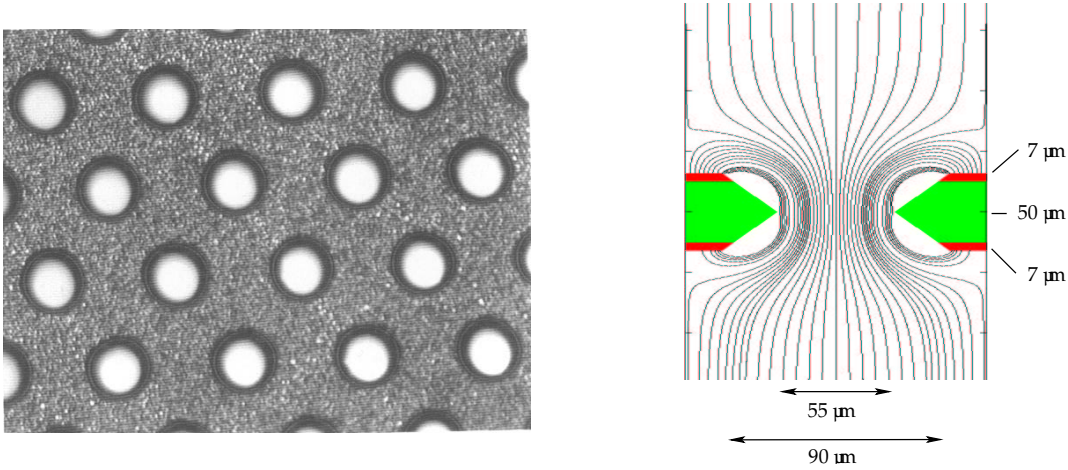


Figure 2.2: *Left:* Microscopical image of a GEM foil of the type used for the HERA-B GEM-MSGC detectors (from [Hil99]). The limited depth of focus causes the inner hole diameter to appear larger than it actually is. *Right:* Simulation of the electrical field across a hole in the GEM (simulation by P. Cwetanski).

GEM-MSGC. The problem of discharges destroying the anode structure of the MSGC could be overcome by introducing the GEM as a first pre-amplifying element into the chamber. In such a combined device, the gas amplification occurs at two well separated places, and the gas gain at the MSGC can be reduced without compromising the chamber efficiency. By lowering the field strength at the MSGC, the discharge probability is lowered by several orders of magnitude. With this separation of the gas amplification, a safe and efficient operation of the GEM-MSGC even in high-rate hadronic beams can be achieved.

2.2.2 Construction of the HERA-B GEM-MSGC

Fig. 2.3 shows a sketch of the GEM-MSGC detector developed for the use in the Inner Tracker of HERA-B. The MSGC wafer is made of 0.4 mm thick alkali-free glass⁴ which is coated with a thin diamond-like carbon coating⁵. This coating is produced on the glass using a vapour deposition method⁶; it has a surface resistivity of typically 10^{14} – 10^{15} Ω/\square , depending on the treatment of the wafer after production. It is needed to prevent the accumulation of ions from the gas amplification process on the surface, which would cause field distortions and so spoil the high-rate capability of the chambers by introducing a rate dependence of the gas gain. On top of the coating, an electrode structure is produced using a lithographic lift-off process⁷. The

⁴AF45 from DESAG, <http://www.schott.com/displayglas/english/products/af45>

⁵proposed by G. Zech and F. Sauli

⁶Fraunhofer Institute for Surface Engineering and Thin Films, Braunschweig, Germany

⁷IMT, Institut für Masken und Teilungen, Greifensee, Switzerland

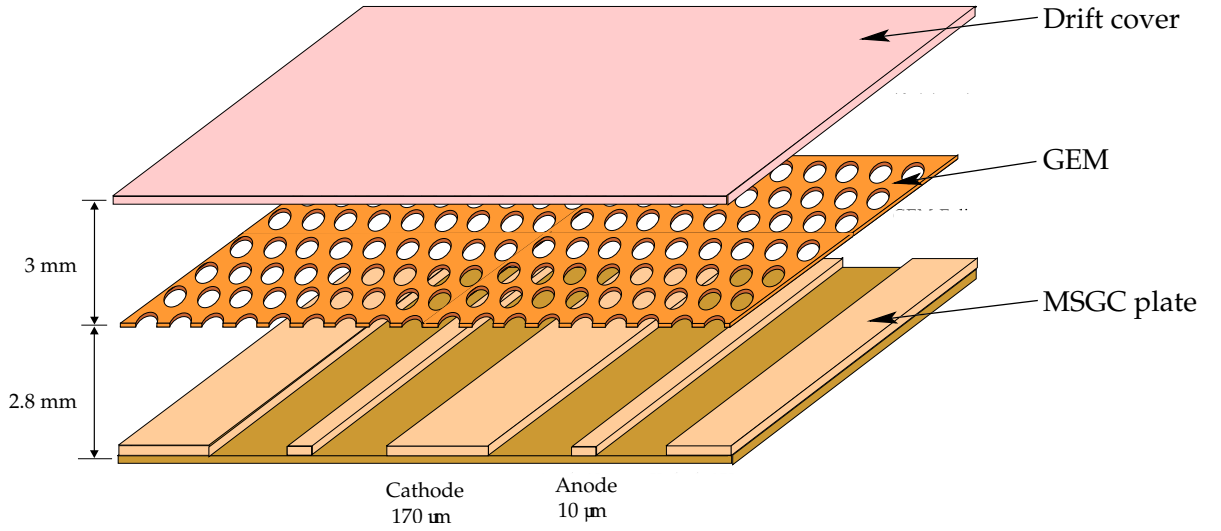


Figure 2.3: Sketch of a GEM-MSGC detector (taken from [Zie98]). The active components are the MSGC plate with the electrode structure and the GEM, which is kept in the middle of the chamber by the chamber frame (not shown). The drift cover contains the drift cathode on one side; it closes the gas volume and provides mechanical stability.

electrodes are made of gold with a thickness of 500 nm; the width of the cathodes is 170 μm , the width of the anodes 10 μm , and the gap between two adjacent electrodes is 60 μm . The resulting pitch is 300 μm . The masks used for the lithographic process were drawn at the Institute of Physics of the University of Zürich, where each individual MSGC plate ('wafer') was also tested for production failures [Wal01].

At a distance of 2.8 mm above the MSGC, the GEM foil⁸ is mounted. It consists of a 50 μm thick Kapton foil with 7 μm of copper on each side, into which a regular pattern of holes is etched. The holes in the Kapton have a diameter of about 55 μm , the diameter of the corresponding holes in the copper is about 90 μm . Due to the production process, the holes are not cylindrical, but have rather an hourglass shape (see Fig. 2.2). They are staggered with a pitch of 140 μm . To avoid sag in the GEM and an ensuing inhomogeneity of the gas gain, the GEM is pre-stretched and glued to a stiff hollow frame milled from G10.

The drift cathode is made of 18 μm copper cladded on a 125 μm Kapton foil and reinforced with a 0.3 mm thick G10 plate. It closes the gas volume and ensures the mechanical stability of the chamber, since the MSGC plate and the frame alone cannot keep the GEM tension. The drift cover is kept at its distance from the GEM by another hollow frame.

To accommodate the different diameters of the proton beam pipe and to be able to be as close as possible to the beam pipe, three different types of chambers are used: The chambers of *Type I* have an outer dimension of $23 \times 25 \text{ cm}^2$ and a recess for the beam pipe of 5.5 cm. The chambers of *Type II* have the same outer dimensions, but a recess of 8 cm. The largest chambers (*Type III*) have an area of $27 \times 27.5 \text{ cm}^2$ and a recess of 12.5 cm. For the chambers of Type III, also the readout pitch is changed to 350 μm . The dimensions of a chamber of Type II are shown in Fig. 2.4, together with the connections for high voltage, gas supply and readout.

The hollow frame is also used to distribute the counting gas to the chamber. Two capillaries glued into the frame serve as inlet and outlet. The gas inlet into the active volume of the chamber is located in the recess for the beam pipe, where the particle density is highest. The counting gas

⁸produced at the CERN Surface Treatment Workshop, EST/SMCI, Geneva, Switzerland

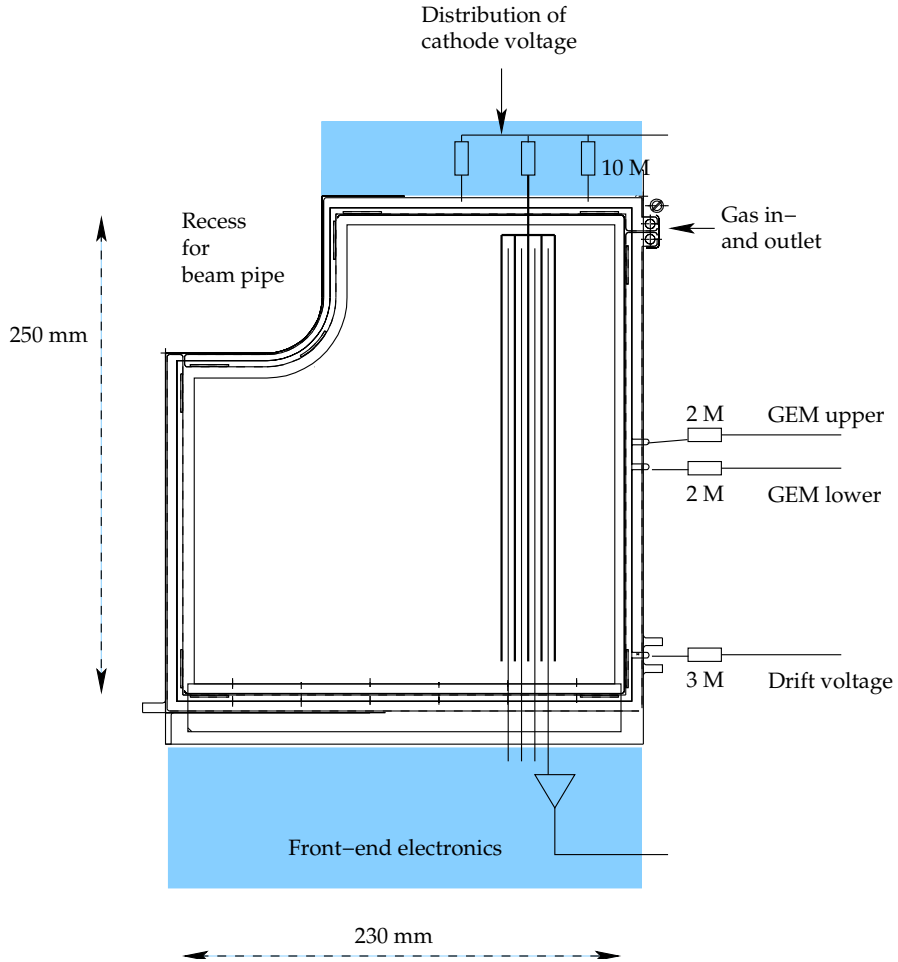


Figure 2.4: Drawing of a chamber of Type II. Also indicated are the orientation of the MSGC structure (not to scale) and the various connections for high voltage and readout electronics. To decouple the chamber from the large cable capacitances, resistors of $3\text{ M}\Omega$ and $2\text{ M}\Omega$ are put in the high voltage supply lines for U_{drift} and the two GEM voltages near the chamber. These resistors act as an overcurrent protection in case of discharges in the chamber. The cathodes are connected to their high voltage in groups of 16 cathodes each; each group has its own protection resistor of $10\text{ M}\Omega$. In total, a chamber contains 48 such cathode groups.

used by the Inner Tracker at HERA-B is an Ar:CO₂ 70:30 mixture. In the original design, the foreseen gas mixture was Ar:DME⁹ (50:50). DME is a much better quencher than CO₂, which leads to a higher safety against discharges in the chamber at a given gas gain. Additionally, the primary ionisation is higher in an Ar:DME 50:50 mixture by about 30%. However, it was observed both at a test beam experiment (Paul Scherrer Institut, π and p with 350 MeV) and in the laboratory (irradiating larger areas with X-rays) that using DME in the counting gas causes massive and rapid ageing of the detector. Unfortunately, also other organic quenchers which were tried either showed ageing or caused other damage to the chambers, so that a mixture of Ar:CO₂ remains as the only viable counting gas.

2.3 Building a Tracking Device with GEM-MSGCs

One GEM-MSGC alone is capable of measuring only one coordinate of a track impact point (perpendicular to the anode strips). In order to build a tracking system with this detector type, several chambers have to be combined, each of them measuring a different projection of the track impact points. These *stereo layers* are arranged such that the desired resolution along the anode strips is obtained. Several layers are combined into *tracking stations* which are distributed along the beam axis.

With four of the L-shaped detectors (depicted in Fig. 2.4), one plane of the complete area around the beam pipe can be covered. In order to avoid dead regions, the detectors are arranged so that their active volumes overlap. The detectors are mounted to support plates made of a sandwich of carbon fibre and Nomex honeycomb (see Fig. 2.5). Layers with different stereo angles are combined into tracking stations (also called *super-layers*).

Each tracking station (of both Inner and Outer Tracker) consists of two separate half-stations, which cover the area to the left and to the right of the beam pipe ($-x$ and $+x$), respectively. Thus the individual stations can be moved out of their nominal position for installation and maintenance. The half-stations of the Inner Tracker are mounted on the frames of the corresponding Outer Tracker stations (see Fig. 2.6) using a support structure made from carbon fibre.

The number of chambers and stereo layers in each of the Inner Tracker stations are shown in Table 2.1. The location of the stations along the beam pipe is indicated in Fig. 2.7. According to their main functions, the tracking stations are grouped in three groups: *Magnet tracking* (MC, in the spectrometer magnet), *pattern recognition* (PC, between magnet and RICH) and *trigger* (TC, between RICH and ECAL) stations. The chambers situated in the TC area are mainly needed by the trigger algorithms to link track seeds from the calorimeter or the muon system to tracks found in the main tracker (stations in PC and MC).

The completed Inner Tracker will consist of 184 chambers. By the end of the run period 1999/2000, all stations except the four half-stations of the TC region were installed and routinely operated, in total 136 GEM-MSGCs.

To be able to identify each chamber uniquely, the following naming scheme was introduced: it consists of the number of the super-layer, two characters to denote the quadrant, and one digit for the layer the chamber is in. For example M12-+2 is the chamber in the second layer of station MS12, in the quadrant covering negative x and positive y . This scheme is used throughout this thesis to denote individual chambers.

⁹dimethyl-ether

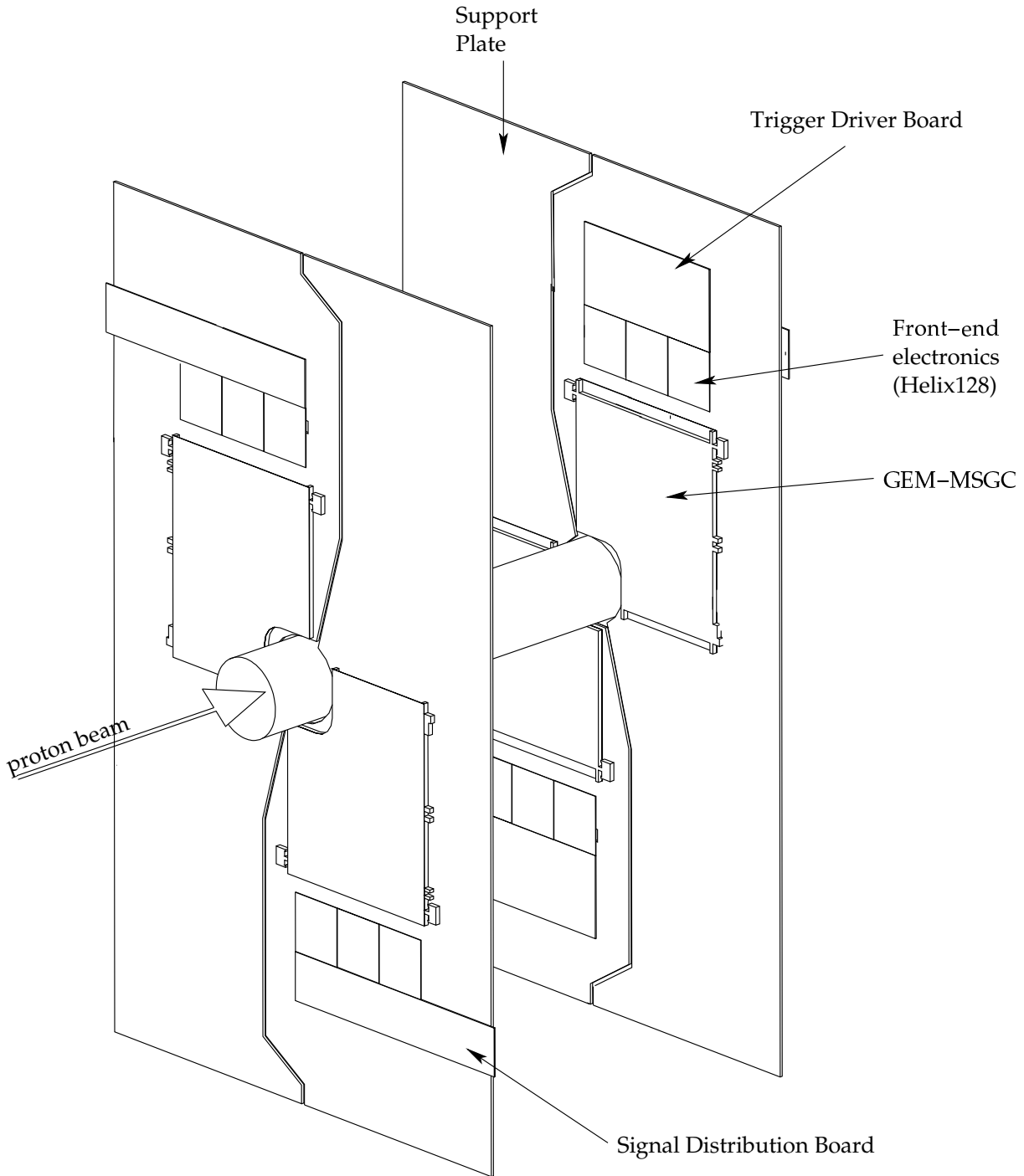


Figure 2.5: Construction of support plates with double layers of GEM-MSGCs (using a technical drawing by S. Hennenberger, Uni Heidelberg). The chambers are mounted on support plates made of a sandwich of carbon fibre and a honeycomb structure. To cover all four quadrants, two layers of support plates are needed. The drawing shows a part of one station which contributes to the first level trigger. Two chambers of the same stereo layer are mounted on the two sides of one support plate.

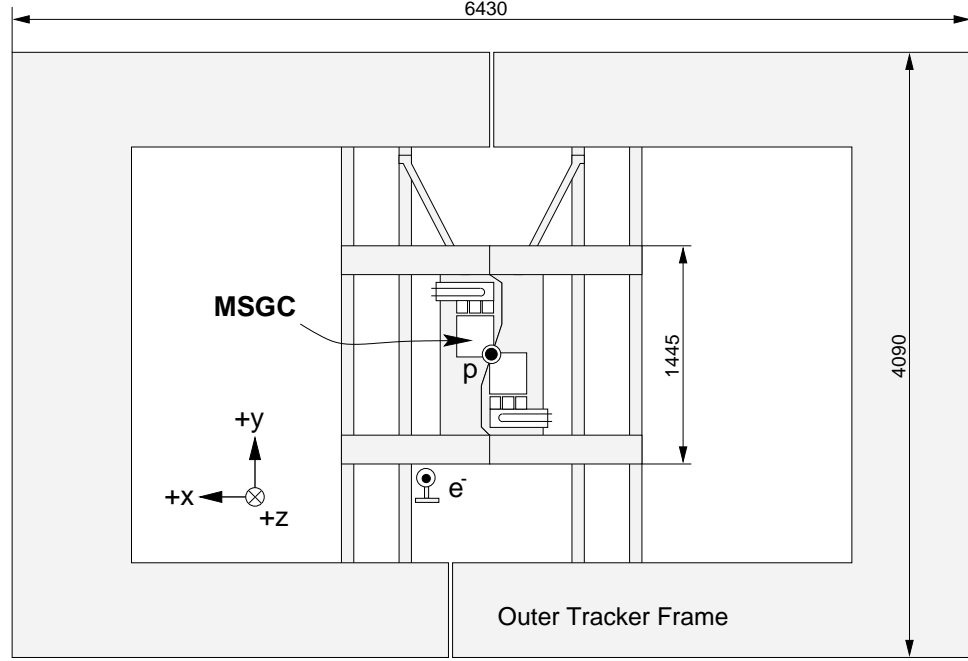


Figure 2.6: Mounting of two Inner Tracker half-stations on the frame of the corresponding Outer Tracker stations (from [Hau98]). The dimensions given are valid for the stations located between the magnet and the RICH.

| Name | Chambers | Type | Stereo angles | Trigger? |
|------|----------|------|----------------------------|----------|
| MS01 | 16 | I | 0, -5, +5, 0 | no |
| MS03 | 8 | I | 0, -5 | no |
| MS05 | 8 | I | 0, +5 | no |
| MS06 | 8 | II | 0, -5 | no |
| MS10 | 32 | II | 0, 0, -5, -5, 0, +5, +5, 0 | yes |
| MS11 | 16 | II | 0, -5, +5, 0 | no |
| MS12 | 16 | II | 0, -5, +5, 0 | no |
| MS13 | 32 | II | 0, 0, -5, -5, 0, +5, +5, 0 | yes |
| MS14 | 24 | III | 0, 0, -5, -5, +5, +5 | yes |
| MS15 | 24 | III | 0, 0, -5, -5, +5, +5 | yes |

Table 2.1: Tracking stations of the Inner Tracker. In the stations contributing to the First Level Trigger, each stereo view is built as a double layer. The trigger signals of the two chambers of the same orientation are ORed directly at the station to increase the trigger efficiency. In the stations MS10 and MS13, there are two additional 0°-layers which are needed by the reconstruction program. These layers do not contribute to the FLT. Of the double layers in MS14 and MS15, only one layer per stereo view is connected to the analogue readout.

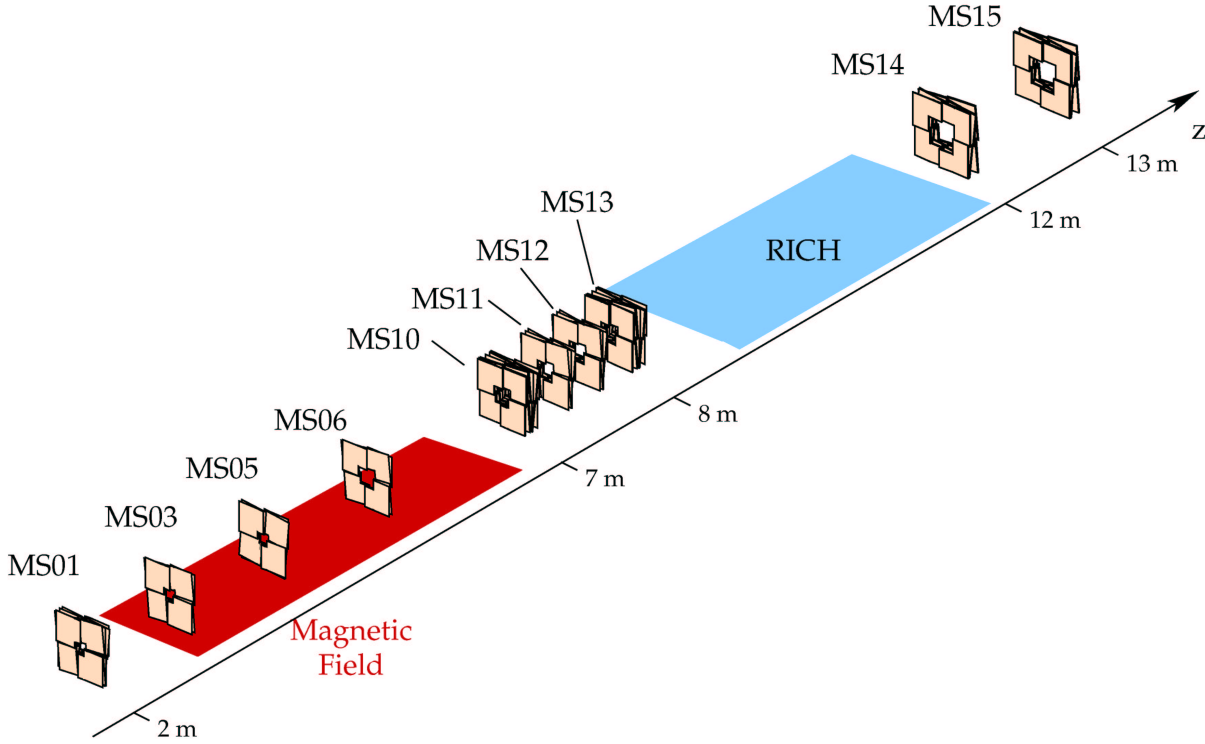


Figure 2.7: Location of the Inner Tracking stations along the beam axis. The z position of the different stations is indicated, as well as the spectrometer magnet and the RICH.

2.4 Chamber Operation and Infrastructure

High Voltage. For the operation of a GEM-MSGC, four different high voltages are needed. These are the *drift voltage*, the voltages for the upper and lower side of the GEM, and the cathode voltage. The Inner Tracker uses a high voltage distribution system which was designed and built at the electronics workshop of the Institute of Physics, Heidelberg. This high voltage distribution system together with the necessary hardware used for slow control is depicted schematically in Fig. 2.8.

The voltages U_{drift} and U_{cath} are generated by a power supply located in the electronics trailer, about 50 m away from the chambers. In order to save cables and power supplies, one output of the power supply provides the high voltage for eight chambers. This distribution is done using about 25 current meter modules A339¹⁰. They provide an eight-fold fan-out of two input voltages, monitoring the current flowing in each individual output channel. If a current exceeds a programmable threshold for a longer time, the module disconnects the outputs from the input to prevent damages of the chambers in case of a malfunction. A separate hardware alarm signal is used to indicate the occurrence of such an exception to an alarm system which works independently of the steering software.

The two voltages needed for both sides of the GEM are derived from U_{drift} using another custom high voltage module, the A344¹¹. The A344 contains eight micro-processor controlled voltage dividers which share the same input voltage. Each voltage divider has two outputs, one for the upper and one for the lower side of one chamber's GEM. Within the limits given by the resistors used for the voltage divider, the difference voltage U_{GEM} can be adjusted individually

¹⁰P. von Walter, http://www.physi.uni-heidelberg.de/~vwalter/Geraete/A339_Current_Meter/A339-6_Man.pdf

¹¹P. von Walter, http://www.physi.uni-heidelberg.de/~vwalter/Geraete/A344_GEM-Verteiler/A344-8_Man.pdf

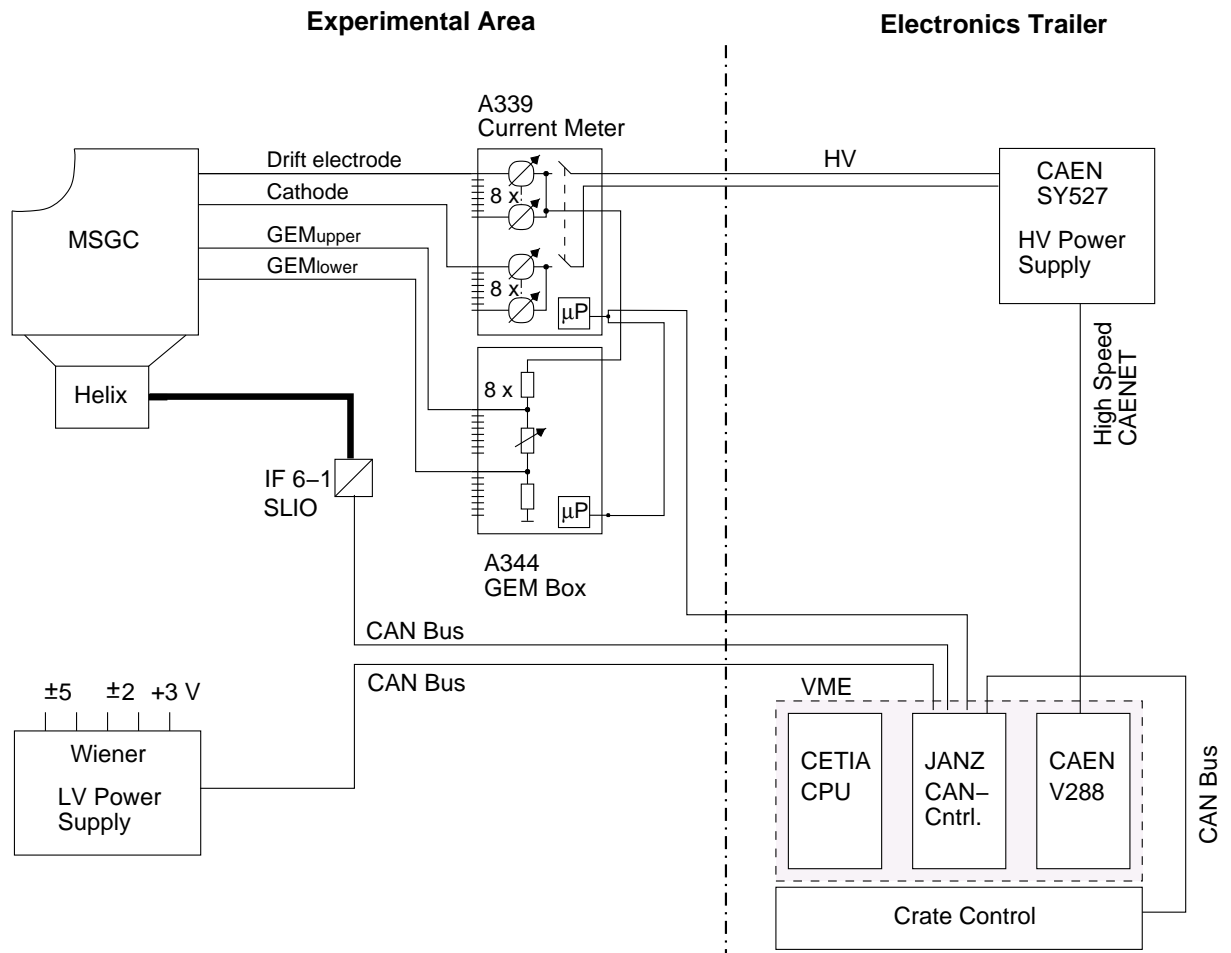


Figure 2.8: Schematic drawing of the Inner Tracker slow control components (adapted from [Hau98]). The high voltage power supply (CAEN SY527) and a VME crate used to control and steer the system are situated in the electronics trailer (*right*), while the high voltage distribution system consisting of current meters A339 and GEM voltage divider A344 is located in the experimental area, under the platform on which the detectors are mounted (*left*). One of the low voltage power supplies is also shown; one such module supplies the electronics of one complete half-station with the necessary power (± 2 V, ± 5 V, $+3$ V).

for each chamber.

Both the current meter modules and the GEM voltage distribution modules are located beneath the detector, in an area which is inaccessible during operation. Therefore, all functions of the high voltage modules are remotely controllable (see [Ger99] and [Wil00b]).

Low Voltage. The low voltage needed by the readout electronics is supplied by a separate power supply unit for each half super-layer. The power supplies are also located beneath the experiment; the cable length is about 15 m between power supply and consumer. The voltages needed are ± 2 V, ± 5 V, and 3 V. In the large stations in the PC area, the currents drawn can reach 15 A or more. The units used are switching power supplies which were specifically modified for the high currents and high inductive load presented by the long cables.

Gas Supply. A constant flow of fresh counting gas through the chambers has to be maintained to prevent the accumulation of polymers and ensuing gas ageing. The gas system has to maintain this flow while keeping the difference between the pressure in the chamber and the ambient pressure within a few hundred μ bar. This is accomplished by monitoring the pressure in a reference volume which is mounted on the support structure of each half super-layer and by adjusting the gas flow accordingly. In total, the gas system comprises sixteen separate regulation circuits which are controlled by a programmable logic controller¹².

¹²Siemens SPS S7

Chapter 3

Readout for the Inner Tracker

The Inner Tracker of HERA-*B* contains well over 10^5 readout channels. In order to cope with this high number of channels, a highly multiplexed readout system is used. In this chapter, the various components needed for the readout of the Inner Tracker are described. The first four sections present the hardware which is used in the readout system: the front-end readout chip Helix128S, the FED system digitising the data, and all the additional electronics which is needed for the transmission of data and control signals to and from the front-end electronics. The last section focuses on the processing software which prepares the raw detector data for hit identification and does the cluster search.

3.1 Readout Chain and Data Flow

The completed Inner Tracker will comprise 184 GEM-MSGCs with about 120 000 analogue readout channels. 136 chambers with 102 000 channels were installed and operated during the run 1999/2000. The front-end electronics with preamplifiers and a first multi-event buffer is mounted directly at the detectors, while the electronics digitising the data is located in the electronics hut (the *trailer*), behind the radiation shield of HERA-*B*, at a distance of about 50 m. To keep the number of cables needed to connect the front-end electronics with the ADCs at a reasonable level and to save readout electronics, a highly multiplexed readout scheme is implemented: Using the custom readout chip Helix128S, the analogue signals of 256 neighbouring detector channels are multiplexed and transmitted serially by one optical fibre to the trailer, where one Flash ADC digitises the signals. The First Level Trigger needs about $10\ \mu\text{s}$ to decide whether to keep or discard an event (FLT latency); the detector data must be kept available for this time. This is performed by an analogue pipeline in the front-end chips.

The complete readout chain of the Inner Tracker is depicted schematically in Fig. 3.1. The HERA-*B* Fast Control System (FCS) provides to all subsystems the **BxClock** (*'bunch crossing clock'*, a clock which is in phase with the crossing of the proton bunches through the experiment), trigger signals and event information (*e. g.* trigger number, bunch crossing number of the triggered event, and a trigger code). From this information, the FED Controller derives the control signals needed to operate the front-end electronics: sample and readout clock, trigger and reset signal. These control signals are distributed to the front-ends using an optical transmission line. In return, the analogue data sent from the front-end electronics is digitised by the FEDs¹, merged with the event information from the FED Controller, and sent to the Second Level Buffers (SLB), where the Second Level Trigger nodes can access the data.

¹Front End Driver boards

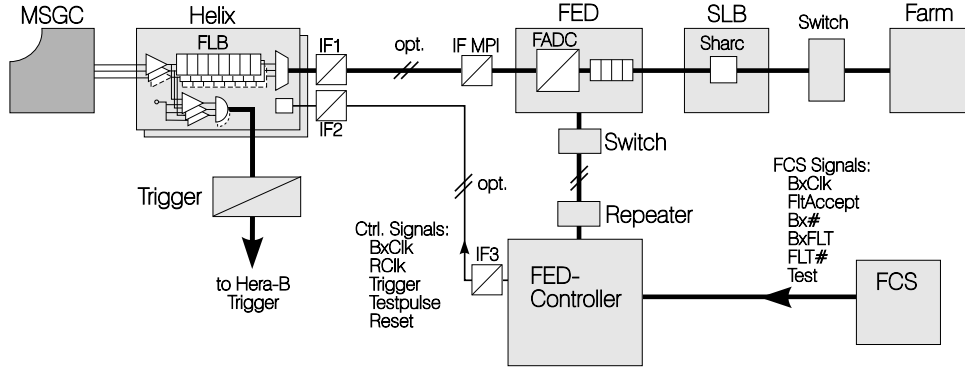


Figure 3.1: The readout chain of the Inner Tracker and its connection to the common Data Acquisition System of HERA-*B* (Figure from [Hau98]).

3.2 Front End Chip: Helix128S

The Inner Tracker uses the ASIC² Helix128S to read out the detectors. The Helix128S was developed by members of the HERA-*B* VDS and ITR groups at the University of Heidelberg's ASIC lab³ for the readout of the Silicon Vertex Detector and the Inner Tracker of HERA-*B*. It is manufactured in a 0.8 μm CMOS process at Austria Micro Systems (AMS, Unterpremstätten, Austria).

The Helix128S contains the electronics for 128 detector channels. It integrates 128 fast, low-noise charge sensitive preamplifiers with following semi-gaussian pulse shapers. The output of the shapers is sampled into an analogue pipeline which provides a maximum latency of 128 sampling intervals and can store up to eight triggers while data is being read out. The output of each shaper is also coupled capacitively into a comparator. The charge stored in the pipeline cells is read out by the pipeline amplifiers; the data are multiplexed and output serially as a sequence of current signals. Since the readout chips are mounted near the detectors, they have to withstand a considerable radiation load over the lifetime of the experiment; they accumulate about 40 krad per operation year. The Helix128S was shown to tolerate radiation doses of 400 krad without severe degradation of performance.

Fig. 3.2 shows a block diagram of the Helix128S, with only one analogue channel drawn. The digital control circuitry is shown at the lower part. The following section describes in more detail the chip's features which are most important from the application point of view. All the details about the chip's design can be found in [FB98, Gla97, Sex97, Tru00].

3.2.1 Input Stage

The first amplifier of the input stage is a low noise charge sensitive preamplifier. At nominal settings, the preamplifier has a gain of 11.2 mV/24000 e^- .⁴ It is followed by a pulse shaper which transforms the voltage step at the output of the preamplifier into a well-defined pulse

²Application Specified Integrated Circuit

³<http://wwwasic.kip.uni-heidelberg.de>. The ASIC lab is a joint institution of the Heidelberg University's Institute of Physics and Kirchhoff-Institute for Physics and the Max-Planck-Institute for Nuclear Physics (MPI-K) in Heidelberg

⁴1 MIP_{Si} = 24000 e^- is the mean charge deposited by a minimum ionising particle (MIP) in a silicon detector of the HERA-*B* vertex detector system; the charge is collected within a few 10 ns [G⁺00, Sec. 24.8]. The charge deposited by a MIP in a GEM-MSGC of the Inner Tracker is about 10⁵ e^- , the signal is however much slower compared to a silicon detector.

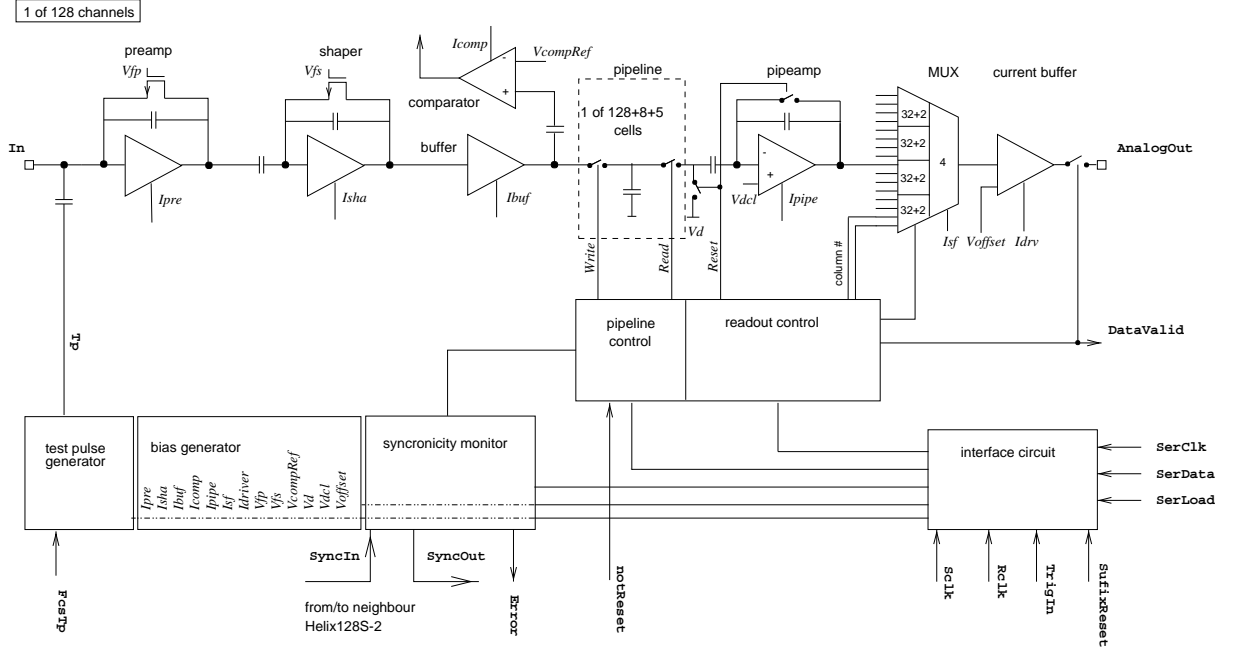


Figure 3.2: Schematic diagram of the Helix128S readout chip (taken from [FB⁺99]). Only one of the 128 analogue readout channels is shown.

which peaks at a time t_{peak} and falls off to zero after time t_{decay} . For the detectors at HERA-B the peak time has to be around 50 ns to comply with HERA's bunch crossing rate of 10.4 MHz. Likewise the shaped signal should be near zero 100 ns after the peak so that the sampled value is not influenced by a signal from the previous sampling interval. To drive the capacitance of pipeline cell, comparator coupling capacitance, and parasitic capacitances of signal lines, the shaper's output is fed into a buffering amplifier.

The feedback resistances and bias currents of all amplifiers of the front-end can be adjusted by programming on-chip voltage and current sources (see Sect. 3.2.7). This allows to select—within certain limits—the desired pulse shape of the front-end. Fig. 3.3 (a) shows a pulse shape scan with the operation parameters used in the 2000 run and a capacitive load comparable to an actual Inner Tracker detector. At a given set of Helix settings, the preamplifier gain, peak time and decay time of the shaper also depend on the capacitance C_{in} which is seen at the input: the higher C_{in} , the lower the peak height and the slower the fall time of the pulse (see Fig. 3.3 (b) and Sect. 4.4).

3.2.2 Comparators

The Inner Tracker is required to deliver fast hit information to the First Level Trigger. For this purpose, the Helix128S contains a comparator for each analogue channel. The output of the shaper is coupled capacitively into the comparator input to suppress slow baseline variations. The comparator can be used with either positive or negative signals; the behaviour can be selected by connecting one pad of the chip to either the positive or the negative supply voltage. The signals of the Inner Tracker GEM-MSGCs are negative, so the comparator polarity is set so that the comparators switch if the input signal is *smaller* than the threshold. All comparators on one chip share a common threshold which can be set in steps of 1.6 mV using one of the on-chip voltage sources. The output of four neighbouring channels is ORed and latched on a

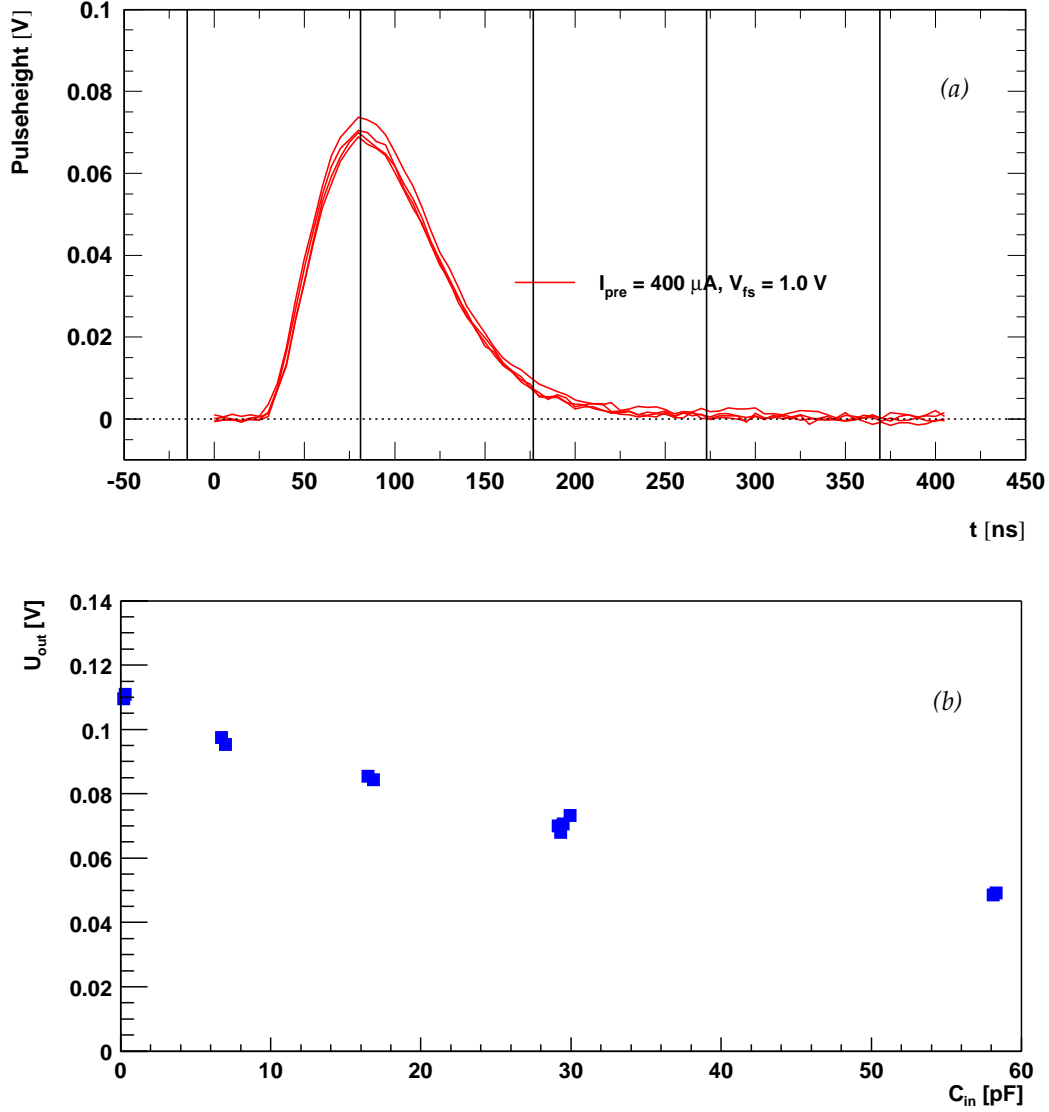


Figure 3.3: (a): Step response of the Helix preamplifier and shaper with a capacitive load of 29.4 pF. The preamplifier settings are those used for the readout of the ITR (see also Sect. 4.4). The peaking time is about 60 ns. The vertical lines indicate the falling edge of the sampling clock with $\nu_{\text{SClk}} = 10.4 \text{ MHz}$ which determines the sampling point. (b) Peak height of the Helix step response as a function of the input capacitance C_{in} . (Helix data from [TDD99]. The receiver circuit used for these measurements has a slightly lower gain compared to the one used in the HERA-B Inner Tracker).

flip-flop with the ‘comparator clock’ (**CompClk**). **CompClk** should be slightly shifted in phase with respect to **SClk** in order to minimise cross-talk to the analogue values sampled into the pipeline. For the Inner Tracker, this phase shift is accomplished by a different routing of the signals **SClk** and **CompClk** on the printed circuit board. The 32 comparator output signals are brought off-chip as active-low open drain signals **notCompOut<31..0>**.

For a discussion of attainable hit efficiencies with the comparator outputs and the measures necessary to reach them, see [Kel01].

3.2.3 Pipeline

The pipeline is a switched array of 129×141 capacitors with a capacity of 850 fF each. 128 of the 129 pipeline rows are connected to the front-end amplifiers, while the last one is used later on to subtract common mode and pick-up from the analogue data.

Writing into and reading from the pipeline is governed by two pointers which walk over the pipeline columns, the *write pointer* and the *read pointer*. They are both advanced at each rising edge of the sampling clock **SClk**. The write pointer indicates the pipeline column which will receive the analogue data of this sample cycle at the falling edge of **SClk**. If a trigger occurs, the pipeline column indicated by the read pointer is tagged. Columns which were tagged are subsequently skipped by the write pointer until they have been read out completely. Up to eight columns can be tagged at any time, so that the pipeline can serve as an eight event deep first level buffer (also called *multi-event buffer*). Loading the analogue values from the pipeline into the multiplexer takes five **SClk** cycles, so that in total a maximal FLT latency of $128 = 141 - 8 - 5$ **SClk**-cycles can be accommodated in the pipeline, if the maximum of eight columns are used for the multi-event buffer.

3.2.4 Readout Cycle

If there is a tagged (*i.e.* triggered) pipeline column available, the analogue data stored in that pipeline column is transferred to the multiplexer and serially sent out synchronised by the external readout clock **RClk**. The Helix supports **RClk** speeds of up to 40 MHz, practically useable are 10 – 30 MHz. The number of the pipeline column is encoded into an eight-bit pattern which is sent directly after the analogue data. This column number can be used to check the synchronisation of a large number of readout chips in a large system. The chip generates a signal **DataValid**, which is kept high while the complete data is being transmitted.

Several Helix chips can be operated in a so-called *daisy-chain* such that their analogue data is sent over the same line, saving cost in the following stages of the readout system. To synchronise the data transmission, a signal called **token** is passed from one chip to the next in the daisy-chain. Only the chip currently holding the **token** is allowed to send its data. In the Inner Tracker, daisy chains of two Helix chips are used; Fig. 3.4 shows a typical readout pattern of a two-chip daisy-chain.

3.2.5 Multi-Event Buffer and Dead Time

With a serial readout of many detector channels as in a Helix daisy-chain, the time needed to transmit the data limits the maximal trigger rate which can be accepted by the readout chips. At an **RClk** speed of 30 MHz, the transmission takes about $9 \mu\text{s}$, which means that at average trigger rates of more than 110 kHz, triggers have to be discarded. This does not seem a serious limitation. However, the triggers arrive not with a fixed frequency, but randomly. Therefore even at much lower average trigger rates, triggers arriving less than $9 \mu\text{s}$ apart have to be discarded. The solution implemented on the Helix to overcome this limitation is the introduction of a

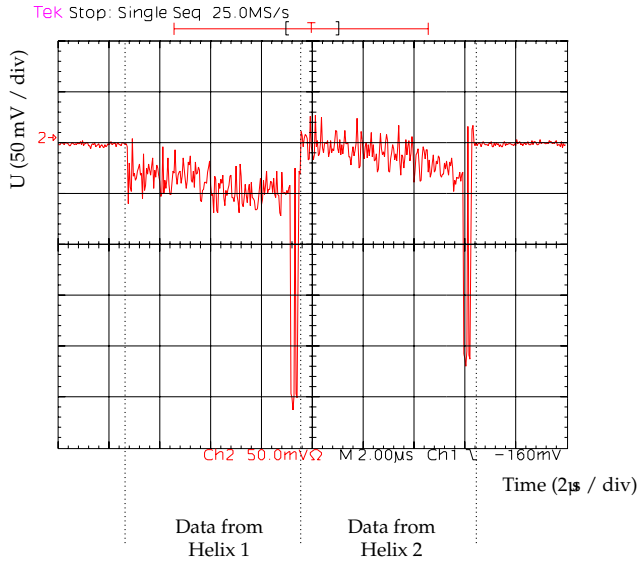


Figure 3.4: Analogue data of two Helix128 in a daisy chain, observed with an oscilloscope at the end of the complete data transmission chain. The RC1k speed was 20 MHz, so that the 128 channels of one Helix are sent in $6.4 \mu\text{s}$. The column numbers sent after each chip’s analogue data can clearly be seen.

multi-event buffer, which acts as a ‘derandomiser’ for the triggers. The average trigger rate which can be accepted without causing too much dead time becomes much higher. The effect of the multi-event buffer on the dead time is illustrated in Fig. 3.5, which shows the result of a simulation of the behaviour of the Fast Control System using different readout speeds and depths of the multi-event buffer (*FIFO depths*). With a readout speed of 10 MHz and one multi-event buffer, the dead time is already larger than 25 % at a trigger rate of 10 kHz, and even with 7 multi-event buffers, only trigger rates of about 30 kHz can be reached before the dead time becomes large. With a readout speed of 30 MHz and a FIFO depth of 7, average trigger rates of more than 70 kHz can be used without producing dead time.

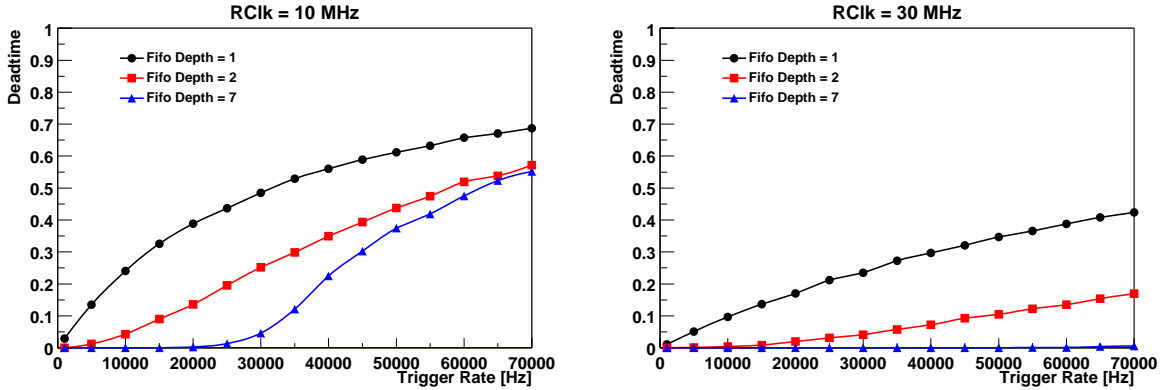


Figure 3.5: Simulation of the readout dead time for two different readout speeds, *left*: 10 MHz, and *right*, 30 MHz. The dead time was simulated for FIFO depths of 1 (*circles*), 2 (*squares*), and 7 (*triangles*).

3.2.6 Testpulse Circuit

A test pulse generator is implemented on the chip which generates a defined test pattern. This test pulse pattern can be used to quickly verify the working condition of the complete readout electronics and to obtain a coarse adjustment of the timing of all clocks. At the rising edge of the signal `FcsTp`, a defined charge pattern is injected into the preamplifiers, creating a stair-case like readout pattern:

- $\approx +2 \text{ MIP}_{\text{Si}}$ in channels $4n$,
- $\approx +1 \text{ MIP}_{\text{Si}}$ in channels $4n + 1$,
- $\approx -1 \text{ MIP}_{\text{Si}}$ in channels $4n + 2$, and
- $\approx -2 \text{ MIP}_{\text{Si}}$ in channels $4n + 3$.

The polarity of the injected charge is toggled after each test pulse. Fig. 3.6 shows a detail of the test pulse pattern generated by one Helix chip.

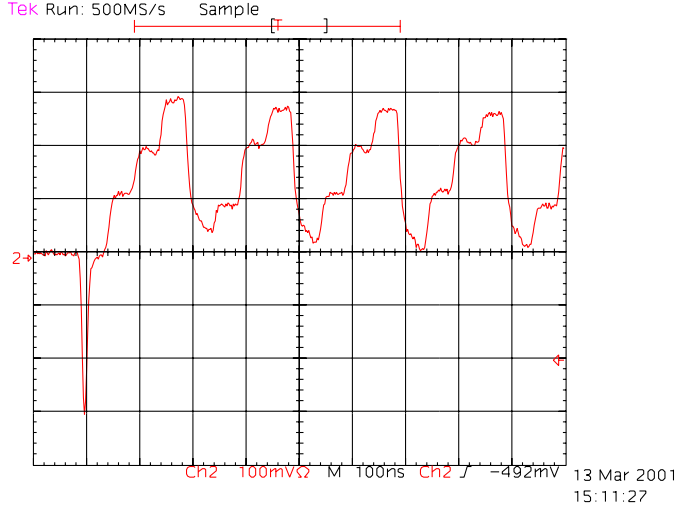


Figure 3.6: Oscilloscope plot of the test pulse pattern seen in sixteen channels. The readout speed was 20 MHz, thus each horizontal division of 100 ns corresponds to two channels. The deviation from an ideal staircase pattern is caused by the pedestal variation, which shifts the analogue value of each channel by a different value.

3.2.7 Programmable Parameters

To obtain a specific operation mode and to compensate later for possible radiation damage the bias currents and voltages of the amplifiers at the front end can be adjusted by programming several on-chip DACs⁵ which control the current and voltage sources. Both bias currents and voltages are adjusted using 8-bit DACs. The output of the current DACs is

$$I_{\text{DAC}} = 2.5 \mu\text{A} \times \text{DAC}, \quad (3.1)$$

while the bias voltages can take any value between the supply voltages V_{ss} and V_{dd} , which are typically $V_{\text{ss}} = -2 \text{ V}$, $V_{\text{dd}} = +2 \text{ V}$:

$$\begin{aligned} U_{\text{DAC}} &= V_{\text{ss}} + \frac{V_{\text{dd}} - V_{\text{ss}}}{256} \times \text{DAC} \\ &\approx -2 \text{ V} + 0.016 \text{ V} \times \text{DAC}. \end{aligned} \quad (3.2)$$

For the comparator threshold V_{compRef} , the DAC voltage is internally divided by 10 in order to obtain a better resolution for setting the threshold.

In a similar manner, the actual latency of the pipeline can be set (register `Latency`), as well as a delay between two consecutive readout cycles (`TokenDelay`). Table 3.1 shows the register settings commonly used by the Inner Tracker for the HERA-*B* run after spring 2000. Individual adjustments of the registers `Vd` and `Voffset` were done for some chips to shift the baseline.

The Helix128S features a simple serial interface to program the register values. The interface consists of a 20-bit deep shift-register, which has the following format (see also Fig. 3.7): the first (most significant) bit is the ‘common set bit’, followed by a six-bit chip address, a five-bit register address and an eight bit register value. If the ‘common set bit’ is set in a data frame,

⁵Digital-to-Analogue Converter

| Register | DAC Value | Value |
|------------|-----------|-------------|
| Ipre | 160 | 400 μ A |
| Isha | 40 | 100 μ A |
| Ibuf | 40 | 100 μ A |
| Icomp | * | * |
| Ipipe | 16 | 40 μ A |
| Isf | 40 | 100 μ A |
| Idriver | 36 | 90 μ A |
| Vfp | 155 | 420 mV |
| Vfs | 192 | 1.0 V |
| VcompRef | * | * |
| Vdcl | 194 | 1.03 V |
| Vd | 72 | −875 mV |
| Voffset | 95 | −515 mV |
| Latency | 127 | |
| SyncReg | 0 | |
| ClkDiv | 0 | |
| TokenDelay | 30 | |

Table 3.1: Adjustable parameters of the Helix and their values used for the Inner Tracker during the Run 2000. The comparators were switched off by setting Icomp and VcompRef to 0 to prevent feed-back and oscillations. Their values will be adjusted such that a sufficient trigger efficiency is reached.

all chips use this data frame, otherwise only those chips whose address matches with **chipaddr** take note of the data. The field **register address** encodes the Helix register whose value is to be modified, and **register value** holds the DAC value for this register.

The register is filled using two signal lines, **SerData** and **SerClk**. At each rising edge of **SerClk** the data in the shift register is shifted one bit to the left and the current value of **SerData** is filled into the least significant bit. If a rising edge of the signal **SerLoad** occurs, the content of the shift register is interpreted by the chip. To save input pads on the chip, the input signals **Trigger** and **RClk** are actually used for **SerData** and **SerClk**. The interface does not allow to read back the values stored in the Helix. The electronics talking to this interface in the Inner Tracker installation is described in Sect. 3.4.3.



Figure 3.7: Serial data frame of the Helix128S. The most significant bit is the common set bit (CSB).

3.2.8 Helix PCB

To read out the 752 channels (Type I and Type II chambers; 756 in the case of Type III chambers) of one Inner Tracker chamber, a total of six Helix chips are needed. Two chips each are mounted on one common PCB⁶ using the *chip-on-board* technology. The chip die is glued directly on the PCB and connected to it by wire bonds. A cover of a special epoxy resin (*‘glob top’*) protects both chip and bond wires from mechanical and environmental damages. It should

⁶Printed Circuit Board

be light tight to prevent a charge-up of the pipeline capacitors due to ambient light. The two chips of one PCB are operated in one daisy-chain.

A thin-film ceramics⁷ contains an over-current protection resistor of $600\ \Omega$ for each channel to prevent destruction of the input amplifiers in case of high-voltage discharges in the chamber. The ceramics also serves as a first pitch adapter from $200\ \mu\text{m}$ to the pitch of the chip's input pads ($41.4\ \mu\text{m}$). The connection between this 'fan-in' and the readout strips on the MSGC is made by a short, about 5 cm long Kapton strip line which also provides the final fan-out from $200\ \mu\text{m}$ to the chamber readout pitch of $300\ \mu\text{m}$ ($350\ \mu\text{m}$ for the chambers of Type III, which are mounted between RICH and ECAL).

Apart from the chips and the ceramics, the Helix PCB only contains a few resistors, some capacitors, and four connectors (see Fig. 3.8). Six solder pads per Helix allow the selection of the chip address.

The Helix PCB comes in two variants: the first one, called *AS7*,⁸ is used for all chambers with the exception of the second chamber in a double-layer of the trigger stations. The *AS7* is connected to the signal distribution board (see Section 3.4) which supplies the necessary voltages and control signals and receives the analogue output data. The other variant of the PCB, the *AS8*, is connected to the trigger driver board which transmits the trigger information to the FLT.

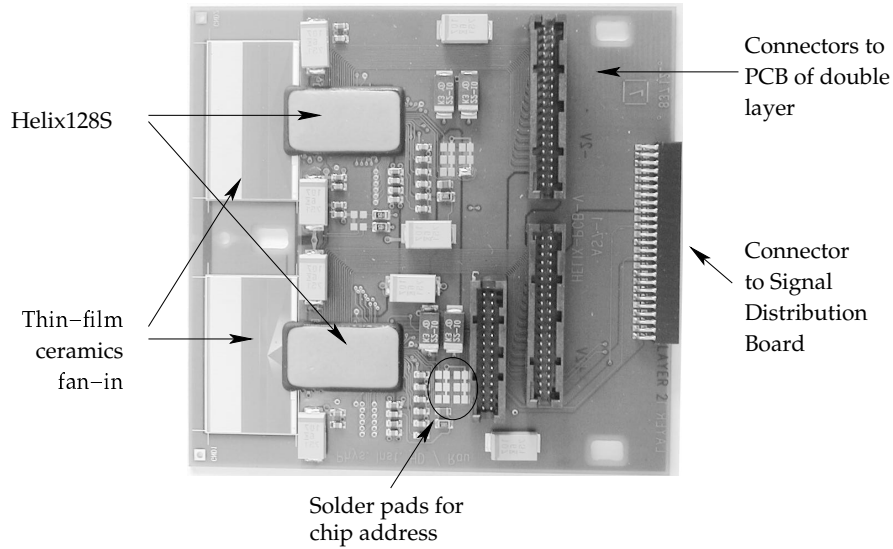


Figure 3.8: Photograph of a Helix PCB (Type *AS7*).

To increase the total trigger efficiency, the layers of the Inner Tracker contributing to the FLT are built as double layers, 2 chambers with the same orientation of their readout strips being mounted on one support plane. The corresponding comparator outputs `notCompOut<i>` of the two chambers of one double layer are ORed using a simple 'wired OR' circuit (see Fig. 3.9) on the Helix PCB *AS8*. The *AS8* contains the pull-up resistors needed for the wired OR of the comparator outputs. It is connected to the Trigger Driver Board which sends the output of the comparators to the Trigger Link Board. One 30-pin connector between an *AS7* and the corresponding *AS8* is used to provide power, clocks and trigger signals to the chips on the *AS8*.

⁷Manufactured by Siegert TFT, Hermsdorf, Thüringen

⁸The Helix PCBs and most of the helper electronics described below were designed at the Electronics Workshop of Uni Heidelberg's Institute of Physics. They are referenced by the project names given by the developers in the workshop.

The same connector routes the analogue output of the *AS8* to the signal distribution board, while the 64 trigger outputs of the *AS7* are routed to the *AS8* board using two additional 40-pin connectors.

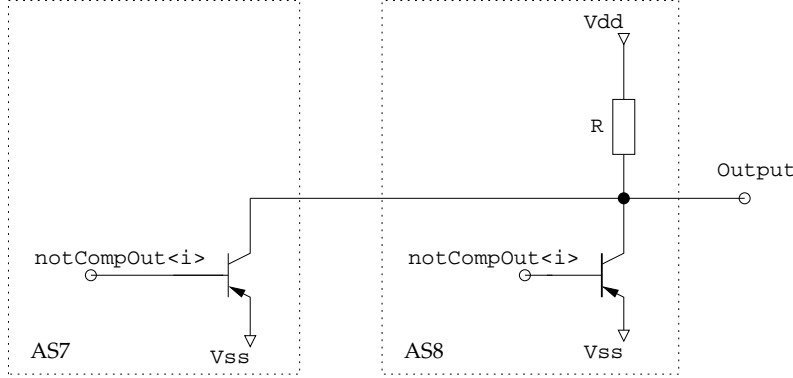


Figure 3.9: Wired OR of two trigger outputs on the Helix PCBs

In the first version of the Helix PCB, the open drain outputs of the comparators were tied between the chip's supply voltages V_{ss} and V_{dd} , with a series resistor of $1\text{ k}\Omega$. The rather high current of 4 mA flowing for each comparator which had switched caused an intolerably large feed-back to the analogue inputs, resulting in oscillations of the complete chip if the comparator thresholds were set low. This problem could be overcome by reducing the output swing of the comparators to 0.75 V and by using a better grounding scheme. The input circuit for the Trigger Driver Board had to be adapted to the reduced output swing (for a complete discussion, read [Kel01]).

Several signals which are generated on the chip are made available on test points on the PCB, which are used for the PCB acceptance test. These include signals which monitor the pipeline operation and the signal *DataValid* which is high as long as the chip is sending its analogue data. The rising edge of *DataValid* may cause cross-talk to the output data; this has to be taken into account when adjusting the sampling point of the ADCs (see Fig. 3.10).

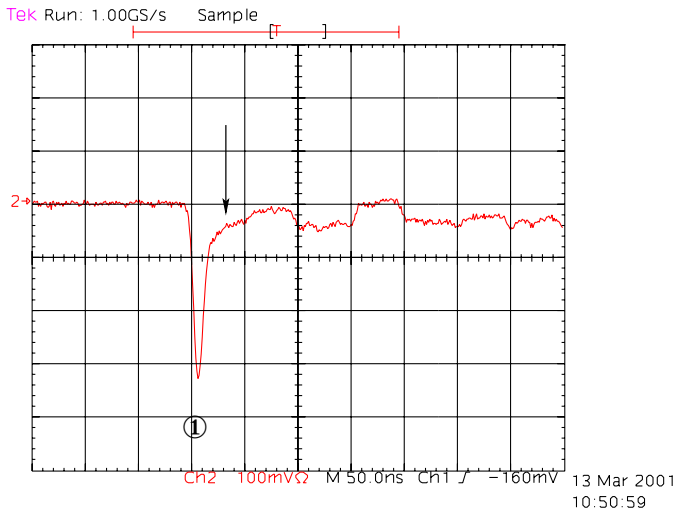


Figure 3.10: The first few channels of an analogue Helix output signal (*RC1k* speed 20 MHz ; one horizontal division corresponds to one read-out channel), showing the cross-talk between *DataValid* and the analogue output: the rising edge of *DataValid* causes distortions in the analogue value for the first channel (①). The sampling point of the FED should be adjusted such that it samples after the first channel's analogue value has settled (arrow).

3.2.9 Helix Versions Used

Several different versions of the Helix128S are used in the Inner Tracker. Each iteration offers some improvements over the previous version; unfortunately, also new bugs and limitations are introduced. The following list describes all Helix versions that have been used in the Inner Tracker installation at HERA-B, together with some of their more serious bugs and possibilities to circumvent them.

Helix 2.2 This version has a satisfactory analogue performance. However, the reference current source on the chip has two problems: it sometimes does not start after power-up, and it tends to oscillate. The start-up problem is circumvented by mounting LEDs on top of the glob top, which are switched on while $\overline{\text{Reset}}$ is active. The incident light then is sufficient to reliably start the current source, if $\overline{\text{Reset}}$ is active for about 30 s.⁹ The oscillation increases the common mode noise and limits the minimal attainable comparator threshold. It can be reduced by additionally connecting a blocking capacitance between the current source's output `IRefOut` and V_{ss} . Chips whose current source oscillates still too much with the blocking capacitor are discarded in the selection process.

Another problem of the 2.2 revision is a feed-back from the open-drain comparator outputs to the analogue input. Both front-end amplifiers and output transistors of the comparator outputs are connected to V_{ss} using the same on-chip power line. At low comparator thresholds the feed-back causes the comparators to oscillate with a frequency of ≈ 5 MHz, making this chip version unsuitable for deriving the signals needed by the First Level Trigger.

The pipeline control logic of the Helix 2.2 contains a bug which can be triggered when two chips are read out in daisy-chain mode. If a trigger signal arrives about 13 `SClk` cycles before the data transmission of the previous event has finished, all subsequent trigger signals are ignored. The FED Controller (see below) circumvents this problem by shifting the trigger signal to an earlier time; the data from the corresponding event has to be discarded because the wrong pipeline column is read out.

Finally, there exists another trigger sequence which stalls the pipeline control logic when the maximum latency is used. This problem is circumvented by limiting the latency to 127 BX cycles.

Helix 3.0 In the version 3.0, the feed-back of the comparator outputs to the analogue inputs was minimised by connecting the front-end and the trigger outputs to different supply lines. To fully profit from this measure, the Helix PCB was modified to decouple the two power connections also on the PCB. The on-chip current source still can oscillate, but the start-up problem is solved.

The first bug in the pipeline logic leading to a stall of operation is fixed, the bug occurring at maximum latency is still present.

Due to a bug in the design software used for this chip version, the pipeline of the version 3.0 is only 136 stages deep, reducing either the maximum latency or the number of events which can be stored in the multi-event buffer on chip. At a latency of 127 `SClk` cycles, two first level buffers can be used.

To be able to build and install the main tracking stations in time for the run 1999/2000, it was decided to use the chip version 3.0 for the double layers contributing to the FLT,

⁹Fortunately, the glob top used for this series of PCBs was not light tight. The Helix chips were protected from ambient light by covering the glob top with a layer of black epoxy glue, leaving a small window for the LED at the correct place.

replacing these chips later during HERA's lumi upgrade shutdown in 2000/2001. To reduce the workload needed for this exchange, the single layers within the trigger stations were equipped with Helix 2.2.

Unfortunately, this mixing of different chip versions within one station of the Inner Tracker led to some problems: Since the Helix 3.0 internally uses the inverted `RC1k` signal for the readout sequencer and a different timing for resetting the pipeline readout amplifier, the timing of the analogue signals of Helix 2.2 and Helix 3.0 are different. To be able to steer the readout of all chambers within one station with the same control signals, the `RC1k` signal fed to the Helix 2.2 chips on these stations was inverted on the signal distribution board. Nevertheless, the available phase space of possible timings (relative delays of `SC1k`, `RC1k` and `Trigger` where all chips of one station are working synchronously) was rather restricted. This difficulty to find a common, reliable timing for both chip versions at once effectively prevented the use of a readout clock speed of 20 MHz during the run 2000.

Helix 3.1a The latest version of the Helix128 chip family corrects most of the bugs of its predecessors. Compared to the version 3.0, it has a non-oscillating reference current source, and the full pipeline length is usable. Also the second bug in the pipeline control logic is fixed, so that the maximum latency of 128 BX cycles can be used. However, the readout timing still differs from the Helix 2.2.

There exists a minor limitation which only occurs on startup: after power-up, all Helix 3.1a in a daisy chain possess the readout token; hence all daisy-chained chips send their analogue data simultaneously. This excess token can be removed by resetting the chips once while they are sending analogue data. After such a reset, the daisy chain works as expected.

Due to the timing differences between the versions 2.2 and 3.1a, all Inner Tracker stations in which mixed chip versions were used are being modified during the HERA lumi-upgrade shutdown (2000/2001): the stations contributing to the FLT will be fully equipped with Helix 3.1a, in all other stations the Helix version 2.2 will be used. No Helix 3.0 will be used in the Inner Tracker after the completion of this upgrade programme.

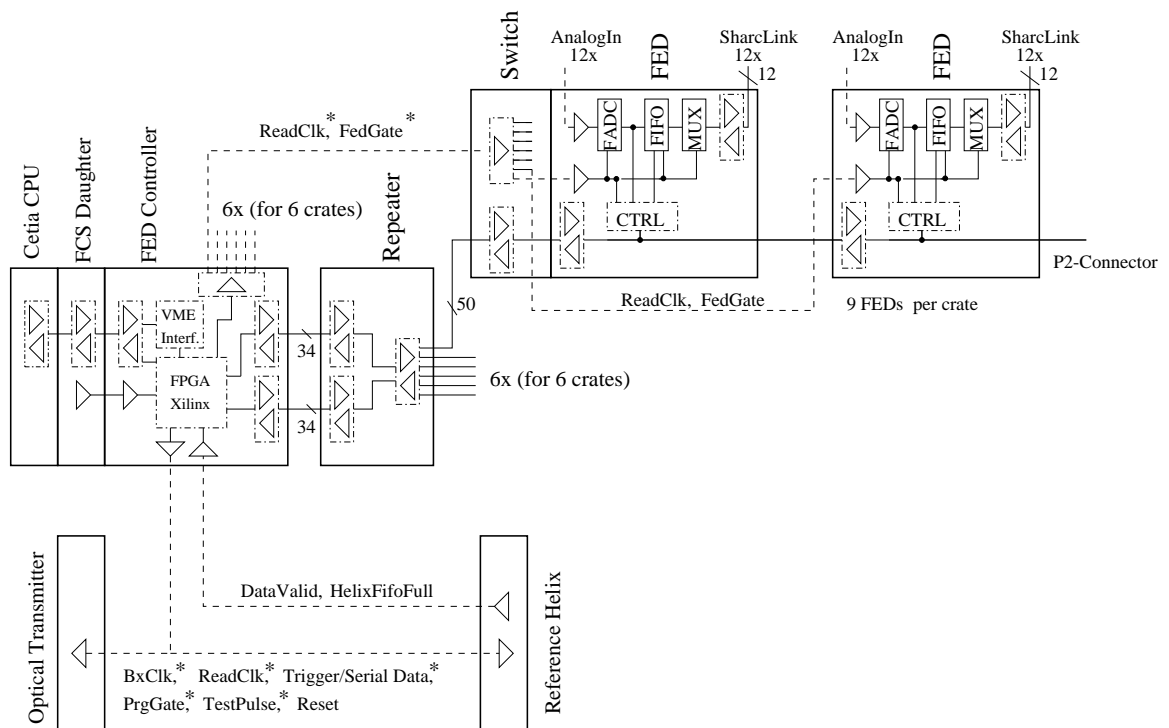
3.3 FED System

The FED system as it is used in HERA-B was developed at the Max-Planck Institute for Nuclear Physics for the readout of both the VDS and the ITR. Its details are described in [Sch99b, Hau98]. It is responsible for

- Communication with the Fast Control System (FCS) which controls the event flow within the experiment. After the FCS receives a trigger decision from the FLT, it generates a trigger number (FLTNum). This number is distributed to the readout systems of all sub-detectors, together with the bunch crossing number (BxFLT) and the event type (FLTType) of the trigger. Since the complete readout system is working asynchronously, the Front End Drivers must include FLTNum and BxFLT for each block of data they deliver, so that the DAQ system can distinguish between the data of different events.
- Implementation of a FIFO for incoming triggers and event information. Since the Helix pipeline implements a First Level Buffer with a depth of eight events, the corresponding event information must be stored until the analogue data for the corresponding trigger is transmitted by the chips.

- Generation of the digital control signals. The FED system receives the trigger information and the HERA bunch crossing clock from the FCS and generates the signals necessary to operate the readout chips: the sample and readout clock (**SC1k** and **RC1k**), trigger (**Trigger**), test pulse (**FcsTp**), and reset (**Reset**) signals.
- Digitisation of the analogue Helix data with a speed of up to 41.6 MHz (4 times f_{BX}).
- Buffering of the data. This is needed since the communication between the FED and the SLBs is asynchronous, while the readout burst from the Helix cannot be interrupted and resumed later on. Without buffering, a congestion in the data transmission from FED to SLB would lead to a loss of analogue data.
- Transmission of the digitised data to the Second Level Buffers.

The FED system is split into different boards called FED Controller, Repeater, Switch and FED Board. All modules are built following the VMEbus specifications. Fig. 3.11 shows a schematic overview over the different components of the FED system.



* = Signals have programmable delays on FED Controller, - - - = Lemo Cables, — = FlatBand Cable or Backplane

Figure 3.11: Schematic overview over the FED system (taken from [Sch99b]). Cestia-CPU, FCS Daughter, FED Controller and FED Repeater are housed in one common VME crate (*left*). The system is started and controlled by a process running on the CPU. The FCS Daughter is connected to the central Fast Control Crate by means of a flat ribbon cable. It sends the received `BxC1k` and trigger information to the FED Controller by means of the custom VME backplane. Using this information, the FED Controller generates the control signals for the readout chips.

FED Controller The FED Controller contains a VME bus interface, programmable delay lines (8 bits with a step size of 0.5 ns) for the control signals for the readout chips, and an FPGA

(field programmable gate array) which controls the operation of the complete FED system. The FED Controller is connected to a FCS daughter which receives the bunch crossing clock and the event and trigger information from the FCS master crate. It derives the signals needed for the operation of the Helix chips from the FCS signals. The settings of the delay lines as well as several other delays can be set using the VME interface.

Repeater and Switch The combination of repeater (located in one VME crate with the FED controller) and several switches (one sitting in each FED crate) distributes the event information from the FED Controller to the 40 FED boards needed to read out the Inner Tracker. A flat-ribbon cable between FED Repeater and FED Switch provides the event information, while the signals `FEDGate` and `RC1kFED` are distributed to the FED Switches directly from the FED Controller via LEMO cables. The connection between FED Switches and Boards within one crate is done using the VME custom back plane.

FED Board The FED Board contains 12 analogue input channels with amplifiers, Flash ADCs (10-bit AD9050 from Analog Devices; only the upper 8 bits are used), data buffers and 8-bit to 4-bit multiplexers which send the data to the SLB according to the Sharc Link Protocol. The analogue input signal is expected to be between 0 V and -1 V; it is inverted by the input amplifier and shifted to the input range of the FADC. Different input levels, which can occur due to offsets in the analogue data transmission chain, can be accommodated with an offset trimmer.

The program running on the FPGA of the FED Controller and several settings of the FED system are loaded at run startup time using the VME interface of the controller. These settings include the registers `HelixBugFix`, which circumvents the bug present in the pipeline control logic of Helix version 2.2, `GateExtension`, which determines how many ‘padding’ bytes besides the $2 \times (128 + 8)$ bytes of Helix data should be sent in a data block, and the delays of the control signals. Also, the FED boards need to be told which detector component (VDS or ITR) they are connected to and how many bytes they have to send to the SHARCs. The settings of the FED Controller registers are described in a configuration file which is loaded into the FED Controller at the beginning of each data taking run. One such file is shown in Appendix A.2.

3.4 Additional Electronics

Additional electronics is needed to provide power to the Helix chips, to supply them with the required clock and trigger signals, and to transmit the analogue data from the experiment into the electronics trailer. Most of these additional systems were designed, tested, and built during the work for this thesis together with the electronics workshop of the Institute of Physics in Heidelberg.

In order to have a complete galvanic separation between the readout electronics at the experiment and the electronics trailer, all signals are transmitted optically. The CAN bus¹⁰ used for slow control purposes is de-coupled optically at the interface boards. This prevents ground loops and pick-up problems associated with them.

Not all components needed for data and control signal transmission are sufficiently radiation hard to survive several years of HERA-*B*-operation in the vicinity of the beam pipe. These parts are moved to a region of the detector where the radiation load is significantly lower. Additionally, all electronics situated in the active area of the detector will contribute to multiple

¹⁰Controller Area Network; a field bus originally developed by the automotive industry. It provides reliable data communication even in an unfavourable environment with high noise levels.

scattering and pair conversions¹¹ and thus to a loss of resolution of the spectrometer, which is another strong motivation to have as little ‘dead’ material as possible in the acceptance of the detector. Finally, any electronics which is mounted directly at the detectors is extremely hard to access and to repair or replace in case of a malfunction. This can only be done after removal and disassembly of a complete half super-layer, which involves some risk to the fragile GEM-MSGCs.

Fig. 3.12 shows the location of the different readout components near a chamber.

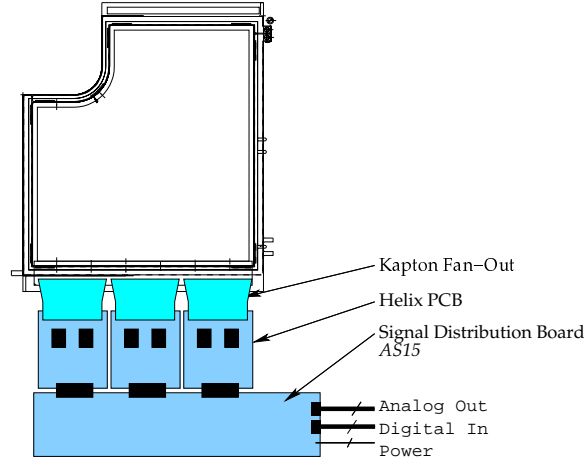


Figure 3.12: Location of the readout components near a chamber.

The *signal distribution board (AS15)* is mounted near to the detector and is directly connected to the Helix PCB. It provides power connection for the Helix chips, distributes the clock and trigger signals and contains a first buffering amplifier for the analogue signals. All components placed on the signal distribution board were tested for sufficient radiation tolerance with X-rays and a ^{60}Co source.

The other interface electronics (responsible for transmission of the analogue data and for reception of the control signals) is located either on the Outer Tracker frame, about 3 m away from the beam pipe, or on the inner walls of the spectrometer magnet, where the radiation level is considerably lower compared to the detector position. These interfaces can be replaced easily in case of defects. The electrical connection between the interface electronics and the signal distribution board is done by two fine-pitch twisted pair cables with 20 lines each. All digital control signals transmitted on these cables are differential signals, and also the analogue data is transmitted differentially to minimise cross-talk and pick-up.

3.4.1 Data Valid Board

The Data Valid Board (*IF7*) has two functions: it distributes the control signals which are generated by the FED controller to the optical senders (see Section 3.4.2), and it provides the FED system with a reference signal which indicates the valid transmission of analogue data from the Helix chips in the experiment. This signal, called **FedGate**, is needed by the FEDs, whose ADCs are constantly sampling the inputs 27 ns after the rising edge of **RClkFED**. Only while **FedGate** is HIGH the analogue data is stored in the buffers of the FED. Immediately afterwards the event trailer information is added, and the data is sent to the Second Level Buffer.

¹¹Typically, a multi-layer PCB has several layers of $15\ \mu\text{m}$ Copper. Cu has a radiation length of $X_0(\text{Cu}) = 1.43\ \text{cm}$.

Even for low trigger rates there is no fixed phase relation between the arrival of a **Trigger** at the Helix and the beginning of data transmission, and at higher trigger rates, when the multi-event buffer on the Helix is fully used, the time between a trigger and the corresponding readout burst depends in a non-trivial way on the previous triggers. Instead of rebuilding the internal logic of the Helix inside the FED Controller to determine the correct starting point for digitisation, the start signal for the FED boards is derived from a ‘reference Helix’ located on the Data Valid Board in the electronics trailer. The Data Valid Board contains a circuit similar to the digital part of the Signal Distribution Board, and a complete Helix PCB is mounted as a piggy-back board. The Helix chips on this PCB receive the same control signals which are sent to the readout chips at the detectors. The **DataValid**-signal of its first chip is buffered and made available at the front-plane of the *IF7* as a TTL¹² signal. The FED Controller uses the rising edge of this **DataValid** signal to generate the needed **FEDGate**.

3.4.2 Digital Control Signals

The proper and synchronous readout requires that all Helix chips within one clock phase get the same signals **Sclk**, **Rclk**, **Trigger**, and **Reset**. These signals are generated by the FED controller and fed as TTL signals into the DataValid module. This converts them to LVDS¹³ and distributes them to optical transmitters, which are placed on interface cards called (*IF9-1*) sitting in a VME crate in the electronics trailer. For each signal line these use an infra-red laser diode (Mitel 1A444 [Mit99], $\lambda = 840$ nm)¹⁴ to transmit the digital signals to the receiving interfaces *IF6-1*, which are situated at the experiment. Here the signals are converted to LVDS and sent to the signal distribution boards using a twisted-pair fine-pitch cable. Up to eight signal distribution boards are connected to this bus. The LVDS-to-TTL and TTL-to-LVDS converters are National Semiconductor’s DS90C31 and DS90C32 [Nat98], which support a ‘multi-drop’ operation mode where up to eight LVDS receivers are connected to one LVDS sender.

3.4.3 Helix Register Loading

Besides the opto-electrical interfaces for the control signals, the *IF6-1* contains a circuit which is used to load the needed register values into the Helix chips. This circuit consists mainly of a CAN bus¹⁵ device, the SLIO [Phi96]. The sixteen in- and output ports of the SLIO can be configured by sending CAN messages to the device; for example, they can be used as digital outputs whose state can be changed by sending more CAN messages. On the *IF6-1* one or two SLIOs are used to generate the signals **SerData**, **SerClk** (multiplexed onto the lines **Trigger** and **Rclk**, respectively), **SerLoad**, and **Reset**.

Since the Helix128S has only a 6-bit chip address, at most $2^6 = 64$ chips attached to a single serial programming bus can be addressed individually. This implies that for the larger half stations with more than eight chambers an additional programming bus is needed. This second programming bus is implemented as a piggy-back card sitting on the *IF6-1*. It only contains an additional SLIO and simply repeats the other control signals which are received from the *IF6-1*. Finally, not more than sixteen SLIOs may be connected to one physical CAN bus at the same time. The installation at HERA-B uses one physical CAN bus per super layer, with the CAN controller attached to the bus in the middle and up to two SLIOs at each end of the cable.

¹²Transistor to Transistor Logic

¹³Low Voltage Differential Signalling; two signal lines having opposite polarity and a low voltage swing of only ≈ 350 mV between the logical states *low* and *high*.

¹⁴In order to comply with safety regulations for laser equipment, the maximum light output power of the senders is limited by hardware measures to $P_{\max} \leq 0.8$ mW. This makes the senders class 3A laser products.

¹⁵Controller Area Network, a field bus [Ets00] used in HERA-B for almost all slow control purposes

Using this three-stage addressing scheme (CANbus id, SLIO address, chip address), each Helix of the Inner Tracker can be addressed and programmed individually.

3.4.4 Signal Distribution Board

The Signal Distribution Board *AS15* (see Fig. 3.13 for a block diagram) is attached to the control signal bus from the optical receiver interface *IF6-1*. It receives all control signals as LVDS and converts them to the signal levels needed by the Helix chips: *SClk*, *RClk*, and *Trigger* as LVDS, *Reset*, *FcsTp*, and *SerLoad* as TTL signals (actually, the Helix needs CMOS compatible signals on these inputs, with signal levels V_{ss} for ‘low’ and V_{dd} for ‘high’). On the *AS15*, standard LVDS-to-TTL and TTL driver ICs are used, which provide the appropriate signal levels with adequate raise and fall times of the signals). It also generates an inverted version of *SClk*, the signal *SClkTTL*, which is passed on to the Trigger Driver Board. The analogue receiver circuit is described in the next section in more detail.

Finally, the *AS15* provides the supply voltages ± 2 V and GND to the Helix PCBs.

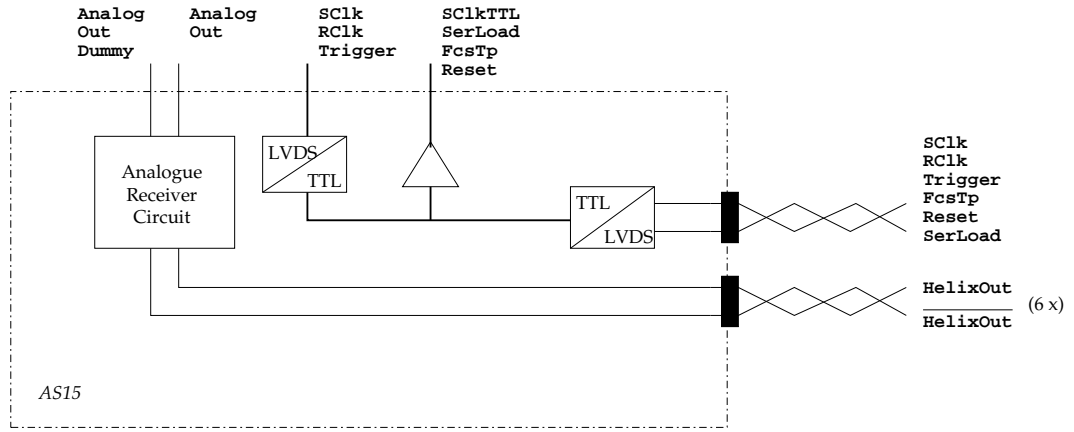


Figure 3.13: Block schematics of the Signal Distribution Board *AS15*. The board contains three interface groups comprising the Analogue Receiver Circuit, the TTL-to-LVDS converter and the TTL-buffer, so that up to three pairs of *AS7–AS8* Helix PCBs can be controlled and read out using one *AS15*.

3.4.5 Analogue Data Transmission

The transmission of the Helix analogue output to the ADCs which are located in the electronics trailer of *HERA-B*, about 50 m away from the experiment, takes place in three stages: the first stage is the receiver circuit on the signal distribution board (*AS15*), directly connected to the front-end PCBs. It converts the current output of the Helix into a differential voltage signal which is driven over ≈ 4 m twisted-pair cable. The analogue receiver circuit is shown in Fig. 3.14. It converts the current signal of the Helix into a differential voltage signal, subtracting *AnalogOutDummy* from *AnalogOut*. The circuit uses the AD8004 [Ana99] which is a fast, high-bandwidth amplifier developed for video applications.

The differential signal is then received by the Interface *IF1-1* where it is converted into an analogue-optical signal. The sender uses an infra-red LED (Mitel 1A194 [Mit94], wavelength $\lambda = 860$ nm) to transmit the data over ≈ 50 m of optical fibre. The optical signals are received by interfaces designed and built at the Max-Planck-Institute for Nuclear Physics, Heidelberg. These receiver interfaces are built as NIM modules and are located in the electronics trailer. Their output is connected directly to the analogue inputs of the FED boards. The transmission

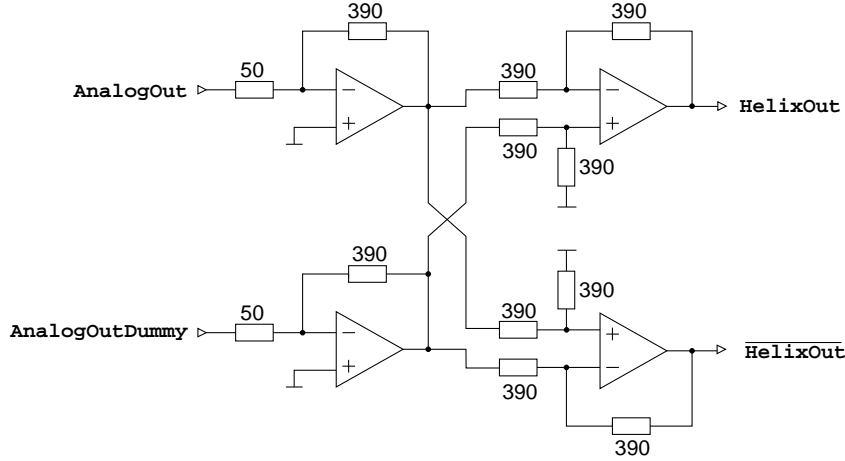


Figure 3.14: The analogue receiver circuit on the signal distribution board. The transimpedance resistance is $390\ \Omega$. The circuit uses the AD8004 amplifier [Ana99] and drives about 4 m of twisted-pair flat-ribbon cable.

chain from optical sender to optical receiver has a total gain of about 1; variations arise mainly from imperfect coupling of the light into the optical fibres.

The total gain of the complete readout chain, from the input of the Helix to the output of the receiving interface, was measured to be

$$g_{\text{fast}} = 58 \frac{\text{mV}}{24\,000\ \text{e}^-} \quad (3.3)$$

for the Helix settings used by the Inner Tracker. Details of this measurement are shown in Appendix C.

3.4.6 Setup in the Electronics Trailer

The cables from the electronics trailer to the experiment are routed through three different cable chains to allow independent movement of the trailer and the three platforms on which the whole experiment is mounted. The cable lengths in the three chains are 48 m to the Magnet platform (MC), 46 m to the central platform (PC), and 52 m to the trigger stations behind the RICH (TC). Since the front-end electronics samples the value of the amplified chamber signal once per bunch crossing, it is important that the sampling point can be adjusted to the maximum value of the shaped pulse. To compensate the different cable lengths (and, to a certain extent, the time-of-flight of the particles through the detectors), three different clock phases are used for the Inner Tracker.

The three clock phases are provided by three FED controllers, which also provide the **RC1kFED** and **FEDGate** signals to the FED boards connected to the corresponding stations. For each clock phase, a separate DataValid board *IF7* is used to generate the correct **FEDGate**. Since the timing of **FEDGate** and **RC1kFED** may differ between different phases, only FEDs of one clock phase may be installed in one common VME crate. For the run period 2001/2002, a fourth clock phase is foreseen to take care of the differences in the timing requirements of the Helix versions 2.2 and 3.1a; the chambers in the PC area (between the magnet and the RICH) contributing to the FLT will be built with Helix 3.1a and will get a separate clock phase.

The actual setup of all readout components in the electronics trailer is described in detail in Appendix A.

3.5 Grounding Scheme

The Helix attached to a GEM-MSGC is quite sensitive to pick-up and other sources of noise. To obtain the optimum analogue performance, a good and reliable grounding scheme must be implemented.

A first version of the grounding scheme was defined and tested during the beam tests at PSI in 1998; its main features are drawn schematically in Fig. 3.15. This grounding scheme was subsequently implemented on all chambers which were used in the tracking stations for the HERA-*B* run period 1999/2000.

The backside of the MSGC-wafer and the drift cover are coated with a self-adhesive aluminium foil of 50 μm (backplane) and 9 μm (frontplane) thickness of Al. The backplane is needed as a reference plane for the signal propagation on the MSGC wafer; it also serves as a shielding. Both back- and frontplane are also used to provide the chamber with a well-defined electrostatic boundary. The backplane is connected to the analogue ground connection of the readout chips by one thin copper wire. All shieldings of HV cables and the analogue ground of the PCBs are connected to one central grounding point.

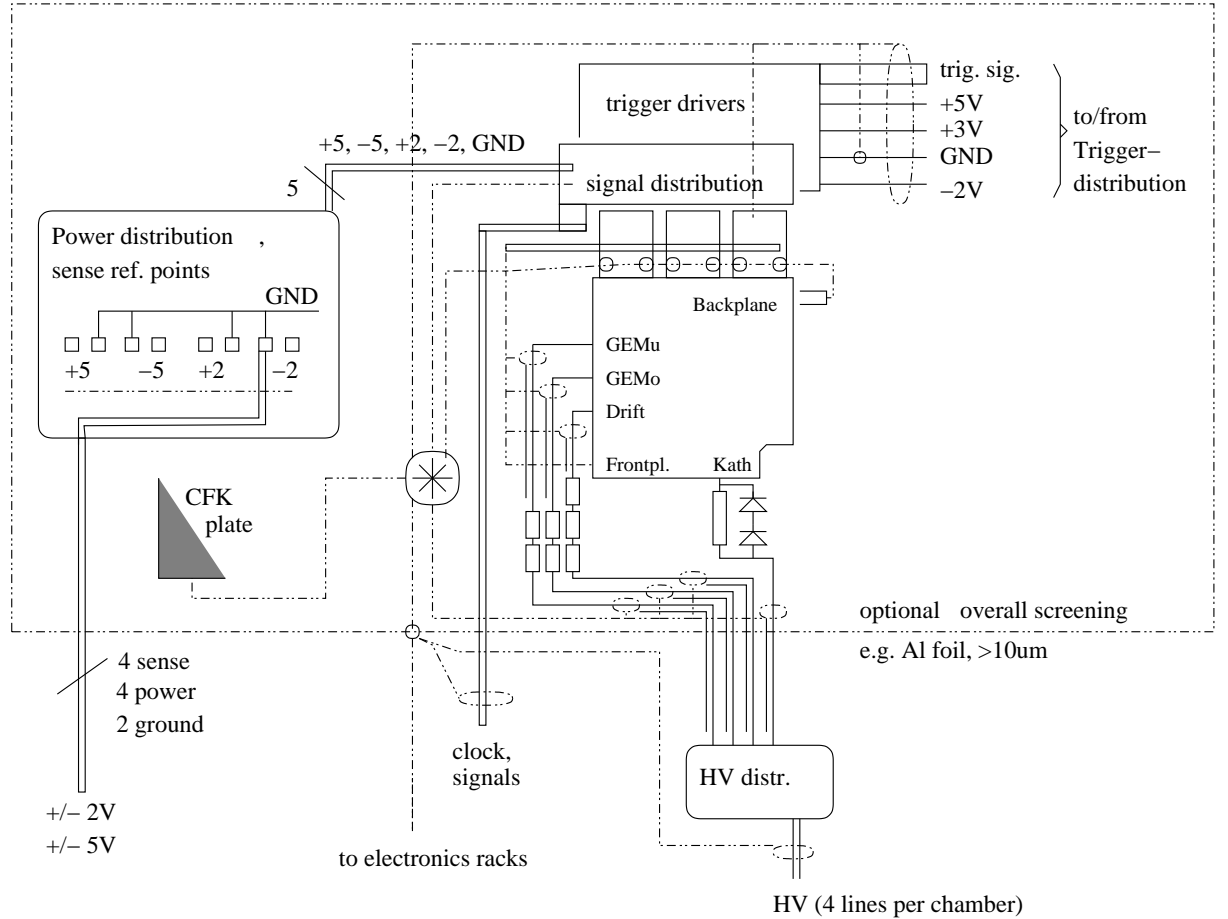


Figure 3.15: The ‘old’ grounding scheme as defined at the PSI test in 1998 and as applied to the Inner Tracker stations in 1999 (figure drawn by U. Straumann). *Dash-dotted* lines denote grounding connections only (no DC currents allowed). The optional screening of a complete station was omitted in the installed stations.

The new, much improved grounding scheme is based on suggestions by H. Spieler and

P. Lichard and the experience of the Zürich group [Wal01] during another beam test in 1999. For the 2001/2002 run of HERA-B all chambers will be equipped with this new grounding scheme. It has basically the same circuit diagram as shown in Fig. 3.15, but is improved in the following aspects:

- The overall mechanical stability of all ground and cable connections is improved. This is achieved by introducing a small PCB to which all HV cables are solidly mounted. These PCBs contain also the overcurrent protection resistors for the high voltage supply lines.
- The central grounding point is replaced by a copper strip on the PCB holding the cables, to which all shielding and ground lines are connected with the shortest possible cables.
- The connection between backplane and ground of the PCBs is made with a $5\ \mu\text{m}$ thin copper foil over the full width of the chamber, it also provides an additional shielding.
- The connection to the backplane and to the (slightly conducting) support plane is made by a conducting epoxy glue.
- The high-voltage connection to the cathode fan-in gets an additional low pass filter.
- The cathode fan-in which holds the current limiting resistors for the cathode strips is shielded by an envelope of Kapton foil with $5\ \mu\text{m}$ of copper.

This grounding scheme was implemented in a test station used for trigger tests which was installed in the position of MS15— in July 2000. The new grounding was shown to improve the noise situation in the readout chips significantly, almost completely eliminating pick-up and baseline variations. It is depicted schematically in Fig. 3.16.

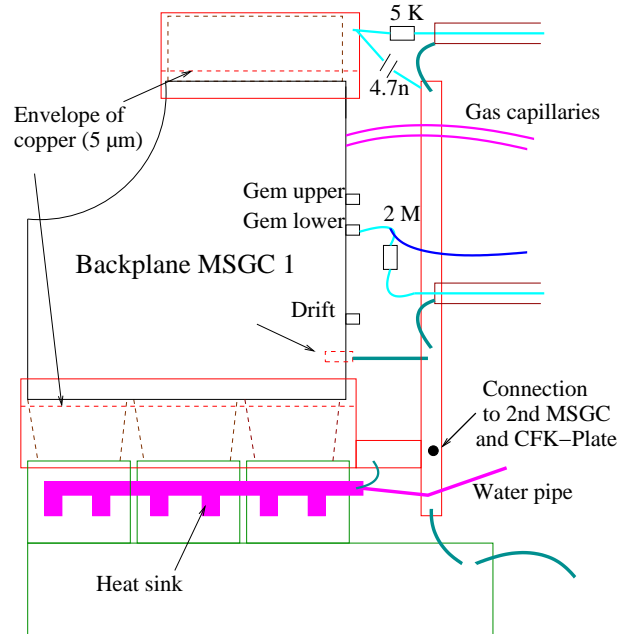


Figure 3.16: The new grounding scheme which is implemented on all Inner Tracker stations for the run 2001/2002 (Figure from [Kel01]).

3.6 Readout Software

This section describes the flow and processing of the raw data read out from the Inner Tracking detectors. Signals from the passage of particles through the detectors have to be identified in the raw data, the data have to be compressed before they can be stored on tape, and a mapping between the hardware identification (given by the FED ID) and the actual chamber has to be provided.

During the work for this thesis, several parts of the software were written specifically for the Inner Tracker, others were adapted to the needs of the ITR from software written by the VDS group. The organisation of the Inner Tracker software with its various packages is described in Appendix B.

3.6.1 Data Format

The output of the FED is one analogue eight-bit value per readout channel. As described above, two Helix128S chips are read out in daisy-chain mode and send their data to one FED. Including the two eight-bit patterns for the column numbers, 272 bytes are needed for the analogue data sent by one Helix PCB. The FED board adds in total fifteen padding bytes in front of and behind the analogue data and one byte to flag error conditions.

Some additional information is needed to identify the source of the specific data block and to synchronise the data with the data from the other sub-detectors. For the Vertex Detector and the Inner Tracker, this information is appended to the block of analogue data. The contents of this *trailer* is prescribed by the DAQ system. The field **Bytecount** indicates the total number of bytes in the data record. **FLTNum** and **BxFLT** tag the record as belonging to a specific event. These two numbers are distributed by the Fast Control System for each trigger and are unique for the lifetime of a record in the DAQ system. **ComponentID** identifies the sub-detector which sends this record; the Inner Tracker's component id for the DAQ is 0200_h.¹⁶ Finally, the exact origin of this data record within one sub-component is coded into **FED Id**. A mapping between **FED Id** and position of the corresponding chips on their chamber is provided by the setup database (see Section 3.6.5). The complete data record including the trailer is 300 bytes long. Fig. 3.17 shows the data format used by the FED system of VDS and ITR.

3.6.2 Pedestal and Noise Following

Before readout strips which have seen a signal can be identified reliably, the raw data have to be corrected for two effects: pedestal values have to be subtracted for each channels, and baseline distortions must be corrected chip by chip. Also, the noise level for each channel has to be determined, since it is used later on in the step of cluster finding.

The analogue values of one chip show slight variation from channel to channel (*pedestal*), which are a characteristic of each individual chip, but may change slowly with time [Wol00]. These variations are mainly caused by small differences in the gain of each channel's pipeline amplifier. Additionally, a minor contribution comes from different values of the capacitors used as pipeline cells.

During processing of the raw data, the pedestal values are determined for each strip averaged over all pipeline columns. This is sufficient because the variation in the analogue signal from pipeline cell to pipeline cell of one channel is rather small (Fig. 3.18) compared to the channel-to-channel variation. Since the pedestal is determined online at the start of each run, the program would need an intolerably high number of events to obtain an estimate for the pedestals for each

¹⁶ A subscript *h* is used to indicate a hexadecimal value.

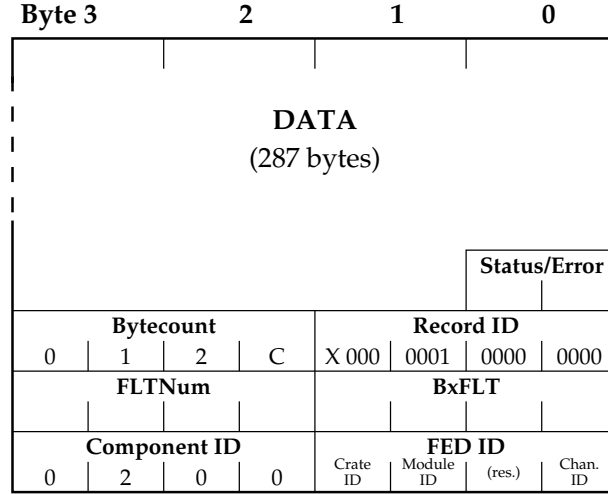


Figure 3.17: Data format of the ITR and VDS raw data in the Second Level Buffers. The field **Bytecount** is always set to $012c_h = 300$. For the ITR, the field **ComponentID** contains 0200_h . The **Status/Error** byte is used by the FED Controller to indicate the occurrence of an error condition to the processing software which reads the data.

column number. This would be especially inconvenient for the online sparsification (see below) which runs in parallel on the 200 PCs of the Second Level Trigger farm.

The estimates for the pedestal and variance values are obtained in an iterative procedure. The pedestal value for one channel is estimated by averaging the raw data of this channel over the last n events. To save computing time, only the sum of the raw data values is updated with each event, while the pedestal estimate is updated only every 2^k th event. If the k th estimate for the pedestal value of channel i is denoted by $p_i^{(k)}$ and the raw data of channel i in the event j by $r_{i,j}$, then the $(k+1)$ st estimate can be written as

$$\begin{aligned}
p_i^{(k+1)} &= \frac{1}{2^{k+1}} \sum_{j=1}^{2^{k+1}} r_{i,j} \\
&= \frac{1}{2} p_i^{(k)} + \frac{1}{2^k} \sum_{j=2^k+1}^{2^{k+1}} r_{i,j} .
\end{aligned} \tag{3.4}$$

The start value $p_i^{(0)}$ is just taken to be $r_{i,0}$. This scheme has the advantage that it gives fast estimates of the pedestal after a few events. After a user-selectable number k_0 of iterations, the number of events entering the calculation is kept fixed, so that every 2^{k_0} events the pedestal values are updated with an average of the last pedestal value and the average of the last 2^{k_0} values of $r_{i,j}$ (typically, a value of $k_0 = 8$ is used). This updating procedure ensures that the pedestal values used for correction of the raw data can follow variations of the chip's output occurring with a large time-constant. Fig. 3.19 shows the variation with time of the pedestal estimate for one channel in the startup phase. Including all data from one channel, regardless whether the channel has seen a signal (which for the Inner Tracker is negative) in an event, biases the estimate for the pedestal value towards lower values. However, the mean occupancy (*i.e.* the probability that a channel sees a signal in an event) seen in the Inner Tracker chambers is only about 5 % at high interaction rates. The presence of these signals shifts the mean value by about 1 to 2 ADC counts, which is still tolerable.

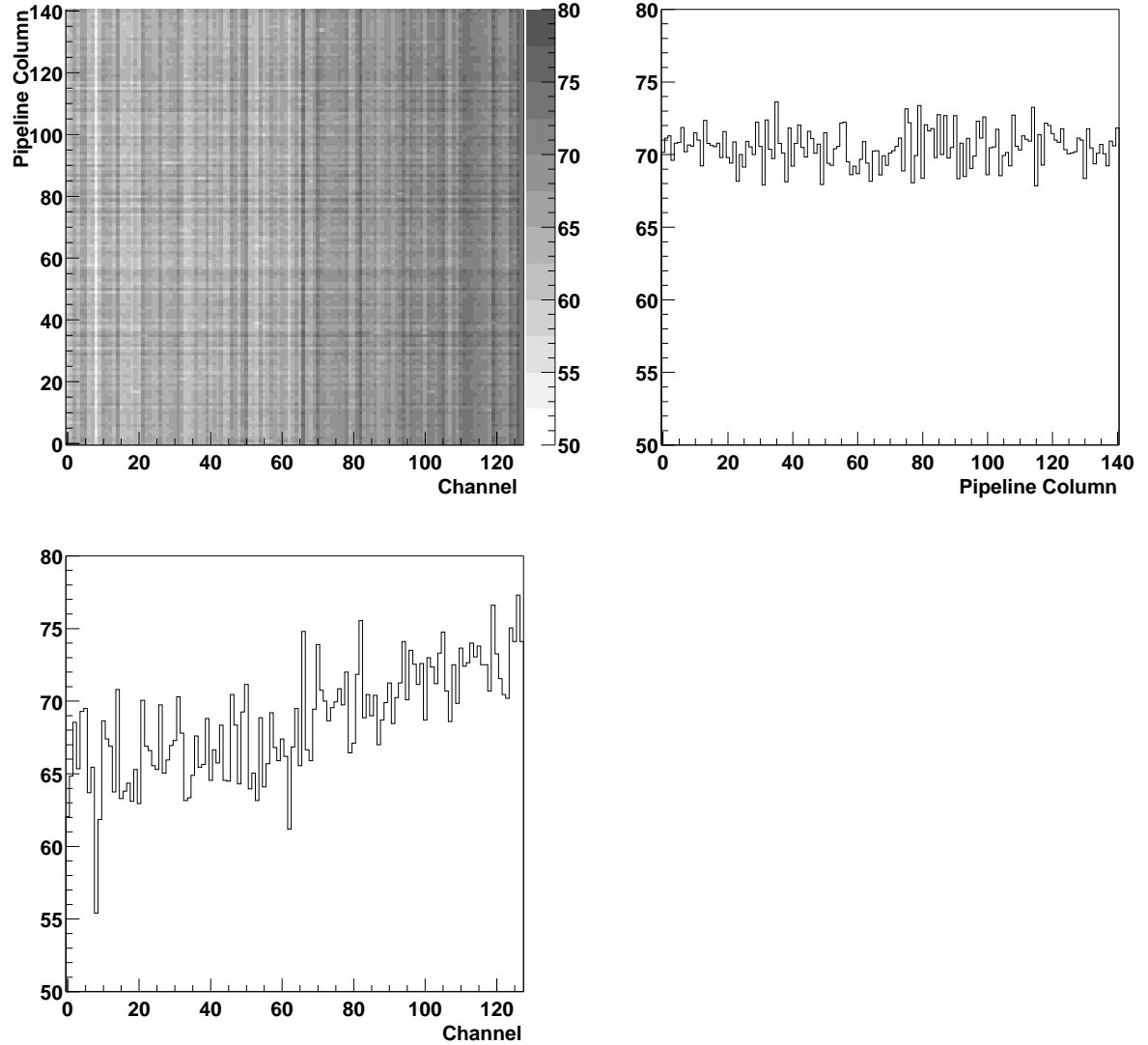


Figure 3.18: *Top left:* Pedestal values (measured in ADC counts) for each pipeline cell of one chip, shown in gray-scale. The channel-to-channel variation is large compared to the variation from pipeline cell to pipeline cell and shows up as vertical bands. *Top right:* Pedestal for one channel (channel 100) as a function of the pipeline column number. The distribution has a width of ≈ 1.2 . *Bottom left:* Pedestal values of all channels of the chip for a fixed column number (column 100). This distribution has a width of about 3.7. All values shown are in ADC counts ($1 \text{ ADC} \hat{=} 1600 e^- = 0.26 \text{ fC}$); for the measurement, the chamber was installed in the experimental area.

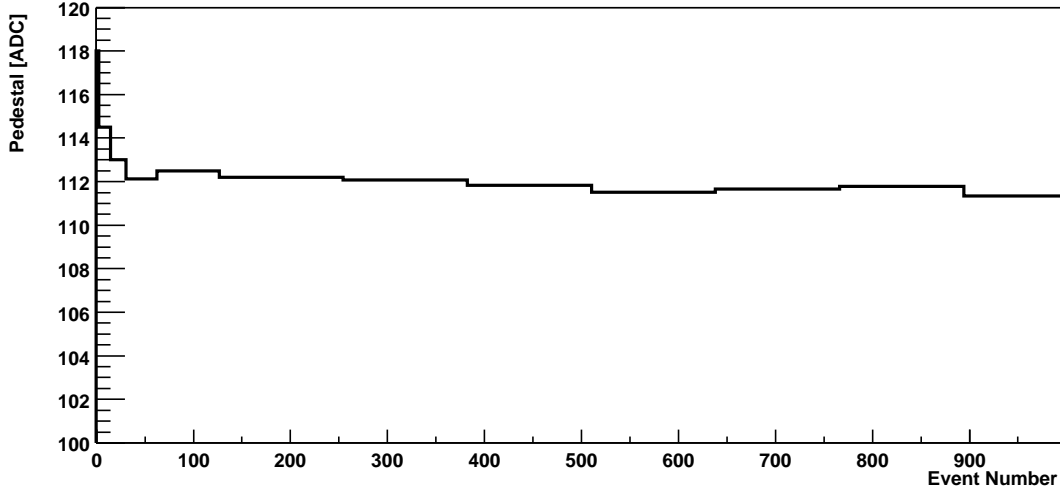


Figure 3.19: Variation of the pedestal estimate of one channel over time. The ‘turn-on’ region can be seen at the left of the plot; after about 128 events the estimate has stabilised and varies only slightly over time.

Low-frequency pick-up results in shifts and distortions of the baseline which can be seen after subtracting the pedestal from the analogue data. These *baseline variations* are removed by fitting a linear spline with five nodes (a piecewise linear function between five points) to the pedestal corrected data and subtracting the result of the fit. For this fit, outliers are not considered. An outlier is defined by showing a signal $|q_{i,j}| > q_{\text{cut}}$ with a typical value of $q_{\text{cut}} = 10$ ADCcounts; these are mainly the hits. Fig. 3.20 shows the pedestal corrected data of one chip with the baseline fit to the data.

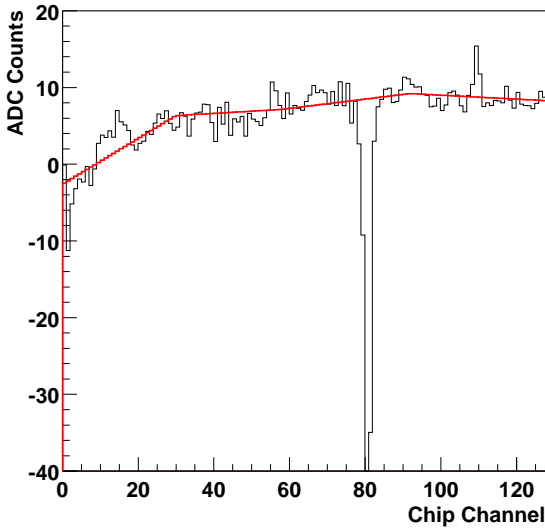


Figure 3.20: Pedestal corrected data of one chip (of chamber M01—1) with the spline function determining the baseline. The signals of channels 79-82 form one cluster from the passage of a particle through the chamber; they are recognised as outliers and disregarded for the spline fit.

The variances of all channels are estimated and followed with an algorithm similar to the pedestal determination. Since pedestal subtraction and baseline correction are ensuring that the mean value of the corrected signals $q_{i,j}$ is at $\langle q_i \rangle = 0$, the variances v_i can be estimated by

averaging $q_{i,j}^2$ like (Eq. 3.4), using

$$\begin{aligned}\text{var}(q_i) &= \langle (q_i - \langle q_i \rangle)^2 \rangle \\ &= \langle q_i^2 \rangle - \langle q_i \rangle^2 = \langle q_i^2 \rangle\end{aligned}$$

Outliers (for example, a real hit) will greatly distort the estimate of the variance obtained by this procedure. Thus the algorithm applies a cut on $q_{i,j}$ and computes a quantity σ_i^2 which is called *subtracted variance*. The cut applied is the same which determines outliers in the baseline fit; channels with $|q_i| > 10$ are considered to be outliers.

3.6.3 Cluster Finder

The cluster finder has the task to identify those readout strips which have collected charge due to the passage of a particle. In the GEM-MSGCs used for the Inner Tracker, the signal caused by one particle is in the most cases distributed over more than one readout strip. Usually two or three adjacent strips show a signal for the passage of one particle through the chamber. These readout strips are grouped by the cluster finder to form one cluster (or ‘hit’).

The first step of cluster finding is to subtract the pedestals from the raw data and apply the baseline correction as described above. Fig. 3.21 shows the results of the pedestal and baseline corrections for one chip for two chambers. The first chip shown is attached to chamber M01—1; it shows a large distortion of the baseline. The impact of the pedestal subtraction can clearly be seen, as well as the need for a baseline correction. The second chip shown is attached to chamber M15—1 which has a much improved grounding scheme, reducing the baseline variation to almost zero. The baseline correction in this special case is not needed, but when applied anyway, does no harm.

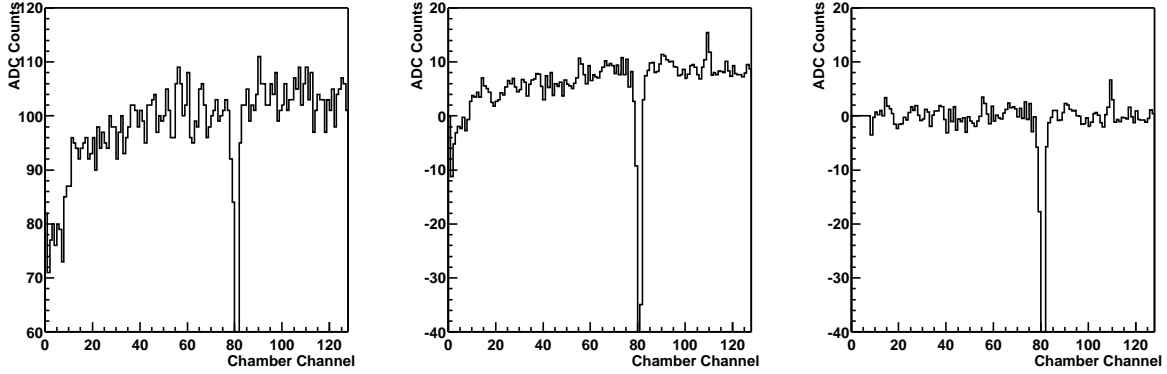
The data of all six chips attached to one chamber are concatenated. These corrected data q_i are then compared channel by channel to the noise level σ_i determined in the previous step. If the signal of the channel i_{start} exceeds its noise estimate by a factor $\sqrt{s_{\text{cut}}}$, this channel is the starting point of a cluster candidate. Only channels with the correct polarity of the signal are considered; for the ITR chambers therefore only channels with corrected pulse heights $q_i < 0$ can be part of a cluster. All consecutive channels which also fulfil the seeding requirement are added to the cluster candidate.¹⁷ Finally, the cluster candidate is accepted if its overall significance is higher than another threshold c_{cut} :

$$\sum_{i_{\text{start}}}^{i_{\text{stop}}} q_i^2 \geq c_{\text{cut}} \sum_{i_{\text{start}}}^{i_{\text{stop}}} \sigma_i^2. \quad (3.5)$$

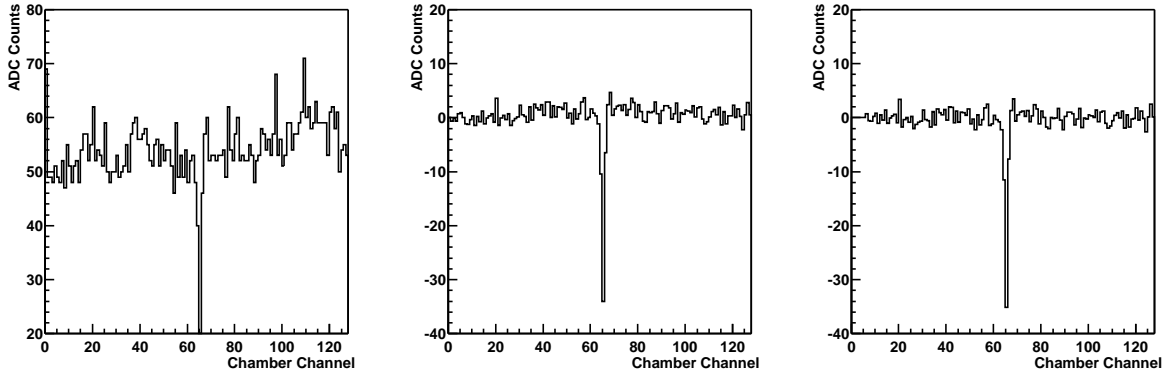
The procedure is illustrated in Fig. 3.22. The shaded band is the channel-by-channel noise scaled with $\sqrt{s_{\text{cut}}} = \sqrt{2}$. In the first chip (channels 0 – 127) two cluster candidates can clearly be seen.

For accepted clusters, the following variables are computed (all sums run over all strips of

¹⁷The algorithm as it was used in the run 2000 does not allow for gaps in a cluster due to disconnected readout strips. This will be changed for the 2001 run.



(a) Chamber M01--1



(b) Chamber M15--1

Figure 3.21: The two correction steps applied to the raw chamber data are the pedestal subtraction and the baseline correction. *Left:* Raw data of one chip. *Middle:* Chip data after pedestal subtraction. *Right:* After baseline subtraction. The upper row (a) shows a chip of chamber M01--1, where the baseline is fluctuating from event to event. As can be seen from the middle plot, after pedestal correction the data is not at about 0, so the baseline correction is needed and works well (right plot). The lower row (b) shows the first chip of chamber M15--1 which shows nearly no baseline fluctuation since it has a much improved grounding scheme. The first eight channels of these particular two chips are not connected to chamber strips, therefore they are set to 0 at the step of baseline correction.

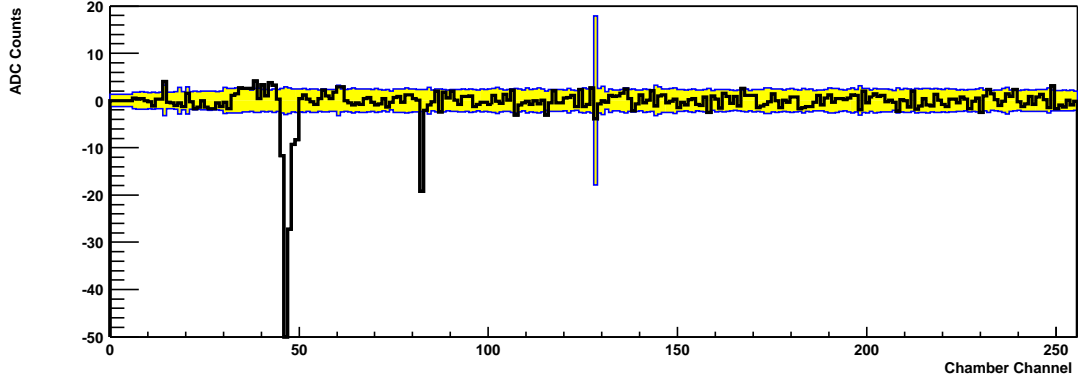


Figure 3.22: Pedestal subtracted data for two chips (*bold line*) and scaled noise (*shaded band*). Strips being more negative than the noise band are considered seeds for a cluster; contiguous groups of such channels are grouped into one cluster if the combined cluster significance exceeds a given threshold. The peak in the noise band at channel 128 denotes the start of the second readout chip. See Section 3.2 for a discussion of this distortion. Around channels 48 and 82, two hits can be seen.

the cluster, the event index j is omitted):

$$\text{Total cluster charge} \quad q_{\text{tot}} = \sum |q_i| \quad (3.6)$$

$$\text{Signal-to-noise ratio} \quad s = \frac{q_{\text{tot}}}{(\sum \sigma_i^2)^{1/2}} \quad (3.7)$$

$$\text{Centre of gravity} \quad \bar{x} = \frac{\sum i |q_i|}{q_{\text{tot}}} \quad (3.8)$$

$$\text{Cluster width} \quad w = i_{\text{stop}} - i_{\text{start}} + 1 \quad (3.9)$$

$$(3.10)$$

The cluster finding algorithm actually works with the subtracted variances σ_i^2 and the squares q_i^2 of the channel pulse heights. Since the noise following already computes the variance for each channel, this saves a time-consuming calculation of $\sqrt{\sigma_i^2}$. The thresholds s_{cut} and c_{cut} can be set at run-time as parameters `seedcut` and `chi2cut`. Since the cluster finder works with the ratio of the signal to the noise level, which are both measured in ADC counts, small variations in the analogue data transmission which are caused by the optical links are cancelled and do not affect the efficiency to detect pulses.

3.6.4 Online Sparsification

Every FED of the ITR sends a data block of 300 bytes per event to the central DAQ system. For the complete readout of all 160 chambers¹⁸ a total number of 480 FEDs is needed. This results in a total data volume of about 140 kB per event from the ITR alone. The data volume has to be reduced in order to save network bandwidth during data taking and storage size on tape. Since the occupancy is only about 5% at the maximum expected interaction rate, it is sufficient to identify all strips which have been hit in an event and to write out only the hit information to get the required reduction in data volume. This procedure is called *sparsification*. However, the

¹⁸Note that the Inner Tracker contains in total 184 chambers, but in the the stations MS14 and MS15, only one of the two layers per stereo view is read out. This is done to save readout channels, while the double layers are needed to reach the required trigger efficiency for the First Level Trigger.

procedure implies a loss of information, since the raw data are discarded after cluster finding. Care has to be taken not to throw away good hits. Lossless data compression algorithms, like those readily available in the `zlib` library [AG95], were also tested, but found to be ineffective to compress the Helix data with reasonable data size and compression speed.

For each event which is accepted by the L2 trigger algorithm, the complete cluster finding for the Inner Tracker is done on the L2 farm node processing the event. Only the condensed hit information is then passed on to the L4 farm. Table 3.2 shows the cluster format used since August 2000. It needs 10 bytes per cluster and includes the centre-of-gravity of the cluster as well as the cluster charge, signal-to-noise ratio, and the number of readout strips assigned to this cluster. In addition to the cluster information, a 24-byte long header containing the run and event number, the pipeline column number of the event, the data format used to store the clusters and the number of clusters is written out once for each event. For test setups and debugging purposes, the complete event data containing the found hits (the ‘sparse event block’) may be written out to disk separately. In the online cluster, the sparse event block is copied into one FED sub-block of the common data format [Res97, ETB98].¹⁹

| Type | Variable | Description |
|-----------|----------|---|
| short int | chamber | <i>ID of the chamber the cluster is found in</i> |
| char | bcharge | <i>cluster charge: $\min(q, 255)$</i> |
| char | b4sn | <i>signal-to-noise ratio: $\min(4S/N, 255)$</i> |
| short int | swidth | <i>start and width of the cluster: $32 * i_{\text{first}} + w$</i> |
| float | cog | <i>centre of gravity</i> |

Table 3.2: Format of cluster information written by the online sparsification process. For each cluster, the information is contained in 10 bytes.

The resulting compression factor which can be achieved with this algorithm obviously depends on the number of clusters found, which in turn depends on the interaction rate and on the parameters for the cluster finder. By default the parameters used online for the run 2000 were `seedcut` = 2, `chi2cut` = 6, which is a rather loose cut. The left plot in Fig. 3.23 shows the size of the ITR data after sparsification for the data taken with a random trigger at an interaction rate of 5 MHz (run 16556; sparsification for this run was done off-line). The compression factor achieved under these running conditions is about 1 : 70. This is an overly optimistic estimate, because the running conditions of this run are not realistic for actual data taking. Table 3.3 shows the mean event size for several runs which were taken with different interaction rates and trigger conditions. With a moderate interaction rate and triggering with the FLT on two lepton candidates, the mean ITR event size is 14 kB, which still gives a sufficient compression ratio of 1 : 10.

Also of importance is the time needed for cluster finding. Since the online sparsification is called during the event building and runs therefore on the nodes of the Second Level Trigger, the time spent finding clusters in the ITR can cause dead time of the SLT if there are no more free Second Level Processors available. The right hand side of Fig. 3.23 shows the time needed to process the ITR data on a normal computer used for off-line analysis (PentiumIII at 750 MHz); the mean time is about 30 ms per event. The processing of one chip (pedestal and baseline subtraction and updates of pedestal and noise estimates) takes 17 μ s per readout chip, while the cluster finder needs 92 μ s per chamber.²⁰ About half the time is spent doing the pedestal

¹⁹Since the data part of a SLB block is limited to only 32 kB, this induces a hard cut on the number of accepted hits, $n < 3200$. This was not a major concern for the run 2000 and will be changed for the next run period.

²⁰These timings were measured with the profiler `gprof` [GKM82].

| Run # | IA-Rate [MHz] | Trigger | $\langle s_{\text{ITR}} \rangle$ [kB] |
|-------|---------------|------------------------|---------------------------------------|
| 16556 | 5 | Random | 2.4 |
| 17137 | 2 | Single Lepton, SLT | 10 |
| 17173 | 5 | di-lepton, FLT+SLT | 14 |
| 17253 | 2 | Single Lepton, FLT+SLT | 11 |

Table 3.3: Mean event size of the ITR data after online sparsification for several runs taken during the run period 2000 with different trigger conditions and interaction rates.

and baseline correction, the cluster finder itself needs the rest.

The CPUs of the SLT farm run at about half the speed (PentiumII at 400 MHz), so the time one SLT node spends finding ITR clusters is about 60 ms. It would be desirable to reduce the time needed for sparsification, but it is not quite clear how a major speedup could be achieved since the code already has been optimised for speed. For the inclusion of the Inner Tracker hit information into the Second Level Trigger algorithms, a dedicated hit finder has to be written which works only on the small regions of interest.

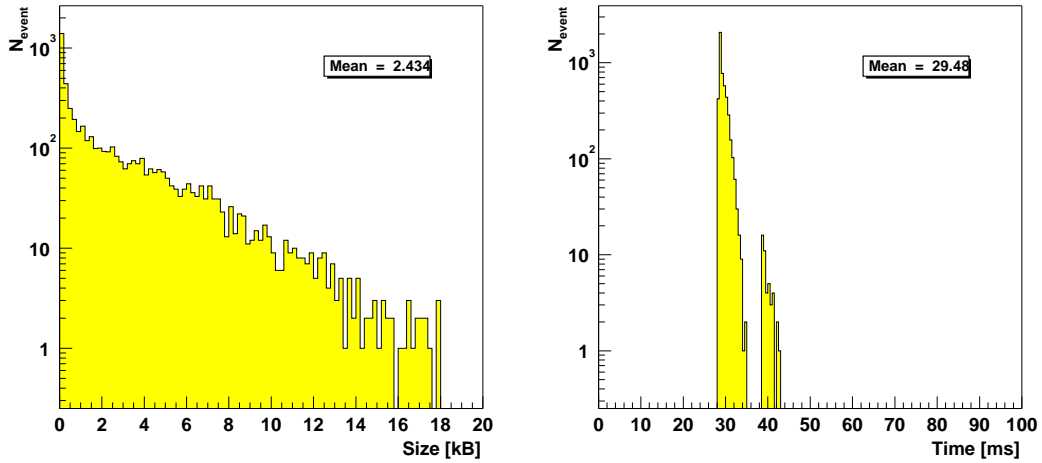


Figure 3.23: *Left:* Compression achieved with the online sparsification for the run 16556 with an interaction rate of 5 MHz. The mean event size after sparsification is 2.4 kB, while before it is 140 kB. *Right:* Time needed for the sparsification. The second, smaller peak to the right indicates those events during which the estimates for pedestal and noise are updated. The mean processing time is 30 ms on a computer with a 750 MHz PentiumIII processor.

3.6.5 Configuration and Setup Database

Knowledge about the connections between chambers, chips, FED boards, and SLBs as well as the actual position and orientation of the detectors is required at many different stages during data acquisition, reconstruction and analysis. It is important to have a consistent description of the hardware configuration at all these stages. Therefore all the information needed is stored in a setup database and read only from there both by the online processes and the reconstruction and analysis programs running later on.

The ITR configuration and setup database uses the usual HERA-B database infrastructure, which is basically the Berkeley Database (an open-source database which is freely available;

it is maintained by Sleepycat Software Inc. [Sle]), together with a thin layer which hides the Berkeley DB interface and provides persistent storage of tables of data with a user-defined format. Different versions of the same table are distinguished by a pair of numbers (major, minor) which can be used to encode *e.g.* the creation date of a table revision. On top of this table structure another layer, called LEDA, is put which provides the persistent storage of relations between the rows of two tables and a fast navigation through these relations.

For all processes in HERA-B, access to the databases is provided by several database server processes. The communication between clients accessing the databases and the servers uses the HERA-B general-purpose communications protocol RPM [RPM].

The set of tables describing the Inner Tracker can be classified in three categories according to their content:

Setup: This set of tables describes the hardware setup. It comprises the tables `ITR_Chamber`, `ITR_Chip`, `ITR_Fed` and `ITR_FedSlb` and contains information about the hardware installed. Connections between *e.g.* chips and chambers are mapped to relations between rows of these tables. The tables `ITR_nede` and `ITR_nesl` reproduce the nominal detector geometry, describing the location of the chambers in the experiment. They are a copy of the corresponding geometry tables of the reconstruction program ARTE [ART]. Strictly speaking, the presence of `ITR_nede` and `ITR_nesl` in the setup database is redundant, since their information already is stored in the ARTE geometry description. It is however not possible for all online processes to access the ARTE geometry, therefore the relevant information has to be reproduced.

The table `ITR_TFU` is intended to provide a mapping for the connections between the chambers and the Track Finding Units (TFUs) of the First Level Trigger. It was not yet used during the run 2000.

All these tables change only if hardware is installed in or removed from the experiment. They can be accessed using the database server `/ITR_Setup`.

Monitoring: The tables `ITR_Noise`, `ITR_Ped` and `ITR_Chanstat` are provided to store information about the noise level, the pedestal values and the channel status of each single channel. With the exception of `ITR_Chanstat` the content of these tables was not used during the run 2000. It is foreseen to have the online monitoring process update of these tables at least on a daily base in the future. These three tables are stored on the server `/ITR_MONITOR`.

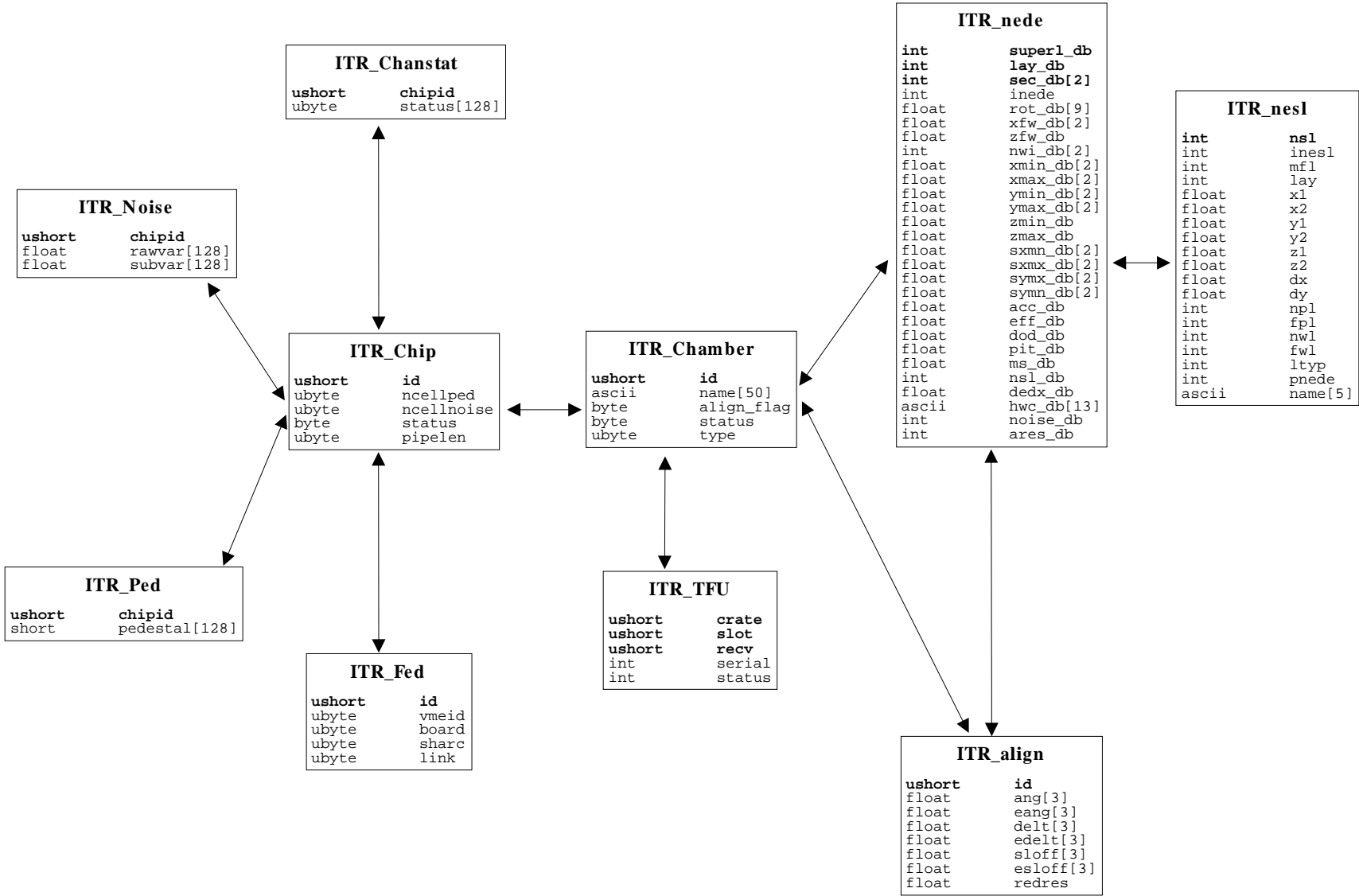
Alignment: The differences between the nominal and the actual position of the chambers are stored in the table `ITR_Align`. This table is stored in a separate server, `/ITR_Align`; its content changes typically once every few runs.

The structure of the complete set of tables is depicted in Fig. 3.24.

3.6.6 Online Monitoring

Since the process of online sparsification discards most of the analogue output, certain aspects of the readout system can no longer be monitored and checked by reading the sparsified hit information. These include information about the pedestal value and noise level found for each readout channel as well as the proper synchronisation of all readout chips. In addition, it is highly desirable during data taking to have a fast assessment of the quality of the data being written to tape, so that errors in the readout system can be spotted at the earliest moment possible. The shift-crew operating the detector should be notified of error conditions which

Figure 3.24: Overview over the ITR Setup database tables



could affect the data adversely. For this task, several monitoring processes, one for each sub-detector of HERA-*B*, are running on dedicated monitoring nodes, which have the same access to the raw data as the nodes of the SLT. A special monitoring trigger reads out the complete detector with a rate of about 50 Hz. These monitor events are discarded from the normal data stream.

The *Second Level Monitoring* processes are expected to perform basic checks which ensure the functioning of the detector and readout hardware. Another level of monitoring is running on the nodes of the Fourth Level Trigger farm. There the complete detector information is available, including reconstructed tracks and vertices. The monitoring code on the Fourth Level is able to do more sophisticated checks which include *e.g.* the synchronisation of all sub-detectors, or the quality of the reconstructed tracks and vertices.

The first version of the monitoring developed for the Inner Tracker is described in [Buc00]. It contains basic checks of the raw data quality, but does not yet issue alarms. A much improved version is under development [Wun02].

Chapter 4

Commissioning of the ITR Readout System

This section describes the steps performed to commission the readout of the Inner Tracker after the installation in the experiment. The experience of the first year of operation is reported, and first performance results of the Inner Tracker as a tracking device are presented, proving the tracking capability of the system.

4.1 Preparatory Beam Tests

The first test of the complete readout electronics attached to a GEM-MSGC operated in a particle beam was done at the PSI¹ in 1998. During this test, five GEM-MSGCs were operated and read out with the complete readout chain up to the digital signal processors which act as Second Level Buffers in HERA-B. Also, the electronics providing the trigger information to the FLT was used for the first time in a realistic environment [Kel01]. The chambers were situated in the π M1 test area which provides a high-intensity (p , π^+)- or π^- -beam of 350 MeV. The main goal of this beam test was to establish the high-rate capabilities of the final GEM-MSGCs. The full intensity of the beam of up to $7 \cdot 10^7 \text{ s}^{-1}$ (which corresponds in beam centre to a flux density of about $10^4 \text{ mm}^{-2} \text{ s}^{-1}$) was used for these high-rate tests, while for the dedicated readout studies the particle rate was reduced such that efficiency measurements could be performed easier.

A trigger was realized using the coincidence of two small ($5 \times 5 \text{ mm}^2$) scintillators located downstream of the chambers. The data of the test chambers were read out using the VME interface of the SHARC boards and written to disk over an ethernet network, limiting the event rate to about 10 Hz.

During the test intensive work was done on a grounding scheme which provided a sufficiently pick-up free readout. This grounding scheme was then implemented for the main series production (see Sect. 3.5 and Fig. 3.15). Some problems with the interface electronics receiving the digital control signals could be identified (the optical receiver used in the first version of the board was also sensitive to ionising particles, thus the chips received spurious clock or reset signals). They were subsequently eliminated by redesigning the electronics. The main results of the test beam experiment can be found in [S⁺98]. It was shown that the readout system could be operated with the required performance.

¹Paul-Scherrer-Institut, Villigen, CH

4.2 Installation in HERA-B

The installation of the Inner Tracker chambers in HERA-B during the year 2000 took place in several steps. During the monthly maintenance days of HERA, which were extended to ‘mini-shutdowns’ of 48 h for HERA-B, one or at most two half-stations could be inserted and fully connected to the infrastructure and to the external readout electronics, while also maintenance work was being performed on the already installed chambers. The last chamber of the main tracker was installed in May 2000.

4.2.1 Cabling Cross-checks

Even with the highly multiplexed readout scheme, quite a high number of connections have to be made for the readout of the complete Inner Tracker. The association of one FED with one region of a chamber is done using the setup database, which is manually generated from the installation protocol. It is important to perform cross checks to validate this mapping. A convenient means to verify the correct mapping is to look at correlations between hits of two chambers which are mounted right behind each other. If there are no wrong assignments, a correlation should be visible over the whole length of a chamber. If the distance $x_1 - x_2$ of hits in two chambers is plotted, the position of the peak also indicates the relative rotation of the two chambers.

Fig. 4.1 shows the hit correlation between two chambers of one half station; two chambers of the same orientation which are mounted right behind each other show a narrow correlation, while chambers of different stereo angle show a much broader correlation. Using these correlation plots, wrong assignments of chips to chambers can easily be detected. Also, if one chamber is mistakenly assigned to a wrong quadrant, it will show no hit correlation with its neighbours.

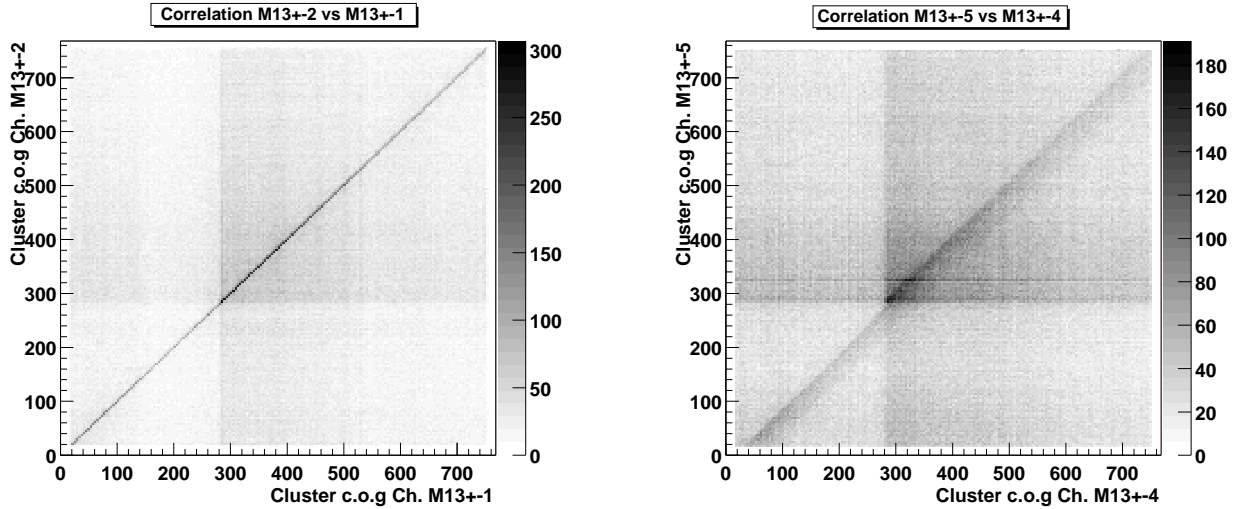


Figure 4.1: Hit correlations between two chambers of one half-station. *Left:* the two chambers M13+−1 and M13+−2 form one double-layer; they are mounted right behind each other on one support plate. The hit correlation is extremely narrow. *Right:* M13+−4 and M13+−5 are also mounted close to each other, but M13+−4 belongs to a plane with a stereo angle of +5°, and M13+−5 is a 0° layer. Also in this case there is a clear hit correlation visible, but it is much broader.

Considering the distances $x_1 - x_2$ of all hits in two neighbouring chambers can also help to determine the relative orientation of the two chambers. This is illustrated in Fig. 4.2. In the large tracking stations MS10 and MS13, there are in total four layers with a stereo angle of 0°,

which can be identified easily looking at the hit distance plots for all chambers. After this, the remaining chambers can be assigned their stereo layers according to the shifts of the correlation peak. For the 2000 installation, it was not necessary to use these correlations to obtain a correct assignment of chambers to their positions, but it helped to gain confidence that the mapping present in the database is reliable.

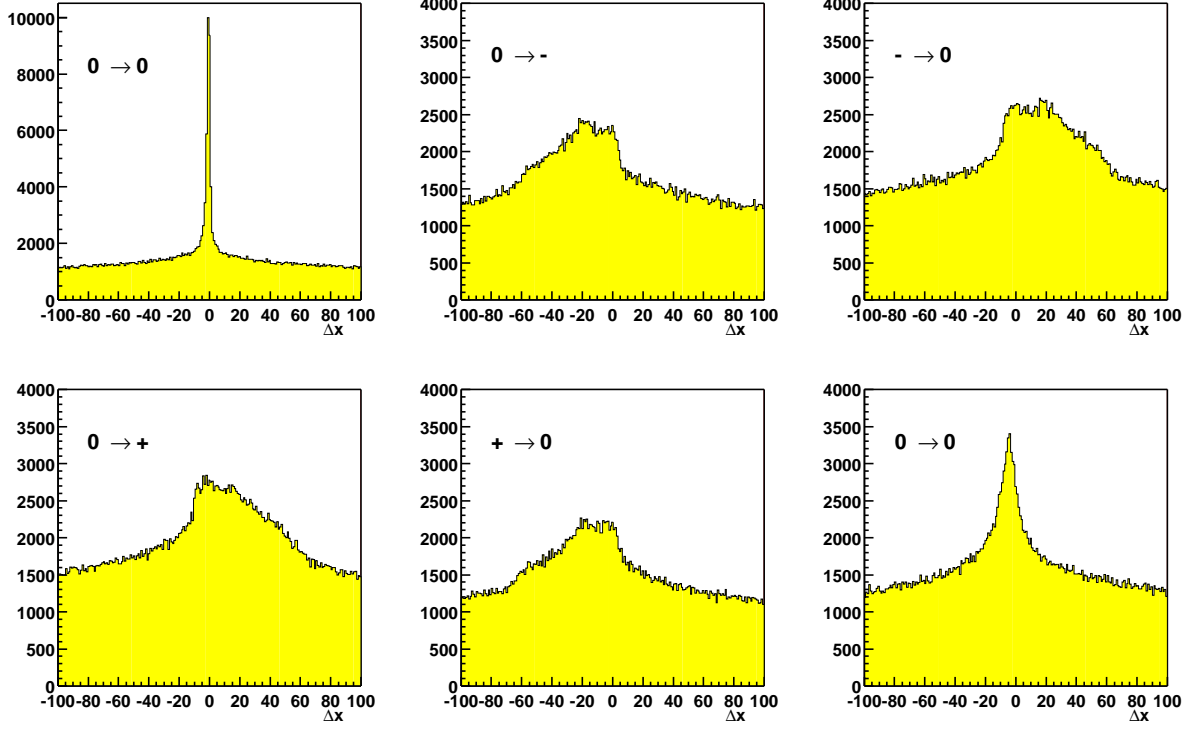


Figure 4.2: Differences $\Delta x = x_1 - x_2$ measured in units of the readout pitch of hits in two neighbouring chambers. There is a clear, sharp correlation peak visible for chambers of the same orientation ('0 → 0', *top left*), while the correlation is much broader, asymmetric and shifted for chambers of different stereo angles (e.g., '- → 0', *top right*). The last plot ('0 → 0', *bottom right*) shows the hit correlation of the chambers M13+−1 with M13+−5 which have both 0° stereo angle, but are separated by about 7.5 cm in z . The correlation peak is symmetric, but shifted towards negative values of Δx . This is because the tracks are not parallel to the beam pipe, but bend outwards with a mean track angle of $\langle \theta_x \rangle \approx 31$ mrad.

The remaining ambiguity between two chambers of one double-layer cannot be resolved with these simple methods. However, the alignment procedure for the Inner Tracker is sensitive also to shifts in z ; with its results, three mistakes in the half-station MS10− could be identified [Zeu01a].

With help of these cross-checks, all misassignments between chips and chambers could eventually be found, and the database describing the geometry was updated to correctly reflect all connections and chamber positions.

4.3 Timing and Synchronisation

The readout of all subdetectors of HERA-*B* has to be synchronous in such a way that the data read out from each subdetector for a given trigger are from the same event. Since all components have a pipelined readout and the clock and trigger information is distributed over

large distances, the synchronisation of the data must be monitored. The bunch structure of the HERA proton ring (see Fig. 4.3) which is caused by the filling procedure of the storage ring provides an excellent means to synchronise the detectors.

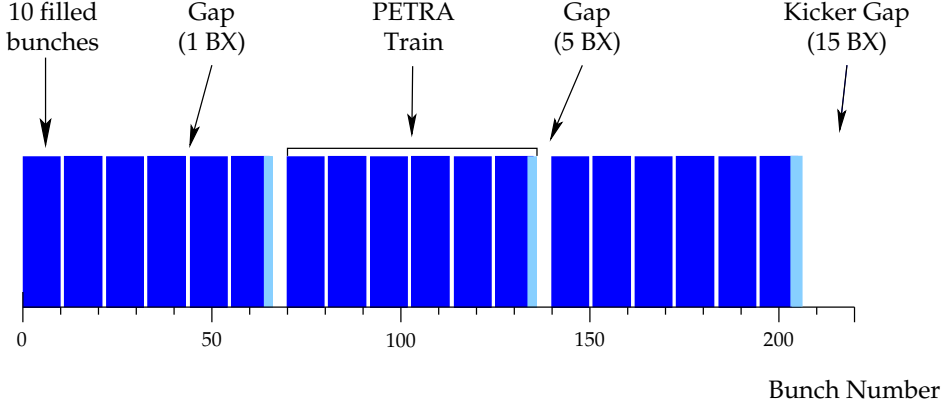


Figure 4.3: The bunch structure of the HERA proton beam reflects the different pre-accelerators which are used to fill HERA: Ten bunches of protons are accelerated in DORIS. Six of these *trains* are stored in PETRA, with a gap of one BX in between. PETRA accelerates the protons to 39 GeV, then they are injected into HERA. This scheme is repeated twice, with gaps of 5 BX between the PETRA trains. In the end, 180 proton bunches are stored in HERA. The large *kicker gap* of 15 BX at the end is used to safely dump the beam at the end of a run.

Fig. 4.4 shows the bunch crossing spectra found in the Vertex Detector and the Inner Tracker during a run taken with a random trigger (run 14468). The first bunch after the large kicker gap is seen in both detectors at its nominal position 202, indicating the synchronous readout of both subsystems. During data taking, the bunch crossing spectra of all subsystems are checked online by the Data Quality Monitor process. In the first bunch crossing of the kicker gap (BX 185) there are more hits found in the ITR than in the VDS, and the small gaps are more filled in the BX spectrum of the ITR. This can be explained by the different detector capacitances at the input of the Helix front-end, which influence the length of the shaper signal (see also Sect. 4.6).

The other free parameter of the readout timing is the sampling point. In order to obtain an optimal ratio of signal to noise, the Helix should sample the signal at its maximum value. This optimum sampling point is much harder to determine than the overall synchronisation; the reasons for this will be explained in detail below. Several timing scans were done during which the phase of the `SClk` sent to the readout chips was systematically varied with respect to the `BxC1k` provided by the FCS. The result of one such timing scan is shown in Fig. 4.5: The mean cluster charge of all hits is plotted as a function of the `SClk` delay. There is a small peak visible around a delay of 80 ns for the chambers of MS13– and around 60 ns for the chambers of MS01– (‘magnet chambers’). This time difference is consistent with the time of flight a relativistic particle needs for the distance of 6 m between the two stations. However, the peak is not so pronounced as one would naively expect from the step response of the Helix front-end. This will be addressed in more detail below (Sect. 4.6).

4.4 Optimisation of Pulse Shaping

One point of concern during the commissioning was the pulse shape of the Helix front-end. Since the total capacitance seen by the preamplifier is quite large, the resulting shaped pulse is rather long. This affects adversely the performance of the Inner Tracker: The cluster-finding algorithm

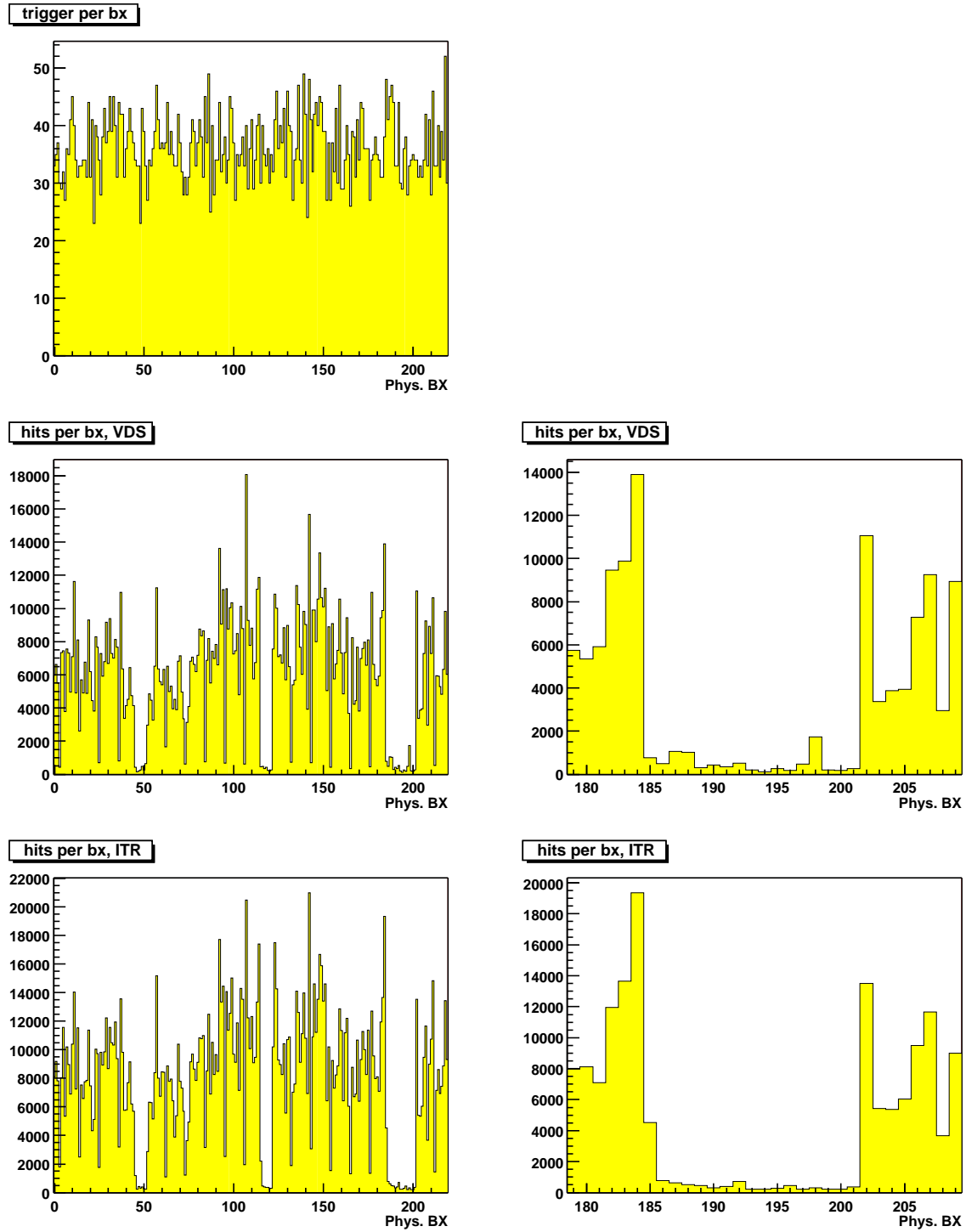


Figure 4.4: Distribution of triggers (*top*) and clusters found in the vertex detector (*middle*) and the Inner Tracker (*bottom*) as a function of the bunch crossing number ('BX spectra'). The data is from run 14468, for the ITR all clusters with a signal-to-noise ratio smaller than 4 were excluded. The amount of 'coasting beam' in this run was very low, as can be seen by the extremely clear BX spectrum of the VDS.

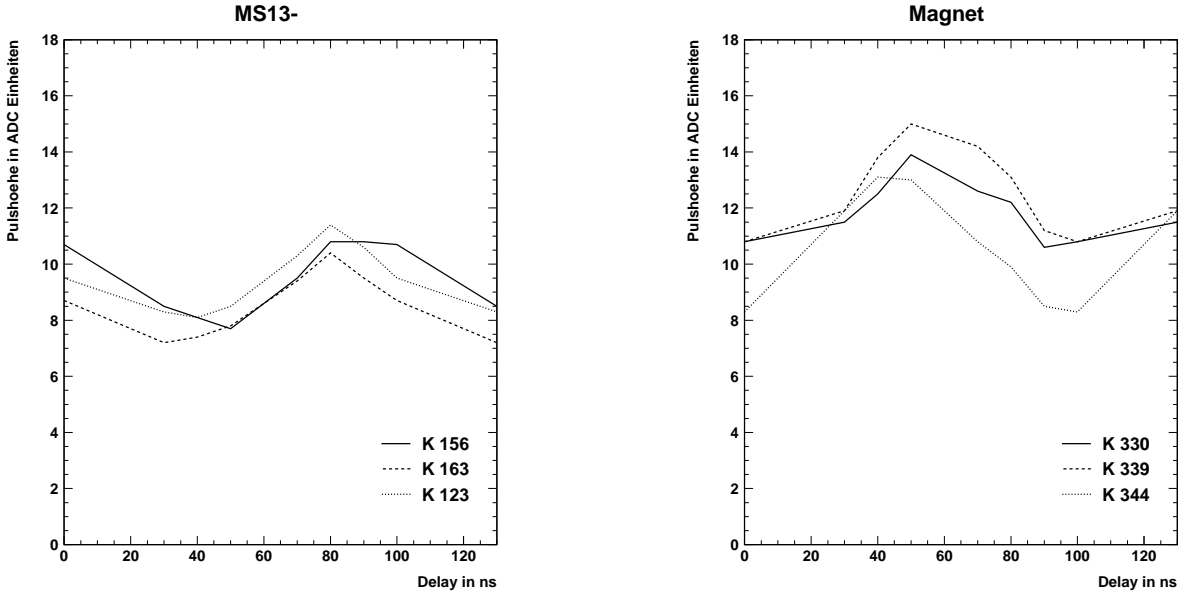


Figure 4.5: Timing scan (runs 12354 – 12365): the mean cluster charge of all hits found is plotted as a function of the SClk phase delay (from [Buc00]) for some chambers of the stations MS13– (*left*) and MS01– (*right*). There is a barely visible maximum of the pulse height at $\delta t_1 = 80$ ns for MS13–, resp. $\delta t_2 = 60$ ns for MS01–.

works with a fixed threshold in the ratio signal-to-noise to identify clusters. If the signal from a pulse seen in the bunch-crossing n is still large enough in the bunch-crossing $n + 1$, it will also be detected by the cluster finder in this ‘wrong’ bunch-crossing. If the probability for such ‘late hits’ is large, the reconstruction program gets too many fake hits, which leads to an increase of ghost tracks² and computing time needed to reconstruct tracks. It was therefore necessary to find a set of parameters for the Helix front-end which gives the optimum performance.

| | Ipre [μ A] | Vfs [V] |
|------|-----------------|---------|
| Slow | 200 | 1.5 |
| Fast | 400 | 1.0 |

Table 4.1: Helix settings used for the slow and the fast signal shape. The ‘slow’ settings correspond to the default values given in the Helix Manual [FB⁺99].

The two different settings used are listed in Table 4.1. The ‘slow’ setting corresponds to the default settings recommended in the Helix User Manual. It was used in the first place since these settings were optimised for minimal noise of the chip. The ‘fast’ settings are the result of extensive measurements of the chip’s noise and pulse form performed at the ASIC laboratory and verified with the Inner Tracker installation. The resulting pulse shapes are shown in Fig. 4.6. In both cases the peak time is about the same within a few ns, with the fast signal showing a larger total gain of the front-end³.

The optimum sampling point is on the peak of the signal. At the next bunch crossing after the peak, the slow signal has fallen off to 24 % of the peak value, while the fast signal has decayed to 11 % of its peak value. At the bunch crossing $n + 2$, the fast signal is essentially at

²A *ghost track* is a reconstructed track consisting of hits which do not belong to the passage of one particle (a ‘real’ track).

³For the ‘fast’ setting, not only the time constant of the signal shaper is changed, but also the bias current of the preamplifier. This makes the output of the preamplifier faster, and increases the peak height.

zero, while the slow signal is still at 7 % of the peak value.

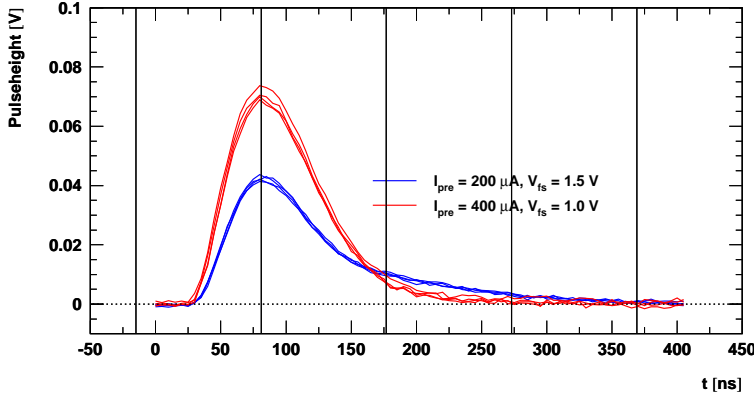


Figure 4.6: Helix pulse shapes with the slow (*black curve*, lower peak) and fast (*gray curve*, upper peak) shaping used for the Inner Tracker (Response of the Helix front-end to a unit step of 1MIP_{Si} at the input. Data from [TDD99], capacitive load of $C_{\text{load}} = 29.4\text{ pF}$ at the inputs).

The effect of the faster shaping can be seen nicely in the comparison of the bunch crossing spectra seen in two runs (Fig. 4.7) which were taken within one hour of each other such that the beam conditions did not change notably: with the slow shaping the empty gaps, where no interactions should occur, are filled up. With the fast shaping, the bunch structure is much cleaner: the small gaps of one bunch are more pronounced, and the left edge of the bigger gaps is also steeper (see also [Wil00b]).

The contribution of ‘coasting beam’⁴ was small in these two runs. This can be seen from Fig. 4.8 which shows the bunch crossing spectrum seen by the hodoscope counters of the Target control system. The higher number of hits in the empty bunches which is seen by the Inner Tracker with the slow shaping is therefore clearly an effect of the pulse shape of the front end electronics.

The electronic gain of the front-end amplifiers is much higher with the fast shaping than with the slow shaping. However, since the main contribution to the noise comes from the very first stage of the front-end, there is not much to be gained for the signal-to-noise ratio by increasing the front-end gain. This can be seen by comparing the mean pulse height of hits which were associated with reconstructed tracks and the mean noise level found in a chamber (see Fig. 4.9). The pulse height in ADC counts is higher for the fast shaping, but the noise level increases almost by the same factor; so the net gain in the signal-to-noise ratio is small.

⁴The longitudinal phase space of the particles in a storage ring is divided by the *separatrix* in two regions. Particles which are inside the regions enclosed by the separatrix are on stable orbits, in phase with the RF system, only performing betatron oscillations around the equilibrium position. These particles form the bunches. If a proton loses enough energy to leave its bunch, but still remains within the momentum acceptance of the storage ring, it can circulate in the ring out of phase with the bunches. These de-bunched protons are called *coasting beam*. Since interactions of the coasting beam protons with the HERA-B target are not correlated with the crossing of a bunch, such events cannot be properly reconstructed. They give rise to a constant background of interactions also during empty bunches. Due to the dispersion in the beam optics, the coasting beam contribution is largest when target wires *below* and *outside* the beam are used.

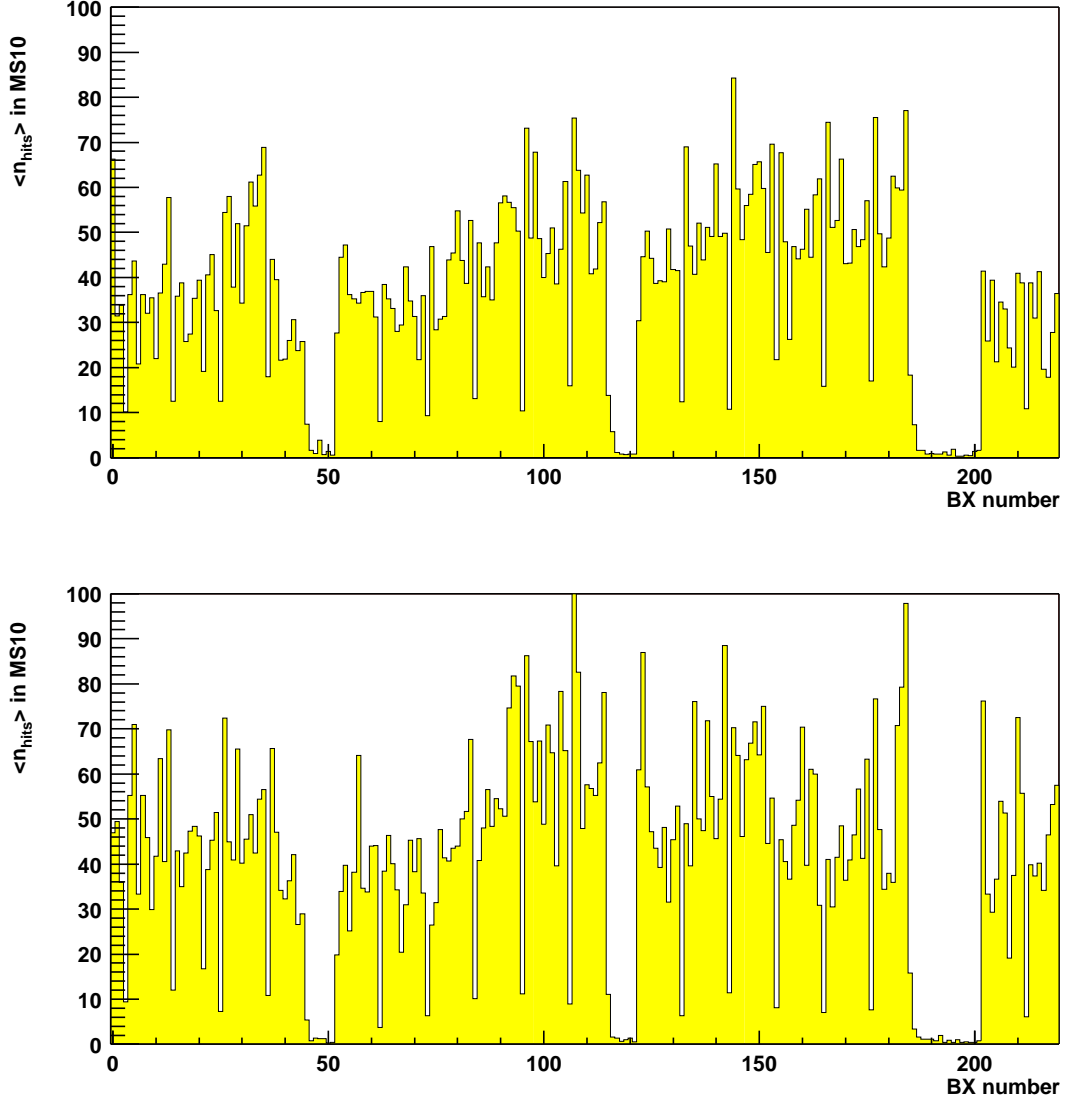


Figure 4.7: Bunch crossing spectrum for slow (*top*, run 14462) and fast (*bottom*, run 14468) shaping: The mean number $\langle n_{\text{hits}} \rangle$ of hits per event found in all chambers of ITR station MS10 is plotted as a function of the bunch crossing (BX) number. The data for both runs were taken with a random trigger at an interaction rate of 10 MHz. The chamber voltages were set at $U_{\text{drift}} = -2.4$ kV, $U_{\text{GEM}} = 420$ V, $U_{\text{cath}} = -490$ V. The target wire used was *inner II*. Only hits with a signal-to-noise ratio greater than 4 are shown in these plots.

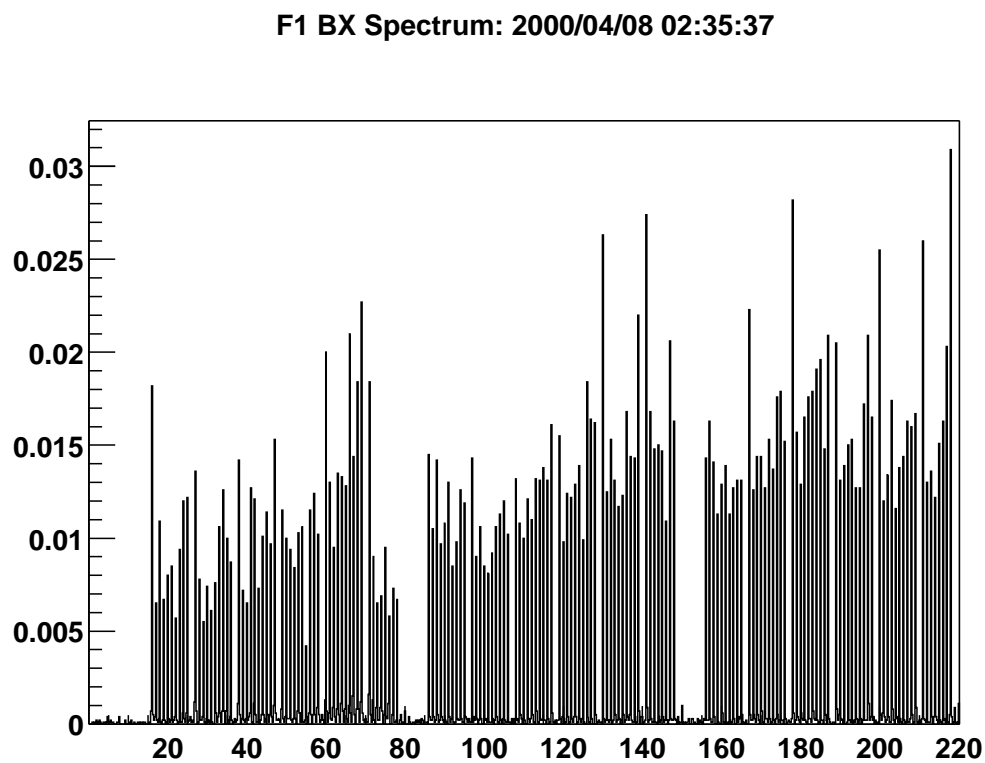


Figure 4.8: Bunch crossing spectrum seen by the scintillator counters which are used for target steering during the run 14462: the contribution of each bunch to the total interaction rate is plotted as function of the bunch crossing number. Each bunch crossing is resolved in four separate time slices of 24 ns. The fraction of interactions from coasting beam, which can be seen as entries in the gaps between the PETRA trains, is very small.

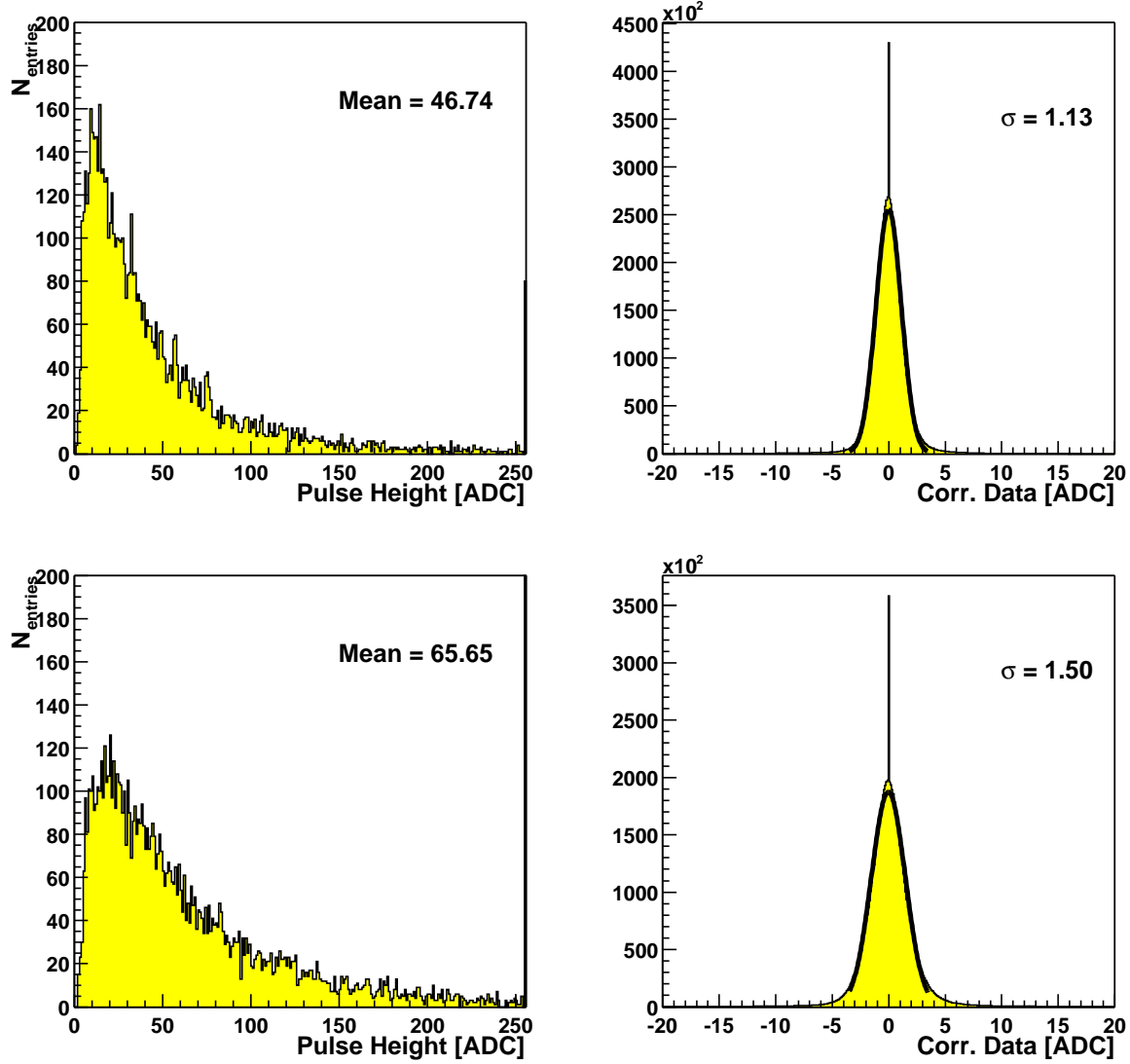


Figure 4.9: Pulse height distribution (*left*, in ADC counts) and noise (*right*, in ADC counts) for the chamber M13++1 in two runs with different Helix shaping: slow shaping (*top*, run 14462) and fast shaping (*bottom*, run 14468). For both runs the chamber was operated with identical high voltage settings ($U_{\text{drift}} = 2.4$ kV, $U_{\text{cath}} = 490$ V, $U_{\text{GEM}} = 420$ V). Only hits which were associated to reconstructed tracks are used for the pulse height distribution. The noise is estimated by computing the variance of the pedestal and baseline corrected signals (*right* column). With the fast shaping, the Helix front-end has a higher electronic gain; this can clearly be seen by the higher mean pulse height. However, also the noise level as measured in ADC counts increases by nearly the same factor; this indicates that the main source for the noise is the preamplifier itself. Thus there is not much to be gained for the signal-to-noise ratio by using the fast signal shape.

4.5 Operation Experience and Performance

This section presents the operation experience gained and first results obtained during the HERA-*B* run period 2000. The emphasis here is put on the readout system. The performance of the chambers themselves is described in detail in a HERA-*B* note [K⁺01].

4.5.1 Variation of Analogue Gain

With the analogue data read out from the chambers, each readout chip transmits the number of the pipeline column which was used to store the data for this event (see Sect. 3.2.4). The number is encoded as an eight-bit value and transmitted as eight separate analogue values, one value encoding the bit ‘0’, another encoding ‘1’. At the receiving side, the amplitude of this signal can be used to monitor the electronic gain of the readout chain. For this purpose, the software processing the raw data computes for each event the height h of the column number signals from the values v_i used to encode the bits ‘0’ and ‘1’ as $h := \max v_i - \min v_i$ (see Fig. 4.10). These heights are then averaged for each chip over many events.

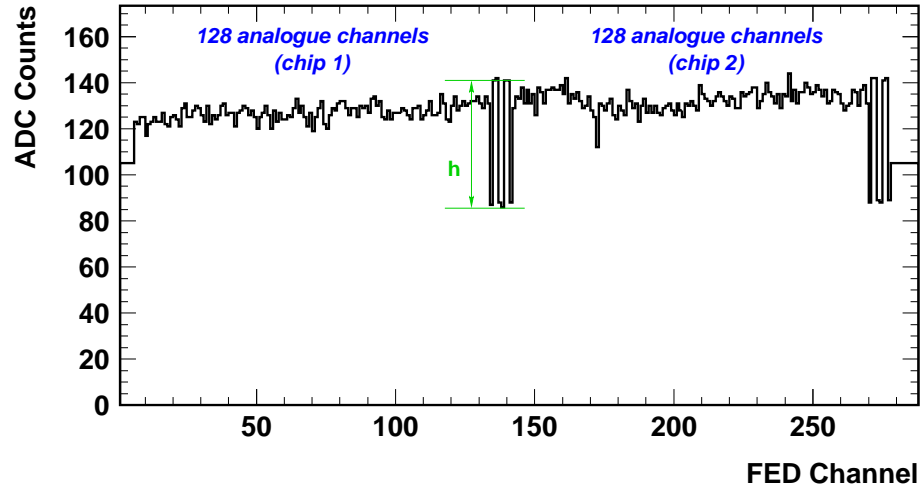


Figure 4.10: Definition of the ‘pipeline column number height’ h . The eight bits of the column number are encoded by the Helix as eight output levels v_i . The height of the column number signal h is defined as $h = \max v_i - \min v_i$; it is averaged over many (≈ 200) events for each chip.

Due to the maximally allowed variation of process parameters during the production of the readout chips, the column number height is expected to be the same for all chips within 10 % [FR99]. Fig. 4.11 shows a laboratory measurement of the pipeline column number height of 24 Helix chips. For this measurement, the analogue data of all chips was transmitted via the same optical transmission chain, and the analogue signal was then measured with an oscilloscope. The distribution has a relative width (defined as rms / mean of the distribution) of only 2%, showing that indeed the chip-to-chip variation is very small.

The distribution of the column number heights found in the analogue data of all chips installed in the experiment is shown in Fig. 4.12. This measurement was made using data from a run in which the online sparsification was switched off, so that the full analogue information is available in the data files. As can clearly be seen, the distribution is significantly broader than expected from the pure chip-to-chip variations alone; the two chips of one PCB very often show a similar height of the column number. This can be explained by differences in the analogue transmission lines, which are common for the two chips of one PCB. One source for the observed

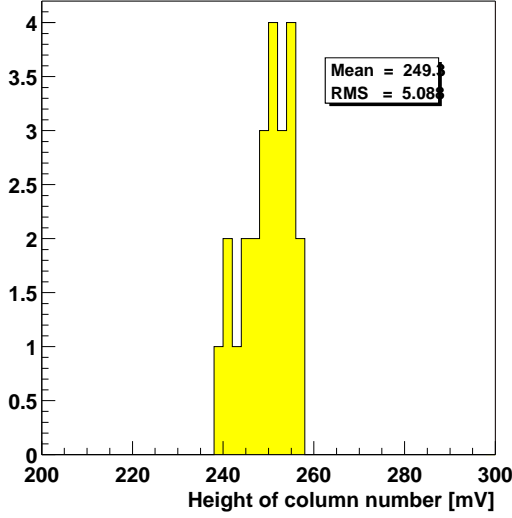


Figure 4.11: Height of the pipeline column number of 24 Helix chips, measured with the identical optical transmission chain. The distribution has a relative width of 2%.

large variations is the coupling of the output of the senders into the optical fibres; the intensity in the fibre strongly depends on mechanical tolerances of the connectors (a displacement of only $250\ \mu\text{m}$ reduces the fibre-coupled power to 80% of its maximal value [Mit94, Fig 1]). Also slight variations in the electronics due to tolerances of the components used cannot be precluded.

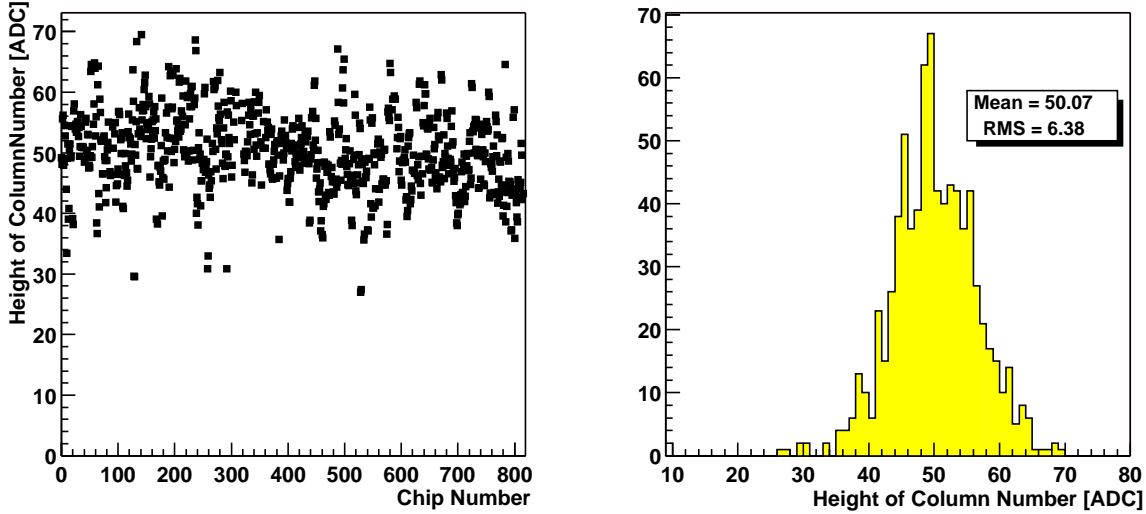


Figure 4.12: Distribution of the height of the pipeline column number in the analogue data of Run 16556. *Left plot:* Mean column number height for each chip (numbered arbitrarily; the two chips of one PCB appear as consecutive chip numbers). *Right plot:* Mean column number height for all chips. The distribution has a relative width of 13%, which is larger than expected from the chip-to-chip variations alone.

The cluster finder is not affected by these variations since its thresholds are defined in terms of the signal-to-noise ratio where such variations cancel out (as long as the signal is larger than the resolution of the ADCs). However, if one wants to compare the pulse height of two chambers, these variations have to be taken into account. The algorithm processing the raw data does this

by computing a mean column number height averaged over all readout chips and subsequent scaling of all data after pedestal and baseline correction to this mean value. This correction also has to be applied when comparing noise levels determined for different readout chips.

4.5.2 Time Stability of Noise and Pedestal Estimates

As described in Sect. 3.6.2, the pedestal and noise values for each channel are constantly updated during the online sparsification process. The performance of the cluster finding algorithm depends critically on reliable noise and pedestal values for every readout channel. It is therefore important to monitor these values, which should ultimately be the job of the online monitoring process running on the L2 farm. This monitoring process was not yet running reliably during all runs of the run period 2000, and experience how to extract and compress the relevant information had to be gained.

Since the raw data from which noise and pedestal values can be calculated are lost for runs in which the online sparsification is switched on, runs with the sparsification switched off were taken on a regular basis. The raw data written to tape allows to compute noise and pedestal values offline and to check for differences occurring with short or long time constants. These checks also serve as an important input for the design of the monitoring process mentioned above.

A detailed study of the long-term noise and pedestal behaviour of several chambers was performed by R. Wolf [Wol00]. It was shown that the pedestal values do not change significantly over time periods of many weeks. However, the noise estimates can vary with running conditions. Therefore it is advisable to keep the online determination of pedestal and noise values at it is implemented; the online monitoring and checks on data quality have to be improved, especially to make sure that the values determined online for noise and pedestal are reasonable.

4.5.3 Stability of Readout System

During the run period of 2000, several instabilities in the readout system of the Inner Tracker were observed. The quality of the data read out from the Inner Tracker was low for many data taking runs. Several sources for these instabilities could be identified:

- Low voltage power supplies: The low voltage power supplies⁵ failed from time to time during operation for reasons yet unknown; several times, a power supply itself was damaged, developing a short in the input stage. The effect could not be reproduced in a test setup with a fully equipped Inner Tracker station outside the experimental area, nor at the manufacturer's. Nevertheless, the measurements indicate that the voltage regulation suffered from bad connections at the power supply and from large feedback due to the long cables between supply and consumers. Several measures to make the power supplies behave more stably were implemented for the 2002 run, which address some of the weak points found in the lab; the connections of the cables to the power supply were improved, and the regulation of the output voltage was exchanged by a version which is optimised for long cable lengths at the output.
- Non-automatic programming of Helix settings, since the program to load the Helix settings was not included in the general HERA-B slow control framework. If the Helix registers are loaded during data taking, the readout chips are not properly synchronised any more and the data read out is corrupted. This happened accidentally a few times.

⁵made by Plein & Baus, Burscheid, Germany

- Other failures in the readout chain. These included failures in the electronics (notably the optical transmission of the control signals) and other, not yet fully understood malfunctions. There are various symptoms visible in the data, among them a simultaneous, sudden increase of the number of hits found per event. In some runs, a sudden drop in the number of hits found is observed instead. These failures always affected several chambers in one run. It is not yet clear whether all these symptoms are caused by a common shortcoming of the readout system.

The first two items above are somewhat annoying, but will not seriously affect the performance of the Inner Tracker in future runs. The power supplies are upgraded, and an increased number of spare parts is available to react quickly to any malfunction. In addition, the AC power lines for the low voltage power supplies will be equipped with filters to eliminate higher frequency noise which may disturb the operation of the power supplies [KK01]. The software for loading the Helix registers is currently being improved for the next run period to have a fully automated loading of the chip parameters which is synchronised with the central data acquisition [Wie01].

The last problem described above is more serious. Several attempts are being made to identify the source of the problem. These analyses and their first results are presented in the following.

Full Events. A first observation indicating problems in the readout system was a sudden increase in the number of hits found in individual chambers [Wil00a]. This problem was observed in runs with and without online sparsification, so for a part of the problematic runs, the full raw data can be accessed. One example of the occurrence of this problem is shown in Fig. 4.13; the data are from the unsparisified run 16556. Here, the number n_{hits} of hits found per event in three chambers of station MS01 are plotted as a function of the event number. In two chambers, M01 -1 and M01 $+1$, there is a sharp rise in n_{hits} around event 4150, while the M01 $+4$ does not show a different behaviour before or after this event. It was verified that after event 4150 the readout chips of those chambers which showed many hits actually stopped to send analogue data. The resulting hits still found by the cluster finder are fake hits, produced by subtracting the pedestal from a completely flat baseline and then applying the cluster finding algorithm.

As can be seen in Fig. 4.13, two chambers show the sudden increase of hits at the same time; this rise is also seen in several other chambers of the half-station MS01 $-$. The simultaneous increase cannot be explained by single-event upset⁶ in the readout chips, which is highly unlikely to occur simultaneously in two readout chips.

In several runs which were checked, groups of chambers belonging to the same half-station showed similar drop-outs, but not all chambers of one half-station were affected. No correlation with the chip version could be found. However, these drop outs occurred at different times in different half-stations, thus making one single external cause (a huge spike in the noise found in the experimental hall, for example) rather improbable. The simultaneous occurrence points to the optical transmission chains which provides clock and trigger signals to all chambers of one half-station. Another possibility is a short power outage ('power-glitch') which could produce spurious clock or reset signals.

Other Readout Drop Outs. Similar failures as described above could be seen in several runs, also in those where the online sparsification was switched on. Here, the diagnosis is more

⁶SEU, a transient malfunction, especially in the digital part of the chip, which is caused by an ionising particle depositing charge in a small area. This charge then can lead *e.g.* to spurious output signals of a flip-flop.

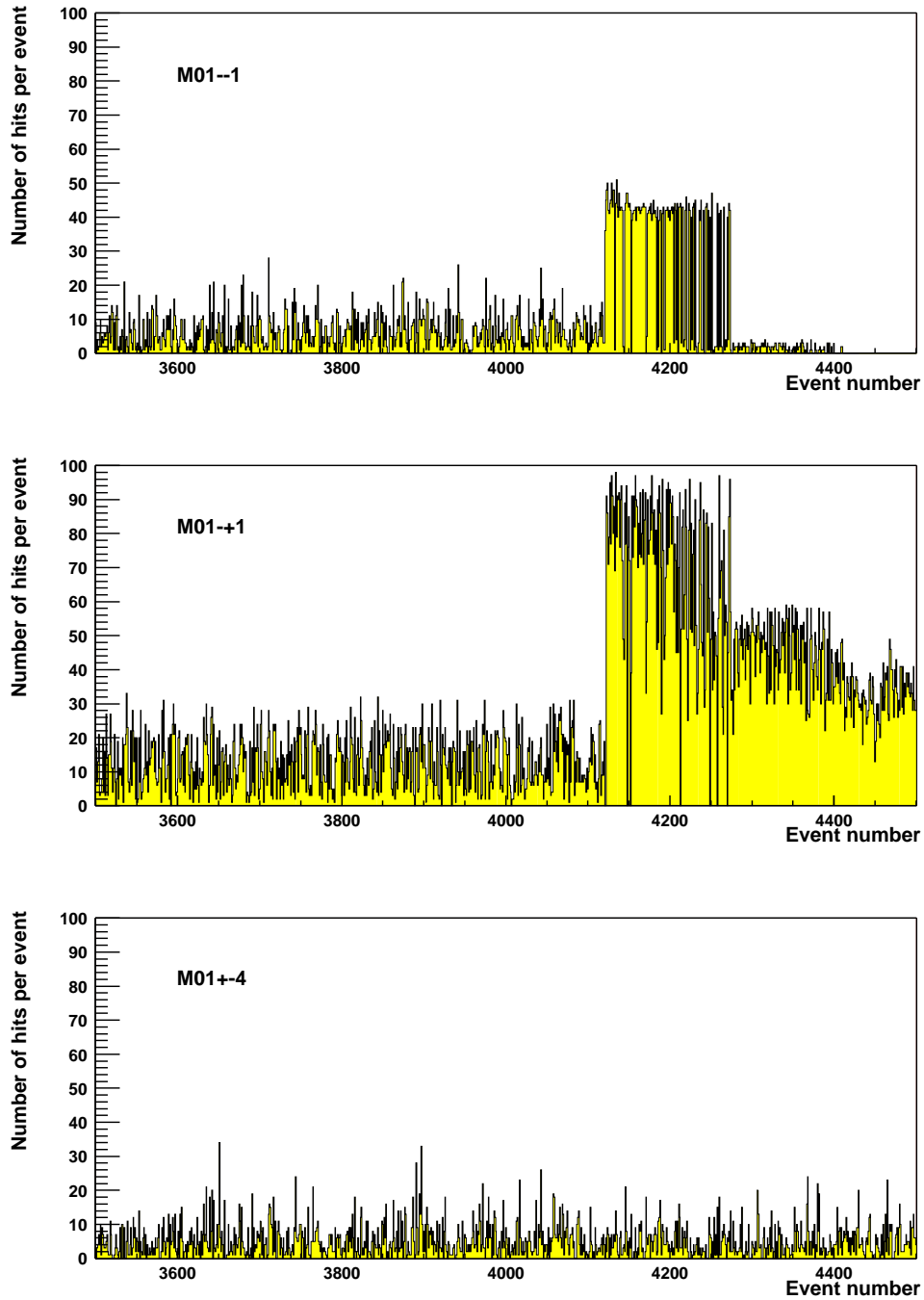


Figure 4.13: Number of hits n_{hits} found per event as a function of the event number in the run. The plot shows the time evolution of n_{hits} for three chambers of station MS01 during the run 16556.

difficult, since the information on the raw data is not available any more. In all instances observed so far, the readout of several chambers of one half-superlayer simultaneously starts behaving abnormally, and does not recover until the end of the run.

Conclusions At the moment⁷, the origin of the failures is still unknown, so no definite conclusions can be drawn; the investigations of this problems are ongoing. The occurrence of simultaneous problems in several chambers of one half super-layer excludes single-event upset in the readout chips as the sole cause. Similarly, it is unlikely that the sparsification software is the cause of the problem, since also unsparisified runs show these readout malfunctions; the software however fails in checking for the occurrence of such exceptional conditions and (in conjunction with the data quality monitor) sending an alarm to the shift crew. This will be implemented before the start of the HERA-*B* run 2001. A possible reaction to the occurrence of a malfunction could be sending a reset signal to the readout electronics of the complete detector.

4.5.4 Noise Behaviour

The electronic noise of the readout chip depends on the capacitance seen at the input of the preamplifier, and also on the preamplifier settings used. For the settings used by the Inner Tracker, $V_{fs} = 1.0$ V and $I_{pre} = 400$ μ A, the equivalent noise charge q_i was measured in the laboratory as [Tru00]

$$q_i = 355 e^- + 35.6 e^- \cdot \frac{C_{in}}{\text{pF}}. \quad (4.1)$$

Connected to a GEM-MSGC of the Inner Tracker, which presents a load capacitance of about 25 pF,⁸ the Helix is therefore expected to show an intrinsic noise of

$$q_i = 1\,240 e^-. \quad (4.2)$$

In addition to the intrinsic noise of the Helix, two other sources of thermal noise need to be considered: both the protection resistor of $R_1 = 600$ Ω and the finite resistance of the anode strips of about $R_2 = 1.37$ k Ω contribute thermal noise. The mean squared noise voltage v_R^2 of a resistor R connected to the input of an amplifier with a bandwidth $\Delta\nu$ is (Johnson noise)

$$v_R^2 = 4k_B T \Delta\nu R, \quad (4.3)$$

or, converting the noise voltage to an equivalent noise charge q_R^2 in electrons,

$$q_R^2 = 4k_B T \Delta\nu R \left(\frac{C}{e} \right)^2 e^- \quad (4.4)$$

where C is the load capacitance seen at the input of the amplifier, T is the absolute temperature in Kelvin ($T = 300$ K is assumed), $k_B = 1.38 \times 10^{-23}$ J K⁻¹ is the Boltzmann constant and e denotes the elementary charge. The bandwidth of the Helix front-end is about $\Delta\nu = 10$ MHz. For the noise contribution of the anode strip, only the part of the strip between the signal origin and the connection to the readout chip is important; for a rough estimate one can take $C \approx \frac{1}{2}C_{in}$. For the series protection resistor, the relevant capacitance is C_{in} .

⁷April 2001

⁸The capacitance of one anode strip to the neighbouring cathodes was measured to be 16 pF, the capacitances of the ceramics pitch-adaptor is 2 pF, and the capacitance of the anode to the backplane is estimated to be about 2.5 pF. The Kapton strip-line and parasitic capacitances on the readout chip are estimated to be of the order of a few pF each, resulting in a capacitance of about 22 pF. A direct measurement yielded (30 ± 3) pF, which is probably too large by a few pF due to stray capacitances in the measurement equipment. The value of $C_{in} = 25$ pF is therefore a reasonable assumption.

The total noise of a Helix connected to an Inner Tracker chamber is therefore expected to be

$$q_{\text{Helix}}(C_{\text{in}}) = \sqrt{q_i^2(C_{\text{in}}) + q_{R_1}^2(C_{\text{in}}) + q_{R_2}^2(C_{\text{in}}/2)} \\ \approx \sqrt{(355 + 35 \times C_{\text{in}}/\text{pF})^2 + (62 \times C_{\text{in}}/\text{pF})^2 + (94 \times \frac{1}{2}C_{\text{in}}/\text{pF})^2} e^- . \quad (4.5)$$

Taking a load capacitance of $C_{\text{in}} = 25 \text{ pF}$, the total equivalent noise charge is therefore

$$q_{\text{Helix}}(25 \text{ pF}) = 2310 e^- . \quad (4.6)$$

Other sources of noise present in the complete readout system are the optical link and the ADC itself. The total amplification of the analogue transmission chain and the resolution of the ADC was designed in such a way that the ADC is just able to resolve the thermal noise of the Helix. The contribution of these two sources to the system noise is small: Fig. 4.14 (*right*) shows the distribution of baseline corrected ADC values for one chamber (M01 – 4) where the signal distribution board was not working, but the analogue sender was still connected to the FED input. The width of the peak is about $\sigma = 0.1 \text{ ADC}$. This translates into an equivalent noise charge of about $q_{\text{link}} = 160 e^-$, which has to be added to q_{Helix} of Eq. 4.5 in quadrature. The

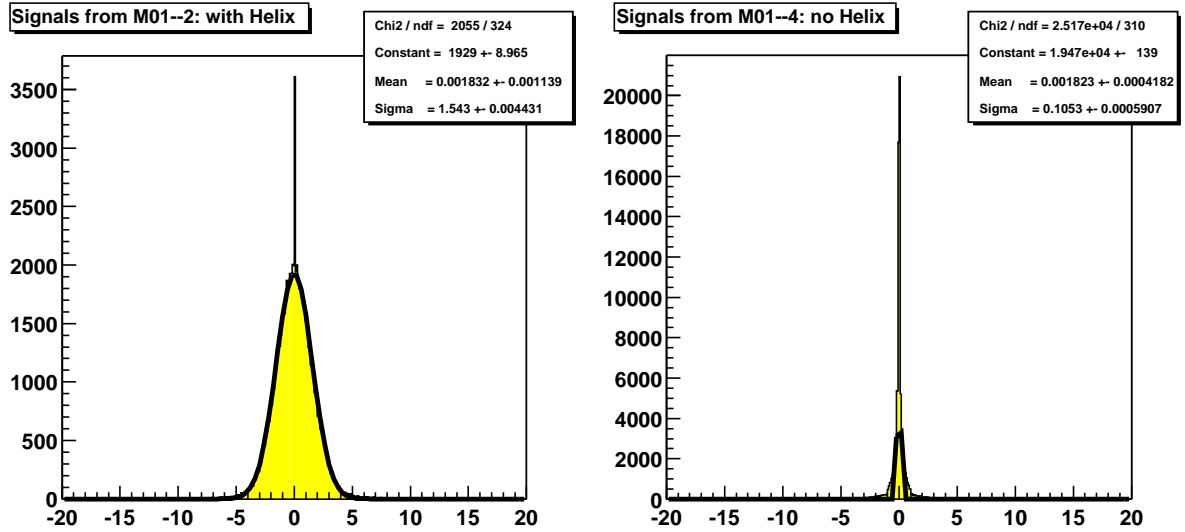


Figure 4.14: Distribution of the pedestal and baseline corrected signals for all channels of chamber M01 – 2 (*left*) and M01 – 4 (*right*), measured in ADC counts. The signal distribution board of M01 – 4 does not work properly, therefore no analogue signals from the readout chips are seen in the data. Hence the width of the distribution reflects the noise contribution coming from the remaining transmission electronics, including the digitisation errors of the ADC.

actual width of the pedestal and baseline corrected data found in one chip is depicted in Fig. 4.14 (*left*). The distribution has a nearly gaussian shape with a width of

$$\sigma_{\text{data}} = 1.54 \text{ ADC} \hat{=} 2490 e^- , \quad (4.7)$$

which is consistent with the noise expected from the calculations above (Eq. 4.6), considering that for the GEM-MSGC C_{in} has a relatively large error.

4.5.5 Chamber Occupancies

At HERA-*B*, the flux of charged particles from the target per normal area da located at a radial distance r_{\perp} from the beam axis is approximately proportional to

$$\frac{dN}{da} \propto \frac{1}{r_{\perp}^2} = \frac{1}{x^2 + y^2} . \quad (4.8)$$

Since only the x -coordinate is measured directly with the GEM-MSGCs, the expected occupancy (*i.e.* the probability that a certain readout strip shows a signal in an event, or the average number of hits seen by a readout strip) is the integral of Eq. 4.8 over the length of the chamber in y , taking into account the recess for the beam pipe.

Fig. 4.16 shows the measured occupancies of three chambers in a run where the interaction rate was set to 5 MHz and a random trigger was used. The different sizes of the recess for the beam pipe can be seen. Near the beam pipe, the occupancy is basically flat; for the long readout strips, the occupancy decreases approximately like $1/x$, as would be expected from integrating 4.8 over y .

The mean occupancy found in all chambers of station MS13– with a threshold of 2.5 in the cluster signal-to-noise ratio is shown in Fig. 4.15 as a function of the chosen interaction rate. The occupancy varies linearly with the interaction rate, showing that up to at least 20 MHz no saturation effects are visible. However, at the chosen threshold, the number of fake clusters due to noise is not negligible, which can be seen by the intercept of the curves; also, interactions from coasting beam will contribute to a constant offset. The data used for this plot is from a rate-scan in April 2000; all chambers were operated at the same high voltage settings. The occupancies of chambers M13–+1 and M13–+3 differ by about a factor 2; this reflects the fact that the gas amplification of different chambers at the same high voltage settings is not equal (see also Sect. 4.5.6 and 4.5.7).

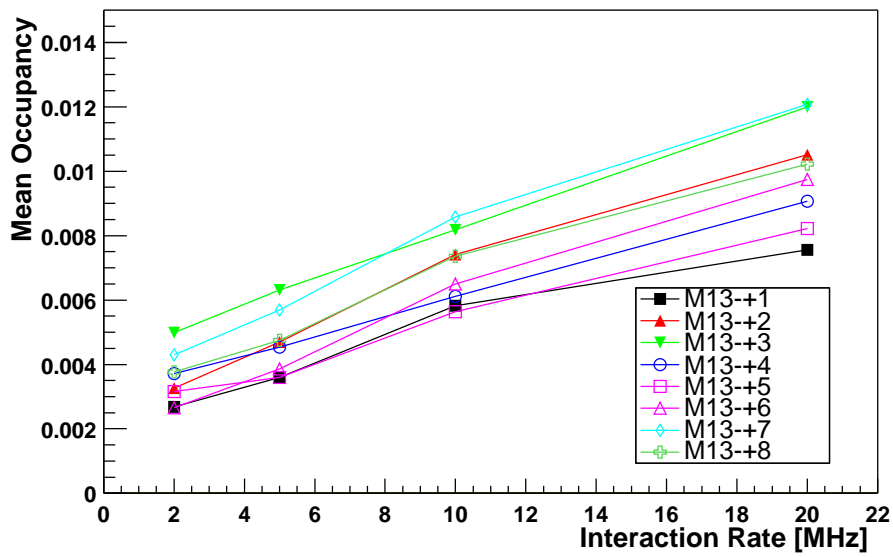


Figure 4.15: Mean occupancies of all chambers of station MS13— as a function of the chosen interaction rate. The data was taken with a random trigger, and a signal-to-noise threshold of 2.5 was applied to the clusters found. The mean occupancies rise linearly with the interaction rate, showing that there are no saturation effects visible in the chambers up to rates of 20 MHz. Extrapolating all curves to 0 MHz, one sees a non-vanishing intercept. This indicates that with the used threshold many noise clusters are found. The data used for these plots were taken during a rate-scan in April 2000 (runs 14566 – 14569); all chambers were operated with $U_{\text{drift}} = 2.4$ kV, $U_{\text{cath}} = 490$ V and $U_{\text{GEM}} = 490$ V, resulting in a rather low gas gain.

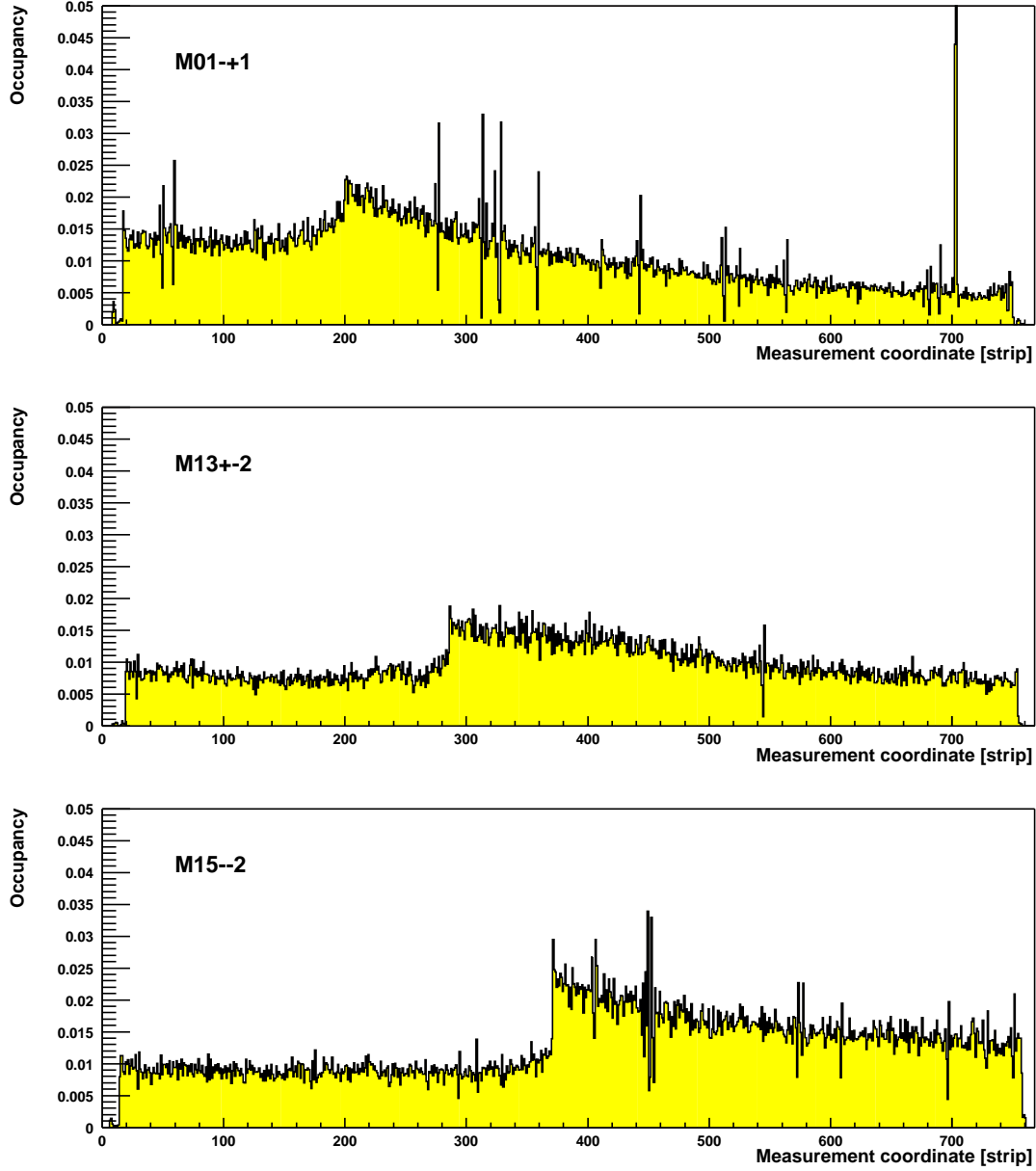


Figure 4.16: Occupancies for three chambers of the three different types used in the Inner Tracker: M01+-1 (*top*) is of Type I (chambers used in the magnet), M13+-2 of Type II, and M15--2 of Type III. All three chambers have a stereo angle of 0° ; therefore the occupancies rise steeply where the recess for the beam pipe ends. In chamber M01+-1 some hot channels around strip 710 are visible. Only clusters with a signal-to-noise ratio of $S/N > 4$ are used for this plot; the data are from run 17021 with an interaction rate of 5 MHz and a random trigger.

4.5.6 Chamber Performance

Cluster Properties. The distributions of pulse height, signal-to-noise ratio, and cluster width for all clusters found in one chamber are shown in Fig. 4.17. The pulse height and signal-to-noise spectra are completely dominated by hits with small pulse heights. This can be partly explained by the rather slow pulse shape, which is a result of the rather large detector capacitance ($C_{\text{in}} \approx 25$ pF) and the shape of the input signal (see Sect. 4.6). Due to this, a signal can be detected also in the following bunch crossing with a non-vanishing probability, giving a hit with a small pulse height. Another contribution comes from background interactions, which are not necessarily in time with a bunch crossing and are therefore not sampled at the maximum of the pulse, and certainly noise hits are also seen. The clusters found have a mean width of $\langle w \rangle \approx 2.8$ readout strips.

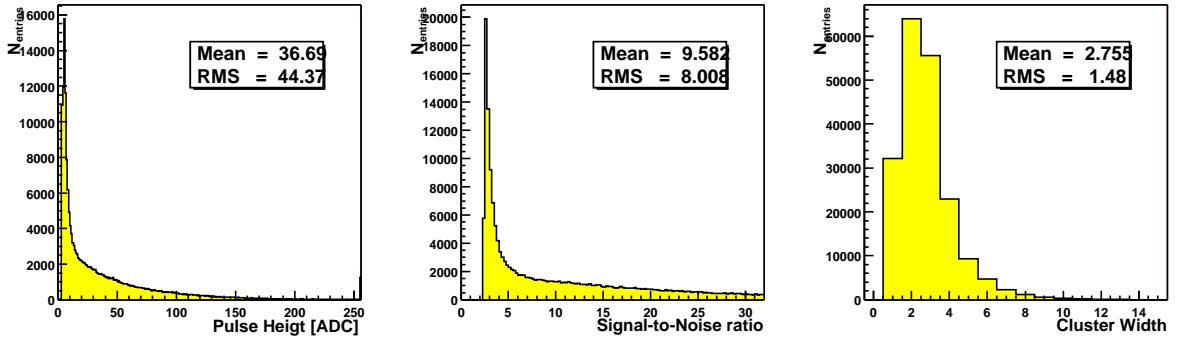


Figure 4.17: Distributions of pulse height (in ADC counts), signal-to-noise ratio, and cluster width (in readout strips) for all clusters found in chamber M13+3 in 10 000 events of the run 17021.

By reconstructing tracks and regarding only hits used for the reconstruction, hits from the wrong bunch crossings are strongly suppressed. The resulting spectra are shown in Fig. 4.18. A separation between noise and signal peak can be seen both in the pulse height and the signal-to-noise distribution. Only about 10 % of all hits found were used to reconstruct tracks. This number is so low mainly because of two reasons: The reconstruction used for these plots was restricted to search for tracks only in the Inner Tracker; many real tracks leave the Inner Tracker and continue in the Outer Tracker. These tracks could not be found, and therefore no hits belonging to these tracks could be identified. The other reason is an intrinsic momentum cut used by the reconstruction program: only tracks with a momentum of $p > 1$ GeV are considered.

Gas Gain. At the beginning of the run period 2000, all chambers were operated with the same high voltage settings. It was then observed that chambers within one station, where they are exposed to the same particle flux, showed drift currents differing by as much as a factor of two (see [K⁺01]). The same behaviour was found in the mean pulse height of clusters associated with reconstructed tracks, and also the signal-to-noise ratios are different for different chambers (see Fig. 4.19). Likewise, the measured chamber efficiencies varied between 65 % and 90 %. The reason for this variation is most probably a variation in the GEM geometry. This can result in different field geometries and therefore different gas gains at the same operation voltages.

The (blue) squares in Fig. 4.20 show the mean pulse height and the mean signal-to-noise ratio for all chambers of the station MS13-. The chambers show mean pulse heights between 20 and 55 ADC counts. The gas amplifications were equalised by individually adjusting U_{GEM} , the voltage difference across the GEM, until all chambers showed approximately the same drift currents.

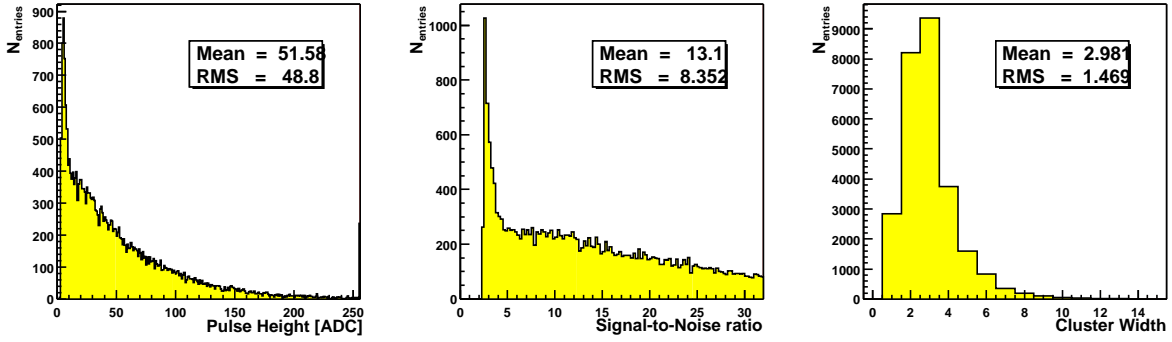


Figure 4.18: Pulse height, signal-to-noise ratio, and cluster width for clusters found in chamber M13+3 which were used to reconstruct tracks in the Inner Tracker. The same 10 000 events as in Fig. 4.17 were used.

The resulting distribution of pulse heights and signal-to-noise ratios is shown in Fig. 4.20 as the (red) triangles. The spread in the mean pulse height is lower, although there are still chambers which show a much higher gas gain than the average.

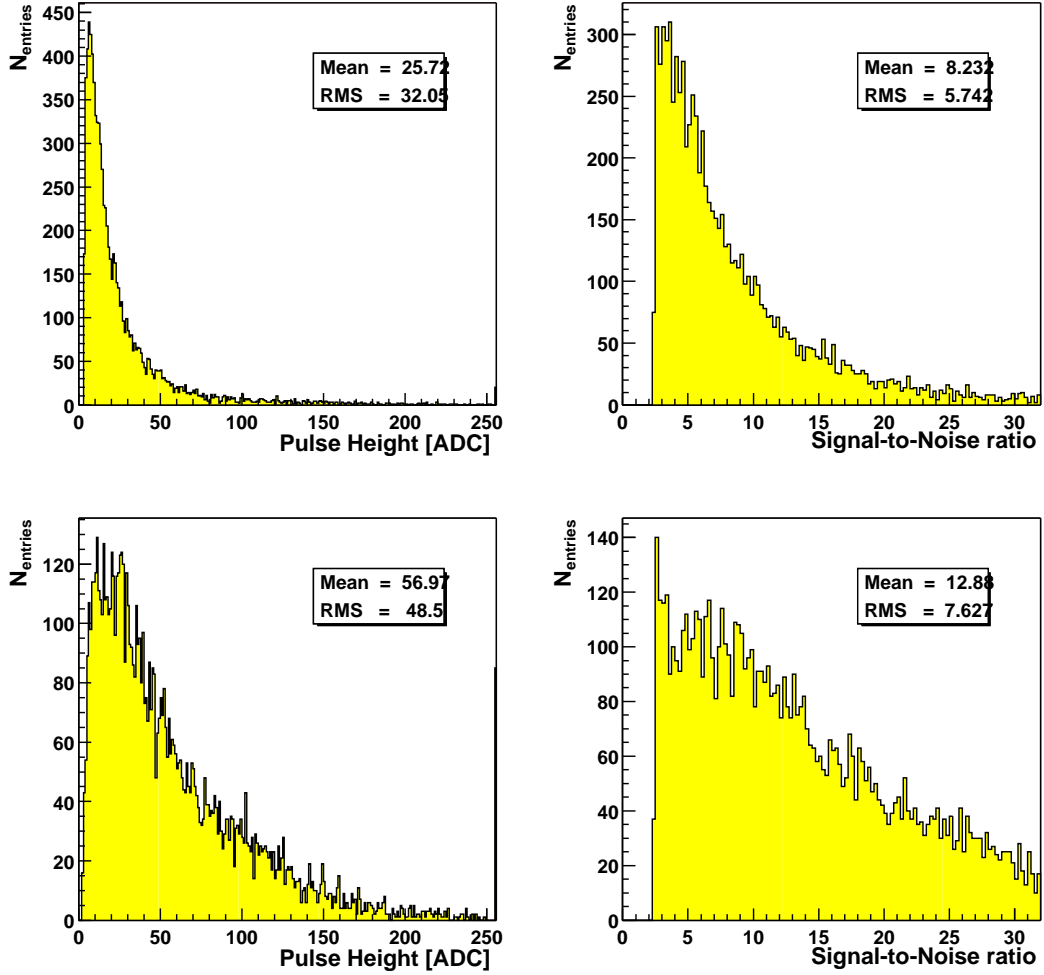


Figure 4.19: Pulse height (cluster charge) and signal-to-noise ratio of clusters associated with reconstructed tracks for the two chambers M13--1 (*top*) and M13+3 (*bottom*). Both chambers were operated with the same high voltage settings, $U_{\text{drift}} = 2.5$ kV, $U_{\text{cath}} = 490$ V and $U_{\text{GEM}} = 420$ V. For chamber M13--1, only the steeply falling edge of the pulse height spectrum is above the threshold of the cluster finder, while for chamber M13+3 the maximum starts to appear over the threshold. The difference in pulse height and signal-to-noise ratio is caused by different gas amplification factors in the chambers; the most probable source for this is a variation in the GEM geometry, causing different GEM gains.

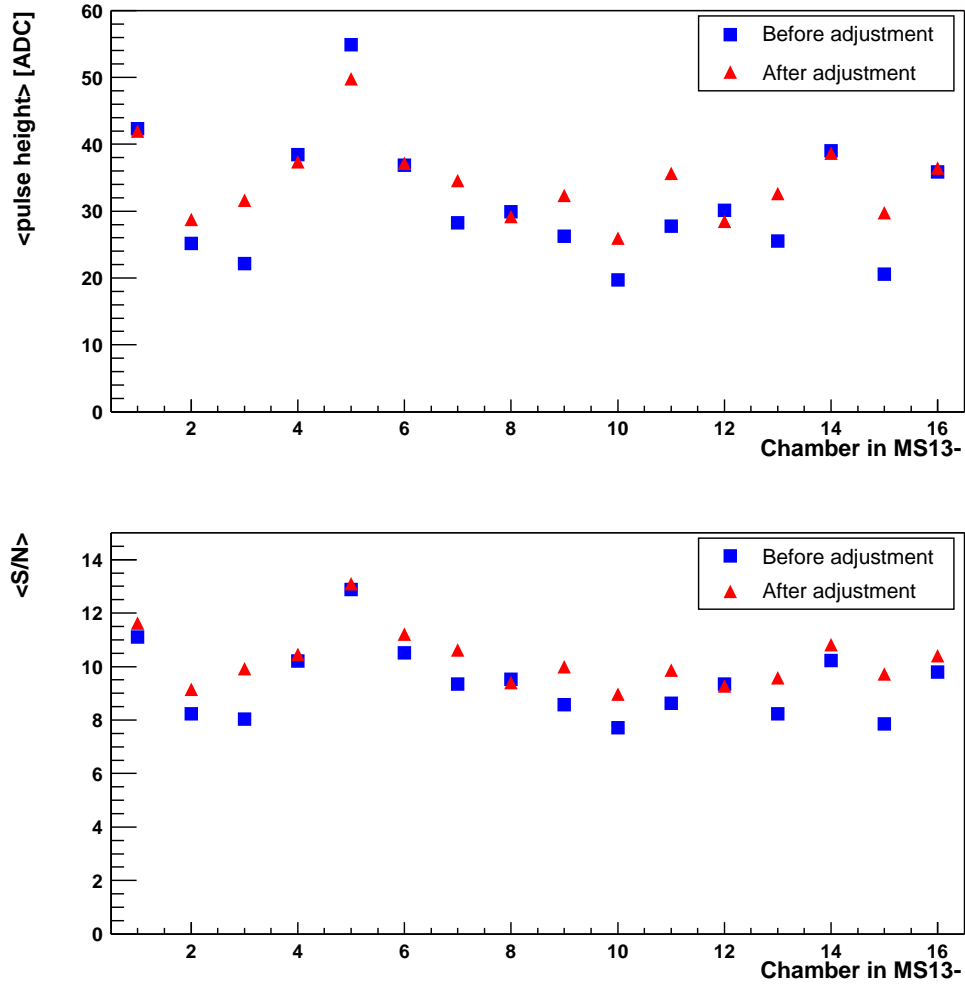


Figure 4.20: Mean pulse height (*top*) and signal-to-noise ratio (*bottom*) of all chambers of station MS13—: the *blue boxes* show the data from run 16556, where all chambers were operated with the same high voltage settings, and the *red triangles* show the data from run17021, where the GEM voltages were raised for several chambers in order to equalise the gas gain.

4.5.7 Chamber Efficiency

In this section, the procedure used to determine the efficiency in the chambers of the first superlayer of the Inner Tracker is described, and measured chamber efficiencies for chambers of the first station MS01 are presented.

As a first approach to measure the hit efficiency of the GEM-MSGC detectors in HERA-B, external tracks which are reconstructed in the Vertex Detector System are used. The tracks are extrapolated as straight lines into the first superlayer of the Inner Tracker, using the end point (x_e, y_e, z_e) and the slopes $\tan \theta_x, \tan \theta_y$ which are provided by the track reconstruction program. For the chambers with a stereo angle α , the impact point (x_t, y_t) is rotated into the coordinate system of the chamber:

$$\begin{pmatrix} u_t \\ v_t \end{pmatrix} = \begin{pmatrix} \cos \alpha & -\sin \alpha \\ \sin \alpha & \cos \alpha \end{pmatrix} \begin{pmatrix} x_t \\ y_t \end{pmatrix}. \quad (4.9)$$

The first coordinate of the impact point (u_t, v_t) can then be compared with the measurement coordinate u_h of the hits in the chambers. The hit efficiency of a chamber is then defined as

$$\varepsilon_{\text{hit}} = \frac{N_{\text{ass}}}{N_{\text{tot}}}, \quad (4.10)$$

where N_{tot} denotes the total number of tracks in the track sample, and N_{ass} is the number of tracks to which a hit could be assigned.

The efficiency which is calculated like this from matching tracks with hits depends crucially on the quality of the tracks. If the track sample contains many ‘clones’ (*i.e.* reconstructed tracks which are duplicates of each other) or ‘ghosts’ (*i.e.* reconstructed tracks whose hits do not belong to the passage of one single particle through the detectors), the efficiency is biased to low values. Therefore, only reconstructed track segments which pass the following requirements are used for the efficiency determination:

1. Before the track search is started, data from readout chips in the VDS which show an unusually high number of hits are discarded (using a selection routine provided by M. Bräuer [Brä01]).
2. At least 9 hits of the VDS are used to reconstruct the track segment. This ensures a good rejection of tracks with low quality.
3. The segment is a pure VDS segment; no hits from the Inner Tracker contribute. This eliminates any bias on the efficiency which would be introduced if Inner Tracker hits were used in the track definition.
4. The extrapolated track segment passes through the sensitive volume of all four chambers of a quadrant.
5. The track segment is isolated: no other track segments are passing the chamber in a disc with radius 5 mm centred around the impact point (u_t, v_t) of a segment.
6. While determining the efficiency of chamber i , the other three chambers in the same quadrant have a hit which is close to the track. These three hits serve as a confirmation of the track.

A few examples of the correlation of the u -coordinate of the track impact points with all hits found in an ITR chamber are shown in Fig. 4.21. There is an acceptance gap visible around $u_{\text{track}} \approx -15$ cm. Due to several defect readout chips in the Vertex Detector, no tracks with $n_{\text{hits}} > 9$ can be found in this region (see also Fig. 4.22).

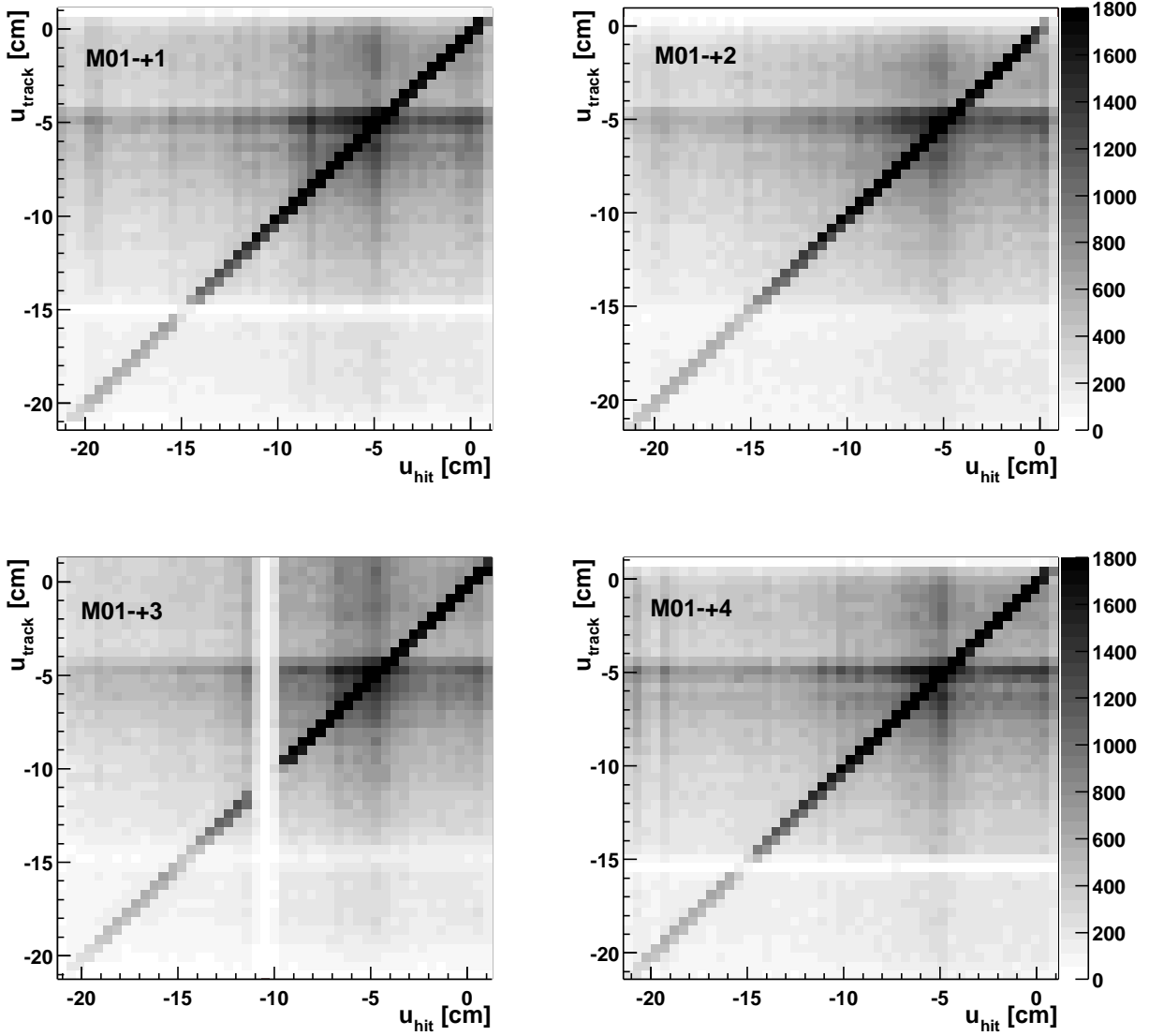


Figure 4.21: Correlation between impact points of accepted VDS tracks and hits in the chambers M01-+1 – M01-+4 of the first station of the Inner Tracker. Around $u_{\text{hit}} \approx -11$ cm, chamber M01-+3 has an inefficient region due to three disconnected cathode groups, corresponding to a region of 1.4 cm where no hits are found. This region shows up as a white vertical band in the correlation plot. The narrow band around $u_{\text{track}} \approx -15$ cm is not populated with track segments, due to several bad readout chips in the VDS and the hard requirement to find more than 9 hits in the VDS (see also Fig. 4.22).

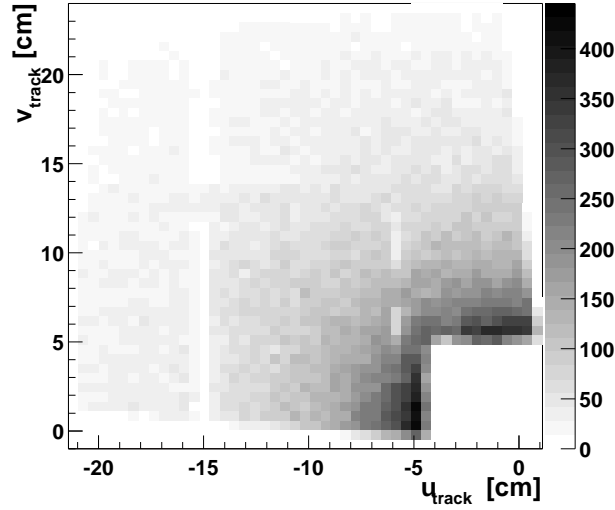


Figure 4.22: Distribution of the impact points (u, v) of all VDS tracks extrapolated into the quadrant $(x < 0, y > 0)$ of the first layer of MS01. The tracks shown pass the quality cuts 1.–4. described in the text ($n_{\text{hit}} > 9$, no ITR hits, passing through all four layers of one quadrant of MS01). The recess of the Inner Tracker chambers for the beam pipe is visible in the lower right corner of the histogram. There is a band around $u_{\text{track}} \approx -15$ cm where no reconstructed tracks are found.

The resulting residuals $\Delta u = u_{\text{track}} - u_{\text{hit}}$ are plotted in Fig. 4.23. Over a flat combinatorial background the residual peak is clearly visible; the core of the peak has a width of about $\sigma_u \approx 0.5$ mm. To account for still existing shifts in the residuals, in a first pass over the data the position \bar{u} of the residual peak is determined.⁹ Only hits which are near the track, as defined by

$$|u_{\text{track}} - u_{\text{hit}} - \bar{u}| < \delta_{\text{max}} \quad (4.11)$$

with $\delta = 0.15$ cm, are subsequently counted as efficient hits. They are indicated as the shaded histograms in Fig. 4.23.

The efficiency is then calculated as a function of the measurement coordinate u using Eq. 4.10. The result is shown in Fig. 4.24. With the exception of an inefficient region in the chamber M01+3 due to cathode shorts, the efficiencies are constant within 5 %, which is sufficient for tracking. In chamber M01+2, there is also a region with reduced efficiency visible around $u = -5$ cm, where the recess for the beam pipe ends. The main contribution to this inefficiency comes from a very small region at one corner of the chamber (see Fig. 4.25). The mean efficiencies derived from these measurements are shown in Table 4.2.

With this method (but slightly different cuts, and also taking into account the known broken readout strips, which may lead to an additional inefficiency), the chamber efficiencies were determined as a function of U_{GEM} to find the correct operation point. The result of this measurement is shown for seven chambers of the station MS01 in Fig. 4.26 [Zeu01b]. It turned out that the chamber efficiencies varied between 65% and 91% when the chambers were operated with identical high voltage settings. The efficiency variation is correlated with variations in the drift currents, pulse heights, and the signal-to-noise ratio: chambers with low efficiency also have a low drift current and show a low pulse height. It was this observation which led to the

⁹Although both the Vertex Detector and the Inner Tracker are very well aligned internally, the global alignment between these two subdetectors is not yet very good. Therefore a shift between the VDS track segments and the Inner Tracker hits is not surprising; the shift is about 2 mm for the period considered here (run 17137).

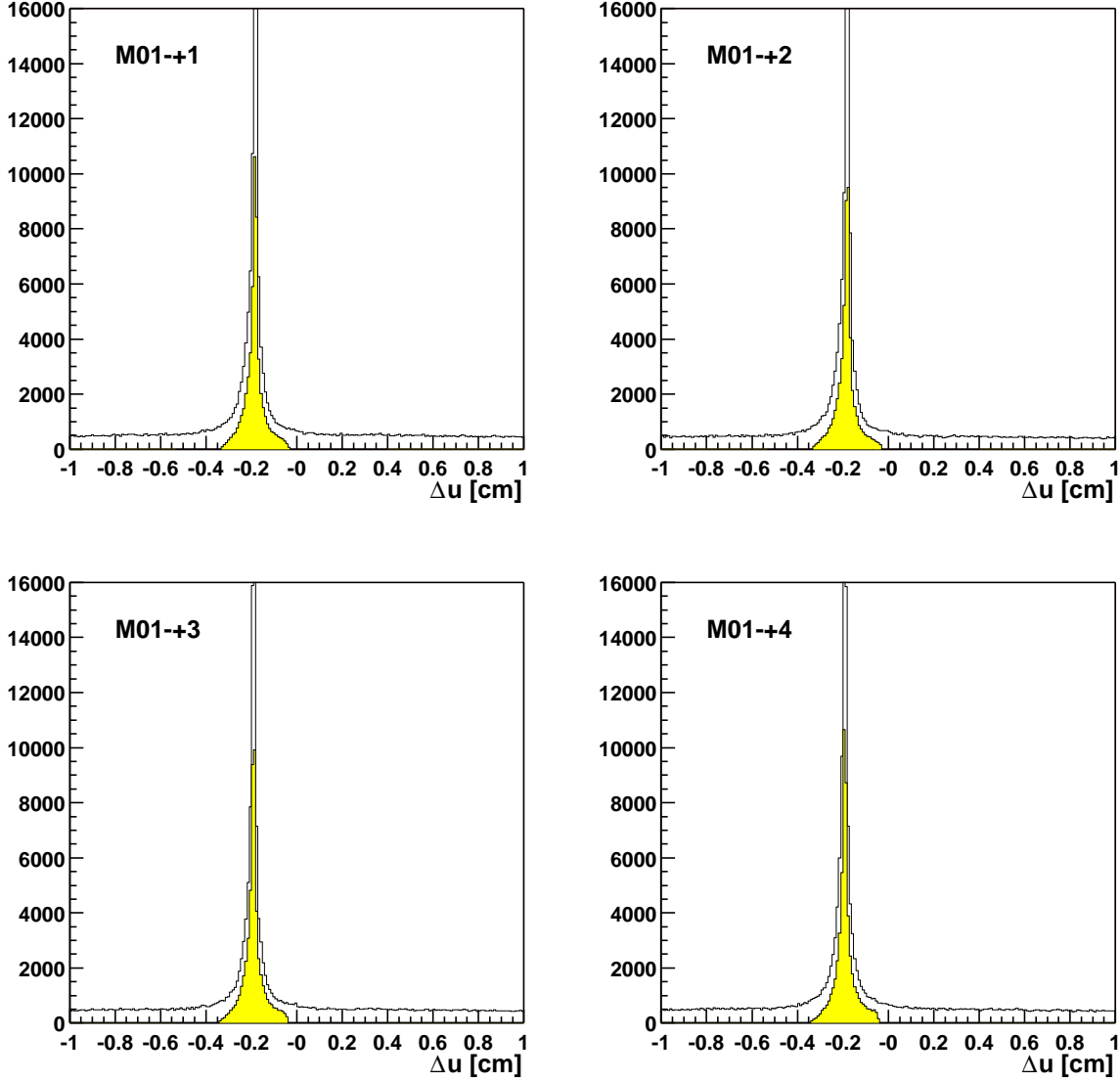


Figure 4.23: Residuals $\Delta u = u_{\text{track}} - u_{\text{hit}}$ between all track segments passing the first three quality criteria (see text) and all Inner Tracker hits (*open histograms*). The position of the residual peak is shifted systematically towards negative Δu , with a mean value of $\bar{u} \approx 2$ mm for all four chambers. This shift shows the need for a global alignment correction between the Vertex Detector and the Inner Tracker. For all four chambers, the gaussian core of the residual peak has a width of $\sigma \approx 0.1$ mm. The *filled histograms* show the ‘efficient hits’ which were associated with a good reconstructed track segment as defined in the text.

| Chamber | ε | $\Delta\varepsilon(\text{stat.})$ |
|---------|---------------|-----------------------------------|
| M01-+1 | 0.931 | 0.001 |
| M01-+2 | 0.883 | 0.001 |
| M01-+3 | 0.891 | 0.001 |
| M01-+4 | 0.909 | 0.001 |

Table 4.2: Efficiencies of the chambers of MS01-+, determined as described in the text. For chamber M01-+3, the inefficient region was omitted for this calculation. The systematic error is obtained by varying the track requirements, it amounts to about 1 % for all chambers.

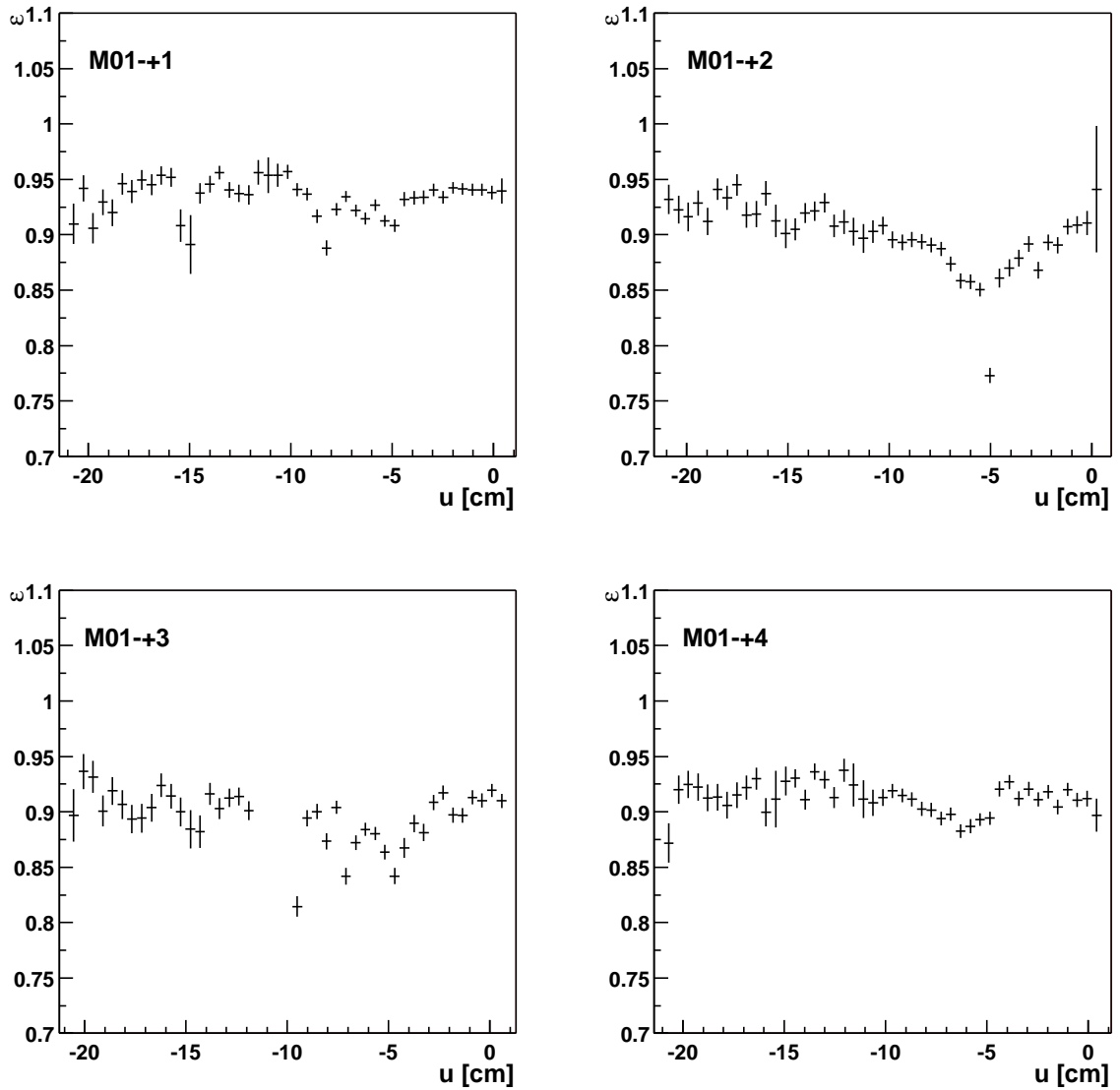


Figure 4.24: Efficiencies of the chambers in the quadrant MS01-+, determined with good VDS tracks. The errors given are the statistical error only. The efficiency is more or less constant over the whole chamber, with two exceptions: the dead region in M01-+3 is clearly visible, and in M01-+2 there is a less efficient region around $u \approx -5$ cm, which is where the recess for the beam pipe ends.

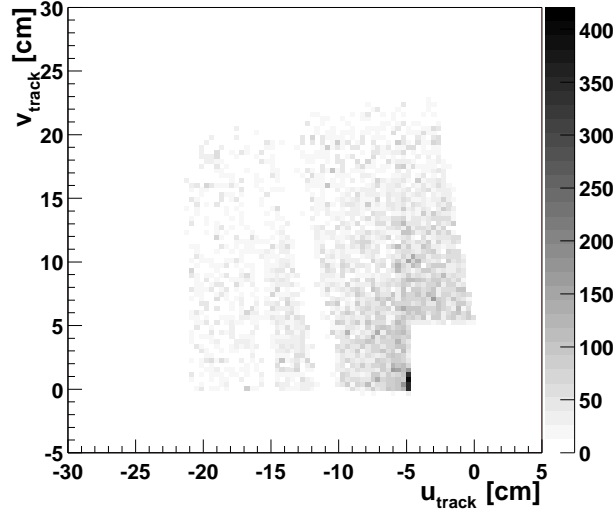


Figure 4.25: Distribution of inefficient tracks in chamber M01+2. The entries were weighted with the radial distance $r_{\perp} = \sqrt{u_{\text{track}}^2 + v_{\text{track}}^2}$ to compensate the radial decrease of hit and track densities. For a uniformly inefficient chamber, the histogram should be uniformly filled. In this chamber, however, the majority of inefficient tracks are clustered in the lower right corner of the chamber, at $u \approx -5$ cm and $v \approx 0$ cm.

conclusion that the gas amplification in the chambers differs significantly. Variations in the gas amplification were anticipated, though not so large as actually found in HERA-*B*, and the high voltage system was designed to accommodate them by allowing to individually adjusting the gas amplification of each chamber by adjusting U_{GEM} . The result of this adjustment is shown in Fig. 4.26, where also the finally chosen operation points are indicated. Finally, hit efficiencies $\varepsilon_{\text{hit}} > 90\%$ could be reached with all chambers. The saturation of the efficiency at values below 100% is not yet completely understood; a part of this inefficiency can be traced back to rare events in which no analogue data was sent by the readout chips.

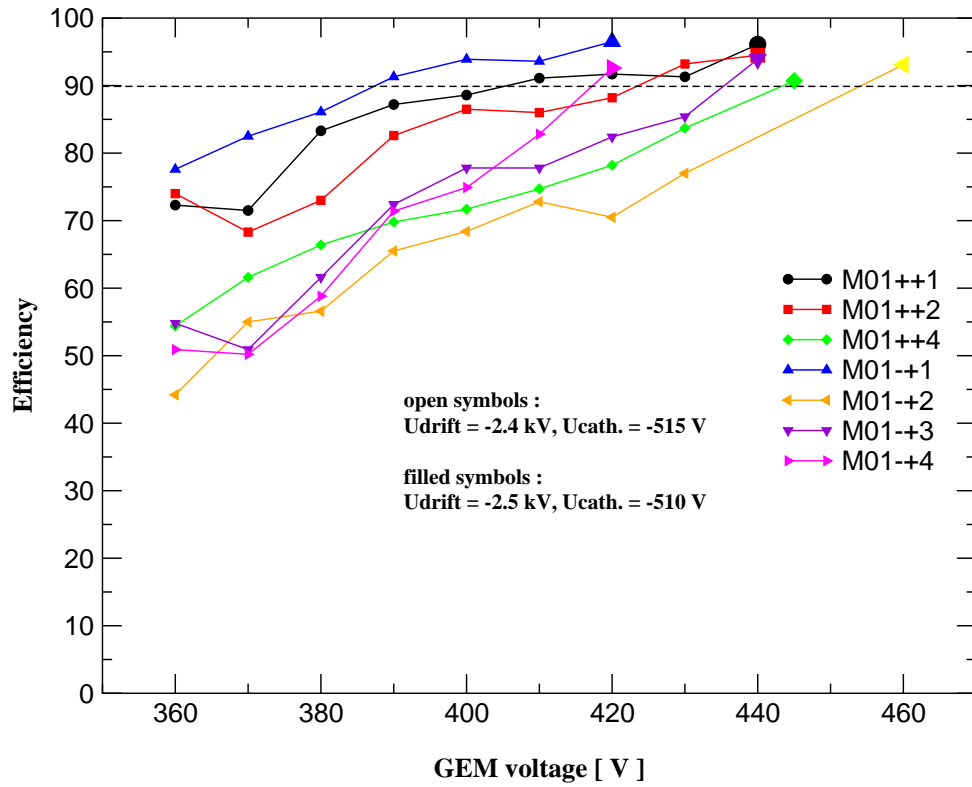


Figure 4.26: Chamber efficiencies for seven chambers of MS01 as a function of U_{GEM} [Zeu01b]. The efficiencies were determined as described in the text; the larger, filled symbols at the right end of each curve indicate the final operation point chosen. Efficiencies above 90% could be reached; the chambers were operated for about 6 weeks with these high voltage settings without the occurrence of significant problems.

4.6 Simulation of Pulse Shapes

The result of both the SCLk delay scan and the slow fall-off seen at the beginning of the gaps in the BX spectra cannot be easily understood, if only the step response of the Helix frontend is considered. Especially the nearly flat dependence of the mean cluster charge as a function of the sampling point, where one would rather expect a shape similar to the Helix pulse shape, is hard to understand. Additionally, the pulse height distributions do not show any indication of a Landau spectrum, which would have been expected based on experience in test stands in the laboratory.

For a better understanding of the behaviour of the readout system, the time evolution of the chamber signal which is seen by the preamplifier has to be taken into account. This has then to be folded with the Helix step response to obtain a realistic description of the signal which is sampled into the pipeline. The effect of interactions in previous bunch crossings must also be taken into account. The results presented here are based on a simulation performed by B. Schmidt [Sch99a, Sch01].

4.6.1 Time Evolution of the Chamber Signals

The main contribution to the signal seen on the anode strip of a MSGC comes from the ion cloud produced in the gas amplification process, which influences charge on the anode while drifting away from it. The electrons produced in the avalanche in the vicinity of the anode strip only give a small contribution. The exact fraction of this contribution to the signal is not known; for this simulation, it is assumed that only 10% of the total signal comes from the electrons. This fraction arrives instantaneously at the anode. The time behaviour of the main part of the signal is determined by the speed of the ion cloud. The ion drift was calculated numerically and can be parametrised with the sum of two exponentials. The total time evolution of the current flowing on the anode assumed for this simulation has the form

$$i(t) = 0.9 a_0 (a_1 e^{-t/\tau_1} + a_2 e^{-t/\tau_2}) + 0.1 \delta(t) \quad (4.12)$$

where the parameters a_i , and $\tau_{1,2}$ are taken from the numerical calculation. The current $i(t)$ is normalised such that the total charge q_0 accumulated on the anode is 1:

$$q_0 = \int_0^\infty dt i(t) = 1$$

The shape of the current is depicted in Fig. 4.27.

The step response of the Helix front-end was taken from [TDD99]; it was parametrised with the function

$$r(t) = b_0 t e^{-b_1 t} (e^{b_2 t} - 1) \quad (4.13)$$

where the parameters b_i were determined by a fit of Eq. 4.13 to the measured pulse shape. This function is then convoluted with the current signal on the anode strip to obtain the signal which is then sampled into the pipeline:

$$h(t) = (i \star r)(t) = \int_{-\infty}^{+\infty} dt' i(t') r(t - t') \quad (4.14)$$

Both the fit and the result of the convolution are shown in Fig. 4.28. The measured peak height corresponds to an input charge of $\text{MIP}_{\text{Si}} \hat{=} 24\,000 e^-$. For the simulation, a normalised Helix pulse shape $r_0(t)$ is used such that the maximum value is $r_0(t_{\text{max}}) = 1$ for a unit input charge.

A minimum ionising particle passing through the counting gas of a GEM-MSGC will produce on the average 10 primary clusters. The number of primary clusters is assumed to follow a

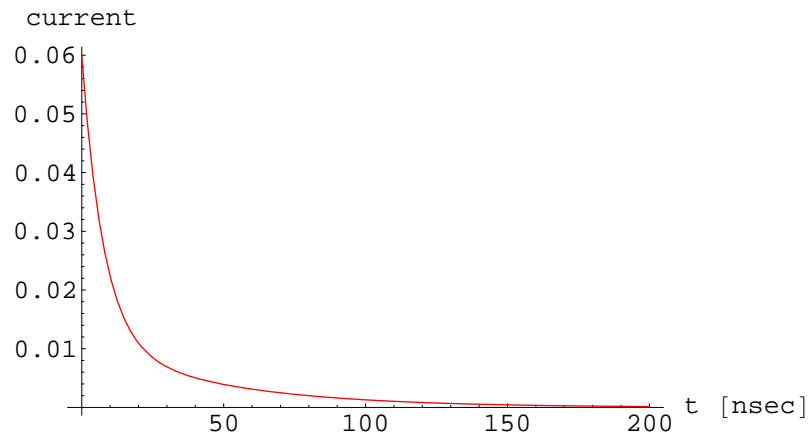


Figure 4.27: Time evolution of the signal seen on an anode strip (simulation).

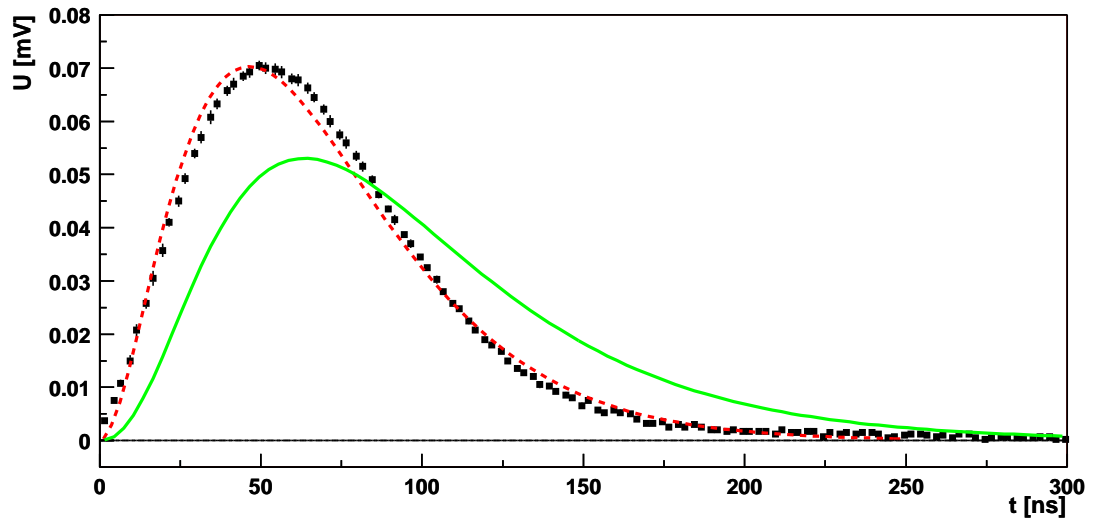


Figure 4.28: Helix step response (*filled points*) with the result of a fit to the signal shape (*dashed curve*) and its convolution with the anode signal induced by the drift of one ion cloud (*full curve*)

Poisson distribution. To a good approximation, the number n_c of primary electrons contained in a cluster is distributed according to a simple power law (see for example the measurements of [FHS91]),

$$p(n_c) \propto n_c^{-\alpha}. \quad (4.15)$$

The exponent α is adjusted such that the expectation value for the number of generated primary electrons is $\langle n_c \rangle = 2.4$, which is the correct value for an Ar:CO₂ (70:30) mixture. Numerically, $\alpha = 2.3418$. The clusters are assumed to be distributed uniformly along the path of the particle. With the applied fields, the electrons take about 60 ns to drift from the drift electrode to the GEM or to traverse the transfer gap. The signal seen by the readout chip is the superposition of the signals produced by the successive gas amplification of all clusters. The simulation proceeds as follows:

1. Generate the number of primary clusters n_p , such that on the average both above and below the GEM $\langle n_p \rangle = 10$ clusters are created (neglecting the small difference in the gap height above and below the GEM).
2. Generate the number $n_c^{(i)}$ of primary electrons in each cluster (i) according to the power law (4.15).
3. Generate drift times $t^{(i)}$ (*i.e.* the distance to the MSGC wafer) for all clusters, uniformly in the interval $[0, 60]$ ns.
4. Simulate gas amplification: the gas amplification with a mean gas gain g_0 is assumed to follow an exponential distribution $g(x) = \lambda \exp(-\lambda x)$, with $\lambda = g_0^{-1}$. Two amplification factors are generated, g_{GEM} for the amplification at the GEM, and g_{MSGC} . The mean amplification is taken to be $g_{0,\text{GEM}} = 15$ and $g_{0,\text{MSGC}} = 200$, resulting in a mean total gain of $g_{\text{tot}} = 3000$.
5. For a primary cluster from above the GEM, the charge arriving at the anode is

$$q^{(i)} = n_e^{(i)} g_{\text{GEM}}^{(i)} g_{\text{MSGC}}^{(i)},$$

while for the primary clusters generated in the transfer gap, the factor $g_{\text{GEM}}^{(i)}$ is set to 1.

6. The signal $s(t)$ which is produced by the Helix front end from the clusters of one track passing through the chamber is then

$$s(t) = \sum_{i=0}^{n_p} n_e^{(i)} g_{\text{GEM}}^{(i)} g_{\text{MSGC}}^{(i)} h(t - t^{(i)}) \quad (4.16)$$

where $h(t)$ is the convolution of the Helix step response with the time evolution of the current on an anode strip (Eq. 4.14).

Fig. 4.29 shows some simulated events and the response of the Helix front-end to the chamber signals. For large chamber signals, the Helix response is still large in the following bunch crossing.

This simulation does not take into account the effects of diffusion and oblique tracks, which both lead to a cluster width $\langle w \rangle > 1$. Quantitative predictions should therefore be taken with a grain of salt; nevertheless, the behaviour of the chamber signals measured with the Helix can be understood better with this simulation. Some results will be presented in the next section.

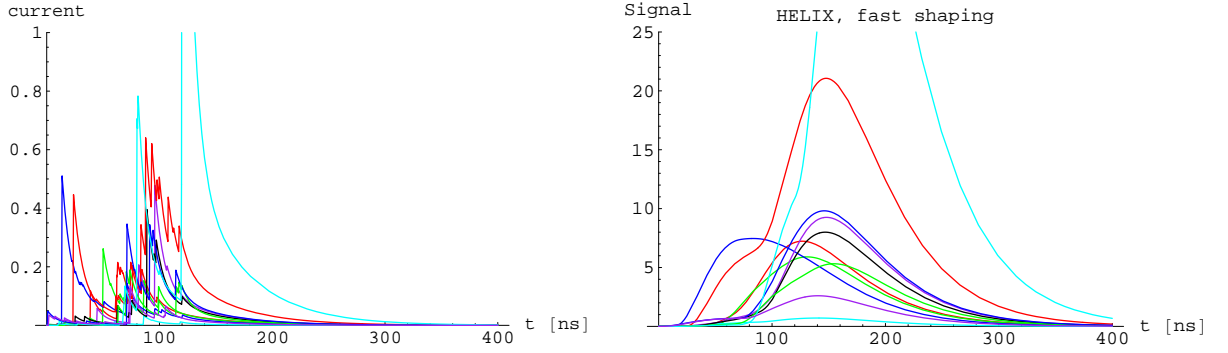


Figure 4.29: Simulated chamber signals (*left*) and the response of the Helix front-end (*right*). The input charge was normalised to the nominal chamber gain g_{tot} , so the Helix signal (*right plot*) is measured in units of electrons/ g_{tot} .

4.6.2 Results of the Simulation

The simulated response of the Helix front-end ($s(t)$ of Eq. 4.16) can now be used to study the behaviour of the readout during an SC1k timing scan and to get a better understanding of the cluster charge distributions and the gaps in the bunch crossing spectra.

Pulse Height Spectrum The simulated pulse height spectrum is shown in the left plot of Fig. 4.30. For plotting this spectrum it was assumed that the proper bunch crossing of the pulse is known, such that only the maximum of the Helix response is sampled. The pulse height distribution shows the expected Landau peak. However, at HERA-*B* interactions can occur at any bunch crossing. Therefore, the pulse height spectrum is a superposition of samples from the correct bunch crossing with samples from previous and later bunch crossings. The effect of this superposition is depicted in the right plot of Fig. 4.30. The pulse height spectrum is completely dominated by entries at small pulse heights which come from sampling the Helix signal at the wrong bunch crossing. This last distribution can be compared to the experimentally found pulse height spectrum of all pulses in Fig. 4.17.

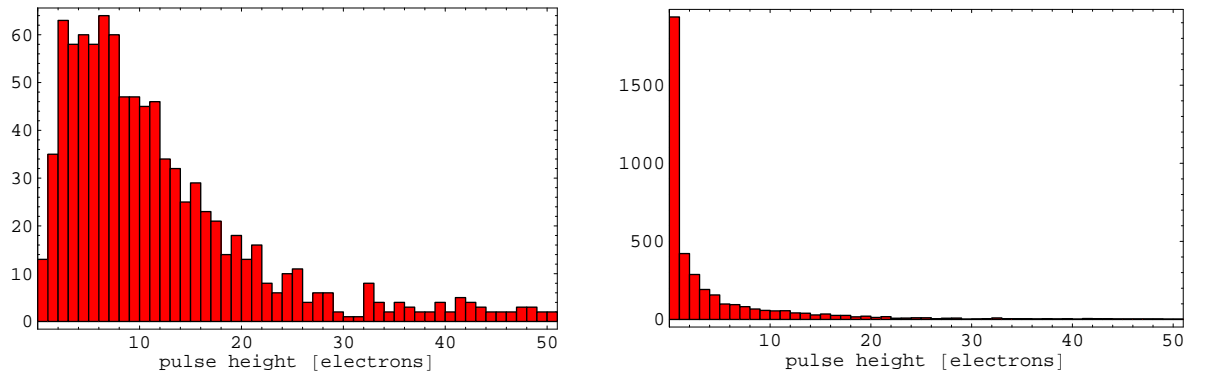


Figure 4.30: Distribution of the pulse heights (simulation). *Left:* Only the correct bunch crossing $n = 1$ is sampled. *Right:* The contribution of the bunch crossings $n = 0, 2, 3$ is added to the samples of the correct bunch crossing. Again, the pulse height is measured in units of electrons per nominal gain.

If one only looks at events from the first bunch crossing after the kicker gap, one expects

only a ‘contamination’ from the next bunch crossing. This is illustrated in Fig. 4.31.

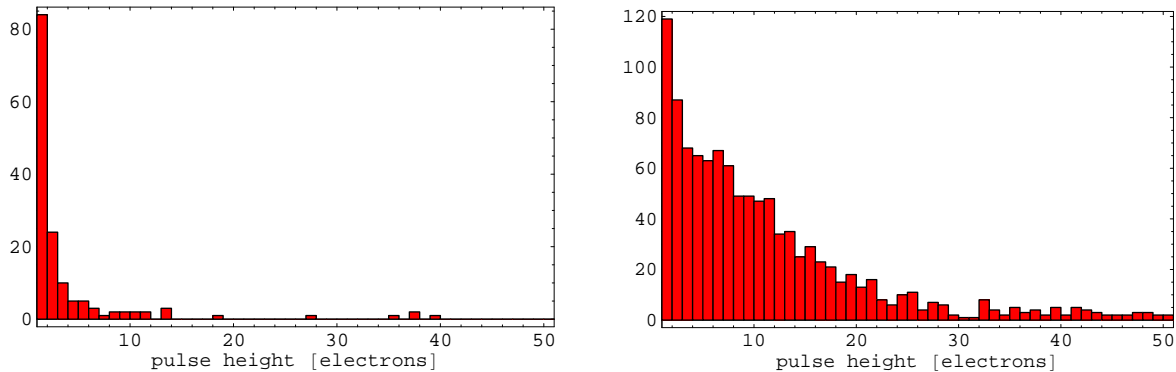


Figure 4.31: Distributions of the pulse heights (simulation). *Left:* only hits from the following bunch crossing are plotted. *Right:* Pulse height spectrum found for the correct bunch crossing with the contribution of the following bunch crossing. The pulse height is measured in units of electrons per nominal gain. A distribution like this is expected for events from the first BX after the kicker gap. A threshold of 1 was applied to both spectra.

Therefore, to obtain a pulse height spectrum from which one can infer the gas gain of the chamber, hits belonging to the correct bunch crossing have to be chosen. This can be done by reconstructing tracks and only considering those hits which are associated with a track. Even then, wrongly reconstructed tracks will contribute some hits from wrong bunch crossings, spoiling the pulse height distribution.

Timing Scan The optimal sampling point must be determined experimentally for the chambers installed in the experiment (see Sect. 4.3). The method used to determine the timing for the 1999/2000 run period relied on the pulse height of all clusters found by the cluster finder. The expectation was to find back the Helix pulse shape in a plot of the mean pulse height versus the delay of SC1k. There is a maximum visible in these plots (see Fig. 4.5), but it is not very pronounced.

This behaviour can be understood by considering not only the hits found in the correct bunch crossing, which would give the expected shape (Fig. 4.32, *left*). Taking also into account the samples from the wrong bunch crossings, the delay curve drastically changes shape: the maximum is still visible and approximately at the correct place, but the minimum is filled up (Fig. 4.32, *right*). Despite this change of the pulse height curve by the presence of hits from wrong bunch crossings, the optimal sampling point still can be recognised. This justifies the method used to find the correct timing.

Restricting the events to come only from the first bunch crossing after the kicker gap, the resulting delay scan curve looks more like the one with only the correct hits (see Fig. 4.33). There is a clear influence of the hits from the following bunch crossing seen, which leads to smaller mean pulse heights at large delays δt , but again the position of the peak is essentially unchanged (and moreover it is sufficient to determine the sampling point within about 10 ns). This could be exploited for the re-commissioning of the readout system or the run period 2002 to obtain an improved estimate for the correct sampling point.

Conclusions. Although the simulation is certainly far from perfectly modelling the processes of gas amplification actually taking place in the GEM-MSGCs, it allows to gain a better understanding of the observed behaviour of the chamber signals.

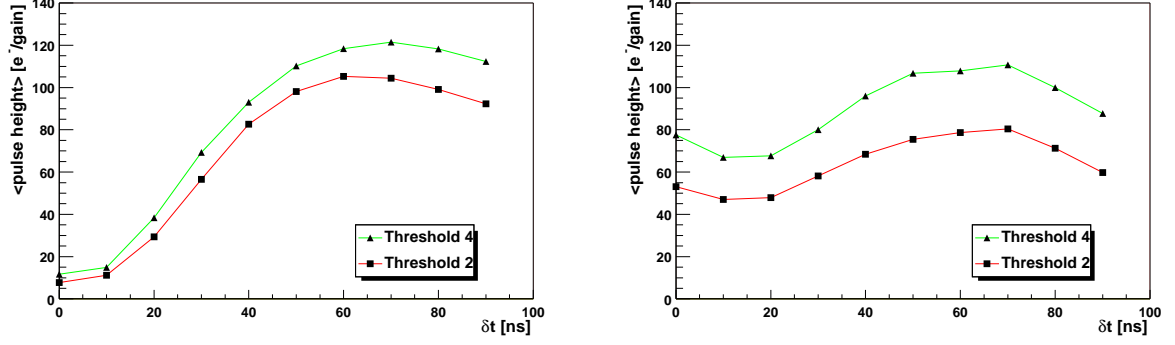


Figure 4.32: Simulated delay scan of the sample clock: the mean pulse height measured in electrons per gain is plotted as a function of the delay δt of the sampling point. Two different thresholds were applied to the raw pulse height spectra. *Left:* Only the correct bunch crossing contributes to the pulse height spectrum. The shape of the front-end's response to a chamber signal is reproduced; the pulse height shows a maximum where also the Helix response is maximal. *Right:* Also hits from events from the following and the previous two bunch crossings contribute. The maximum is still visible, but much less pronounced.

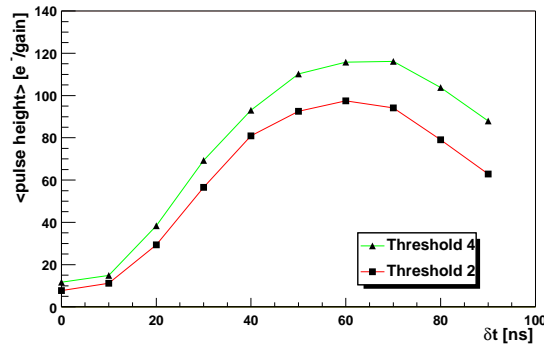


Figure 4.33: Simulated delay scan where only the correct and the following bunch crossing contribute. There are many more hits with low pulse height found for large delays δt : here, the signal from the correct bunch crossing starts to decay, and the signal from the following bunch crossing is at the steep rising edge of the front-end response.

Using the fast signal shaping, the Helix step response meets the requirement that after 100 ns, any signal has essentially vanished. However, the signal on the anode produced by the passage of one particle through the chamber consists of a series of exponentially decaying pulses which significantly lengthen the resulting output of the Helix shaper. This results in a much higher probability that the signal from a given bunch crossing is above the detection threshold in one or more of the following bunch crossings. Together with the presence of very large pulses, this effect increases the number of small pulses which are found by the cluster finder, resulting in a steeply falling pulse height spectrum and an almost flat dependence of the mean pulse height on the sampling point. The tracking performance is not seriously affected by this, since finding a track requires the coincidence of many hits in different layers.

4.7 Summary and Outlook

During the work for this thesis, parts of the readout system for the HERA-*B* Inner Tracker were developed and tested. The system was improved using the experience gained in several beam test experiments. The final readout system for the complete Inner Tracker was installed at HERA-*B* and fully commissioned. Most of the software needed for beam tests and tests while commissioning was developed and improved; the software running online while data taking was developed and commissioned successfully.

The experience gained during the HERA-*B* run period 2000 showed that the readout system is working close to the design specifications. Some problems still exist in the system, mainly concerning the stability of the readout during long data-taking runs. These problems are not yet fully understood, but work is ongoing to find and eliminate the cause of the problem. The overall performance of both the readout hardware and the software was found to be more than satisfactory for the first year of operation.

Part II

Drell-Yan Physics at HERA-*B*: A Feasibility Study

Chapter 5

The Drell-Yan Process

One of the physics processes which could be part of an alternative physics programme for HERA-*B* besides CP violation is the Drell-Yan process—the production of lepton pairs with high invariant mass in hadron-hadron collisions.

The invariant mass spectrum of lepton pairs produced in hadron-hadron collisions shows several sharp peaks—the charmonium and bottomium families of resonances—over a continuum which falls off steeply with increasing invariant mass M_{γ^*} of the lepton pair. This direct off-resonance production of lepton pairs in hadron-hadron collision is called Drell-Yan process. In the quark-parton model, it can be visualised by the annihilation of a quark and an antiquark into a virtual photon, which subsequently decays into a pair of leptons $\ell^+\ell^-$.

Perturbative QCD makes definite predictions about the angular distribution of the lepton pairs. In pion-nucleon scattering, these predictions were found to be violated, but to present this effect has not been measured in proton-nucleon scattering. Another interesting possibility with Drell-Yan pairs is the measurement of the gluon content of the proton at high values of the momentum fraction x . Via first-order QCD corrections, the Drell-Yan cross section is sensitive to the gluon content of the proton. These processes dominate the cross section in the region of phase space where $p_{T\gamma^*} > M_{\gamma^*}/2$.

This chapter summarises briefly the most important facts about Drell-Yan production; in the next chapter, the prospects of HERA-*B* to contribute to this field are evaluated.

5.1 Perturbative QCD Predictions

In the leading order ($\mathcal{O}(\alpha_s^0)$), the production of lepton pairs in hadron-hadron collisions takes place by quark-antiquark annihilation into a virtual photon, $q\bar{q} \rightarrow \gamma^* \rightarrow \ell^+\ell^-$. The Feynman diagram for this process on the parton-level is shown in Fig. 5.1. The partonic cross section can be computed in full analogy to the creation of hadrons in electron-positron annihilation [ESW96]:

$$\hat{\sigma}_{q(p_1)\bar{q}(p_2)\rightarrow\ell^+\ell^-} = \frac{4\pi\alpha^2}{3\hat{s}} \frac{Q_q^2}{N} \quad (5.1)$$

where $\hat{s} = (p_1 + p_2)^2$ is the centre-of-mass energy available for the process, Q_q is the charge of the quark, and $N = 3$ is a colour factor taking into account that the quark and the anti-quark must carry colour and the corresponding anti-colour to be able to annihilate. The differential cross-section for the production of a lepton pair with mass M is

$$\frac{d\hat{\sigma}_{q\bar{q}\rightarrow\ell^+\ell^-}}{dM^2} = \frac{4\pi\alpha^2}{3M^2} \frac{Q_q^2}{N} \delta(\hat{s} - M^2) \quad (5.2)$$

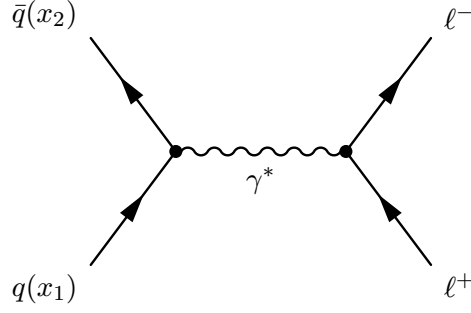


Figure 5.1: Feynman diagram of the Drell-Yan process in the quark-parton model.

Since the incoming particles are not free quarks but are always part of a hadron, the total observed cross section also depends on the parton densities $f_{i/h}(x)$, *i.e.* the probabilities to find a parton of type i with a momentum fraction x in a hadron h . The cross section $\sigma_{h_1 h_2 \rightarrow \ell^+ \ell^-}$ to produce a lepton pair in a hadron collision is obtained by weighting the partonic cross section with the parton densities $f_{i/h}(x)$, integrating over all possible momenta and summing over all possible parton combinations:

$$\sigma_{h_1 h_2 \rightarrow \ell^+ \ell^-} = \sum_q \int dx_1 dx_2 f_{q/h_1}(x_1) f_{\bar{q}/h_2}(x_2) \hat{\sigma}_{q\bar{q} \rightarrow \ell^+ \ell^-} \quad (5.3)$$

The general idea behind this ansatz is illustrated in Fig. 5.2 (usually, the Monte-Carlo event generators employ exactly this description to simulate hard scattering processes).

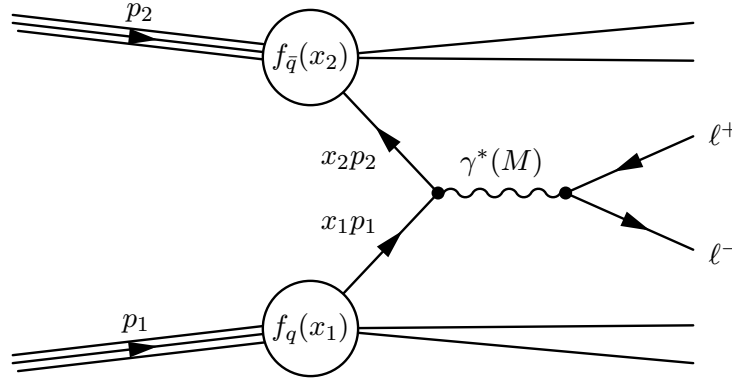


Figure 5.2: Quark-parton model description of the production of a lepton pair in a hadron-hadron collision. The incoming hadrons have momenta p_1 and p_2 , while the partons entering the hard subprocess carry the momentum fractions x_1 resp. x_2 .

The differential cross section is then

$$M^4 \frac{d\sigma}{dM^2} = \frac{1}{N} \frac{4\pi\alpha^2}{3} \tau \mathcal{F}(\tau) \quad (5.4)$$

with
$$\mathcal{F}(\tau) = \int_0^1 dx_1 dx_2 \delta(x_1 x_2 - \tau) \left(\sum_q Q_q^2 (f_{q/h_1}(x_1) f_{\bar{q}/h_2}(x_2) + (q \leftrightarrow \bar{q})) \right). \quad (5.5)$$

It only depends on the dimensionless variable $\tau = \hat{s}/s$, and therefore exhibits a scaling behaviour.

A crucial prerequisite for the validity of Eqs. 5.3 and 5.4 is the assumption that all their ingredients are uncorrelated with each other, so that the cross section can be written as the

convolution of a hard elementary scattering process and some soft elements (the parton density functions) which describe the non-perturbative aspects of the reaction under consideration. This *factorisation hypothesis* is generally believed to be correct to all orders in perturbation theory. If further non-perturbative effects are present which cannot be absorbed into the parton density functions, factorisation not necessarily applies.

Perturbative QCD prescribes corrections to the predictions of the quark-parton model. At lowest order in α_S , these corrections include gluon loops for the incoming quarks, but also the initial-state radiation of gluons by the quarks, and a process which is analogous to Compton scattering known from QED. The relevant Feynman graphs are shown in Fig. 5.3.

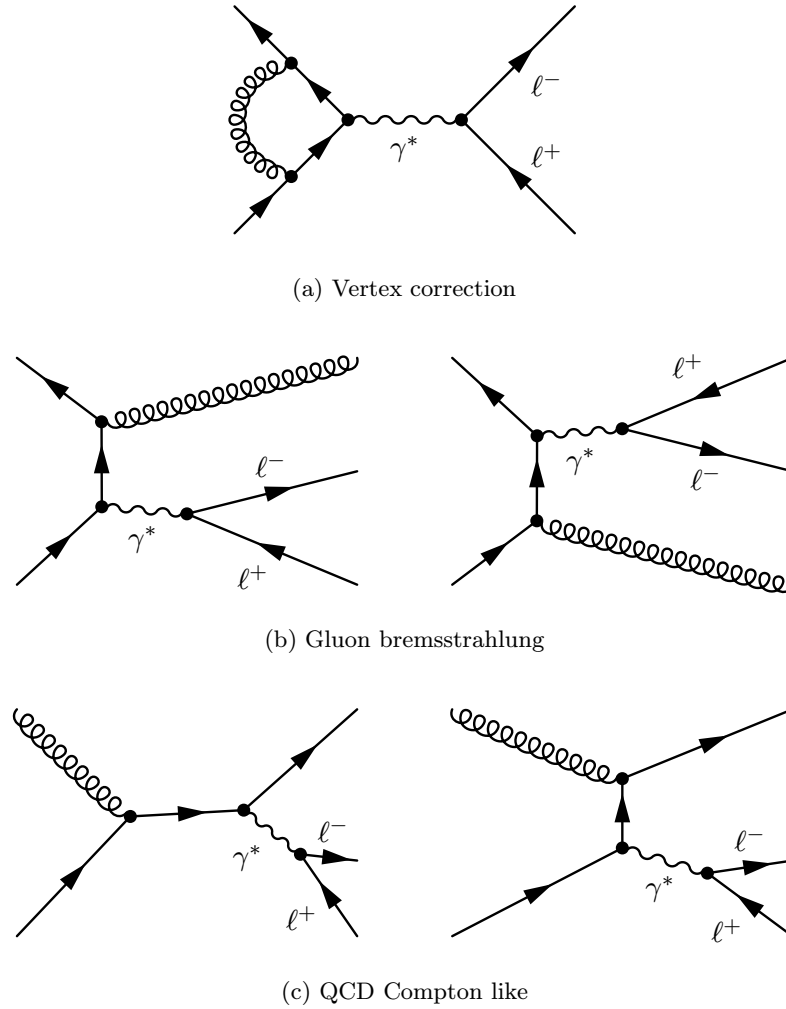


Figure 5.3: Leading and next-to-leading order QCD corrections to the Drell-Yan process: (a) vertex correction, (b) gluon bremsstrahlung, and (c) QCD Compton scattering.

Each single of these correction terms exhibits by itself a divergence: ultraviolet divergences from the loop diagrams, infrared divergences from the contribution of soft gluons, and collinear divergences from the splitting of the initial state partons. However, all but the collinear divergences cancel each other, and the collinear divergences can be absorbed into renormalized parton distribution functions $f_{i/h}(x, \mu)$ which then acquire a dependence on the renormalisation

scale μ (see for example [ESW96]). The cross section can then be written as

$$\sigma_{h_1 h_2 \rightarrow \ell^+ \ell^-} = \sum_q \int dx_1 dx_2 f_{q/h_1}(x_1, M^2) f_{\bar{q}/h_2}(x_2, M^2) \left[\hat{\sigma}_0 + \frac{\alpha_S(M^2)}{2\pi} \hat{\sigma}_1 + \dots \right]_{q\bar{q} \rightarrow \ell^+ \ell^-} \quad (5.6)$$

At the energies and masses which are attainable at fixed-target experiments, the $\mathcal{O}(\alpha_s)$ correction is positive and large, reaching 50% or more. This (unexpectedly large) contribution of the second term in the perturbation series explains the discrepancy between the measurements of the first Drell-Yan experiments and the $\mathcal{O}(\alpha_s^0)$ prediction of the quark-parton model. The main contribution comes from the vertex correction; the other graphs play an important role only at high transverse momenta $p_{T\gamma^*}$ of the lepton pair.

5.2 Angular Distributions and the Lam-Tung Relation

In the naive quark-parton model, the angular distribution of the produced lepton pair is characteristic of the decay of a transversely polarised virtual photon,

$$\frac{d\sigma}{d\Omega} \propto 1 + \lambda \cos^2 \theta, \quad (5.7)$$

where θ is the polar angle of the lepton in the rest frame of the virtual photon and $\lambda = 1$. This was confirmed by the earliest Drell-Yan experiments within the measurement errors. The inclusion of the leading order QCD processes leads to a somewhat more complicated angular distribution,

$$\frac{1}{\sigma} \frac{d\sigma}{d\Omega} = \left[\frac{3}{4\pi} \frac{1}{\lambda + 3} \right] \left(1 + \lambda \cos^2 \theta + \mu \sin 2\theta \cos \phi + \frac{\nu}{2} \sin^2 \theta \cos 2\phi \right), \quad (5.8)$$

where ϕ is the azimuthal angle. The coefficients λ , μ , and ν play the role of structure functions; they are independent of the angles θ and ϕ , but may be functions of the transverse momentum $p_{T\gamma^*}$ or the mass M_{γ^*} of the virtual photon. In this thesis, they are expressed in the Collins-Soper frame ([CS77], see also App. D). If the centre-of-mass energy is small enough that the contribution from the Z -boson to the Drell-Yan production is negligible, $\mu = 0$. λ is predicted to be still close to 1.

In analogy to the Callan-Gross relation which links the structure functions $F_1(x)$ and $F_2(x)$ of deep inelastic scattering (DIS), the parameters λ and ν are related by the so-called Lam-Tung relation [LT80],

$$1 - \lambda - 2\nu = 0. \quad (5.9)$$

In contrast to the Callan-Gross relation (which shows scaling violation at $\mathcal{O}(\alpha_s^1)$), the Lam-Tung relation is not modified by first-order QCD corrections. It is still approximately valid after inclusion of higher order terms in the perturbation series; Higher order corrections predict $1 - \lambda - 2\nu$ to be slightly *positive*.

5.2.1 Violation of the Lam-Tung Relation

In the 1980's two experiments measuring the properties of the Drell-Yan muon pairs produced in π - N scattering found experimentally that the Lam-Tung relation does not hold for the complete phase space. These two experiments were:

NA10 The NA10 experiment was located in the CERN North Area and used a pion beam with momenta of 140 GeV, 194 GeV, and 286 GeV on tungsten and deuterium targets [A⁺84].

E615 The experiment E615 at Fermilab used a 252 GeV pion beam on a tungsten target [B⁺86].

Both experiments were forward spectrometers with a target located in front of a beam dump. After the beam dump, a massive hadron absorber suppressed most of the hadronic activity, and only the produced muons were measured. The geometrical acceptance of both experiments covered mostly the forward hemisphere with $0 < x_F < 1$.

As an example of the results of these two experiments, Fig. 5.4 shows the parameters of the angular distribution (Eq. 5.8) measured by NA10 as a function of the transverse momentum $p_{T\gamma^*}$ of the lepton pair. At high $p_{T\gamma^*}$, the Lam-Tung relation is clearly violated, which can be seen most strikingly in the data from the 194 GeV pion beam. E615 saw a similar effect of about the same magnitude. Both experiments see a deviation from the Lam-Tung relation which has the opposite sign compared to predictions of higher-order QCD calculations.

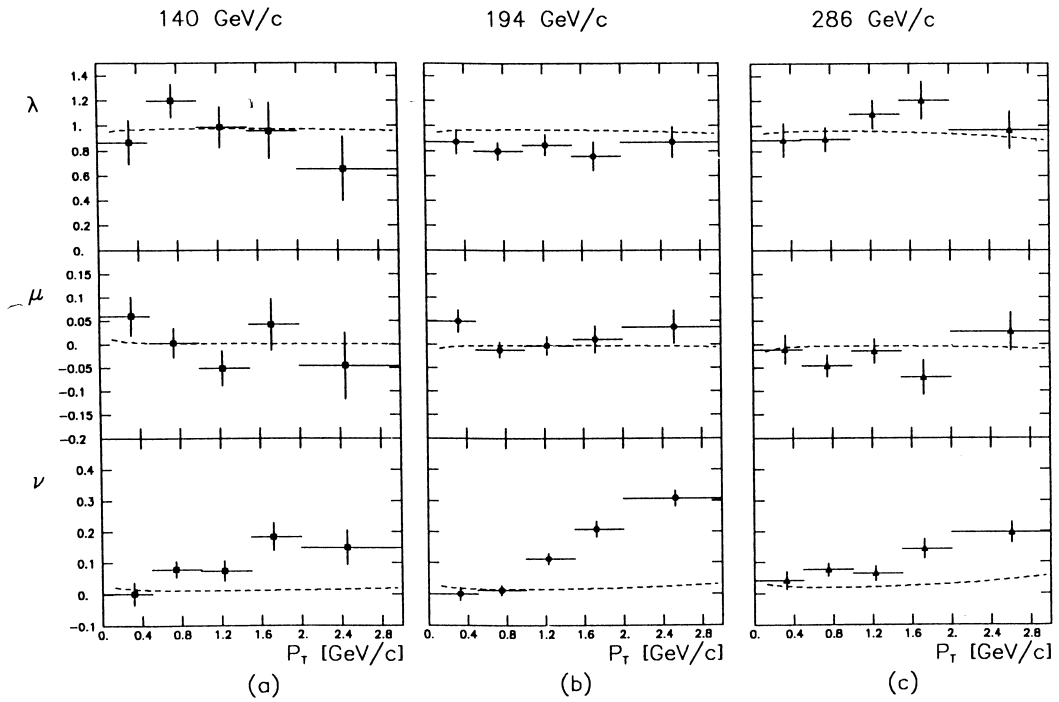


Figure 5.4: NA10 results on the coefficients λ , μ , and ν as functions of the virtual photon's transverse momentum in π - N scattering for three different pion momenta (from [G⁺88]). The dashed lines show the prediction of a next-to-leading order QCD calculation. The measured values of ν deviate clearly from the prediction at larger $p_{T\gamma^*}$.

5.2.2 Theoretical Models

After the discovery that the Lam-Tung relation is violated, several theoretical models were applied to the Drell-Yan process or newly developed to explain the origin of the violation. Some of these models and their predictions are presented shortly in the following.

Higher Twist Contributions

Higher-twist contributions [BB79, Ber80] to the cross section can be visualised as additional interactions with the spectator quarks of the hard scattering process (one such process is depicted

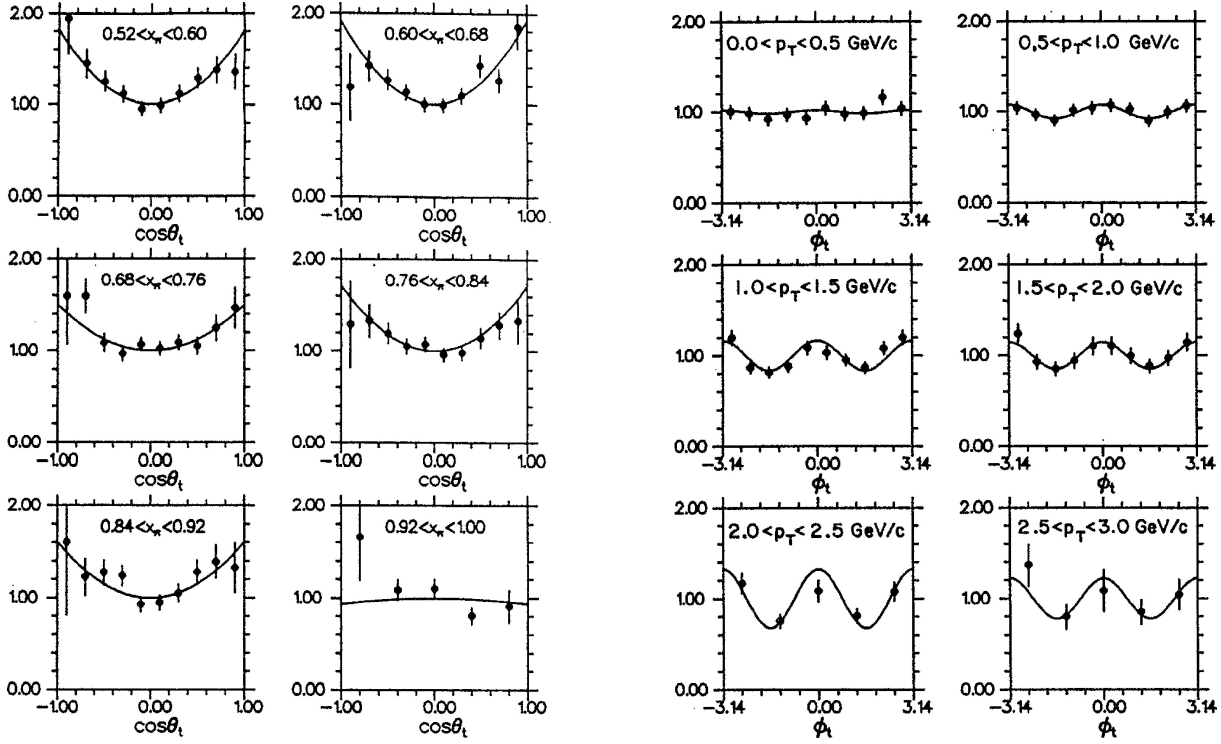


Figure 5.5: Angular distributions of the Drell-Yan muon pairs in the mass range $4.05 < M_{\gamma^*} < 8.55$ GeV, measured in the scattering of a 252 GeV π^- beam off a tungsten target by the E615 collaboration [C⁺89]. The angles are defined in the Gottfried-Jackson frame (see App. D). *Left:* $\cos \theta_{GJ}$ in bins of the momentum fraction x_π . At very high x_π , the virtual photon acquires a longitudinal polarisation, resulting in a drastic change of the shape of the $\cos \theta$ distribution. *Right:* ϕ_{GJ} for different transverse momenta $p_{T\gamma^*}$ of the muon pair, integrated over $|\cos \theta_{GJ}| < 0.6$. The modulation with $\cos 2\phi_{GJ}$ is clearly visible at higher $p_{T\gamma^*}$. The lines are the result of a fit to the $\cos \theta$ - ϕ -plane.

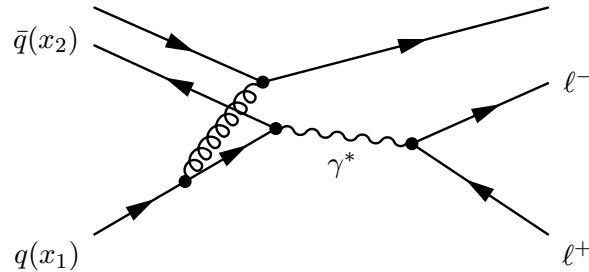


Figure 5.6: One of the higher-twist graphs contributing to Drell-Yan production in π - N scattering.

in Fig. 5.6). These sub-processes probe the short distance dynamics of the hadronic wave function.

The ideas of this model are extended and applied to the Drell-Yan production in [BBKM94]. The angular dependence is parametrised in exactly the same way as in Eq. 5.8, but the parameters λ , μ , and ν are expressed as explicit functions of the kinematical variables $x_L \equiv 2p_T/\sqrt{s}$, p_T^2/M^2 , and M^2/s . In this model, the leading contribution to μ is of the order $\sqrt{p_T^2/M^2}$, and ν is of the order p_T^2/M^2 . The model predicts a suppression of the terms violating azimuthal symmetry with increasing M^2 .

The resulting predictions for the parameters assuming a special parton distribution function of the pion as well as the Lam-Tung violation are plotted in Fig. 5.7, where they are compared to data from E615. The predictions are highly sensitive to the actual parton density function used to describe the pion (different lines in Fig. 5.7). The model is able to reproduce the data fairly well at low p_T , but fails especially to describe the large value of ν at larger p_T . The experimentally found, large values for ν are in contradiction to the predicted suppression with p_T^2/M^2 of the coefficient of the $\cos 2\phi$ -term. It should be much smaller than the $\cos \phi$ -term, which only is suppressed with p_T/M .

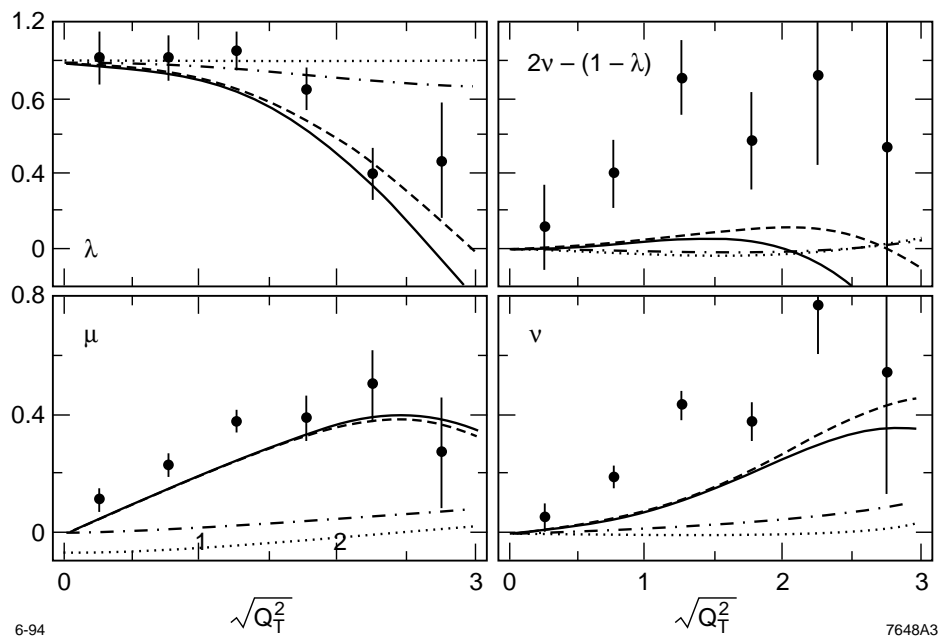


Figure 5.7: Fit of a higher-twist model to the measured angular distributions of E615. From [BBKM94], experimental data from E615 [C⁺89]. The lines correspond to different assumptions about the pion wave function.

No model calculations have so far been done for proton-nucleon scattering.

Colour Domains and Break-Down of Factorisation

A different explanation of the observed violation of the Lam-Tung relation is based on the idea that the QCD vacuum most likely has a non-trivial structure. Interactions between the incoming partons and the vacuum can then lead to spin and momentum correlations between the partons, violating one of the fundamental assumptions of the factorisation hypothesis. One possibility for such a non-trivial vacuum structure are Colour Domains [NR84]. In this model, the vacuum is full of fluctuating chromoelectric and chromomagnetic fields, which are spontaneously generated,

and which, in analogy to ferro-magnetism, are constant within randomly oriented domains of size $\sim 1/\Lambda_{QCD}$. These domains are large enough that they can be considered a constant background field for hard scattering processes. Analogous to the build-up of a transverse polarisation in e^- storage rings due to synchrotron radiation, quarks sailing through such a colour domain also can become polarised.

A phenomenological model applying these ideas to the Drell-Yan process was proposed in [BNM93]. The initial state partons in a Drell-Yan process acquire a transverse polarisation due to the chromomagnetic force as they travel through the constant background field. To be able to annihilate into a virtual photon, the colliding quark and anti-quark must carry colour i and the corresponding anti-colour \bar{i} ; therefore they are deflected in the chromomagnetic field in the same direction, introducing a spin and transverse momentum correlation. This correlation contradicts one of the main prerequisites for the factorisation ansatz to calculate the Drell-Yan cross section in perturbative QCD.

The model of [BNM93] introduces a correlation parameter κ ($\kappa = 0$: no correlation, $\kappa = 1$: full correlation) which is taken to depend on the transverse momentum $p_{T\gamma^*}$,

$$\kappa = \kappa_0 \frac{p_{T\gamma^*}^4}{p_{T\gamma^*}^4 + m_T^4}, \quad (5.10)$$

with κ_0 and m_T free parameters of the model. Including this correlation in the calculation of the angular distribution modifies the Lam-Tung relation to read

$$1 - \lambda - 2\nu \approx -4\kappa, \quad (5.11)$$

and the predicted deviation from the Lam-Tung relation is *negative*. The values for λ and μ are essentially unchanged compared to the perturbative QCD calculation. Fig. 5.8 shows a fit of the model to the data measured by NA10.

In contrast to higher-twist contributions, the effects of the spin correlation need not vanish in the high-energy limit.

5.2.3 Concluding Remarks

The Drell-Yan process has been known and observed for many years; it was one of the main processes to determine the quark structure function of the pion. However, perturbative QCD fails to describe some aspects of Drell-Yan production. The prediction of perturbative QCD concerning the angular distribution of the lepton pairs fails to describe the experimentally found data at high transverse momenta. Several models were applied to this phenomenon; most of them try to include some non-perturbative aspects to explain the observed deviation. The existing data (mostly from πN scattering) is not sufficient to distinguish between different models.

The break-down of the Lam-Tung relation, which was established in πN scattering, has not yet been measured in pN reactions. At least one model (of [BNM93]) links the deviation of the angular dependence from perturbative QCD predictions to the existence of a non-trivial vacuum structure, which in turn leads to a break-down of factorisation. There is considerable theoretical and experimental interest in such a measurement.

5.3 DY as Surrogate for Prompt Photon Production

Another very interesting physics topic which can be pursued with the high-mass lepton pairs generated in the Drell-Yan process is the measurement of the gluon density in the proton. This was proposed by Berger et al. in 1998 [BGK98]. The QCD compton like graphs (see Fig. 5.3

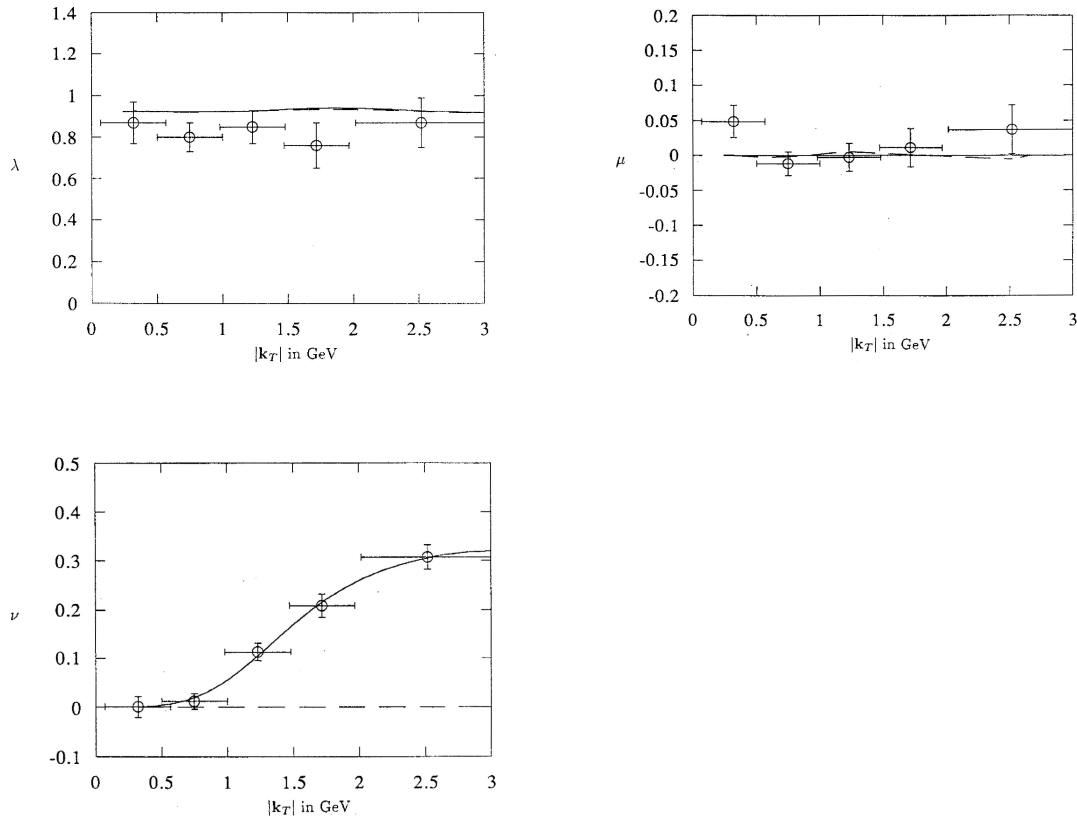


Figure 5.8: $p_{T\gamma^*}$ dependence of the parameters λ , μ , and ν as measured by NA10 [G⁺88] and a fit of the model proposed in [BNM93] to the data (*solid lines*). The *dashed lines* show the prediction of the parton model (Figures from [BNM93]).

(c)) dominate the Drell-Yan cross section as soon as the transverse momentum $p_{T\gamma^*}$ of the virtual photon is about as large as its mass M ; typically, the region with $p_{T\gamma^*} > M_{\gamma^*}/2$ is taken. A calculation of the cross section ratios of the two contributions from $q\bar{q}$ annihilation and qg scattering for the region of phase space kinematically accessible by HERA-*B* is shown in the left plot of Fig. 5.9 ([Kla01]). It averages over all masses M_{γ^*} in the range $4 < M_{\gamma^*} < 9$ GeV and over the accessible range in x_F .

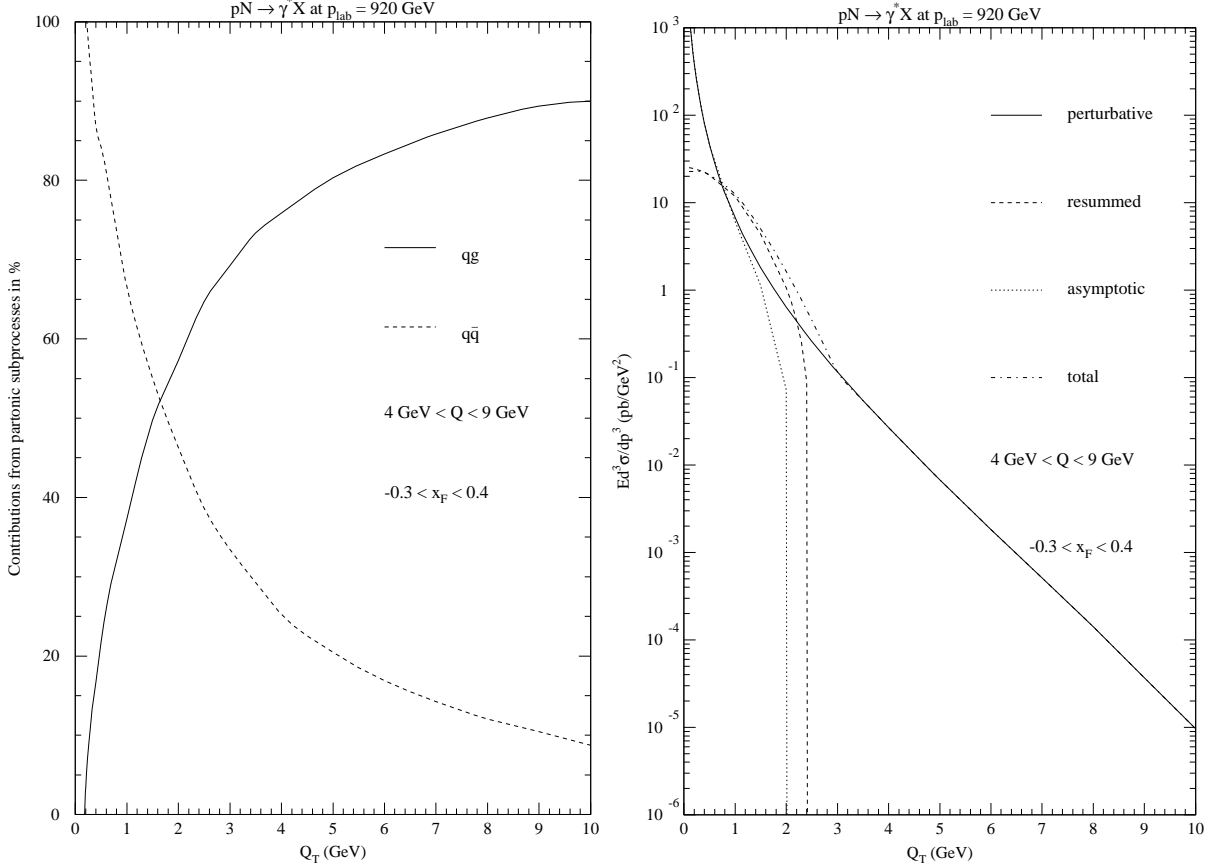


Figure 5.9: *Left:* Relative contributions of the processes $q\bar{q} \rightarrow \gamma^* \rightarrow \ell^+\ell^-$ and $qg \rightarrow q\gamma^* \rightarrow q\ell^+\ell^-$. *Right:* Invariant inclusive cross section $Ed^3\sigma/dp^3$ as a function of the lepton pair transverse momentum Q_T . Both plots are calculated for the mass region $4 < M_{\gamma^*} < 9$ GeV and a beam energy of 920 GeV, where HERA-*B* could contribute ([Kla01]).

The process is quite similar to the prompt photon production which has been extensively used to measure the gluon content of the proton. However, using the Drell-Yan mechanism with its virtual photon has some theoretical and practical advantages over the prompt photon measurements. To measure the prompt photon cross section, typically an isolation criterion is needed to distinguish between prompt photons and *e.g.* decaying π^0 . These isolation cuts not only lower the background, but also the signal; photons which are emitted collinear to the outgoing quark cannot be found. Additionally, theoretical predictions have to take the isolation criteria into account to produce an *isolated* cross section. These complications are absent if the emitted photon is virtual, *i.e.* in Drell-Yan production.

Like in prompt photon production, measuring the gluon density in the proton with Drell-Yan pairs is sensitive to momentum fractions of the gluon of $x_g \approx 2p_{T\gamma^*}/\sqrt{s}$. For HERA-*B*, this means that the range up to $x_g \approx 0.3$ is accessible, if enough statistics can be collected

at $p_{T\gamma^*} \approx 6$ GeV. The sensitivity of the process to the gluon density is shown in Fig. 5.3, where various models for the proton structure, differing mostly in their description of the gluon content, are used to calculate the cross section [Kla01]. Some of the parametrisations used for this calculation are shown in the right plot of Fig. 5.3. Due to the relatively low \sqrt{s} compared to hadron-hadron colliders, a much wider range in x_g is open to HERA-*B*, resulting in a large sensitivity to the gluon density in a region where it is up to now only poorly constrained.

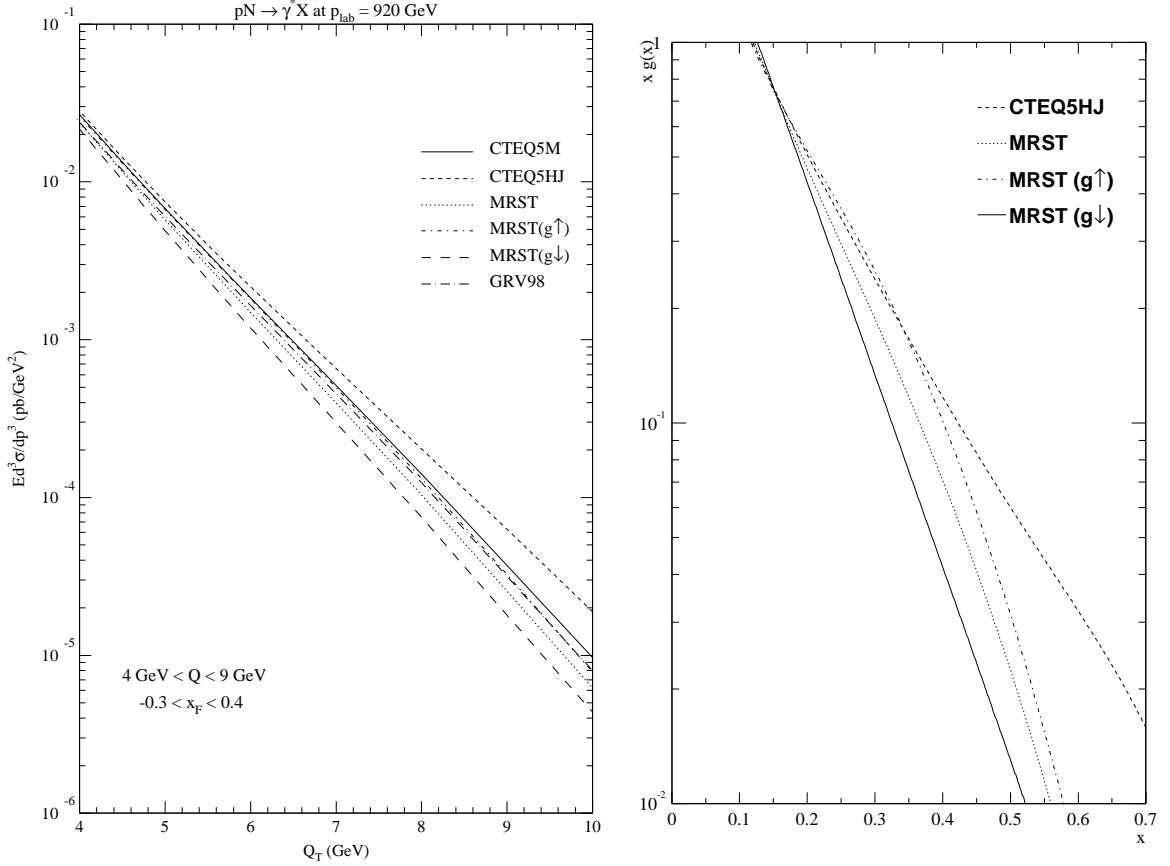


Figure 5.10: *Left:* Drell-Yan cross section in next-to-leading order QCD, computed for the kinematical range accessible at HERA-*B* [Kla01]. The different lines show the result of calculations using different parton density functions for the proton, which differ mainly in their description of the gluon content at relatively large x_g . As can be seen from the different curves, HERA-*B* is very sensitive to the gluon structure function. *Right:* Parametrisation of the gluon density $g(x)$ by some of the structure function sets used in the cross section plot ([PB95], used scale $Q = 6.5$ GeV).

The cross section falls off very steeply with increasing $p_{T\gamma^*}$ (see Fig. 5.9, right plot); only about 1% of the high-mass Drell-Yan events have a $p_{T\gamma^*} > 3$ GeV. At least for the high mass region of Drell-Yan production it will probably be quite difficult for HERA-*B* to make a precision measurement in 2002. At lower masses, the cross section is much higher, but (as will be explained in more detail in the next chapter) the expected background is also huge. Therefore, this topic was not pursued further for this thesis. It should, however, be kept in mind for re-evaluation if the detector and trigger performance in 2002 turn out to be significantly better than the minimal expectation, especially since the sensitivity to the gluon density is rather large.

Chapter 6

Prospects of doing Drell-Yan Physics at HERA-*B*

The physics potential and prospects of HERA-*B* in the field of Drell-Yan physics were evaluated for the proposal of a revised physics programme for HERA-*B*. Only the muon channel was considered, because it is expected to be experimentally cleaner than the electron channel (to obtain a good mass resolution for electrons with the ECAL, bremsstrahlung has to be taken into account. Requiring two bremsstrahlung clusters drastically reduces the event rate). However, HERA-*B* offers the unique possibility to study both electron- and muon-pair production at the same time.

6.1 Geometrical Acceptance

In order to produce a measurement of cross-sections or angular distributions which can be compared with results of other experiments, effects of the detector geometry and setup which influence for example angular distributions must be corrected for. It is also necessary to check that the angular acceptance is sufficient for a significant measurement of angular distributions.

Usually, the geometrical acceptance is determined by a Monte-Carlo study in which the events which could be accepted by the detector are compared to all generated events. For a study of the acceptance of HERA-*B* for Drell-Yan muon pairs, 20 000 Drell-Yan events were generated with the usual HERA-*B* Monte-Carlo chain, including the full detector simulation and reconstruction.¹

The definition of geometrical acceptance is to a certain extent arbitrary; for the study presented here the definition of acceptance was inspired by the trigger and reconstruction system of HERA-*B*. Therefore, a track is considered to be in the geometrical acceptance of the detector if it passes through enough layers of the Muon System to produce a pretrigger signal. To allow the First Level Trigger and the subsequent reconstruction software to follow the track and to reconstruct the track parameters reliably, an accepted track has to pass through a minimum number of tracking stations. Finally, the production vertex has to be reconstructed, so the track should also be measured by the Vertex Detector System. These requirements are checked with the so-called Monte-Carlo Impact Points (MIMPs), which are computed during the detector simulation of a generated event. They are simply the entry and exit points of a track passing

¹HERA-*B* uses a combination of two Monte-Carlo generators to simulate events: PYTHIA [Sjö94] is used for any hard scattering process, including the production of heavy quarks; the underlying event and inelastic interactions are simulated using FRITIOF [Pi92]. The implementation is described in a HERA-*B* note [IKL99].

the sensitive volume of a detector component. The requirements used for this study are:

1. The track is able to generate a pretrigger signal in the muon system: it produces at least one MIMP each in the third and fourth super-layer of the Muon Pad Chambers or the Muon Pixel System.
2. The Main Tracker is able to follow the track seed generated by the pretrigger towards the target: the track passes through the sensitive volume of the first super-layer of the Muon System, and it produces at least 15 MIMPs in at least 3 different super-layers of the Main Tracker (the combination of Outer and Inner Tracker). This condition also takes care of those tracks which leave the Inner Tracker at some point, but are subsequently measured in the Outer Tracker.
3. To obtain a good measurement of the di-lepton vertex, each track of the lepton pair should be measured by the Vertex Detector System, passing at least 3 super-layers and producing at least 5 MIMPs.

The geometry description used for this study² is valid for the detector configuration which is expected to be used in the HERA-B run 2001/2002: the acceptance of the Vertex Detector System extends down to 10 mrad, and both Inner and Outer Tracker are fully installed and equipped.

The Drell-Yan cross section is a steeply falling function of the invariant mass M_{γ^*} of the lepton pair. For an analysis of Drell-Yan pairs, events in the mass regions of the charmonium (J/ψ , ψ' , ...; $2.9 \leq M_{\gamma^*} \leq 4$ GeV) and bottomium (Υ -family; $8.5 \leq M_{\gamma^*} \leq 11$ GeV) have to be discarded to exclude the decay products of the quarkonia. Although in the small mass region ($M_{\gamma^*} < 2.9$ GeV) there are many Drell-Yan events expected, it is not clear if these events can be fully disentangled from the background. At higher masses and higher transverse momenta, the background is expected to be much smaller (see Sect. 6.2 for a discussion of the various contributions to the background). Therefore, the study of the geometrical acceptance was limited to the high-mass region $4 \leq M_{\gamma^*} \leq 8.5$ GeV.

The distributions of the most important kinematic variables for all generated and the accepted events are shown in Fig. 6.1. The resulting acceptance functions are shown in Fig. 6.2. Also shown in these figures is the contribution of the inner detectors to the geometrical acceptance. For this, a track is flagged to be measured mainly in the Inner Tracker if it has more than 16 MIMPs in the Inner Tracker which are distributed over more than 3 superlayers.

The following features of the geometrical acceptance can be seen:

- The acceptance increases with increasing invariant mass M_{γ^*} and transverse momentum $p_{T\gamma^*}$ of the virtual photon. For large M_{γ^*} and $p_{T\gamma^*}$, the opening angle of the two leptons in the laboratory is larger, decreasing the probability that one of the muons escapes through the beam pipe.
- The HERA-B spectrometer covers the central region of production in the overall proton-nucleon centre-of-mass system. This can be seen from the acceptance as function of x_F and y^* , the rapidity of the virtual photon in the hadronic centre-of-mass system. The range $-0.4 < x_F < 0.2$ is covered by HERA-B with an acceptance larger than 0.1; with very low acceptance, this range extends even further to about -0.5 and 0.3 . For events where the γ^* is produced in the forward hemisphere, *i.e.* at $x_F > 0$ (and $y^* > 0$), at least one of the tracks of the lepton pair is very close to the beam pipe and can only be measured by the inner detectors, the Muon Pixel System and the Inner Tracker.

²Version 0.0902

- The angular acceptance extends to large values of $|\cos \theta_{CS}|$, where values up to $|\cos \theta_{CS}| \approx 0.7$ can be measured with reasonable acceptance. Again, at large $|\cos \theta_{CS}|$, the inner detectors play an important role. As a function of the azimuthal angle ϕ_{CS} , the acceptance is more or less flat.

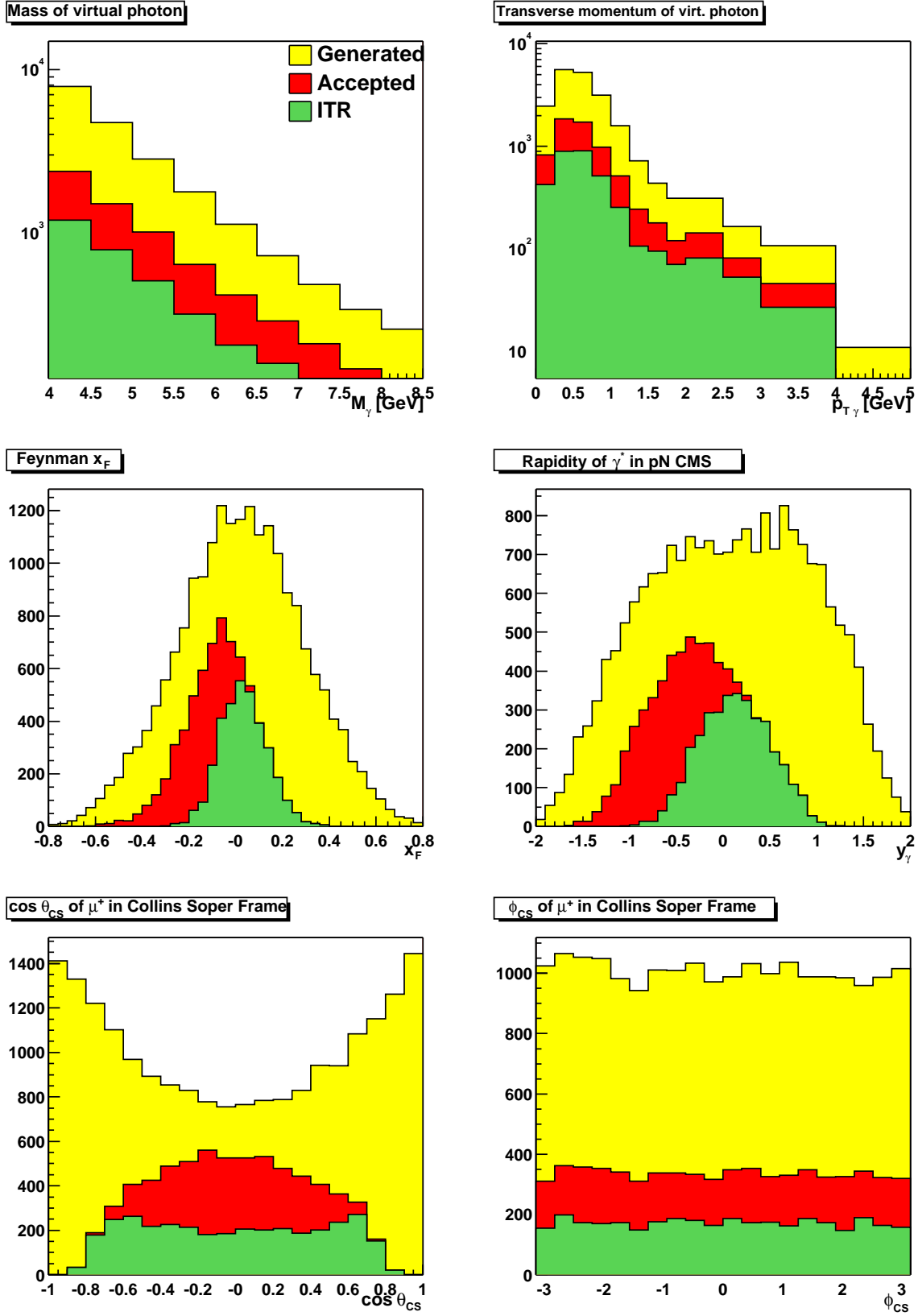


Figure 6.1: Generated and accepted events. The lowest histogram in each plot shows those events in which the Inner Tracker contributed significantly to the measurement of at least one track; for these tracks, more than 16 Inner Tracker MIMPs in more than three superlayers were required.

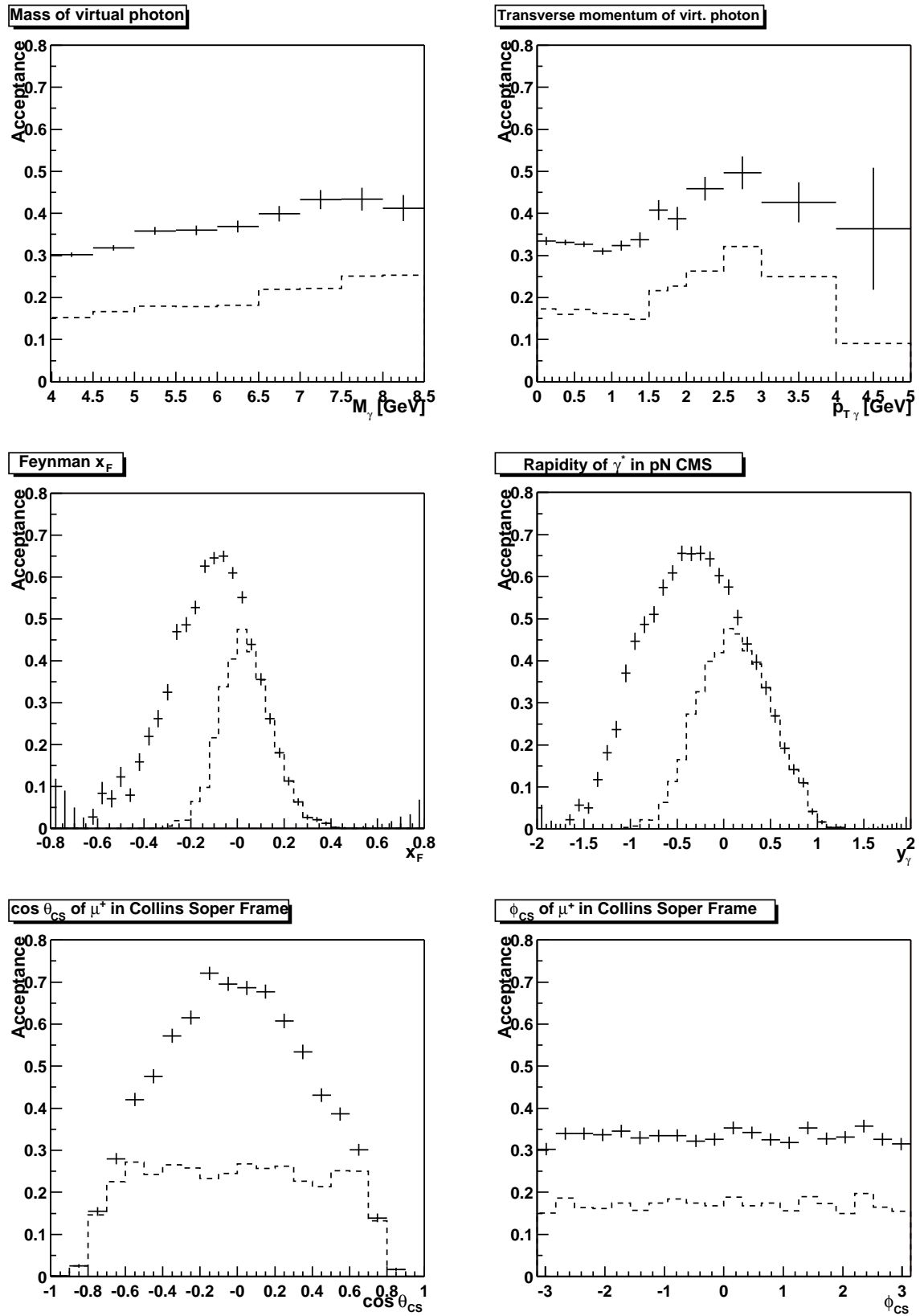


Figure 6.2: Geometrical acceptance for Drell-Yan pairs with invariant masses $M_\gamma^* \geq 4$ GeV. The dashed histogram shows the fraction of events in which at least one of the muon tracks was mainly reconstructed with the Inner Tracker, as defined in the text.

6.1.1 Detector Resolution and Acceptance Correction

Using the full detector simulation and reconstruction, the resolution of the angular variables $\cos\theta_{CS}$ and ϕ_{CS} can be estimated. Fig. 6.3 shows the correlation between the generated and reconstructed quantities for simulated events which pass the analysis chain described in Sect. 6.3. The resolutions obtained from this study are obtained from fits of Gaussians to the residual histograms; the fit results are

$$\sigma_{\cos\theta_{CS}} = (8 \pm 0.2) \times 10^{-4} \quad (6.1)$$

$$\sigma_{\phi_{CS}} = (14 \pm 1) \text{ mrad} \quad (6.2)$$

$$\sigma_M = (60 \pm 2) \text{ MeV} \quad (6.3)$$

The narrow peak in the $\Delta\phi_{CS}$ residual is sitting on a broader distribution with a width of about 70 mrad. Nevertheless, the resolution is good enough to allow a bin-wise acceptance correction, if one chooses the bin widths so that the contamination of events from the wrong bins is small enough. With $\pi/5$ wide bins, the migration from neighbouring bins in ϕ_{CS} is about 10 %. Alternatively, an unfolding method has to be used to correct for the finite detector resolution.

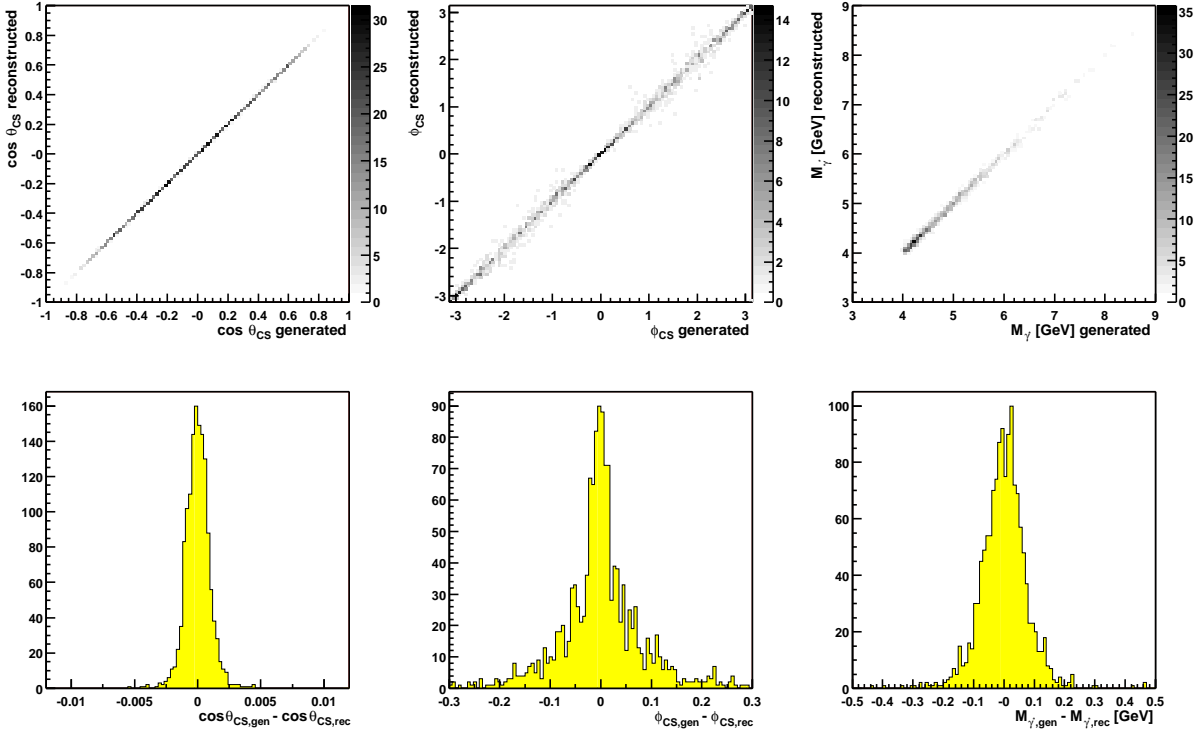


Figure 6.3: *Top:* Correlations between the generated and reconstructed kinematic variables $\cos\theta_{CS}$, ϕ_{CS} and M_{γ^*} for Drell-Yan events in the high-mass region. *Bottom:* Resulting residual distributions $X_{\text{gen}} - X_{\text{rec}}$ for the three kinematic variables. Only events which were selected by the same analysis routine presented in Sect. 6.3 are used for these plots.

6.2 Background

In the previous section it was shown that the acceptance of the HERA-B spectrometer for Drell-Yan pairs is excellent as a function of $p_{T\gamma^*}$ and the angles θ and ϕ . Compared to usual

fixed-target experiments, HERA-*B* covers a different region in x_F . There exists an overlap in the forward region where data from HERA-*B* can be compared to the results of other experiments like NuSEA, but the acceptance is largest for the region of central production.

6.2.1 Sources of Background

The experimental signature of Drell-Yan production is simple, but by no means unique: they contain a pair of oppositely charged muons with a high invariant mass and possibly a high transverse momentum, where both muon tracks originate in the primary vertex of the interaction. There is no constraint on the invariant mass of the muon pair which could be exploited.

Besides the Drell-Yan mechanism, there exist several other sources for muon pairs: pions and kaons, which are produced copiously in the proton-nucleon interaction, decay predominantly into muons; also D mesons (open charm production) or their decay products can decay into muons. Finally, hadronic punch through (hadrons which penetrate the absorber in front of the Muon System) can also produce tracks which are identified as muons by the reconstruction program. If two such tracks are found in one event, they can look like a Drell-Yan pair. The background from these sources therefore is called *irreducible*. It is thus important to obtain an estimate about the expected rate with which background events are produced; ideally some kinematic cuts can still be identified which cut into the background but leave the interesting signal basically intact. In the final analysis, the remaining irreducible background has to be subtracted statistically.

The three sources for background are discussed in more detail below. It should be noted that the background studies are not final. Most of the estimates presented here are based on simple Monte Carlo studies (and these with a rather low statistics) and estimates for the cross sections. The study concentrates on the high-mass Drell-Yan region with $4 \text{ GeV} < M_{\gamma^*} < 8.5 \text{ GeV}$.

The inelastic cross section for incident protons with a momentum of 920 GeV on a titanium target is about

$$\sigma_{\text{inel,Ti}} = 13 \text{ mb/nucleon} , \quad (6.4)$$

while the Drell-Yan cross section for the high-mass region is about

$$\sigma_{\text{DY}}(4 \text{ GeV} < M_{\gamma^*} < 8.5 \text{ GeV}) \approx 0.38 \text{ nb/nucleon} . \quad (6.5)$$

This last number is obtained from the Drell-Yan cross section published by E772 ([M⁺94], 800 GeV protons on a deuterium target). Since the Drell-Yan cross section exhibits scaling in the variable $\tau = M^2/s$, a mass range of $4 \text{ GeV} < M_{\gamma^*} < 8.5 \text{ GeV}$ at HERA-*B* with $\sqrt{s} = 41.6 \text{ GeV}$ corresponds to a mass range of $3.7 \text{ GeV} < M'_{\gamma^*} < 7.9 \text{ GeV}$ at E772 with $\sqrt{s} = 38.8 \text{ GeV}$. A smooth function is fitted to the measured cross section of E772, continued to the needed lower values of M_{γ^*} , and then integrated over the mass range indicated above (see [Hus01] for details).

The inelastic cross section is about 3.4×10^7 larger than the Drell-Yan cross section. For comparison, the cross-section to produce prompt J/ψ s in proton-nucleon collisions was measured by E789 at a beam energy of 800 GeV to be about [S⁺95]

$$\sigma_{J/\psi} = 420 \text{ nb/nucleon} . \quad (6.6)$$

To study the contribution of decay-in-flight muons and punch through, 100 000 minimum bias events (inelastic proton-nucleon interaction, no specific hard subprocess) were generated, simulated and fully reconstructed. Reconstructed tracks with more than 4 hits in the Muon System were flagged according to the generator particle which was found in front of the Muon Absorber and the generated decay chain leading to this particle. Depending on the decay chain, a track is assigned to one of the classes listed in Table 6.1. The reconstruction program extrapolates the reconstructed tracks found in the main tracker into the Muon System and computes a ‘muon likelihood probability’ for each track to which hits in the Muon System could be assigned [Fom00], making also use of the shape of the hit distribution around the track.

| Particle | Decay chain | Class |
|----------|-----------------------|--------|
| μ | μ | MUON |
| μ | $\pi \rightarrow \mu$ | PI |
| μ | $K \rightarrow \mu$ | K |
| μ | $h \rightarrow \mu$ | HADRON |
| hadron | | PUNCH |

Table 6.1: Track classes used for the background study. A muon which originates from the primary vertex is flagged as MUON, muons from the decay of a π , K , or other hadron are flagged according to their mother particle, and hadrons creating hits in the Muon System are classified as PUNCH.

Decay In Flight Muons. Since the HERA-B detector has its hadron absorber only right in front of the Muon System, the produced pions and kaons can decay in flight as they travel through the detector. Their dominant decay mode is into muons, $\pi^\pm \rightarrow \mu^\pm \nu$ with 99.99% resp. $K^\pm \rightarrow \mu^\pm \nu$ with 63.5% which will be identified by the Muon System. In the 10^5 events analysed, about 4700 events showed one muon from the decay of a hadron.

The resulting muon likelihoods l_{mmu} which are determined by the Muon System reconstruction software are shown in the left plot of Fig. 6.4. The particles arriving in the Muon System are true μ s, therefore the muon likelihood is not suited to identify decay in flight muons. However, the p_T spectrum of the muons (shown in Fig. 6.4, right plot) is rather soft. 14 % of all muons have a $p_T > 0.7$ GeV, and only 3 % pass a cut of $p_T > 1.0$ GeV. Therefore one expects only 1 in 2×10^6 inelastic interactions to have two muons with a transverse momentum higher than 1 GeV from the decay in flight of hadrons. However, this suppression must be scaled with the huge ratio of the inelastic and Drell-Yan cross sections of about 3×10^7 ; the expected background rate from decay-in-flight muons alone is therefore about 60 times the Drell-Yan production rate.

A different study [BS01] used the usual HERA-B Monte-Carlo chain, but forced subsequently two of the produced pions to decay into muons. They found that 2×10^{-6} of all inelastic interactions contain a muon pair from pion decays with a mass larger than 4 GeV; this again yields a background contribution of about 60 times the rate of Drell-Yan production.

Hadronic punch-through. If the momentum of a produced hadron is large enough, it has a chance to penetrate the hadron absorber in front of the Muon System and to be misidentified as a muon. There is a difference, however, between true muon tracks and hadronic punch through: a hadron passing through the absorber has a high probability to produce a shower of particles which are then measured by the Muon System. By requiring that the hits from a ‘good’ muon are isolated, punch-through can be suppressed to a great extent. The muon reconstruction program exploits this fact; tracks which have a large number of muon system hits in their vicinity are assigned a low likelihood to be a muon. This is illustrated in Fig. 6.5, where the muon likelihood is shown for the simulated punch through tracks. In the total simulated sample of 10^5 events, 822 punch through tracks were found. A very loose cut on the muon likelihood of $l_{mmu} > 0.1$ removes 70 % of them, and only about 6 % survive a cut of $l_{mmu} > 0.9$. As for the decay-in-flight muons, the p_T spectrum is very soft; only 1.6 % of the punch through tracks which pass the soft cut on the muon likelihood have a transverse momentum of $p_T > 1$ GeV.

Open Charm Production. At the centre-of-mass energies available at HERA-B, the production of open charm mesons (mesons which contain one c quark, mainly D^0/\bar{D}^0 and D^+/D^-) has a cross section of about [BM⁺98]

$$\sigma_{\text{opencharm}} \approx 15 \mu\text{b/nucleon} . \quad (6.7)$$

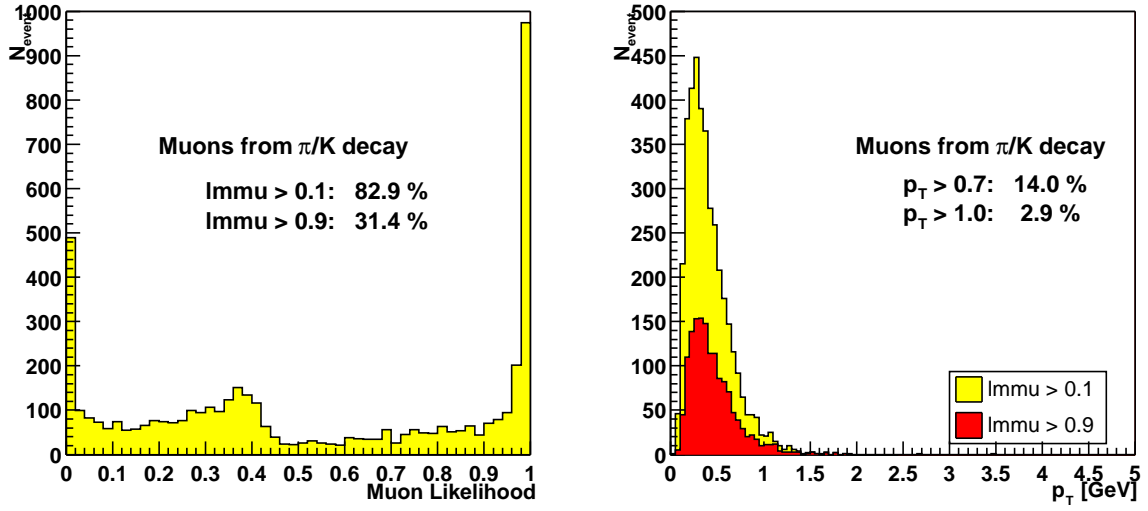


Figure 6.4: Muons from decaying π and K (simulation): *Left:* Muon likelihood l_{mmu} as determined by the reconstruction software using information of the Tracking and Muon Systems. Since the particle arriving in the Muon System is really a μ , a cut on l_{mmu} does not help to distinguish between decay-in-flight muons and Drell-Yan muons. *Right:* p_T spectrum of muons with a muon likelihood $l_{\text{mmu}} > 0.1$. The p_T spectrum is rather soft; only ≈ 3 % of all tracks survive a cut of $p_T > 1$ GeV. Also indicated is the p_T spectrum for tracks with $l_{\text{mmu}} > 0.9$ (dark shaded histogram).

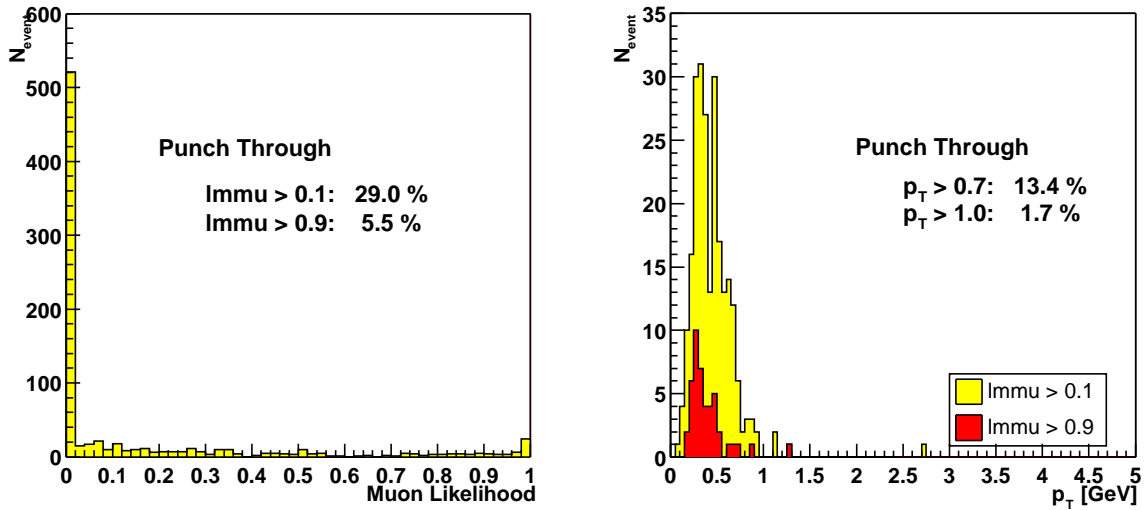


Figure 6.5: Simulation of punch through tracks: *Left:* Muon likelihood as determined by the reconstruction software. Most of the hadrons, about 70 %, are already rejected by a very loose cut on the muon likelihood $l_{\text{mmu}} > 0.1$. *Right:* p_T spectrum of punch through tracks with a muon likelihood $l_{\text{mmu}} > 0.1$. Also shown is the p_T spectrum for tracks with $l_{\text{mmu}} > 0.9$ (dark shaded histogram).

Both produced D mesons can decay semi-leptonically (the fraction of events with one muon in the final state is about 15 %), yielding a pair of oppositely charged muons. However, the p_T spectrum is again rather soft, so that only ≈ 3 % of the muons surpass a threshold of 1 GeV [HER00a]. The probability that the two charmed mesons decay each into high- p_T muons is approximately $(0.15 * 0.03)^2 = 2 \times 10^{-5}$. Scaled with the ratio of the cross sections for open charm and Drell-Yan production, the rate for this background contribution is about the same as the Drell-Yan production rate. However, this estimate does not take into account that the invariant mass spectrum falls off very steeply (see for example [BM⁺98, Fig. 12]), so that most of the di-muon pairs from open charm decay are well below the high-mass region of Drell-Yan production considered here.

6.2.2 Reducing the Background

From the background estimates described above it becomes clear that random background from sources like decay in flight and open charm is a major problem for studies of the Drell-Yan process at HERA-B. Other means to reduce the background without removing too many of the interesting physics events have to be devised.

One possibility to reduce the background is to increase the p_T cut. Since the p_T spectra of the muons which contribute to the background fall off more steeply than those of ‘signal’ muons from either $J/\psi \rightarrow \mu\mu$ decay or Drell-Yan production, this will improve the signal-to-background ratio. This however is also bought with a loss of signal events if the hard p_T cut is applied already by the trigger algorithms. The p_T distributions of the muons of simulated Drell-Yan events in the high mass region and $J/\psi \rightarrow \mu\mu$ decays from promptly produced J/ψ s are shown in Fig. 6.6. Of interest are only those events which fall into the geometrical acceptance of the spectrometer (lower two histograms in Fig. 6.6). For these events, a p_T -cut of 1 GeV removes almost no Drell-Yan events and only 26 % of the prompt J/ψ events. At $p_T > 1.2$ GeV, about 1 % of the Drell-Yan events and 40 % of the J/ψ s are removed. During the 2000 run, the detector triggered on muon tracks with a $p_T > 0.7$ GeV. The trigger scenario proposed for the 2002 run assumes a threshold of $p_T > 1$ GeV, and even higher cuts are being considered [HER01].

Another possibility to fight the background on an event-by-event basis is to try and localise the decay vertex on a track. Since the masses of π and μ differ (but only by about 30 MeV), the muon from the $\pi \rightarrow \mu\nu$ decay has a slightly different momentum compared to the pion. By piecewise re-fitting the track, a sudden increase in the χ^2 could indicate the occurrence of a decay in flight. An early study to find such kinks from decays in flight was performed in 1996 by M. Titov [Tit96], using however very optimistic assumptions on the resolutions of the tracking detectors. The method developed in this study allowed to suppress pion decays by only about a factor of 2–3, due to the low momentum kick, but $K \rightarrow \mu\nu$ decays (which have decay momenta of about 230 MeV) by about a factor of 10. A similar study needs to be redone using the knowledge gained about the actual detector resolutions and the dead material which contributes to multiple scattering.

Finally, the estimates given above are only based on statistical arguments about the probabilities of decays. The number of generated events in which two pions decayed simultaneously was too small to study for example the mass spectrum of the resulting Drell-Yan like muon pairs. Similarly, the constraint that the two muons have to form a common vertex which coincides with the primary production vertex could not be exploited.

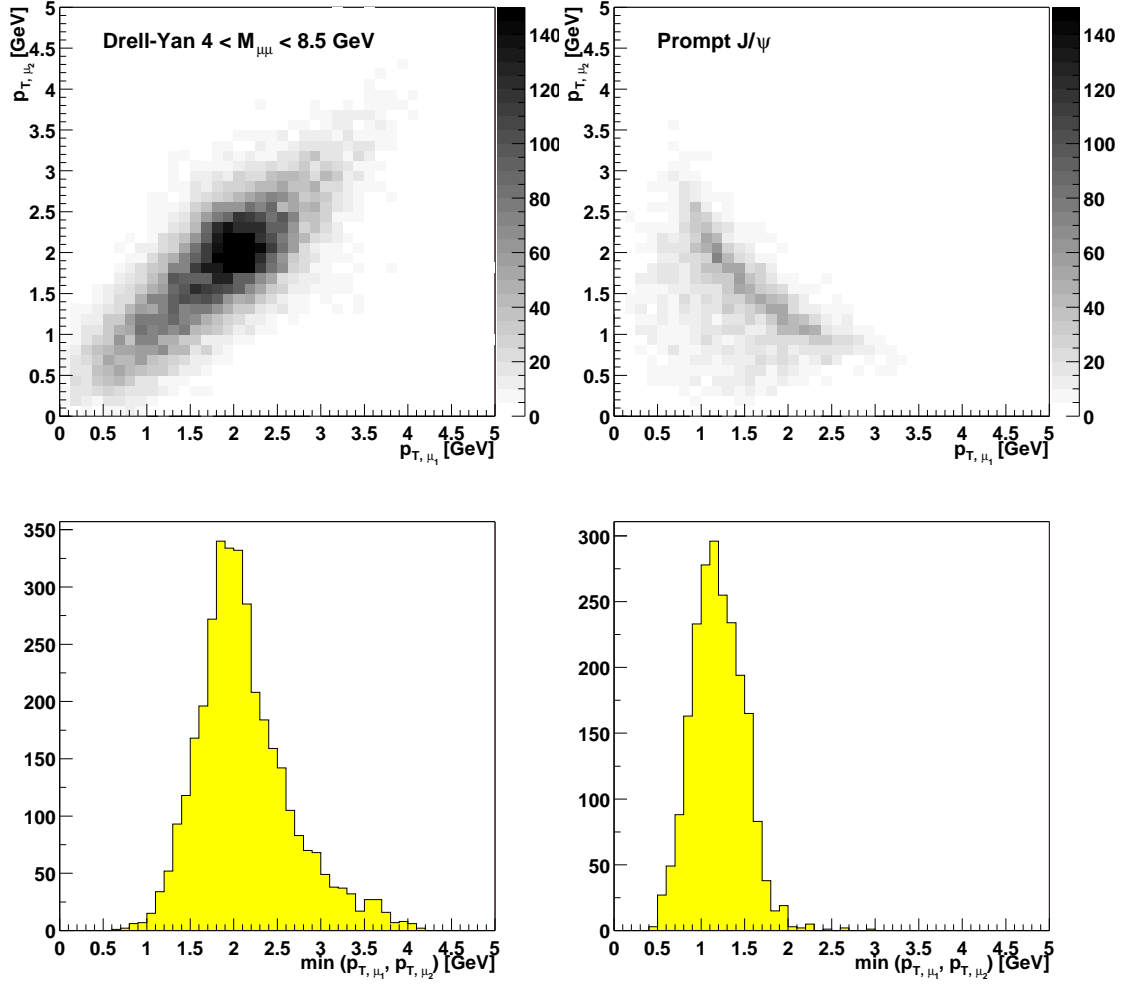


Figure 6.6: *Top row:* Distribution of transverse momentum of both muons for simulated Drell-Yan events in the high mass region (*left*) and for simulated J/ψ events (*right*; both plots use the same gray scale). All generated events are shown. *Bottom row:* Distributions of the minimal p_T of the two muons for simulated events which fall into the acceptance of the spectrometer. *Left:* High-mass region 4–8.5 GeV of Drell-Yan production. *Right:* Prompt J/ψ production.

6.3 Expected Event Rate

To estimate the number of Drell-Yan events which could pass the complete trigger and reconstruction chain of HERA-B, data from the run period 2000 was used. The runs analysed were triggered with the First Level Trigger which counted coincidences of pretrigger signals in the Muon System, followed by the Second Level Trigger algorithm which had to find the corresponding tracks. The aim of this analysis is to obtain a sample of $J/\psi \rightarrow \mu\mu$ events which is as clean as possible. The mass constraint available for J/ψ decays helps to gain confidence that what remains after all analysis cuts is indeed the signal. With the same cuts the sideband of the di-muon mass spectrum is then analysed, in order to find an indication for the production of Drell-Yan muon pairs.

The detector and trigger system improvements which are being performed during HERA's luminosity upgrade in 2000/2001 all aim to improve the rate of triggered J/ψ events which are recorded on tape. The same improvement factors which are estimated for the J/ψ rate are taken to obtain the expected number of recorded Drell-Yan events during the run 2002.

6.3.1 J/ψ Search in 2000 Data

To extract the number of J/ψ and background events, the mass spectrum is fitted with the sum of a background function $b(M)$ and a gaussian $s(M)$ for the signal:

$$b(M) = \frac{1}{n_{\text{bins}}} \exp[p_0 + p_1 M] \quad (6.8)$$

$$s(M) = \frac{N_{J/\psi}}{n_{\text{bins}}} \frac{1}{\sqrt{2\pi}\sigma_{J/\psi}} \exp\left[-\frac{1}{2} \frac{(M - M_{J/\psi})^2}{\sigma_{J/\psi}^2}\right], \quad (6.9)$$

with n_{bins} the number of bins per GeV in the histogram used. The number B of background events below the J/ψ peak is then computed as the area below the background function in the mass region of the J/ψ :

$$B = \int_{2.9 \text{ GeV}}^{3.3 \text{ GeV}} b(M) dM. \quad (6.10)$$

To measure the improvements with each cut, the signal-to-background ratio S/B and the *significance* $\Sigma = S/\sqrt{B}$ are used.

Event Selection

The data used in the analysis presented here were taken in July and August 2000, using a di-muon pretrigger signal as the first requirement. With the development of better algorithms and the availability of more components of the First Level Trigger, the trigger conditions varied during this period. The pretrigger algorithm searched for coincident hits in the last two super-layers of the Muon System; these coincidences were then passed by the First Level Trigger network to the Second Level Trigger; in a subsample of the runs, one track found by the FLT was required. The Second Level Trigger algorithm then used only the pretrigger seeds as starting points for its track search.

The data were re-processed in early 2001 making use of a much improved detector alignment. The following cuts were applied to obtain a clean sample of di-muon events:

Preselection. The preselection requires that both reconstructed muon tracks can be matched with the trigger tracks found by the SLT algorithm. The SLT trigger tracks had to fulfil the following requirements ([Pet01], see also [Hus01]): The pretrigger seeds have to be separated

by a distance of more than 50 cm to suppress background from random coincidences in the pretrigger system. Starting from the pretrigger seeds, the SLT algorithm then looks for hits in the 0° layers of the first two super-layers of the Muon System. Next, tracks are searched in the Outer Tracker; a track is accepted if it matches the track segment found in the Muon System and if its transverse momentum is in the range of approximately $0.7 < p_T < 2.5$ GeV. Using a lookup table for the magnetic field, the tracks are then propagated through the spectrometer magnet. Finally, track segments in the Vertex Detector System are reconstructed and matched to the OTR tracks using the track position and slopes determined at the start of the track segments. A positive trigger decision is issued for events with two such tracks.

Track Quality. For the reconstruction of each track, at least 10 hits in the Vertex Detector System and 15 hits in the Main Tracker have to be used. Since the Inner Tracker was not participating in the trigger during the 2000 run, only a small fraction of the used tracks uses Inner Tracker hits. Finally, the refit of the track parameters has to yield a good track quality, which is measured in the fit $\chi^2/\text{d.o.f.}$ The distribution of $\chi^2/\text{d.o.f.}$ for all reconstructed tracks which enter this analysis is shown in Fig. 6.7 together with the cut used. A rather loose cut of $\chi^2/\text{d.o.f.} < 20$ is used to remove badly reconstructed tracks.

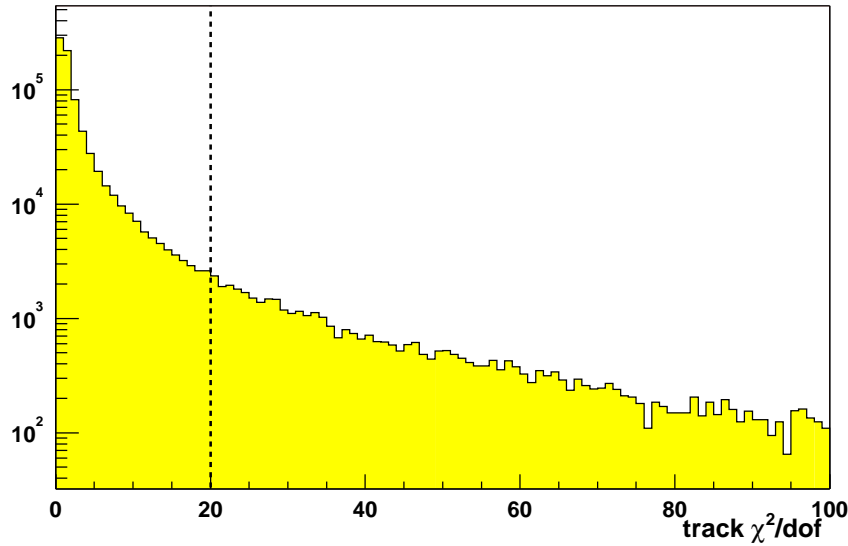


Figure 6.7: Distribution of the fit quality $\chi^2/\text{d.o.f.}$ of all muon candidate tracks in the event sample. The vertical dashed line indicates the cut used in the analysis to remove exceedingly bad tracks.

Kinematic Cuts. The following kinematic cuts were applied to the tracks:

- The sum $p_{z,1} + p_{z,1}$ of the longitudinal momenta of both muon candidates must not exceed the beam momentum of 920 GeV.
- The reconstructed momenta p_i are required to be greater than 5 GeV.
- The transverse momentum $p_{T,i}$ of each track is greater than 1.0 GeV.

The first cut rejects tracks where the reconstruction program combined wrong track segments into one track, resulting in a wrong determination of the track momentum. The other cut on

the track momentum is also a safeguard against wrongly reconstructed tracks: only tracks with $p \geq 5$ GeV have a chance to arrive at the muon system. The p_T cut was motivated by the background studies described in Sect. 6.2.

Vertex Cuts. Since Drell-Yan production takes place directly in the proton-nucleon collision, the muon pair should have its origin at the target wire. The reconstruction program combines as many tracks as possible into the primary production vertex. The di-lepton vertex was fitted separately. Only events in which the position of the primary vertex was consistent with one of the used target wires were regarded. The di-lepton vertex was required to be—within the fit errors—at the same position as the primary vertex.

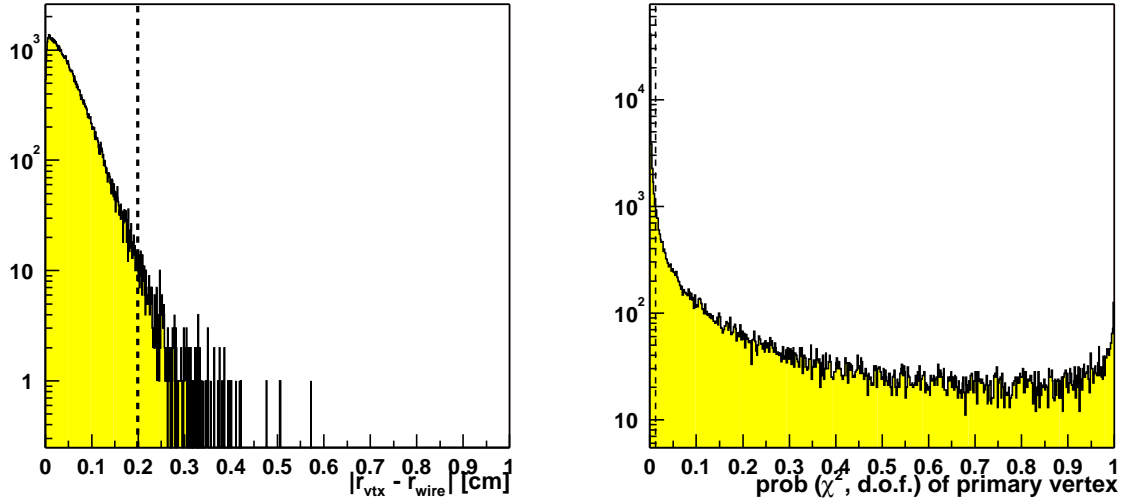


Figure 6.8: Vertex cuts applied to the analysed events. *Left:* The separation $r \equiv |r_{\text{vtx}} - r_{\text{wire}}|$ between the primary vertex and the nearest target wire is calculated as $r^2 = \Delta x^2 + \Delta z^2$ for vertical wires and $r^2 = \Delta y^2 + \Delta z^2$ for horizontal wires. *Right:* Distribution of the probability $\text{prob}(\chi^2, \text{d.o.f.})$ of the vertex fit. A cut of $\text{prob}(\chi^2, \text{d.o.f.}) > 0.005$ is applied to remove vertices for which the fit failed.

Particle Identification. To make sure that the considered tracks are muons with high probability, at least 5 hits in the Muon System have to be associated with each track. Additionally, the muon likelihood l_{mmu} as determined by the muon system has to be larger than 0.9. The efficiency of a cut on the muon likelihood on signal and background events is shown in Fig. 6.9. At a cut of $l_{\text{mmu}} > 0.9$, the background is suppressed by a factor of 2.1 relative to the signal, while still 66 % of all signal events survive.

Finally, the RICH particle identification is used to remove particles which are positively identified not to be muons. If the RICH reconstruction is able to match a track with a Cherenkov ring, it also assigns likelihoods to the track for the hypotheses that the particle was an electron, pion, muon, kaon or proton. Tracks which have a matching RICH ring and which have a likelihood larger than 0.1 to be a kaon or a proton are removed from the sample. The principle of particle identification with the RICH is illustrated in Fig. 6.10.

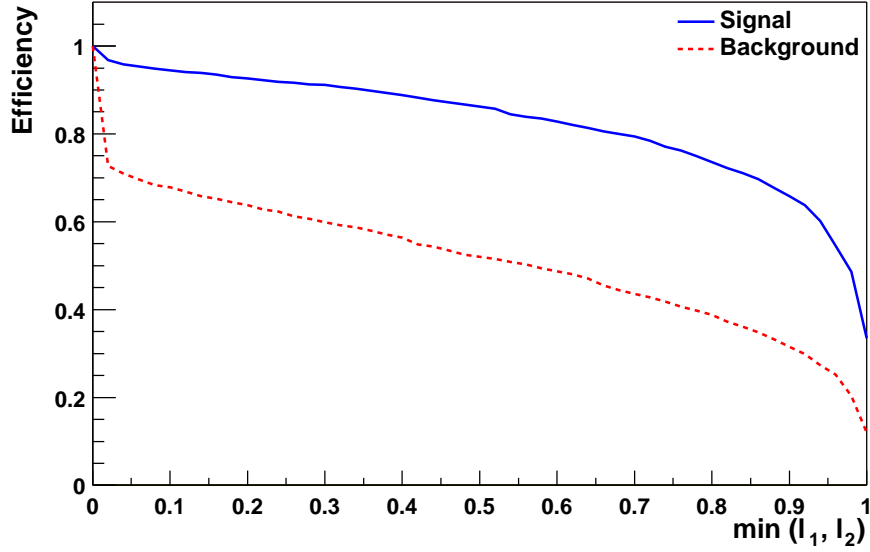


Figure 6.9: Effect of the cut on the Muon Likelihood as determined by the Muon reconstruction program on the signal and background events. For this plot, the cut on the muon likelihood was varied, while all other cuts described in the text were kept constant. The parameter $N_{J/\psi}$ of the fit of Eq. 6.9 was taken as the number of signal events, while the area below the J/ψ peak was used for the background.

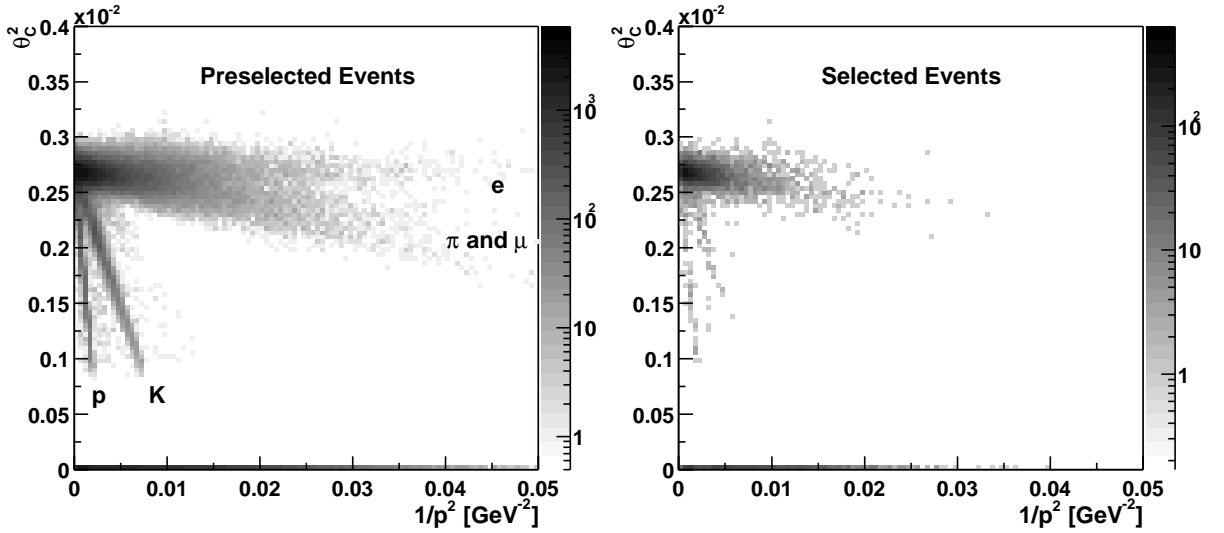


Figure 6.10: Particle ID with the RICH: Depending on their mass, the different particles populate bands in the θ_C^2 - $1/p^2$ plane. The proton and kaon bands are well separated, except at highest momenta. On the other hand, even at moderate momenta, a clear separation of π , μ , and e is difficult. In the analysis shown here, the RICH is used to remove clearly defined p and K (*right plot*). The horizontal bands at $\theta_C^2 = 0$ represent those events for which no RICH hypothesis was computed.

Discussion of the Cuts

The effect of all applied cuts on the number of J/ψ candidates and the background below the J/ψ peak is summarised in Table 6.2. The combined signal efficiency of the cuts is shown in Fig. 6.11, where also a comparison to a Monte-Carlo simulation is given. The combined effect of all cuts is to increase the signal-to-background ratio S/N from 1.1 (as found in the preselected data) to 8.5 and the significance from 67 to 81.

| # | Cut | $N_{J/\psi}$ | N_{bg} | S/B | Σ |
|---|--|-------------------|----------|-------|----------|
| 0 | Preselection | 4004 ± 88 | 3546 | 1.129 | 67.24 |
| 1 | Track Quality: $\chi^2/\text{d.o.f.} < 20.00$ | 2927 ± 69.73 | 1839 | 1.591 | 68.24 |
| 2 | $p_{z,1} + p_{z,2} < 920 \text{ GeV} \wedge p_i > 5.0 \text{ GeV}$ | 2927 ± 69.8 | 1835 | 1.595 | 68.32 |
| 3 | $p_{Ti} > 1.0 \text{ GeV}$ | 2679 ± 63.9 | 1226 | 2.186 | 76.54 |
| 4 | $ z_{\text{vtx}} - z_{\text{wire}} < 2.00 \text{ mm}$ | 2122 ± 53.4 | 672.2 | 3.157 | 81.86 |
| 5 | $\text{prob}(\chi^2, \text{dof}) > 0.005$ | 1280 ± 40.82 | 354.5 | 3.61 | 67.98 |
| 6 | Muon ID: > 5 hits per track | 1249 ± 40.32 | 315.4 | 3.959 | 70.32 |
| 7 | Muon ID: $l_{\text{mmu}} > 0.90$ | 841.7 ± 29.85 | 118.5 | 7.104 | 77.33 |
| 8 | RICH Particle ID | 766.9 ± 29.31 | 90.25 | 8.497 | 80.72 |

Table 6.2: Cuts applied to the di-muon sample and number of J/ψ candidates and background events surviving each cut. A detailed description of the cuts can be found in the text. Also indicated are the signal-to-background ratio S/B and the significance $\Sigma = S/\sqrt{B}$ obtained.

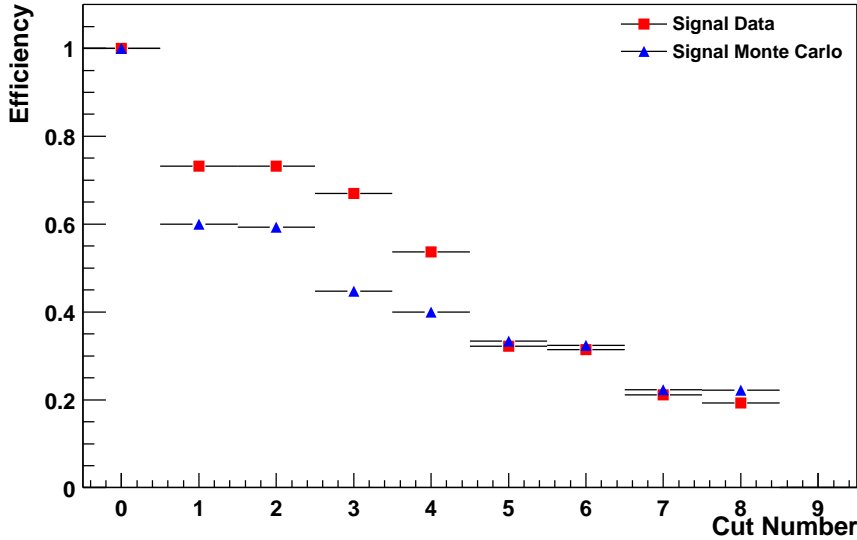


Figure 6.11: Signal efficiency of the different cuts. The plot shows the signal efficiency where all cuts up to and including the current one are applied. For the definition of the cuts see Table 6.2. *Squares:* Data. *Triangles:* Monte-Carlo simulation of prompt J/ψ production; one J/ψ was generated per event, no additional background events were added.

The total signal efficiency is rather low, about 20 %. The total efficiency for the simulated events agrees with this number fairly well, although at different cut levels there are large discrepancies. The Monte Carlo simulation did not generate background events, and the mean

multiplicity of charged tracks in di-muon events is higher in data than in the present Monte Carlo ([Mas01]); thus deviations are to be expected.

The two cuts which have the largest impact in reducing the number of J/ψ candidates found in the data are the track quality cut (#1) and the vertex probability cut (#5). Both cuts rely on a good estimation of the errors on the track parameters; if the errors are not calculated correctly, the χ^2 of the track fit is not a too reliable criterion. Similarly the vertex fit routine uses the track errors as input to compute the χ^2 -probability of the vertex fit. Also the cut on the Muon Likelihood l_{mmu} (#7) removes a large fraction of signal events. The MuonID program which computes l_{mmu} also uses the track errors while extrapolating a track into the Muon System. Therefore, a hard cut on l_{mmu} as used in this analysis implies also a hard cut on the track χ^2 .

It is hoped that with an improved understanding of the tracking routines, the error determination becomes more reliable and cuts on significances more meaningful. For a final analysis, the effect of the cuts has to be studied more systematically; the definition of the cuts will probably change.

Results

The final di-muon mass spectrum is shown in Fig. 6.12. It contains 767 ± 29 J/ψ candidates and 90 background events below the J/ψ peak. Also shown in the figure is the mass spectrum of an estimate for the combinatorial background. Under the assumptions that the probability to find a background muon of any sign is independent of its charge and independent of the charge of the other background muon, the number of background events below the signal spectrum is given by

$$N_{\text{bg}}^{+-} = 2\sqrt{N^{++}N^{--}} \quad (6.11)$$

where N^{++} and N^{--} are the number of $\mu^+\mu^+$ and $\mu^-\mu^-$ pairs [A⁺98].

From the fit to the signal spectrum, also the width $\sigma_{J/\psi}$ and the peak position $M_{J/\psi}$ can be extracted:

$$\sigma_{J/\psi} = (53 \pm 2) \text{ MeV} \quad (6.12)$$

$$M_{J/\psi} = (3083 \pm 2) \text{ MeV} . \quad (6.13)$$

The mass value is slightly lower than the literature value of $(3096.87 \pm 0.04) \text{ MeV}$ [G⁺00]. The width reflects the mass resolution of the HERA-B spectrometer; it is however significantly larger than the width obtained by a Monte-Carlo study (see for example [Hus01]). It is expected that with a further improved alignment of the tracking detectors and possibly a better global alignment also the mass resolution can be still improved.

The high mass region of the invariant mass spectrum is shown in Fig. 6.13. There are 8 background events (as estimated by taking the like-sign distributions as in Eq. 6.11) and 17 events with an unlike-sign muon pair, resulting in

$$N_{\text{DY candidates}} = 9 \pm 5 \quad (6.14)$$

candidates for Drell-Yan events.

Under the assumption that geometrical acceptance, trigger efficiency and reconstruction efficiency are approximately the same for J/ψ events and Drell-Yan events at high mass, the expected number of Drell-Yan events can be inferred from the observed number of J/ψ s and the

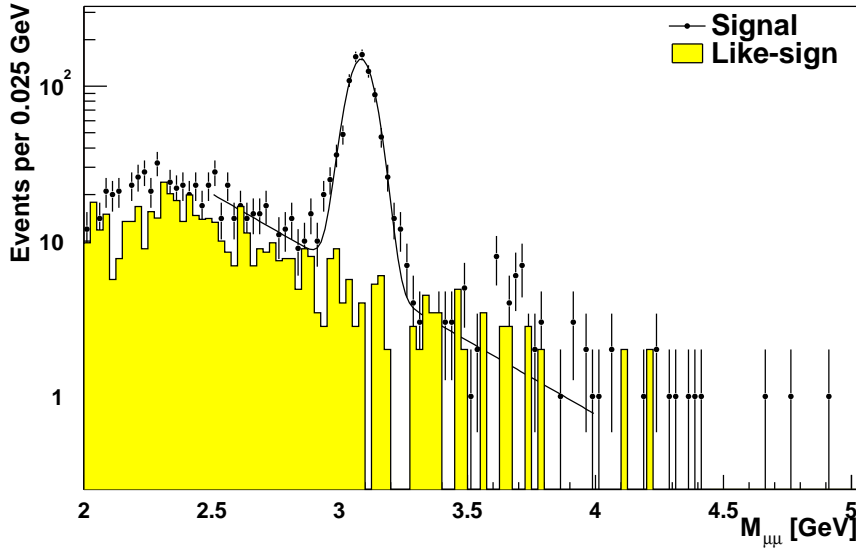


Figure 6.12: J/ψ signal found in the 2000 triggered data with the analysis cuts described in the text. The shaded histogram shows an estimate for the combinatorial background; see the text for its definition.

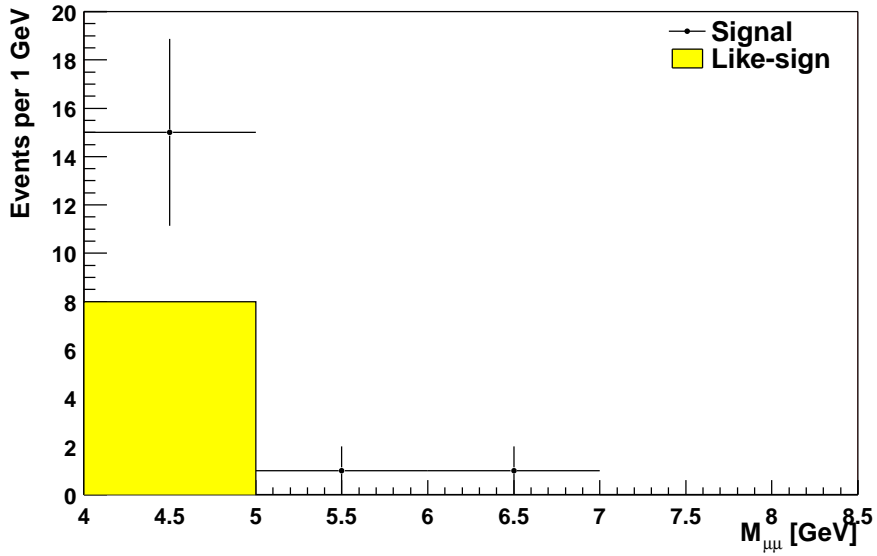


Figure 6.13: The high mass region in the 2000 triggered data with the analysis cuts described in the text. The shaded histogram shows an estimate for the combinatorial background; see the text for its definition.

ratio of the two cross sections. This estimation yields

$$\begin{aligned}
 N_{\text{DY}}^{\text{expected}} &= N_{J/\psi} \frac{\sigma_{\text{DY,highmass}}}{\sigma_{J/\psi} \times \text{BR}(J/\psi \rightarrow \mu\mu)} \\
 &= (767 \pm 29) \times \frac{0.38 \text{ nb/nucleon}}{420 \text{ nb/nucleon} \times 0.0588} \\
 &\approx 12 \pm 0.5 .
 \end{aligned} \tag{6.15}$$

However, the observed excess of unlike-sign muon pairs compared to the like-sign pairs is too small and has too large an error to draw any definite conclusions from this; $N_{\text{DYcandidates}}$ is consistent both with the number of expected Drell-Yan pairs and with 0. Also, the differences in geometrical and trigger acceptance, as well as in the reconstruction efficiency have to be studied in more detail.

All candidate Drell-Yan events were scanned by hand; one of the candidates is shown in Fig. 6.14. It is one of the cleanest in the sample; many events show a much higher multiplicity.

6.3.2 Expected Improvements and Impact on J/ψ Rate

During the HERA luminosity upgrade shutdown in 2000/2001, all components of HERA-*B* are repaired and upgraded [HER01]. The main improvements are:

- Inefficient and dead regions in the tracking detectors are eliminated.
- The overall efficiency of the Muon Pad System (which is used as input for the Muon Pretrigger) and the Muon System as a whole is expected to increase.
- The Inner Tracker and the Muon Pixel System are going to be used in the decision of the Second Level Trigger. The Inner Tracker is now fully commissioned and will be able to reliably deliver high-quality data.
- Additionally, the ITR is completely equipped with readout chips which will allow also the FLT to use the ITR. However, the ITR trigger contribution still needs to be commissioned.
- The optical links transmitting the detector information to the Track Finding Units (TFUs) are made more reliable.
- The coincidence matrix inside the TFUs is changed such that it can cope better with a non-ideal detector.
- Two different multiplicity vetoes will be employed to block events with very high activity already at the pretrigger level.

In addition, the trigger scenario which will most probably be used is requiring one muon track found by the FLT and a muon pair found by the SLT ($\text{FLT}_{1\mu} + \text{SLT}_{2\mu}$). This scenario has two main advantages: first, the SLT algorithm is more flexible in handling dead or inefficient detector regions. Compared to requiring two FLT tracks, this leads to an increased efficiency. Second, the information from the inner detectors (Muon Pixel System and Inner Tracker) can be used directly for triggering; during the 2000 run, the Inner Tracker was not feeding data to the FLT, so the complete commissioning work still remains to be done. Until this is completed, the inclusion of the inner detectors in the SLT decision still makes use of the coverage of the forward hemisphere.

The effect of these improvements on the detector and trigger efficiencies and the expected J/ψ rate is summarised in Table 6.3 (from [HER01]). Assuming a ‘realistic’ scenario for the

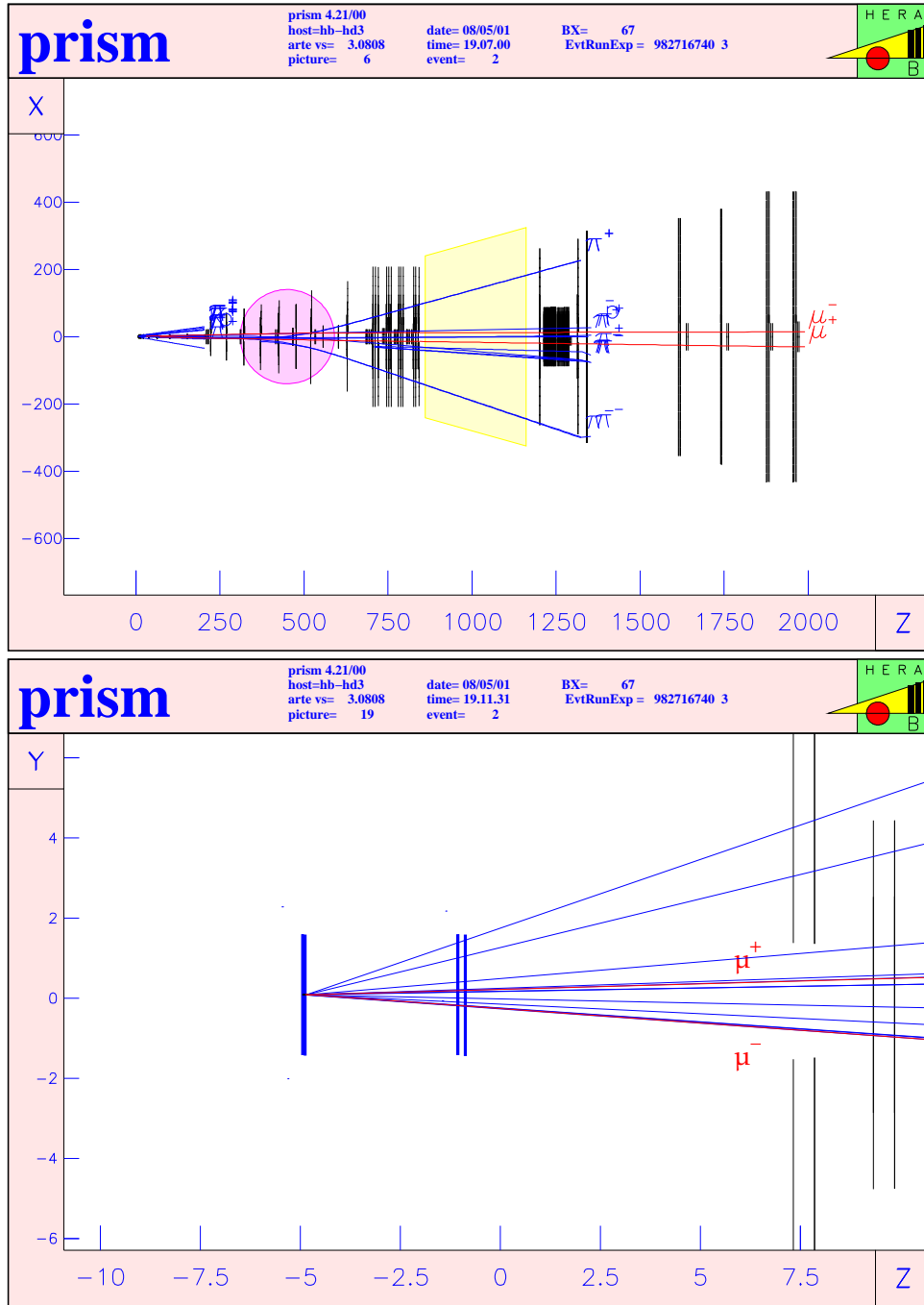


Figure 6.14: One of the Drell-Yan candidates selected by the analysis (Run 16740, event 9827). *Top:* View on the xz -plane (the bending plane of the magnet). *Bottom:* yz view of the target region (all dimensions in cm). There is only one primary vertex found in this event. The muon pair has an invariant mass of 6.1 GeV and a transverse momentum of $p_T = 1.3$ GeV; the primary vertex is 0.6 mm away from the target wire (the separation has a significance of only $\Delta r/\sigma_r = 1.7$).

improvements of the detector upgrade (*i.e.* one which is generally considered within the collaboration to be achievable), a rate of J/ψ triggered and written to tape of 1500 h^{-1} can be expected. The maximal rate which is conceived as achievable is 4100 h^{-1} .

| Contribution | 2000 | prob. | max. |
|-----------------------------------|-------|-------|------|
| Geometry ($p > 5 \text{ GeV}$) | 0.55 | 0.55 | 0.55 |
| MU-Pretrigger | 0.24 | 0.52 | 0.66 |
| Low angle coverage | 0.60 | 1.00 | 1.00 |
| FLT track efficiency | 0.36 | 0.65 | 0.89 |
| SLT pair eff & reconstruction | 0.11 | 0.41 | 0.64 |
| J/ψ efficiency | 0.003 | 0.076 | 0.21 |
| J/ψ rate [h^{-1}] | 52 | 1500 | 4100 |

Table 6.3: Expected improvements for the $J/\psi \rightarrow \mu\mu$ rates in single-FLT / double-SLT mode (from [HER01]). The J/ψ rate given in the last line is based on an assumed interaction rate of 5 MHz which is produced at one Carbon and one Titanium wire, except column 1 (2000 run: C only). The J/ψ rates are predictions using the J/ψ cross section; the actually observed J/ψ rate with this trigger mode (and different analysis cuts than used in the analysis presented in this thesis) was 37 h^{-1} . *prob* and *max* denote different scenarios for the effect of the detector upgrade: *max* is the optimum which is conceived as achievable, and *prob* denotes the scenario which is considered to be most probably reachable.

6.3.3 Expected Drell-Yan Rate in 2002

With the expectation on the J/ψ rates shown above, the anticipated rates and event numbers for Drell-Yan production can be calculated. The acceptance is different for prompt J/ψ and high-mass Drell-Yan events; it is a factor of about 1.25 larger for J/ψ than for high-mass Drell-Yan.³ The trigger and reconstruction efficiencies are assumed to be the about the same for both event classes. With these assumptions and a cross section ratio of $\sigma_{\text{DY,highmass}}/\sigma_{J/\psi} \approx 0.015$, the expected rate of triggered and reconstructed Drell-Yan events is in the range of $18 - 50 \text{ h}^{-1}$, with 18 h^{-1} being the most probable rate.

An estimate of the total time available for data-taking is difficult, since both detector and trigger have to be recommissioned after the shutdown. The number quoted usually is half a ‘HEP year’⁴, *i.e.* $5 \times 10^6 \text{ s} \approx 1390 \text{ h}$. This leads to the expectation of having 26 000 high-mass Drell-Yan events on tape at the end of 2002, or if all detector improvements work optimally, up to 70 000 events.

6.4 Measuring the Angular Distribution

To measure if the Lam-Tung relation is violated also in proton-nucleon collisions, it is necessary to extract the parameters λ , μ , and ν of Eq. 5.8 with sufficient precision. In this section, two methods are presented: a direct fit to the two-dimensional angular distribution of the Drell-Yan pairs, and a more indirect method using the method of moments. This last method is based on a suggestion by G. Bohm [Boh01]. The statistical power of the two methods is evaluated using a simple Monte-Carlo model.

³A detailed comparison of the geometrical acceptances for J/ψ and Drell-Yan events can be found in [Hus01].

⁴The time a typical experiment at a storage ring can actually take data during one year is about $1/3 \text{ year} \approx 10^7 \text{ s}$

6.4.1 Expected Shape of the Angular Distributions

The true shape of the angular distribution is shown in Fig. 6.15; the left plot assumes that the Lam-Tung relation is valid, the right plot uses the values for the parameters λ , μ , and ν which were measured by the NA10 collaboration.

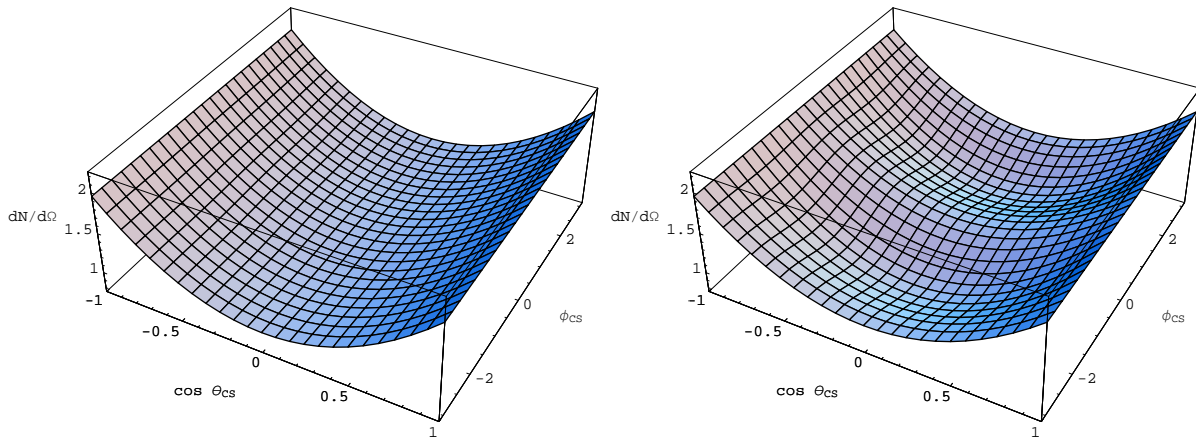


Figure 6.15: Angular distribution of the Drell-Yan process measured in the Collins-Soper frame. *Left:* Expected angular distribution according to Eq. 5.8, with the additional assumption that the Lam-Tung relation holds ($\lambda = 0.96$, $\mu = 0$, $\nu = (1 - \lambda)/2$). *Right:* Expected angular distribution with violation of the Lam-Tung relation in the range $p_{T\gamma^*} > 1.5$ GeV with $\lambda = 0.96$, $\mu = 0$, $\nu = 0.2$ (as measured by NA10 [G⁺88]).

This distribution, however, is not the one which can be measured directly: the non-uniform geometrical acceptance of the spectrometer has to be taken into account. To demonstrate the effect, the acceptance which was determined in Sect. 6.1 was assumed to depend only on $\cos \theta$. The shape of the $\cos \theta$ acceptance function was parametrised with a polynomial $\alpha(\cos \theta)$. The distribution $\alpha(\cos \theta) d\sigma/d\Omega$ is shown in Fig. 6.16; it corresponds to the directly observable angular distribution. Any measurement of the coefficients has to correct the measured distribution for the acceptance; at large $|\cos \theta|$ this will lead to large weights which have to be applied to the events and consequently to a larger statistical error.

Common to all measurements which have shown to the present date that the Lam-Tung relation is violated is the fact that at moderate transverse momenta (around 0.5 – 1.5 GeV) of the muon pair, $\lambda \approx 1$ within a few percent, but ν becomes significantly larger than 0. This effect can be observed even without correcting for the detector acceptance, and probably even with a small event sample. By integrating the angular distribution over $\cos \theta$, one obtains the ϕ dependent distributions shown in Fig. 6.17. The deviation of the Lam-Tung violating scenario from the non-violating one is clearly visible even in the uncorrected distribution.

6.4.2 Direct Fit

The most direct way to determine the coefficients of the angular distribution is to plot the angular distribution found in the data after acceptance correction and background subtraction into a two-dimensional histogram and to perform a full fit of the function

$$f(\cos \theta, \phi; N, \lambda, \mu, \nu) = N \left[1 + \lambda \cos^2 \theta + \mu \sin 2\theta \cos \phi + \frac{\nu}{2} \sin^2 \theta \cos 2\phi \right] \quad (6.16)$$

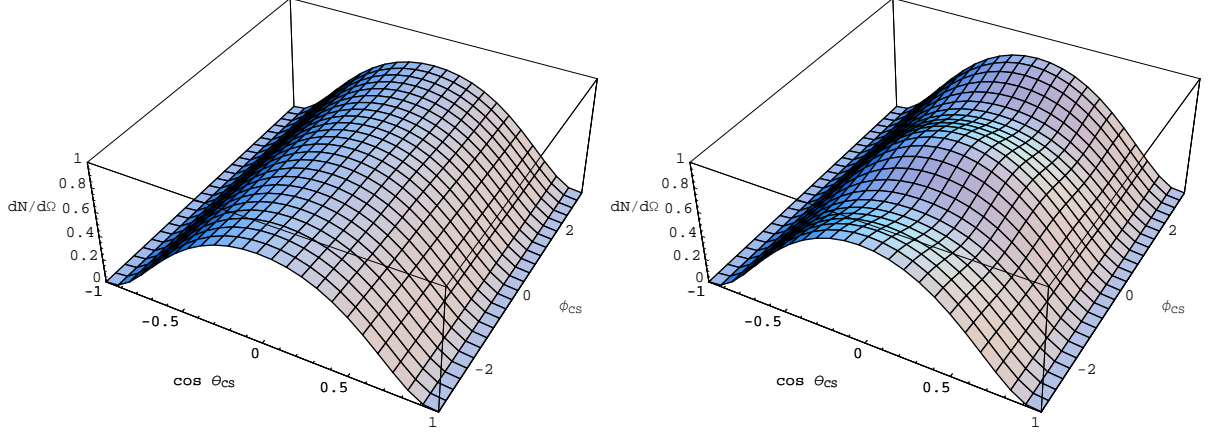


Figure 6.16: Angular distribution which can directly be measured with the real HERA-*B* detector; the acceptance in $\cos \theta_{CS}$ as determined in Sect. 6.1 was parametrised with a polynomial and multiplied to the original distributions. *Left:* Lam-Tung relation holds. *Right:* Angular distribution with violation of the Lam-Tung relation as measured by NA10.

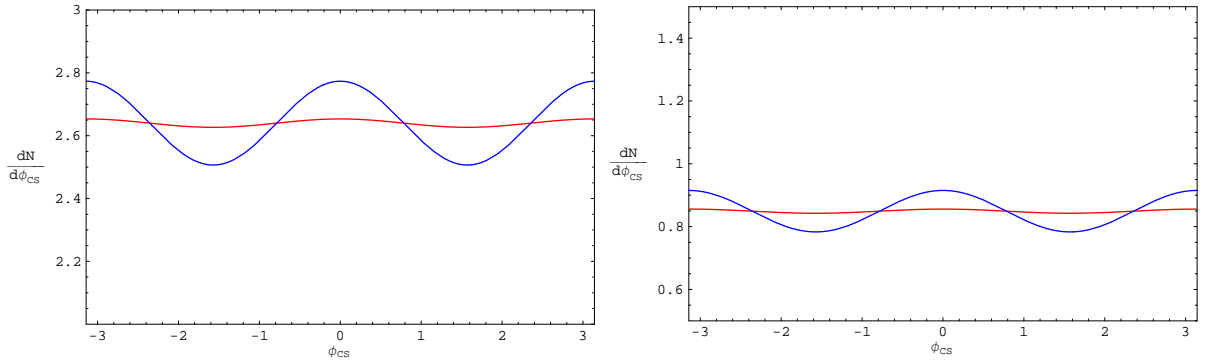


Figure 6.17: Distribution of ϕ_{CS} , integrated over the whole range of $\cos \theta_{CS}$. *Left:* true angular distribution, *right:* distribution with real detector acceptance. In both plots, the nearly horizontal curve corresponds to the case that the Lam-Tung relation holds; the sine-shaped curve uses the parameters $\lambda = 0.96$ and $\mu = 0.2$ as in Fig. 6.15 and 6.16. Note the suppressed zero in both plots; the deviation from a straight line is about 5% in the left plot, and about 8% in the right plot.

to the histogram. This procedure has to be performed for several intervals in $p_{T\gamma^*}$. The error to the parameters attainable by this method crucially depends on the number of events which are available. Since the expectation for the number of triggered and reconstructed Drell-Yan events in 2002 is rather limited under realistic assumptions for the detector and trigger performance, it is

To get an impression of the statistical power of this method, a simple toy model was used (which did not take into account the detector acceptance). According to the angular distribution Eq. 5.8 and again using the parameters measured by NA10 in the region with $p_{T\gamma^*} > 1.5$ GeV, $(\lambda, \mu, \nu) = (0.96, 0, 0.2)$, N_0 pairs of $(\cos\theta, \phi)$ were generated and filled into a two-dimensional histogram with ten bins along each axis. The function $f(\cos\theta, \phi; N, \lambda, \mu, \nu)$ of Eq. 6.16 was then fitted to this histogram, and the fit results λ_{fit} and ν_{fit} were extracted and filled into separate histograms. This procedure was repeated several times; the relative error on the fit parameters attainable was then taken to be $\sigma_\lambda = \text{rms}(\lambda_{\text{fit}})/\langle\lambda_{\text{fit}}\rangle$. The number N_0 of signal events was varied in a range which could be expected for the HERA-B run 2002. The result of this simulation is shown in Fig. 6.18. A significant measurement of λ and ν seems only possible with about 10 000 signal events. However, assuming independence of the fit parameters, the significance of the violation of the Lam-Tung relation $v = 1 - \lambda - 2\nu$ is given by $\Delta v = \sqrt{\Delta\lambda^2 + 2\Delta\nu^2}$. For the parameters chosen for this simulation, $v \approx -0.36$. With only 5 000 signal events, the error on v is then $\Delta v \approx 0.12$, allowing a significant measurement of the violation at the 3σ level. Acceptance correction and statistical background subtraction will certainly introduce another error, which could not be quantified by this study.

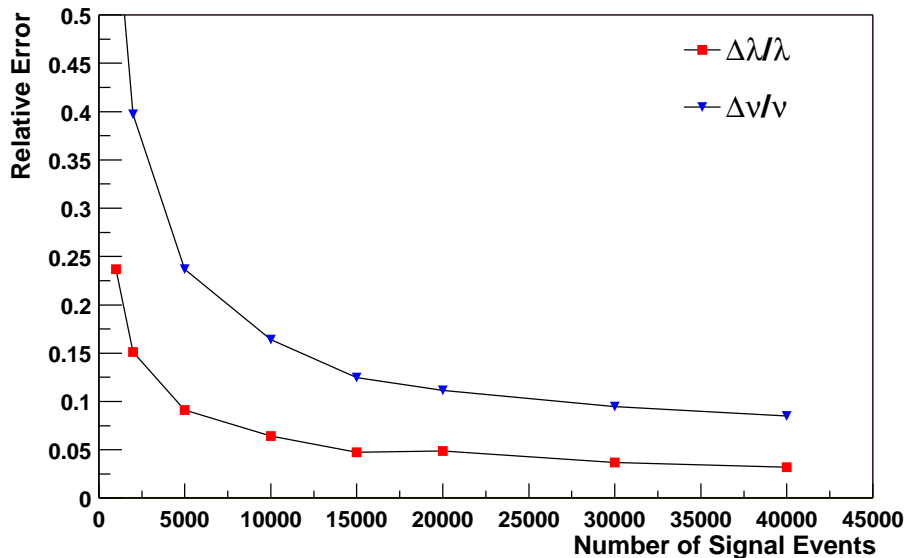


Figure 6.18: Simulation of the statistical power of a two-dimensional fit to the angular distribution. A detailed description of the method to obtain the errors is given in the text.

6.4.3 Method of Moments

A different approach to measure the coefficients of the angular distributions is the method of moments which is computationally simpler than a fit to a two-dimensional distribution. For this method, one chooses a suitable set of orthogonal functions $p_i(\Omega)$ and computes the first

moments of the distribution $f(\Omega)$:

$$\alpha_i \equiv \langle p_i(\Omega) \rangle = \int d\Omega p_i(\Omega) f(\Omega) \quad (6.17)$$

The angular dependence of the Drell-Yan cross section can be expanded in terms of the Legendre polynomials P_n and associated Legendre polynomials P_l^m , which are defined as follows:

$$P_l(\cos \theta) = \frac{1}{2^l l!} \frac{d^l}{d(\cos \theta)^l} (\cos^2 \theta - 1)^l \quad (6.18)$$

$$P_l^m(\cos \theta) = (1 - \cos^2 \theta)^{m/2} \frac{d^m}{d(\cos \theta)^m} P_l(\cos \theta) . \quad (6.19)$$

With these polynomials, the angular dependence of the Drell-Yan cross section (Eq. 5.8) can be written as [Boh01]

$$\begin{aligned} \frac{1}{\sigma} \frac{d\sigma}{d\Omega}(\cos \theta, \phi) &= \frac{1}{4\pi} \left(1 + \frac{2\lambda}{\lambda + 3} P_2(\cos \theta) \right. \\ &\quad \left. + \frac{2\mu}{\lambda + 3} P_2^1(\cos \theta) \cos \phi + \frac{\nu}{2(\lambda + 3)} P_2^2(\cos \theta) \cos 2\phi \right) , \end{aligned} \quad (6.20)$$

where the used (associated) Legendre polynomials are

$$P_2(\cos \theta) = \frac{1}{2} (3 \cos^2 \theta - 1) \quad (6.21)$$

$$P_2^1(\cos \theta) \cos \phi = \frac{3}{2} \sin 2\theta \cos \phi \quad (6.22)$$

$$P_2^2(\cos \theta) \cos 2\phi = 3 \sin^2 \theta \cos 2\phi \quad (6.23)$$

The resulting moments are

$$\alpha_0 \equiv \langle P_2(\cos \theta) \rangle = \frac{2}{5} \frac{\lambda}{\lambda + 3} \quad (6.24)$$

$$\alpha_1 \equiv \langle P_2^1(\cos \theta) \cos \phi \rangle = \frac{3}{5} \frac{2\mu}{\lambda + 3} \quad (6.25)$$

$$\alpha_2 \equiv \langle P_2^2(\cos \theta) \cos 2\phi \rangle = \frac{3}{5} \frac{2\nu}{\lambda + 3} , \quad (6.26)$$

and the Lam-Tung relation 5.9 translates into

$$2\alpha_0 + \alpha_2 - \frac{1}{5} = 0 . \quad (6.27)$$

Conversely, the usual parameters λ , μ and ν are expressed in terms of the moments α_i as

$$\lambda = \frac{15\alpha_0}{2 - 5\alpha_0} \quad (6.28)$$

$$\mu = \frac{5\alpha_1}{2 - 5\alpha_0} \quad (6.29)$$

$$\nu = \frac{5\alpha_2}{2 - 5\alpha_0} , \quad (6.30)$$

and the errors on λ , μ and ν are (assuming that the α_i are statistically independent):

$$\Delta\lambda^2 = \left(\frac{30}{(2 - 5\alpha_0)^2} \Delta\alpha_0 \right)^2 \quad (6.31)$$

$$\Delta\mu^2 = \left(\frac{25\alpha_1}{(5\alpha_0 - 2)^2} \Delta\alpha_0 \right)^2 + \left(\frac{5}{5\alpha_0 - 2} \Delta\alpha_1 \right)^2 \quad (6.32)$$

$$\Delta\nu^2 = \left(\frac{25\alpha_2}{(5\alpha_0 - 2)^2} \Delta\alpha_0 \right)^2 + \left(\frac{5}{5\alpha_0 - 2} \Delta\alpha_2 \right)^2. \quad (6.33)$$

The α_i are obtained by computing the mean value of the functions (6.21)–(6.23); this amounts to computing the mean value of three histograms. The statistical error on α_i is to a good approximation given by the rms of the distribution divided by the square root of the number of entries:

$$\sigma(\alpha_i) = \frac{\text{rms}(\alpha_i)}{\sqrt{N_i}}. \quad (6.34)$$

The same toy model as describe above in Sect. 6.4.2 was used to get an impression of the statistical power which this method offers. The result is shown in Fig. 6.19. Except at very small numbers of events, both methods yield nearly the same relative errors for λ and μ . For very small data samples, the method of moments has an advantage.

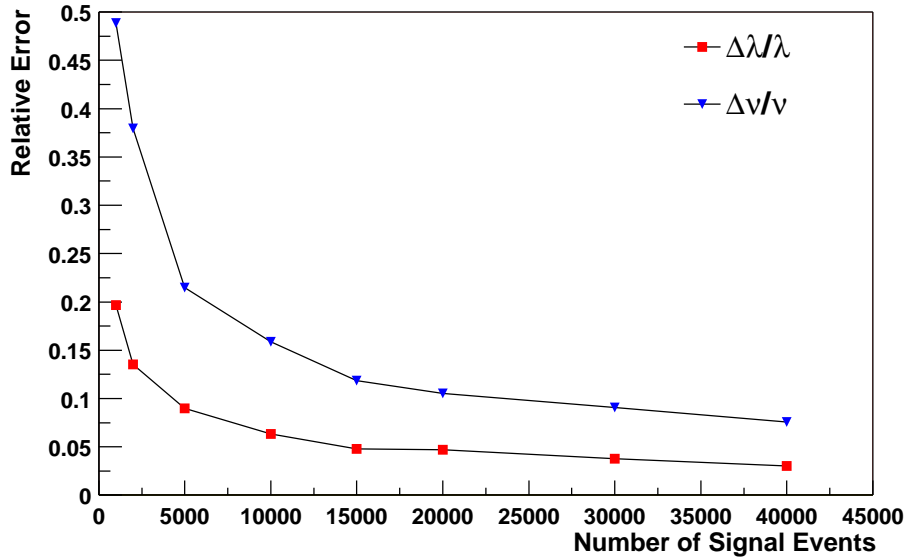


Figure 6.19: Simulation of the statistical power of the method of moments to extract the parameters λ and ν . A detailed description of the method to obtain the errors is given in the text.

6.5 Summary

The results of the feasibility study for Drell-Yan physics at HERA-B can be summarised as follows:

- The HERA-B spectrometer has an excellent acceptance for Drell-Yan muon pairs over a wide range of the kinematical variables $p_{T\gamma^*}$ and M_{γ^*} . It covers the central region of

production, $-0.4 < x_F < 0.3$. The angular acceptance in the angle ϕ_{CS} is flat, and polar angles up to $|\cos \theta_{CS}| \approx 0.7$ can be measured.

- The background situation is not finally clarified. Some more detailed studies are still needed to gain confidence that the combinatorial background can be reduced to a tolerable level.
- In the di-muon data taken during the 2000 run, a sample of 9 ± 5 candidates for Drell-Yan production at high masses was found after background subtraction, with rather hard cuts on the track and vertex quality and the particle identification. With the same cuts, 767 produced J/ψ were identified. The ratio of found high-mass Drell-Yan muon pairs to muon pairs from J/ψ is consistent with the ratio of the respective cross sections.
- Expected event rate: with reasonable ('probable') assumptions on the effects of the detector improvements, a sizeable amount of Drell-Yan events can be triggered on and reconstructed. Depending on the detector performance, a sample of 25 000 Drell-Yan events at high masses is expected for one year of running at an interaction rate of 5 MHz. Measuring a violation of the Lam-Tung relation of the size measured in earlier πN experiments is well within reach of HERA-B.
- *Drell-Yan physics at HERA-B is difficult, but certainly not impossible, assuming a reasonable detector performance. However, for a precision measurement the detector performance must be better than the minimum assumed above.*

Chapter 7

Summary and Conclusions

The experiment HERA-*B* which was proposed and designed to measure \mathcal{CP} violation in the decay of neutral B -mesons is presently being commissioned at DESY. HERA-*B* is designed as a high rate experiment, with particle fluxes reaching $2 \times 10^4 \text{ mm}^{-1} \text{ s}^{-1}$ in the innermost part, which poses severe requirements to the detectors and the readout electronics installed near the chambers. The readout systems of all sub-detectors have to cope with trigger rates of 50 kHz without producing sizeable dead time.

One of the main components of the detector is the Inner Tracker, which is built of Micro-Strip Gas Chambers with a Gas Electron Multiplier (GEM-MSGC). In total, the Inner Tracker contains 184 GEM-MSGCs with more than 120 000 analogue readout channels; 136 of these chambers with 102 000 readout channels were installed and operated during the run period 1999/2000. For readout, the Inner Tracker uses the ASIC Helix128S, which was specifically developed for the readout of HERA-*B*'s micro-strip detectors (Vertex Detector System and Inner Tracker). The Helix128S provides the front-end electronics for 128 readout channels, a pipeline which can store the detector data until the First Level Trigger has reached a decision, and a serial output of the analogue data. It also contains a comparator for each channel, which is used to derive hit information for the First Level Trigger. The Front End Driver (FED) system which controls the readout and digitises the data is common to both the Vertex Detector and the Inner Tracker.

During the work done for this thesis, several modules of the additional electronics which is needed for the readout of the Inner Tracker were developed. The readout electronics was improved and extensively tested both in the laboratory and in test beam experiments at the Paul Scherrer Institute, Villigen. Using the experience gained during these beam tests, the design of the readout system was finalised. At HERA-*B*, the readout system was extended from small test installations to the full system for the complete Inner Tracker, in parallel to the installation of tracking stations during 1999/2000. The programs needed for the control of the readout system were developed, as well as the software used to process the raw data for the subsequent data analysis programs.

The detector was still in the commissioning phase during most of the run period of 2000. Nevertheless, it could be shown that the readout system performs well, according to its specifications. Some problems were encountered concerning the stability of the readout system during long data taking runs, affecting the quality of the Inner Tracker data. The cause of these failures is still under investigation, but weak points which were identified are eliminated. During the luminosity upgrade shutdown of HERA in 2000/2001, the complete Inner Tracker chambers were equipped with a new grounding scheme, resulting in a reduced pick-up. Apart from these hardware improvements, also the readout software will be updated for the run period 2002, allowing the Second Level Trigger to make use of the Inner Tracker data; also the diagnostic

tools which monitor the system performance online are upgraded.

In the second part of this thesis, the prospects of HERA-*B* to contribute to the field of Drell-Yan physics are evaluated. Perturbative QCD fails to explain the angular distribution of the produced lepton pairs which was measured by earlier Drell-Yan experiments studying πN scattering. Several theoretical models apply non-perturbative ideas to explain the angular distribution and its change with $p_{T\gamma^*}$. It is of considerable interest to measure the angular distribution also in pN scattering, at higher centre-of-mass energies, and to compare model predictions to the experimentally found distributions.

Drell-Yan production was considered as one of the physics topics for the 2002 run of HERA-*B*. The analysis presented in this thesis is restricted to the channel $pN \rightarrow \mu^+ \mu^- X$ at high invariant masses of the muon pair; $4 < M_{\gamma^*} < 8.5$ GeV. The geometrical acceptance as a function of the important kinematical and angular variables was studied and confirmed to be excellent. The expected background is mainly random combinations of muons from $\pi/K \rightarrow \mu\nu$ decays. A cut in p_T of the single muons can reduce the background by large factors, but more detailed studies are still needed to obtain a reliable estimate for the background.

An analysis of the di-muon triggered data taken during the run 2000 finds—with hard cuts on muon identification and track and vertex quality—about 770 $J/\psi \rightarrow \mu^+ \mu^-$ decays and, after background subtraction, 9 ± 5 candidates for Drell-Yan production in the high mass range, consistent with the ratio of the cross sections. Scaling this number of events with the improvements of the detector, about 26 000 high-mass Drell-Yan events are expected for the run 2002. This will allow to get a first measurement of the angular distribution of the Drell-Yan muons, but, due to the limited statistics, only in rather large bins of p_T . Nevertheless, an interesting measurement is possible.

Appendix A

Readout Setup

A.1 Location of Readout Electronics

The complete readout electronics of the Inner Tracker is housed in three racks in the ground floor of HERA-*B*'s electronics trailer. It comprises nine VME crates and six NIM crates. One additional VME crate holds the CAN bus interfaces needed for slow control and Helix steering purposes as well as a CAEN interface to steer the HV power supply.

| <table><tr><th>FED Switch</th><th>Crate ID 1</th></tr><tr><td>FED 0x00</td><td>MS11-</td></tr><tr><td>FED 0x01</td><td>MS11-</td></tr><tr><td>FED 0x02</td><td>MS11+</td></tr><tr><td>FED 0x03</td><td>MS11+</td></tr><tr><td>FED 0x04</td><td>MS12-</td></tr><tr><td>FED 0x05</td><td>MS12-</td></tr><tr><td>FED 0x06</td><td>MS12+</td></tr><tr><td>FED 0x07</td><td>MS12+</td></tr><tr><td></td><td></td></tr><tr><td></td><td></td></tr></table> | FED Switch | Crate ID 1 | FED 0x00 | MS11- | FED 0x01 | MS11- | FED 0x02 | MS11+ | FED 0x03 | MS11+ | FED 0x04 | MS12- | FED 0x05 | MS12- | FED 0x06 | MS12+ | FED 0x07 | MS12+ | | | | | <table><tr><th>CETIA</th><th>hb-vme59</th></tr><tr><td>SHARC 0x02</td><td>ITR_ MS11-</td></tr><tr><td>0x03</td><td>MS01-</td></tr><tr><td>0x04</td><td>MS11-</td></tr><tr><td>0x05</td><td>MS01-</td></tr><tr><td>0x06</td><td>MS11+</td></tr><tr><td>0x07</td><td>MS01+</td></tr><tr><td>0x08</td><td>MS11+</td></tr><tr><td>0x09</td><td>MS01+</td></tr><tr><td>0x0a</td><td>MS12-</td></tr><tr><td>0x0b</td><td>MS03+</td></tr><tr><td>0x0c</td><td>MS12-</td></tr><tr><td>0x0d</td><td>MS03-</td></tr><tr><td>0x0e</td><td>MS12+</td></tr><tr><td>0x0f</td><td>MS05-</td></tr><tr><td>0x10</td><td>MS12+</td></tr><tr><td>0x11</td><td>MS05+</td></tr><tr><td></td><td></td></tr><tr><td>0x13</td><td>MS06-</td></tr><tr><td></td><td></td></tr><tr><td>0x15</td><td>MS06+</td></tr></table> | CETIA | hb-vme59 | SHARC 0x02 | ITR_ MS11- | 0x03 | MS01- | 0x04 | MS11- | 0x05 | MS01- | 0x06 | MS11+ | 0x07 | MS01+ | 0x08 | MS11+ | 0x09 | MS01+ | 0x0a | MS12- | 0x0b | MS03+ | 0x0c | MS12- | 0x0d | MS03- | 0x0e | MS12+ | 0x0f | MS05- | 0x10 | MS12+ | 0x11 | MS05+ | | | 0x13 | MS06- | | | 0x15 | MS06+ | <table><tr><th>FED Switch</th><th>Crate ID 0</th></tr><tr><td>FED 0x00</td><td>MS01-</td></tr><tr><td>FED 0x01</td><td>MS01-</td></tr><tr><td>FED 0x02</td><td>MS01+</td></tr><tr><td>FED 0x03</td><td>MS01+</td></tr><tr><td>FED 0x04</td><td>MS03+</td></tr><tr><td>FED 0x05</td><td>MS03-</td></tr><tr><td>FED 0x06</td><td>MS05-</td></tr><tr><td>FED 0x07</td><td>MS05+</td></tr><tr><td>FED 0x08</td><td>MS06-</td></tr><tr><td>FED 0x09</td><td>MS06+</td></tr></table> | FED Switch | Crate ID 0 | FED 0x00 | MS01- | FED 0x01 | MS01- | FED 0x02 | MS01+ | FED 0x03 | MS01+ | FED 0x04 | MS03+ | FED 0x05 | MS03- | FED 0x06 | MS05- | FED 0x07 | MS05+ | FED 0x08 | MS06- | FED 0x09 | MS06+ |
|--|---|------------|----------|------------|------------|-------|----------|-------|----------|-------|----------|-------|----------|-------|----------|-------|----------|-------|--|--|--|-----------|--|-----------|----------|------------|------------|--------------|-------|----------------|---------|----------------|---------|----------------|---------|--------------|-------|--|------------|------------|----------|-------|----------|-----------|----------|-------|-------|------|-------|------|-------|------|-------|------|-------|------|-------|--|--|------|-------|--|--|------|-------|--|------------|------------|----------|-------|----------|-------|----------|-------|----------|-------|----------|-------|----------|-------|----------|-------|----------|-------|----------|-------|----------|-------|
| FED Switch | Crate ID 1 | | | | | | | | | | | | | | | | | | | | | | | | | | | | | | | | | | | | | | | | | | | | | | | | | | | | | | | | | | | | | | | | | | | | | | | | | | | | | | | | | | | | | | | |
| FED 0x00 | MS11- | | | | | | | | | | | | | | | | | | | | | | | | | | | | | | | | | | | | | | | | | | | | | | | | | | | | | | | | | | | | | | | | | | | | | | | | | | | | | | | | | | | | | | | |
| FED 0x01 | MS11- | | | | | | | | | | | | | | | | | | | | | | | | | | | | | | | | | | | | | | | | | | | | | | | | | | | | | | | | | | | | | | | | | | | | | | | | | | | | | | | | | | | | | | | |
| FED 0x02 | MS11+ | | | | | | | | | | | | | | | | | | | | | | | | | | | | | | | | | | | | | | | | | | | | | | | | | | | | | | | | | | | | | | | | | | | | | | | | | | | | | | | | | | | | | | | |
| FED 0x03 | MS11+ | | | | | | | | | | | | | | | | | | | | | | | | | | | | | | | | | | | | | | | | | | | | | | | | | | | | | | | | | | | | | | | | | | | | | | | | | | | | | | | | | | | | | | | |
| FED 0x04 | MS12- | | | | | | | | | | | | | | | | | | | | | | | | | | | | | | | | | | | | | | | | | | | | | | | | | | | | | | | | | | | | | | | | | | | | | | | | | | | | | | | | | | | | | | | |
| FED 0x05 | MS12- | | | | | | | | | | | | | | | | | | | | | | | | | | | | | | | | | | | | | | | | | | | | | | | | | | | | | | | | | | | | | | | | | | | | | | | | | | | | | | | | | | | | | | | |
| FED 0x06 | MS12+ | | | | | | | | | | | | | | | | | | | | | | | | | | | | | | | | | | | | | | | | | | | | | | | | | | | | | | | | | | | | | | | | | | | | | | | | | | | | | | | | | | | | | | | |
| FED 0x07 | MS12+ | | | | | | | | | | | | | | | | | | | | | | | | | | | | | | | | | | | | | | | | | | | | | | | | | | | | | | | | | | | | | | | | | | | | | | | | | | | | | | | | | | | | | | | |
| | | | | | | | | | | | | | | | | | | | | | | | | | | | | | | | | | | | | | | | | | | | | | | | | | | | | | | | | | | | | | | | | | | | | | | | | | | | | | | | | | | | | | | | | |
| | | | | | | | | | | | | | | | | | | | | | | | | | | | | | | | | | | | | | | | | | | | | | | | | | | | | | | | | | | | | | | | | | | | | | | | | | | | | | | | | | | | | | | | | |
| CETIA | hb-vme59 | | | | | | | | | | | | | | | | | | | | | | | | | | | | | | | | | | | | | | | | | | | | | | | | | | | | | | | | | | | | | | | | | | | | | | | | | | | | | | | | | | | | | | | |
| SHARC 0x02 | ITR_ MS11- | | | | | | | | | | | | | | | | | | | | | | | | | | | | | | | | | | | | | | | | | | | | | | | | | | | | | | | | | | | | | | | | | | | | | | | | | | | | | | | | | | | | | | | |
| 0x03 | MS01- | | | | | | | | | | | | | | | | | | | | | | | | | | | | | | | | | | | | | | | | | | | | | | | | | | | | | | | | | | | | | | | | | | | | | | | | | | | | | | | | | | | | | | | |
| 0x04 | MS11- | | | | | | | | | | | | | | | | | | | | | | | | | | | | | | | | | | | | | | | | | | | | | | | | | | | | | | | | | | | | | | | | | | | | | | | | | | | | | | | | | | | | | | | |
| 0x05 | MS01- | | | | | | | | | | | | | | | | | | | | | | | | | | | | | | | | | | | | | | | | | | | | | | | | | | | | | | | | | | | | | | | | | | | | | | | | | | | | | | | | | | | | | | | |
| 0x06 | MS11+ | | | | | | | | | | | | | | | | | | | | | | | | | | | | | | | | | | | | | | | | | | | | | | | | | | | | | | | | | | | | | | | | | | | | | | | | | | | | | | | | | | | | | | | |
| 0x07 | MS01+ | | | | | | | | | | | | | | | | | | | | | | | | | | | | | | | | | | | | | | | | | | | | | | | | | | | | | | | | | | | | | | | | | | | | | | | | | | | | | | | | | | | | | | | |
| 0x08 | MS11+ | | | | | | | | | | | | | | | | | | | | | | | | | | | | | | | | | | | | | | | | | | | | | | | | | | | | | | | | | | | | | | | | | | | | | | | | | | | | | | | | | | | | | | | |
| 0x09 | MS01+ | | | | | | | | | | | | | | | | | | | | | | | | | | | | | | | | | | | | | | | | | | | | | | | | | | | | | | | | | | | | | | | | | | | | | | | | | | | | | | | | | | | | | | | |
| 0x0a | MS12- | | | | | | | | | | | | | | | | | | | | | | | | | | | | | | | | | | | | | | | | | | | | | | | | | | | | | | | | | | | | | | | | | | | | | | | | | | | | | | | | | | | | | | | |
| 0x0b | MS03+ | | | | | | | | | | | | | | | | | | | | | | | | | | | | | | | | | | | | | | | | | | | | | | | | | | | | | | | | | | | | | | | | | | | | | | | | | | | | | | | | | | | | | | | |
| 0x0c | MS12- | | | | | | | | | | | | | | | | | | | | | | | | | | | | | | | | | | | | | | | | | | | | | | | | | | | | | | | | | | | | | | | | | | | | | | | | | | | | | | | | | | | | | | | |
| 0x0d | MS03- | | | | | | | | | | | | | | | | | | | | | | | | | | | | | | | | | | | | | | | | | | | | | | | | | | | | | | | | | | | | | | | | | | | | | | | | | | | | | | | | | | | | | | | |
| 0x0e | MS12+ | | | | | | | | | | | | | | | | | | | | | | | | | | | | | | | | | | | | | | | | | | | | | | | | | | | | | | | | | | | | | | | | | | | | | | | | | | | | | | | | | | | | | | | |
| 0x0f | MS05- | | | | | | | | | | | | | | | | | | | | | | | | | | | | | | | | | | | | | | | | | | | | | | | | | | | | | | | | | | | | | | | | | | | | | | | | | | | | | | | | | | | | | | | |
| 0x10 | MS12+ | | | | | | | | | | | | | | | | | | | | | | | | | | | | | | | | | | | | | | | | | | | | | | | | | | | | | | | | | | | | | | | | | | | | | | | | | | | | | | | | | | | | | | | |
| 0x11 | MS05+ | | | | | | | | | | | | | | | | | | | | | | | | | | | | | | | | | | | | | | | | | | | | | | | | | | | | | | | | | | | | | | | | | | | | | | | | | | | | | | | | | | | | | | | |
| | | | | | | | | | | | | | | | | | | | | | | | | | | | | | | | | | | | | | | | | | | | | | | | | | | | | | | | | | | | | | | | | | | | | | | | | | | | | | | | | | | | | | | | | |
| 0x13 | MS06- | | | | | | | | | | | | | | | | | | | | | | | | | | | | | | | | | | | | | | | | | | | | | | | | | | | | | | | | | | | | | | | | | | | | | | | | | | | | | | | | | | | | | | | |
| | | | | | | | | | | | | | | | | | | | | | | | | | | | | | | | | | | | | | | | | | | | | | | | | | | | | | | | | | | | | | | | | | | | | | | | | | | | | | | | | | | | | | | | | |
| 0x15 | MS06+ | | | | | | | | | | | | | | | | | | | | | | | | | | | | | | | | | | | | | | | | | | | | | | | | | | | | | | | | | | | | | | | | | | | | | | | | | | | | | | | | | | | | | | | |
| FED Switch | Crate ID 0 | | | | | | | | | | | | | | | | | | | | | | | | | | | | | | | | | | | | | | | | | | | | | | | | | | | | | | | | | | | | | | | | | | | | | | | | | | | | | | | | | | | | | | | |
| FED 0x00 | MS01- | | | | | | | | | | | | | | | | | | | | | | | | | | | | | | | | | | | | | | | | | | | | | | | | | | | | | | | | | | | | | | | | | | | | | | | | | | | | | | | | | | | | | | | |
| FED 0x01 | MS01- | | | | | | | | | | | | | | | | | | | | | | | | | | | | | | | | | | | | | | | | | | | | | | | | | | | | | | | | | | | | | | | | | | | | | | | | | | | | | | | | | | | | | | | |
| FED 0x02 | MS01+ | | | | | | | | | | | | | | | | | | | | | | | | | | | | | | | | | | | | | | | | | | | | | | | | | | | | | | | | | | | | | | | | | | | | | | | | | | | | | | | | | | | | | | | |
| FED 0x03 | MS01+ | | | | | | | | | | | | | | | | | | | | | | | | | | | | | | | | | | | | | | | | | | | | | | | | | | | | | | | | | | | | | | | | | | | | | | | | | | | | | | | | | | | | | | | |
| FED 0x04 | MS03+ | | | | | | | | | | | | | | | | | | | | | | | | | | | | | | | | | | | | | | | | | | | | | | | | | | | | | | | | | | | | | | | | | | | | | | | | | | | | | | | | | | | | | | | |
| FED 0x05 | MS03- | | | | | | | | | | | | | | | | | | | | | | | | | | | | | | | | | | | | | | | | | | | | | | | | | | | | | | | | | | | | | | | | | | | | | | | | | | | | | | | | | | | | | | | |
| FED 0x06 | MS05- | | | | | | | | | | | | | | | | | | | | | | | | | | | | | | | | | | | | | | | | | | | | | | | | | | | | | | | | | | | | | | | | | | | | | | | | | | | | | | | | | | | | | | | |
| FED 0x07 | MS05+ | | | | | | | | | | | | | | | | | | | | | | | | | | | | | | | | | | | | | | | | | | | | | | | | | | | | | | | | | | | | | | | | | | | | | | | | | | | | | | | | | | | | | | | |
| FED 0x08 | MS06- | | | | | | | | | | | | | | | | | | | | | | | | | | | | | | | | | | | | | | | | | | | | | | | | | | | | | | | | | | | | | | | | | | | | | | | | | | | | | | | | | | | | | | | |
| FED 0x09 | MS06+ | | | | | | | | | | | | | | | | | | | | | | | | | | | | | | | | | | | | | | | | | | | | | | | | | | | | | | | | | | | | | | | | | | | | | | | | | | | | | | | | | | | | | | | |
| <table><tr><th>FED Switch</th><th>Crate ID 3</th></tr><tr><td>FED 0x00</td><td>MS10+</td></tr><tr><td>FED 0x01</td><td>MS10+</td></tr><tr><td>FED 0x02</td><td>MS10+</td></tr><tr><td>FED 0x03</td><td>MS10+</td></tr><tr><td>FED 0x04</td><td>MS13+</td></tr><tr><td>FED 0x05</td><td>MS13+</td></tr><tr><td>FED 0x06</td><td>MS13+</td></tr><tr><td>FED 0x07</td><td>MS13+</td></tr><tr><td></td><td></td></tr><tr><td></td><td></td></tr></table> | FED Switch | Crate ID 3 | FED 0x00 | MS10+ | FED 0x01 | MS10+ | FED 0x02 | MS10+ | FED 0x03 | MS10+ | FED 0x04 | MS13+ | FED 0x05 | MS13+ | FED 0x06 | MS13+ | FED 0x07 | MS13+ | | | | | <table><tr><th>CETIA</th><th>hb-vme72</th></tr><tr><td>SHARC 0x02</td><td>ITR_ MS10+</td></tr><tr><td>0x03</td><td>MS10-</td></tr><tr><td>0x04</td><td>MS10+</td></tr><tr><td>0x05</td><td>MS10-</td></tr><tr><td>0x06</td><td>MS10+</td></tr><tr><td>0x07</td><td>MS10-</td></tr><tr><td>0x08</td><td>MS10+</td></tr><tr><td>0x09</td><td>MS10-</td></tr><tr><td>0x0a</td><td>MS13+</td></tr><tr><td>0x0b</td><td>MS13-</td></tr><tr><td>0x0c</td><td>MS13+</td></tr><tr><td>0x0d</td><td>MS13-</td></tr><tr><td>0x0e</td><td>MS13+</td></tr><tr><td>0x0f</td><td>MS13-</td></tr><tr><td>0x10</td><td>MS13+</td></tr><tr><td>0x11</td><td>MS13-</td></tr><tr><td></td><td></td></tr><tr><td></td><td></td></tr><tr><td></td><td></td></tr><tr><td></td><td></td></tr></table> | CETIA | hb-vme72 | SHARC 0x02 | ITR_ MS10+ | 0x03 | MS10- | 0x04 | MS10+ | 0x05 | MS10- | 0x06 | MS10+ | 0x07 | MS10- | 0x08 | MS10+ | 0x09 | MS10- | 0x0a | MS13+ | 0x0b | MS13- | 0x0c | MS13+ | 0x0d | MS13- | 0x0e | MS13+ | 0x0f | MS13- | 0x10 | MS13+ | 0x11 | MS13- | | | | | | | | | <table><tr><th>FED Switch</th><th>Crate ID 2</th></tr><tr><td>FED 0x00</td><td>MS10-</td></tr><tr><td>FED 0x01</td><td>MS10-</td></tr><tr><td>FED 0x02</td><td>MS10-</td></tr><tr><td>FED 0x03</td><td>MS10-</td></tr><tr><td>FED 0x04</td><td>MS13-</td></tr><tr><td>FED 0x05</td><td>MS13-</td></tr><tr><td>FED 0x06</td><td>MS13-</td></tr><tr><td>FED 0x07</td><td>MS13-</td></tr><tr><td></td><td></td></tr><tr><td></td><td></td></tr></table> | FED Switch | Crate ID 2 | FED 0x00 | MS10- | FED 0x01 | MS10- | FED 0x02 | MS10- | FED 0x03 | MS10- | FED 0x04 | MS13- | FED 0x05 | MS13- | FED 0x06 | MS13- | FED 0x07 | MS13- | | | | |
| FED Switch | Crate ID 3 | | | | | | | | | | | | | | | | | | | | | | | | | | | | | | | | | | | | | | | | | | | | | | | | | | | | | | | | | | | | | | | | | | | | | | | | | | | | | | | | | | | | | | | |
| FED 0x00 | MS10+ | | | | | | | | | | | | | | | | | | | | | | | | | | | | | | | | | | | | | | | | | | | | | | | | | | | | | | | | | | | | | | | | | | | | | | | | | | | | | | | | | | | | | | | |
| FED 0x01 | MS10+ | | | | | | | | | | | | | | | | | | | | | | | | | | | | | | | | | | | | | | | | | | | | | | | | | | | | | | | | | | | | | | | | | | | | | | | | | | | | | | | | | | | | | | | |
| FED 0x02 | MS10+ | | | | | | | | | | | | | | | | | | | | | | | | | | | | | | | | | | | | | | | | | | | | | | | | | | | | | | | | | | | | | | | | | | | | | | | | | | | | | | | | | | | | | | | |
| FED 0x03 | MS10+ | | | | | | | | | | | | | | | | | | | | | | | | | | | | | | | | | | | | | | | | | | | | | | | | | | | | | | | | | | | | | | | | | | | | | | | | | | | | | | | | | | | | | | | |
| FED 0x04 | MS13+ | | | | | | | | | | | | | | | | | | | | | | | | | | | | | | | | | | | | | | | | | | | | | | | | | | | | | | | | | | | | | | | | | | | | | | | | | | | | | | | | | | | | | | | |
| FED 0x05 | MS13+ | | | | | | | | | | | | | | | | | | | | | | | | | | | | | | | | | | | | | | | | | | | | | | | | | | | | | | | | | | | | | | | | | | | | | | | | | | | | | | | | | | | | | | | |
| FED 0x06 | MS13+ | | | | | | | | | | | | | | | | | | | | | | | | | | | | | | | | | | | | | | | | | | | | | | | | | | | | | | | | | | | | | | | | | | | | | | | | | | | | | | | | | | | | | | | |
| FED 0x07 | MS13+ | | | | | | | | | | | | | | | | | | | | | | | | | | | | | | | | | | | | | | | | | | | | | | | | | | | | | | | | | | | | | | | | | | | | | | | | | | | | | | | | | | | | | | | |
| | | | | | | | | | | | | | | | | | | | | | | | | | | | | | | | | | | | | | | | | | | | | | | | | | | | | | | | | | | | | | | | | | | | | | | | | | | | | | | | | | | | | | | | | |
| | | | | | | | | | | | | | | | | | | | | | | | | | | | | | | | | | | | | | | | | | | | | | | | | | | | | | | | | | | | | | | | | | | | | | | | | | | | | | | | | | | | | | | | | |
| CETIA | hb-vme72 | | | | | | | | | | | | | | | | | | | | | | | | | | | | | | | | | | | | | | | | | | | | | | | | | | | | | | | | | | | | | | | | | | | | | | | | | | | | | | | | | | | | | | | |
| SHARC 0x02 | ITR_ MS10+ | | | | | | | | | | | | | | | | | | | | | | | | | | | | | | | | | | | | | | | | | | | | | | | | | | | | | | | | | | | | | | | | | | | | | | | | | | | | | | | | | | | | | | | |
| 0x03 | MS10- | | | | | | | | | | | | | | | | | | | | | | | | | | | | | | | | | | | | | | | | | | | | | | | | | | | | | | | | | | | | | | | | | | | | | | | | | | | | | | | | | | | | | | | |
| 0x04 | MS10+ | | | | | | | | | | | | | | | | | | | | | | | | | | | | | | | | | | | | | | | | | | | | | | | | | | | | | | | | | | | | | | | | | | | | | | | | | | | | | | | | | | | | | | | |
| 0x05 | MS10- | | | | | | | | | | | | | | | | | | | | | | | | | | | | | | | | | | | | | | | | | | | | | | | | | | | | | | | | | | | | | | | | | | | | | | | | | | | | | | | | | | | | | | | |
| 0x06 | MS10+ | | | | | | | | | | | | | | | | | | | | | | | | | | | | | | | | | | | | | | | | | | | | | | | | | | | | | | | | | | | | | | | | | | | | | | | | | | | | | | | | | | | | | | | |
| 0x07 | MS10- | | | | | | | | | | | | | | | | | | | | | | | | | | | | | | | | | | | | | | | | | | | | | | | | | | | | | | | | | | | | | | | | | | | | | | | | | | | | | | | | | | | | | | | |
| 0x08 | MS10+ | | | | | | | | | | | | | | | | | | | | | | | | | | | | | | | | | | | | | | | | | | | | | | | | | | | | | | | | | | | | | | | | | | | | | | | | | | | | | | | | | | | | | | | |
| 0x09 | MS10- | | | | | | | | | | | | | | | | | | | | | | | | | | | | | | | | | | | | | | | | | | | | | | | | | | | | | | | | | | | | | | | | | | | | | | | | | | | | | | | | | | | | | | | |
| 0x0a | MS13+ | | | | | | | | | | | | | | | | | | | | | | | | | | | | | | | | | | | | | | | | | | | | | | | | | | | | | | | | | | | | | | | | | | | | | | | | | | | | | | | | | | | | | | | |
| 0x0b | MS13- | | | | | | | | | | | | | | | | | | | | | | | | | | | | | | | | | | | | | | | | | | | | | | | | | | | | | | | | | | | | | | | | | | | | | | | | | | | | | | | | | | | | | | | |
| 0x0c | MS13+ | | | | | | | | | | | | | | | | | | | | | | | | | | | | | | | | | | | | | | | | | | | | | | | | | | | | | | | | | | | | | | | | | | | | | | | | | | | | | | | | | | | | | | | |
| 0x0d | MS13- | | | | | | | | | | | | | | | | | | | | | | | | | | | | | | | | | | | | | | | | | | | | | | | | | | | | | | | | | | | | | | | | | | | | | | | | | | | | | | | | | | | | | | | |
| 0x0e | MS13+ | | | | | | | | | | | | | | | | | | | | | | | | | | | | | | | | | | | | | | | | | | | | | | | | | | | | | | | | | | | | | | | | | | | | | | | | | | | | | | | | | | | | | | | |
| 0x0f | MS13- | | | | | | | | | | | | | | | | | | | | | | | | | | | | | | | | | | | | | | | | | | | | | | | | | | | | | | | | | | | | | | | | | | | | | | | | | | | | | | | | | | | | | | | |
| 0x10 | MS13+ | | | | | | | | | | | | | | | | | | | | | | | | | | | | | | | | | | | | | | | | | | | | | | | | | | | | | | | | | | | | | | | | | | | | | | | | | | | | | | | | | | | | | | | |
| 0x11 | MS13- | | | | | | | | | | | | | | | | | | | | | | | | | | | | | | | | | | | | | | | | | | | | | | | | | | | | | | | | | | | | | | | | | | | | | | | | | | | | | | | | | | | | | | | |
| | | | | | | | | | | | | | | | | | | | | | | | | | | | | | | | | | | | | | | | | | | | | | | | | | | | | | | | | | | | | | | | | | | | | | | | | | | | | | | | | | | | | | | | | |
| | | | | | | | | | | | | | | | | | | | | | | | | | | | | | | | | | | | | | | | | | | | | | | | | | | | | | | | | | | | | | | | | | | | | | | | | | | | | | | | | | | | | | | | | |
| | | | | | | | | | | | | | | | | | | | | | | | | | | | | | | | | | | | | | | | | | | | | | | | | | | | | | | | | | | | | | | | | | | | | | | | | | | | | | | | | | | | | | | | | |
| | | | | | | | | | | | | | | | | | | | | | | | | | | | | | | | | | | | | | | | | | | | | | | | | | | | | | | | | | | | | | | | | | | | | | | | | | | | | | | | | | | | | | | | | |
| FED Switch | Crate ID 2 | | | | | | | | | | | | | | | | | | | | | | | | | | | | | | | | | | | | | | | | | | | | | | | | | | | | | | | | | | | | | | | | | | | | | | | | | | | | | | | | | | | | | | | |
| FED 0x00 | MS10- | | | | | | | | | | | | | | | | | | | | | | | | | | | | | | | | | | | | | | | | | | | | | | | | | | | | | | | | | | | | | | | | | | | | | | | | | | | | | | | | | | | | | | | |
| FED 0x01 | MS10- | | | | | | | | | | | | | | | | | | | | | | | | | | | | | | | | | | | | | | | | | | | | | | | | | | | | | | | | | | | | | | | | | | | | | | | | | | | | | | | | | | | | | | | |
| FED 0x02 | MS10- | | | | | | | | | | | | | | | | | | | | | | | | | | | | | | | | | | | | | | | | | | | | | | | | | | | | | | | | | | | | | | | | | | | | | | | | | | | | | | | | | | | | | | | |
| FED 0x03 | MS10- | | | | | | | | | | | | | | | | | | | | | | | | | | | | | | | | | | | | | | | | | | | | | | | | | | | | | | | | | | | | | | | | | | | | | | | | | | | | | | | | | | | | | | | |
| FED 0x04 | MS13- | | | | | | | | | | | | | | | | | | | | | | | | | | | | | | | | | | | | | | | | | | | | | | | | | | | | | | | | | | | | | | | | | | | | | | | | | | | | | | | | | | | | | | | |
| FED 0x05 | MS13- | | | | | | | | | | | | | | | | | | | | | | | | | | | | | | | | | | | | | | | | | | | | | | | | | | | | | | | | | | | | | | | | | | | | | | | | | | | | | | | | | | | | | | | |
| FED 0x06 | MS13- | | | | | | | | | | | | | | | | | | | | | | | | | | | | | | | | | | | | | | | | | | | | | | | | | | | | | | | | | | | | | | | | | | | | | | | | | | | | | | | | | | | | | | | |
| FED 0x07 | MS13- | | | | | | | | | | | | | | | | | | | | | | | | | | | | | | | | | | | | | | | | | | | | | | | | | | | | | | | | | | | | | | | | | | | | | | | | | | | | | | | | | | | | | | | |
| | | | | | | | | | | | | | | | | | | | | | | | | | | | | | | | | | | | | | | | | | | | | | | | | | | | | | | | | | | | | | | | | | | | | | | | | | | | | | | | | | | | | | | | | |
| | | | | | | | | | | | | | | | | | | | | | | | | | | | | | | | | | | | | | | | | | | | | | | | | | | | | | | | | | | | | | | | | | | | | | | | | | | | | | | | | | | | | | | | | |
| <div>Optical Senders IF9-1 for digital control signals</div> | <table><tr><th>CETIA</th><th>hb-vme74</th></tr><tr><td>SHARC 0x02</td><td>ITR_ MS14-</td></tr><tr><td>0x03</td><td></td></tr><tr><td>0x04</td><td>MS14/15-</td></tr><tr><td>0x05</td><td></td></tr><tr><td>0x06</td><td>MS15-</td></tr><tr><td>0x07</td><td></td></tr><tr><td></td><td></td></tr><tr><td></td><td></td></tr><tr><td></td><td></td></tr><tr><td>DataValid</td><td>Φ3</td></tr><tr><td>DataValid</td><td>Φ2</td></tr><tr><td>DataValid</td><td>Φ1</td></tr><tr><td>FED Repeater</td><td></td></tr><tr><td>FED Controller</td><td>Φ3 0xef</td></tr><tr><td>FED Controller</td><td>Φ2 0xee</td></tr><tr><td>FED Controller</td><td>Φ1 0xed</td></tr><tr><td>FCS Daughter</td><td></td></tr></table> | CETIA | hb-vme74 | SHARC 0x02 | ITR_ MS14- | 0x03 | | 0x04 | MS14/15- | 0x05 | | 0x06 | MS15- | 0x07 | | | | | | | | DataValid | Φ3 | DataValid | Φ2 | DataValid | Φ1 | FED Repeater | | FED Controller | Φ3 0xef | FED Controller | Φ2 0xee | FED Controller | Φ1 0xed | FCS Daughter | | <table><tr><th>FED Switch</th><th>Crate ID 4</th></tr><tr><td>FED 0x00</td><td>MS14-</td></tr><tr><td>FED 0x01</td><td>MS14-/15-</td></tr><tr><td>FED 0x02</td><td>MS15-</td></tr><tr><td></td><td></td></tr><tr><td></td><td></td></tr><tr><td></td><td></td></tr><tr><td></td><td></td></tr><tr><td></td><td></td></tr><tr><td></td><td></td></tr></table> | FED Switch | Crate ID 4 | FED 0x00 | MS14- | FED 0x01 | MS14-/15- | FED 0x02 | MS15- | | | | | | | | | | | | | | | | | | | | | | | | | | | | | | | | | | | | | | | | | | |
| CETIA | hb-vme74 | | | | | | | | | | | | | | | | | | | | | | | | | | | | | | | | | | | | | | | | | | | | | | | | | | | | | | | | | | | | | | | | | | | | | | | | | | | | | | | | | | | | | | | |
| SHARC 0x02 | ITR_ MS14- | | | | | | | | | | | | | | | | | | | | | | | | | | | | | | | | | | | | | | | | | | | | | | | | | | | | | | | | | | | | | | | | | | | | | | | | | | | | | | | | | | | | | | | |
| 0x03 | | | | | | | | | | | | | | | | | | | | | | | | | | | | | | | | | | | | | | | | | | | | | | | | | | | | | | | | | | | | | | | | | | | | | | | | | | | | | | | | | | | | | | | | |
| 0x04 | MS14/15- | | | | | | | | | | | | | | | | | | | | | | | | | | | | | | | | | | | | | | | | | | | | | | | | | | | | | | | | | | | | | | | | | | | | | | | | | | | | | | | | | | | | | | | |
| 0x05 | | | | | | | | | | | | | | | | | | | | | | | | | | | | | | | | | | | | | | | | | | | | | | | | | | | | | | | | | | | | | | | | | | | | | | | | | | | | | | | | | | | | | | | | |
| 0x06 | MS15- | | | | | | | | | | | | | | | | | | | | | | | | | | | | | | | | | | | | | | | | | | | | | | | | | | | | | | | | | | | | | | | | | | | | | | | | | | | | | | | | | | | | | | | |
| 0x07 | | | | | | | | | | | | | | | | | | | | | | | | | | | | | | | | | | | | | | | | | | | | | | | | | | | | | | | | | | | | | | | | | | | | | | | | | | | | | | | | | | | | | | | | |
| | | | | | | | | | | | | | | | | | | | | | | | | | | | | | | | | | | | | | | | | | | | | | | | | | | | | | | | | | | | | | | | | | | | | | | | | | | | | | | | | | | | | | | | | |
| | | | | | | | | | | | | | | | | | | | | | | | | | | | | | | | | | | | | | | | | | | | | | | | | | | | | | | | | | | | | | | | | | | | | | | | | | | | | | | | | | | | | | | | | |
| | | | | | | | | | | | | | | | | | | | | | | | | | | | | | | | | | | | | | | | | | | | | | | | | | | | | | | | | | | | | | | | | | | | | | | | | | | | | | | | | | | | | | | | | |
| DataValid | Φ3 | | | | | | | | | | | | | | | | | | | | | | | | | | | | | | | | | | | | | | | | | | | | | | | | | | | | | | | | | | | | | | | | | | | | | | | | | | | | | | | | | | | | | | | |
| DataValid | Φ2 | | | | | | | | | | | | | | | | | | | | | | | | | | | | | | | | | | | | | | | | | | | | | | | | | | | | | | | | | | | | | | | | | | | | | | | | | | | | | | | | | | | | | | | |
| DataValid | Φ1 | | | | | | | | | | | | | | | | | | | | | | | | | | | | | | | | | | | | | | | | | | | | | | | | | | | | | | | | | | | | | | | | | | | | | | | | | | | | | | | | | | | | | | | |
| FED Repeater | | | | | | | | | | | | | | | | | | | | | | | | | | | | | | | | | | | | | | | | | | | | | | | | | | | | | | | | | | | | | | | | | | | | | | | | | | | | | | | | | | | | | | | | |
| FED Controller | Φ3 0xef | | | | | | | | | | | | | | | | | | | | | | | | | | | | | | | | | | | | | | | | | | | | | | | | | | | | | | | | | | | | | | | | | | | | | | | | | | | | | | | | | | | | | | | |
| FED Controller | Φ2 0xee | | | | | | | | | | | | | | | | | | | | | | | | | | | | | | | | | | | | | | | | | | | | | | | | | | | | | | | | | | | | | | | | | | | | | | | | | | | | | | | | | | | | | | | |
| FED Controller | Φ1 0xed | | | | | | | | | | | | | | | | | | | | | | | | | | | | | | | | | | | | | | | | | | | | | | | | | | | | | | | | | | | | | | | | | | | | | | | | | | | | | | | | | | | | | | | |
| FCS Daughter | | | | | | | | | | | | | | | | | | | | | | | | | | | | | | | | | | | | | | | | | | | | | | | | | | | | | | | | | | | | | | | | | | | | | | | | | | | | | | | | | | | | | | | | |
| FED Switch | Crate ID 4 | | | | | | | | | | | | | | | | | | | | | | | | | | | | | | | | | | | | | | | | | | | | | | | | | | | | | | | | | | | | | | | | | | | | | | | | | | | | | | | | | | | | | | | |
| FED 0x00 | MS14- | | | | | | | | | | | | | | | | | | | | | | | | | | | | | | | | | | | | | | | | | | | | | | | | | | | | | | | | | | | | | | | | | | | | | | | | | | | | | | | | | | | | | | | |
| FED 0x01 | MS14-/15- | | | | | | | | | | | | | | | | | | | | | | | | | | | | | | | | | | | | | | | | | | | | | | | | | | | | | | | | | | | | | | | | | | | | | | | | | | | | | | | | | | | | | | | |
| FED 0x02 | MS15- | | | | | | | | | | | | | | | | | | | | | | | | | | | | | | | | | | | | | | | | | | | | | | | | | | | | | | | | | | | | | | | | | | | | | | | | | | | | | | | | | | | | | | | |
| | | | | | | | | | | | | | | | | | | | | | | | | | | | | | | | | | | | | | | | | | | | | | | | | | | | | | | | | | | | | | | | | | | | | | | | | | | | | | | | | | | | | | | | | |
| | | | | | | | | | | | | | | | | | | | | | | | | | | | | | | | | | | | | | | | | | | | | | | | | | | | | | | | | | | | | | | | | | | | | | | | | | | | | | | | | | | | | | | | | |
| | | | | | | | | | | | | | | | | | | | | | | | | | | | | | | | | | | | | | | | | | | | | | | | | | | | | | | | | | | | | | | | | | | | | | | | | | | | | | | | | | | | | | | | | |
| | | | | | | | | | | | | | | | | | | | | | | | | | | | | | | | | | | | | | | | | | | | | | | | | | | | | | | | | | | | | | | | | | | | | | | | | | | | | | | | | | | | | | | | | |
| | | | | | | | | | | | | | | | | | | | | | | | | | | | | | | | | | | | | | | | | | | | | | | | | | | | | | | | | | | | | | | | | | | | | | | | | | | | | | | | | | | | | | | | | |
| | | | | | | | | | | | | | | | | | | | | | | | | | | | | | | | | | | | | | | | | | | | | | | | | | | | | | | | | | | | | | | | | | | | | | | | | | | | | | | | | | | | | | | | | |

Figure A.1: Readout crates for the ITR in the electronics trailer

A.2 Configuration of the FED Controller

```

## PC area
# VME properties of FED controller
controlleraddr      ee

# Xilinx controller register values, DECimal numbers please
roNumOfChips      2          # Gate = roNumOfChips * 136 +
GateExtension     15          #      GateExtension
TriggerDelay      6
DataValidDelay    2
DataValidJitter   0          # 2 bits: 0..3
ReadClkFreq       1          # RClk = n * BxCk; n = 1, 2, (4)

# special registers for Helix bug fixes (IN DECIMAL)
#      for RClk=BxCk: BugFix = 123 - TriggerDelay +-1;
#      for RClk=2*BxCk: BugFix = 115 - 2*TriggerDelay +-1;
#      +-2 depend on the relative phase between RClk and BxCk
HelixBugFix       116          # for trigger sequence bug,

AutoTriggerFLTNum  33
AutoTriggerBxFLT   22
AutoTriggerFLTType  0
AutoTestPulse      0
TestPulseTriggerDelay 7
fcstrigger_enable  1
autogate_enable    0
triggersynch_enable 0
fcstestpulse_enable 0
DelayReset         1

fed_init_file /home/hbitr/fed2/fed_v7a.mcs

# FED register values
controlword 0          # 0: ADC-Data    1: Testdata
bytecount   300
componentid 2

# bit mask (hexadecimal, please) : which FEDs are actually connected
fed_switch[0] 3ff
fed_switch[1] ff
fed_switch[2] ff
fed_switch[3] ff
fed_switch[4] 6          # MS15- test setup
fed_switch[5] 0
fed_switch[6] 0

# delay: one unit corresponds to 0.5ns to 1.0ns
#      settings in decimal, please.
delay_BxCk      20          # BxCk to Helix
delay_FEDGate   20          # digitization gate to FED
delay_PrgGate    0          # programming gate to Helix
delay_RClk     110          # RClk to Helix
delay_RClkToFED 76          # RClk to FEDs
delay_Testpulse 0          # TestPulse to Helix
delay_Trigger   120          # Trigger to Helix

```


Appendix B

Organisation of the ITR Software

This appendix describes in detail the organisation of the Inner Tracker software packages. The information presented here is collected for reference. The structure of the Inner Tracker software follows rather closely that of the Vertex Detector, because the VDS software was taken as a starting point for the ITR. The kind help of the VDS group, especially R. Wanke and B. Schwingenheuer, is gratefully acknowledged.

B.1 Software Packages for Data Processing

The following software packages provide the functionality needed to process the raw data. All packages allow the user to set important parameters either by reading in a plain-text steering file or by reading a special database table called `ITR_Steering`.

itrleda

This module provides an interface to all database tables of the Inner Tracker. It allows the selection of a specific version of the tables and takes care of reading the tables from the database. It also offers a defined interface to write updates of the tables to the database.

ITR_silraw

ITR_silraw contains all functions needed to read event data in various formats. It can cope with the data format used by the common data acquisition system; it provides the following modules with the event data from the Inner Tracker in a unified format.

If there are any raw FED data blocks available, the data of the two chips read out by the FED is identified (using user-selectable ‘datavalid offsets’ to skip the first few bytes not containing analogue data). The pipeline column number found in the analogue data is determined.

ITR_marvin

All real processing of the chip data is done in the module ITR_marvin. First, pedestal and baseline corrections are applied on a chip-by-chip basis, and the estimates for pedestal values and subtracted variances are updated. Then the corrected data of all chips attached to one chamber are joined, using the chip id and the setup database to match chips with chambers. The clusterfinder is then run on the whole data of one chamber, and the found clusters are stored in an internal memory area. Other routines then can access the cluster information by calling a defined interface routine.

itrslt

At the start of a run, the processes running on the Second Level Trigger nodes have to read in the content of the configuration and setup database for all subdetectors. To decrease the network bandwidth needed for the distribution of the constants, only one process per subdetector actually accesses the database server; this *formatter process* then broadcasts the constants to the SLT nodes using the high bandwidth connection provided by the SHARC interface on each node. The package `itrslt` contains the routines which convert the ITR database tables into a format which can be digested by the SLT formatter. The

itrarte

All data processing routines must also be available to the general reconstruction program ARTE. The package `itrarte` provides an interface between the low-level routines accessing the raw data and the high-level reconstruction routines. Using the routines provided by `ITR_marvin`, the sparsified data block which is stored in an event file is read in, if it is present, or the cluster finder is run on the available raw data. The found clusters are then stored in the ARTE table HITB where the track finding routine can access them. Other helper routines

B.2 Organisation on Disk

The source code for all the software packages (with the exception of `itrarte`) can be found in the directory `/afs/desy.de/group/hera-b/ITR/packages/`. Each software package has its own directory, in which subdirectories for the different versions can be found. In each of the version subdirectories, there exists one directory for the source code, and various directories for the binary files for different computer platforms. The utilities to build a complete library reside in `/afs/desy.de/group/hera-b/ITR/libitr<version>`. Application programs which use the ITR software need only to link against `/afs/desy.de/group/hera-b/ITR/libitr<version>/lib.<BINTYPE>/libitr.a`.

B.3 Programs running online

itrfmt

This program is the formatting process which reads the setup and configuration database tables and provides them in a format suitable for broadcasting to all online processes. It is automatically started by the central run control on one of the common DAQ computers.

itr_init_smc

This program controls the operation of the FED Controllers. It runs on the CPU of one readout crate and loads the needed registers (like values for clock delays, configuration of the FED boards, *etc.*) into the FED controllers. For each FED Controller, one instance of `itr_init_smc` is started automatically by the run control software. The central run control is notified about any error conditions occurring during this initialisation phase.

ph

This standalone program was written to load the Helix registers using the readout hardware of the Inner Tracker. Its usage is described in [Gra98]. It is not integrated into the central HERA-B slow control schema, but has to be started by a dedicated Inner Tracker shift crew

between data taking runs. This is error-prone (it could be forgotten, or started while the data is already taken, leading to corrupted data from the Inner Tracker) and certainly not a viable long-term solution. Work is ongoing ([Wie01]) to overcome these weak points and to make the loading of the registers much faster. The new version of the programme will be available for the start of the run 2001/2002.

Appendix C

Total Gain of the Analogue Readout Chain

A measurement of the total gain of the complete analogue readout chain is shown in Fig. C.1. For this measurement, a GEM-MSGC which was fully equipped with readout electronics was used. The charge was injected into the Kapton strip-line connecting the chamber and the Helix PCB. The analogue output was observed with an oscilloscope which was also used to subtract the pedestal. With the receiver circuit described above and the combination of optical sender and receiver, a Helix attached to a GEM-MSGC shows a charge gain of

$$g_{\text{slow}} = 40.7 \frac{\text{mV}}{24\,000 \text{ e}^-} \quad (\text{C.1})$$

This measurement was done with the default Helix settings described in [FB⁺99] and used during the PSI test beam experiments in 1998 and 1999. The settings used in HERA-*B* for most of the run period 2000 differ from these (see Sect. 4.4): the peak height is about 43% larger and the fall time is shorter. Scaling the gain with the peak height, one obtains for the new Helix settings

$$g_{\text{fast}} = 58 \frac{\text{mV}}{24\,000 \text{ e}^-} \quad (\text{C.2})$$

The ADC used in the FED board has an input range of 1 V and a resolution of 8 bits. Thus the conversion factor between ADC counts and charge at the input of the Helix is

$$g_{\text{fast,ADC}}^{-1} \approx 1\,620 \frac{\text{e}^-}{\text{ADC}} \quad (\text{C.3})$$

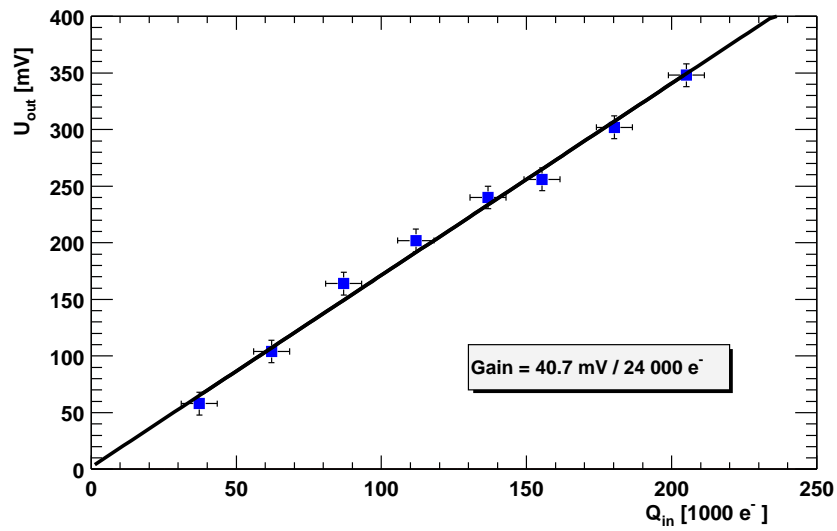


Figure C.1: Measurement of the total gain of the analogue readout chain. The Helix was attached to a GEM-MSGC, the register settings used are those of the Helix manual ('slow shaping').

Appendix D

Kinematics of the Drell-Yan Process

D.1 Kinematical Variables

The kinematics of inclusive $2 \rightarrow 2$ scattering processes are described by a suitable set of only two independent variables. These variables should be invariant under at least a suitable subset of Lorentz transformations, *e.g.* those boosting the laboratory frame into the overall hadronic centre-of-mass system (usually, these are Lorentz boosts along the beam axis, or along z). The invariant cross-section for a reaction can then be expressed in terms of these variables.

Usually, at fixed-target experiments, the chosen variables are x_F and τ . The Feynman scaling variable x_F describes the longitudinal momentum p_z of the scattering product, expressed in terms of the maximally possible momentum $p_{z,\max}$,

$$x_F \equiv \frac{p_z}{p_{z,\max}}. \quad (\text{D.1})$$

In the limit that for each of the particles concerned $p_z \gg m$, x_F is invariant under Lorentz boosts along the z -axis. The maximally allowed longitudinal momentum $p_{z,\max}^*$ in the centre-of-mass system is $p_{z,\max}^* \approx \sqrt{s}/2$, therefore $x_F = 2p_z^*/\sqrt{s}$.

The variable τ is defined as the square of the invariant mass M of the scattering products scaled with the square s of the centre-of-mass energy,

$$\tau \equiv \frac{M^2}{s} \quad (\text{D.2})$$

In the language of the quark-parton model, the hadrons which participate in a scattering process are composed of *partons*. In the infinite momentum frame (where the parton masses can be neglected compared to the momenta), each parton i carries only a fraction x_i of the hadron momentum. A hard scattering process of two hadrons is described by a hard scattering of two partons, while the other partons only play a spectator role. The centre-of-mass energy $\sqrt{\hat{s}}$ which is available for the scattering process is only a fraction of the overall centre-of-mass energy \sqrt{s} of the two hadrons:

$$\hat{s} = x_1 x_2 s \quad (\text{D.3})$$

The variables x_F and τ can be expressed as functions of x_1 and x_2 :

$$x_F = x_1 - x_2 \quad (\text{D.4})$$

$$\tau = x_1 x_2. \quad (\text{D.5})$$

Instead of x_F , the kinematics parallel to the beam axis is frequently expressed in terms of the *rapidity* y ,

$$y \equiv \frac{1}{2} \ln \frac{E + p_z}{E - p_z}. \quad (\text{D.6})$$

Under a Lorentz boost along the z -axis to a frame with velocity β , $y \mapsto y' = y - \tanh^{-1} \beta$; therefore rapidity differences are invariant under these transformations. In the centre-of-mass system, $y^* > 0$ corresponds to the *forward hemisphere*. For high momenta, y can be approximated by the *pseudo-rapidity* $\eta \equiv \ln \tan(\theta/2)$, where θ is the scattering angle.

An alternative variable describing the kinematics perpendicular to the z -axis is the *transverse momentum* p_T :

$$p_T \equiv \sqrt{p_x^2 + p_y^2} \quad (\text{D.7})$$

D.2 Reference Frames

To describe the angular distribution of the decay products, a suitable reference frame has to be fixed. Naturally, the reference frame should be co-moving with the rest frame of the virtual photon; however, the choice of the three-dimensional coordinate system within the reference frame is not unique. Ideally, one would like the z -axis to coincide with the scattering axis of the incoming partons, but the partonic process is not directly observable. Therefore,

For the Drell-Yan process, three common choices for the coordinate system can be found in the literature; they can be transformed into each other by a rotation around the y axis.

Collins-Soper frame: The CS frame [CS77] (depicted schematically in Fig. D.1) is defined as follows:

- The CS frame is comoving to the rest frame of the virtual photon.
- If the virtual photon γ^* has a non-vanishing transverse momentum in the proton-nucleon rest frame, the momentum vectors of proton and nucleon are not collinear in the rest frame of the γ^* . They span a plane which is taken as the (xz) -plane of the CS frame. The angle 2β between the proton and the nucleon directions is given by

$$\tan \beta = \frac{p_{T\gamma^*}}{M_{\gamma^*}} \quad (\text{D.8})$$

where $p_{T\gamma^*}$ is measured in the overall proton-nucleon centre-of-mass system.

- The z -axis of the CS frame is taken to be the bisector of the direction of the incoming nucleon and the negative direction of the incoming proton.

Gottfried-Jackson frame: the z -axis is parallel to the direction of the incoming proton.

u -channel frame: the z -axis is parallel to the negative direction of the incoming nucleon.

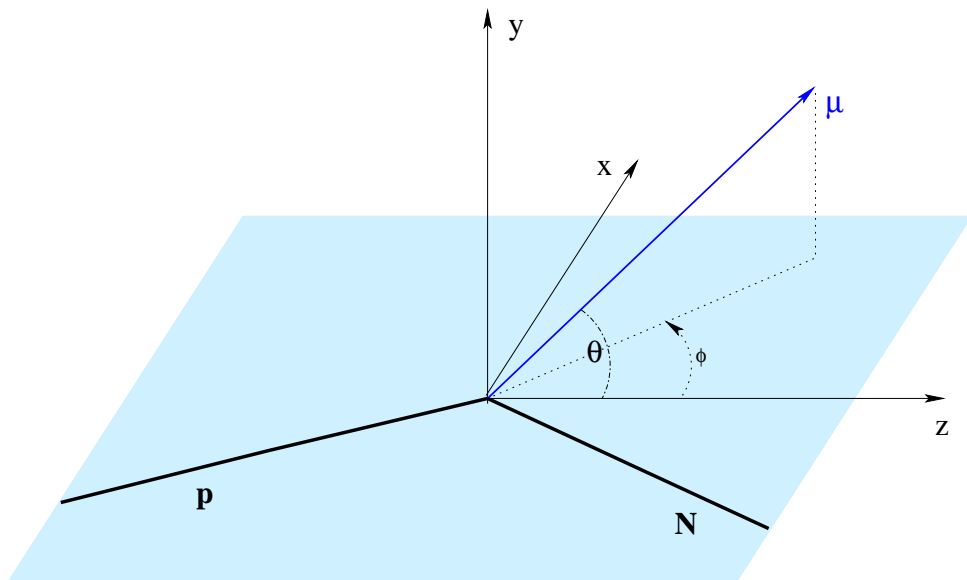


Figure D.1: Definition of the Collins-Soper (CS) frame.

Bibliography

- [A⁺84] L. Anderson et al., [NA10] , *A High Resolution Spectrometer for the Study of High Mass Muon Pairs Produced by Intense Hadron Beams*, Nucl. Instr. Meth. **A223** (1984), 26.
- [A⁺98] M. C. Abreu et al., [NA38] , *A four-dimensional deconvolution method to correct NA38 experimental data*, Nucl. Instr. Meth. **A 405** (1998), 139–152.
- [A⁺00] M. C. Abreu et al., [NA50] , *Evidence for deconfinement of quarks and gluons from the J/psi suppression pattern measured in Pb Pb collisions at the CERN-SPS*, Phys. Lett. **B477** (2000), 28–36.
- [A⁺01a] A. Abashian et al., [BELLE] , *Measurement of the CP violation parameter $\sin 2\phi(1)$ in B/d0 meson decays*, Phys. Rev. Lett. **86** (2001), 2509–2514, hep-ex/0102018.
- [A⁺01b] B. Aubert et al., [BABAR] , *Measurement of CP violating asymmetries in B0 decays to CP eigenstates*, Phys. Rev. Lett. **86** (2001), 2515–2522, hep-ex/0102030.
- [AG95] M. Adler and J.-L. Gailly, *zlib*, 1995,
<http://www.info-zip.org/pub/infozip/zlib/>.
- [Ana99] Analog Devices, Inc., *AD8004 Data Sheet*, 1999,
http://www.analog.com/pdf/AD8004_b.pdf.
- [ART] *ARTE, HERA-B event reconstruction software*,
<http://www-hera-b.desy.de/subgroup/software/>.
- [B⁺86] C. Biino et al., *An Apparatus to Measure the Structure of the Pion*, Nucl. Instr. Meth. **A243** (1986), 323.
- [BAB01] BABAR Collaboration, [BABAR] , *The BABAR Detector*, hep-ex/0105044, Submitted to Nucl. Instr. Meth.
- [BB79] Edmond L. Berger and Stanley J. Brodsky, *Quark Structure Functions of Mesons and the Drell-Yan Process*, Phys. Rev. Lett. **42** (1979), 940–944.
- [BBKM94] A. Brandenburg, S. J. Brodsky, V. V. Khoze, and D. Müller, *Angular distributions in the Drell-Yan process: A Closer look at higher twist effects*, Phys. Rev. Lett. **73** (1994), 939–942, hep-ph/9403361.
- [BEL01] BELLE Collaboration, *The Belle Detector*, submitted to Nucl. Inst. Meth. (2001), KEK Progress Report 2000-4.
- [Ber80] E. L. Berger, *Higher Twist Effects In Deep Inelastic Scattering*, Phys. Lett. **B89** (1980), 241.

- [BGK98] Edmond L. Berger, Lionel E. Gordon, and Michael Klasen, *Massive lepton pairs as a prompt photon surrogate*, Phys. Rev. **D58** (1998), 074012, hep-ph/9803387.
- [BM⁺98] P. Braun-Munzinger et al., *Open charm contribution to dilepton spectra produced in nuclear collisions at SPS energies*, Eur. Phys. J. **C1** (1998), 123–130.
- [BNM93] A. Brandenburg, O. Nachtmann, and E. Mirkes, *Spin effects and factorization in the Drell-Yan process*, Z. Phys. **C60** (1993), 697–710.
- [Boh01] Gerhard Bohm, Private Communication, April 2001.
- [Brä01] Martin Bräuer, Private Communication, March 2001.
- [Bre97] Carola Bresch, *Neuere Untersuchungen von Prototypen der Gas-Mikrostreifen-Kammern (MSGC) des inneren Spurkammersystems des HERA-B Experiments*, Diploma thesis, University of Heidelberg, July 1997.
- [BS01] Gerhard Bohm and Ulli Schwanke, Private Communication, April 2001.
- [Buc00] Verena Buchholz, *Monitoring für das Innere Spurkammersystem von HERA-B*, Diploma thesis, University of Heidelberg, February 2000.
- [C⁺89] J. S. Conway et al., [E615], *Experimental study of muon pairs produced by 252-GeV pions on tungsten*, Phys. Rev. **D39** (1989), 92.
- [CCFT64] J. H. Christenson, J. W. Cronin., V. L. Fitch, and R. Turlay, *Evidence for the 2π decay of the K_2^0 meson*, Phys. Rev. Lett. **13** (1964), 138.
- [CDF⁺00] M. Ciuchini, G. D’Agostini, E. Franco, V. Lubicz, G. Martinelli, F. Parodi, P. Roudeau, and A. Stocchi, *2000 CKM-Triangle Analysis A Critical Review with Updated Experimental Inputs and Theoretical Parameters*, 2000, hep-ph/0012308, submitted to JHEP.
- [CS77] J. C. Collins and D. E. Soper, *Angular Distribution Of Dileptons in High-Energy Hadron Collisions*, Phys. Rev. **D16** (1977), 2219.
- [ESW96] R. K. Ellis, W. J. Stirling, and B. R. Webber, *QCD and Collider Physics*, Cambridge University Press, 1996.
- [ETB98] *Event Tool Box*, 1998,
<ftp://ftp.desy.de/pub/herab/daq/etb.ps>.
- [Ets00] Konrad Etschberger (ed.), *Controller-Area-Network*, 2nd ed., Carl Hanser Verlag, München, Wien, 2000.
- [FB98] Wolfgang Fallot-Burghardt, *A CMOS mixed-signal readout chip for the microstrip detectors of HERA-B*, Ph.D. thesis, University of Heidelberg, 1998.
- [FB⁺99] W. Fallot-Burghardt et al., *Helix128-x User Manual*, February 1999, HD-ASIC-33-0697,
<http://wwwasic.kip.uni-heidelberg.de/~feuersta/projects/Helix/helix/helix.html>.
- [FHS91] Hansjörg Fischle, Joachim Heintze, and Bernhard Schmidt, *Experimental determination of ionization cluster size distributions in counting gases*, Nucl. Instrum. Meth. **A301** (1991), 202–214.

- [Fom00] Boris Fominykh, *Study of muon identification on muon SLT triggered events*, Talk during the HERA-B collaboration week, October 2000.
- [FR99] Martin Feuerstack-Raible, Private Communication, 1999.
- [Ful99] Thomas Fuljahn, *Aufbau und Charakterisierung des schnellen Kontrollsystems für das Experiment HERA-B*, Ph.D. thesis, University of Hamburg, 1999.
- [G⁺88] M. Guanziroli et al., [NA10] , *Angular distributions of muon pairs produced by negative pions on deuterium and tungsten*, Z. Phys. **C37** (1988), 545.
- [G⁺00] D.E. Groom et al., [Particle Data Group] , *Review of Particle Physics*, Eur. Phys. J. **C15** (2000), 1+.
- [Ger99] Martin Gerlowski, *Die Slow Control des HERA-B Inner Trackers und Auswertung von Testmessungen mit kompletter Auslekette*, Diploma thesis, University of Heidelberg, January 1999.
- [GKM82] S. Graham, P. Kessler, and M. McKusick, *gprof: A Call Graph Execution Profiler*, Proceedings of the SIGPLAN '82 Symposium on Compiler Construction, SIGPLAN Notices **17** (1982), no. 6, 120–126.
- [Gla97] Boris Glass, *Analoge Auslese- und Triggerelektronik für Mikrostreifen-Gaszähler*, Diploma thesis, University of Heidelberg, 1997.
- [Gra98] Wolfgang Gradl, *ph — Program Helix via CAN Bus*, May 1998, software manual, <http://www.physi.uni-heidelberg.de/~gradl/herab/ph/>.
- [har98] [BABAR] , *The BABAR Physics Book*, Tech. report, SLAC, October 1998, SLAC-R-504.
- [Hau98] Sebastian Hausmann, *Das Auslesesystem der Inneren Spurkammern bei HERA-B*, Ph.D. thesis, University of Heidelberg, 1998.
- [HER00a] HERA-B Collaboration, *HERA-B Physics in 2001/2002*, Letter to the DESY Directorate, December 2000.
- [HER00b] HERA-B Collaboration, *Report on Status and Prospects*, DESY PRC 00/04, October 2000.
- [HER01] HERA-B Collaboration, *Update of status and plans for 2001/2002*, Internal Report, April 2001, HERA-B 01-064.
- [Hil99] Malte Hildebrandt, *Entwicklung und Bau der Detektoren für das Innere Spurkammersystem bei HERA-B*, Ph.D. thesis, University of Heidelberg, 1999.
- [Hot97] Thomas Hott, *Entwicklung und Test großflächiger Mikro-Streifen-Gas-Kammern für das innere Spurkammersystem von HERA-B*, Ph.D. thesis, University of Heidelberg, 1997.
- [Hus01] Ulrich Husemann, *Prospects of Drell-Yan Physics with the HERA-B Detector*, Diploma thesis, University of Dortmund, March 2001.
- [IKL99] Jenny Ivarsson, Peter Kreuzer, and Thomas Lohse, *PYTHIA and FRITIOF: Event Generators for HERA-B*, HERA-B internal note H, March 1999, HERA-B 99-067.

- [K⁺01] C. Krauss et al., *Inner Tracker Performance in 2000*, HERA-B internal note 01-060, April 2001.
- [Kel01] Stefan Keller, *Aufbau eines Spurtriggers bei HERA-B mit GEM-MSGC Detektoren*, Ph.D. thesis, University of Siegen, 2001.
- [KK01] C. Krauss and A. Köster, Private Communications, May 2001.
- [Kla01] M. Klasen, Private Communications, Jan 2001.
- [L⁺95] T. Lohse et al., [HERA-B Collaboration] , *HERA-B Technical Design Report*, January 1995, DESY-PRC 95/01.
- [LT80] C. S. Lam and W.-K. Tung, *Parton-model relation without quantum-chromodynamic modifications in lepton pair production*, Phys. Rev. **D21** (1980), 2712.
- [Lue57] G. Lueders, *Proof of the TCP theorem*, Annals Phys. **2** (1957), 1–15.
- [M⁺94] P. L. McGaughey et al., [E772] , *Cross-sections for the production of high mass muon pairs from 800-GeV proton bombardment of H-2*, Phys. Rev. **D50** (1994), 3038–3045.
- [Mas00] Silvia Masciocchi, Private Communication, May 2000.
- [Mas01] Silvia Masciocchi, Private Communication, May 2001.
- [Med97] Mike Medinnis, *HERA-B Trigger and DAQ System Architecture*, Talk at Beauty 1997, 1997, HERA-B note, <ftp://ftp.desy.de/pub/herab/slt/talks/b97.ps.gz>.
- [Mit94] Mitel Semiconductor Corp., *1A194 Data Sheet*, 1994, http://www.mitelsemi.com/products/data/datasheets/mitel_1A194_Sep_1994.pdf.
- [Mit99] Mitel Semiconductor Corp., *1A444 Data Sheet*, 1999, <http://www.mitelsemi.com/products/data/datasheets/1a444.pdf>.
- [Nat98] National Semiconductor, *LVDS Quad CMOS Differential Line Driver and Receiver*, 1998, <http://www.national.com/ds/DS/DS90C031.pdf> <http://www.national.com/ds/DS/DS90C032.pdf>.
- [NR84] O. Nachtmann and A. Reiter, *The Vacuum Structure In QCD And Hadron-Hadron Scattering*, Z. Phys. **C24** (1984), 283.
- [Oed88] A. Oed, *Position-sensitive detector with microstrip anode for electron multiplication with gases*, Nucl. Instr. and Meth. **A 263** (1988), 351.
- [PB95] H. Plochow-Besch, *PDFLIB: The Parton Distribution Function Library*, Int. J. Mod. Phys **A10** (1995), 2901–2920, Version 8.04, CERN-PPE W5051 PDFLIB.
- [Pet01] Brian Petersen, Private Communication, May 2001.
- [Phi96] Philips Semiconductors, *P82C150 (SLIO) Data Sheet*, 1996, http://www-eu2.semiconductors.com/acrobat/datasheets/P82C150_2.pdf.
- [Pi92] Hong Pi, *An Event generator for interactions between hadrons and nuclei: FRITIOF version 7.0*, Comput. Phys. Commun. **71** (1992), 173.

- [Res97] Dominik Ressing, *Protocols & Data Formats in HERA-B*, 1997, <ftp://ftp.desy.de/pub/herab/daq/format.ps>.
- [Ric00] Carola Richter, *Development of Micro Pattern Gas Detectors for High Rate Experiments*, Ph.D. thesis, University of Heidelberg, 2000.
- [RPM] *Proposal for a HERA-B Message Handler Interface*, ftp://ftp.desy.de/pub/herab/daq/rpm_doc.ps.
- [S⁺95] M. H. Schub et al., [E789], *Measurement of J/ψ and ψ -prime production in 800-GeV/c proton - gold collisions*, Phys. Rev. **D52** (1995), 1307–1315.
- [S⁺98] U. Straumann et al., *Operation of a large GEM-MSGC detector in a high intensity hadronic test beam using fully pipelined readout electronics*, HERA-B internal note 98-149, October 1998.
- [Sau97] F. Sauli, *GEM: A new concept for electron amplification in gas detectors*, Nucl. Instrum. Meth. **A386** (1997), 531.
- [Sch99a] Bernhard Schmidt, *Simulation of Pulses shapes and Distributions*, unpublished, December 1999.
- [Sch99b] Bernhard Schwingenheuer, *Description of the Hera-B Front-End Electronics for the Silicon Vertex Detector and the Inner Tracker*, July 1999, HERA-B internal note 99-013.
- [Sch01] Bernhard Schmidt, Private communication, March 2001.
- [Sex97] Edgar Sexauer, *Charakterisierung des HELIX 128-Auslesechips für HERA-B*, Diploma thesis, University of Heidelberg, 1997.
- [Sjö94] T. Sjöstrand, *High-energy-physics event generation with PYTHIA 5.7 and JETSET 7.4*, Comp. Phys. Commun. **82** (1994), 74, Long Writeup CERN-TH.7112/93.
- [Sle] Sleepycat Software, <http://www.sleepycat.com/>.
- [TDD99] U. Trunk, F. Dehnhardt, and H. Deppe, *Helix Pulseshape Scans*, 1999, <http://wwwasic.kip.uni-heidelberg.de/~feuersta/projects/Helix/PulseShapeSpace/-index.html>.
- [Tit96] Maxim Titov, *Studies of Background for Muon Identification at the HERA-B Experiment*, Internal Note, 1996, HERA-B 96-137.
- [Tru00] Ulrich Trunk, *Development and Characterisation of the Radiation tolerant HELIX128-2 Readout Chip for the HERA-B Microstrip Detectors*, Ph.D. thesis, University of Heidelberg, 2000.
- [Vis96] Sven Visbeck, *Untersuchungen von Prototypen der Mikrostreifen-Gaskammern (MSGC) des inneren Spurkammersystems des HERA-B Experiments*, Diploma thesis, University of Heidelberg, September 1996.
- [Wag00] Gregor Wagner, *Aufbau und Test der mit Digitalen-Signal-Prozessoren realisierten Komponenten des Datennahmesystems von HERA-B*, Ph.D. thesis, University of Hamburg, 2000.

-
- [WAH⁺57] C. S. Wu, E. Ambler, R. W. Hayward, D. D. Hoppes, and R. P. Hudson, *Experimental Test of Parity Conservation in Beta Decay*, Phys. Rev. **105** (1957), 1413–1414.
- [Wal01] Thomas Walter, *Contributions to the Development of Microstrip Gas Chambers (MSGC) for the HERA-B Experiment*, Ph.D. thesis, University of Zürich, 2001.
- [Wie01] Dirk Wiedner, PhD thesis in preparation, 2001, private communications.
- [Wil00a] Malika Wilde, *Anwachsen der Anzahl der Hits pro Ereignis*, October 2000, internal note.
- [Wil00b] Malika Wilde, *Die Slow-Control der Inneren Spurkammern bei HERA-B und Untersuchungen zu geeigneten Hochspannungs-Parametern der GEM-MSGCs*, Diploma thesis, University of Heidelberg, April 2000.
- [Wol83] Lincoln Wolfenstein, *Parametrization of the Kobayashi-Maskawa Matrix*, Phys. Rev. Lett. **51** (1983), 1945.
- [Wol00] Roger Wolf, *Report*, DESY Summer Student Programme 2000, September 2000.
- [Wun02] Sonja Wunderlich, *in preparation*, Ph.D. thesis, University of Heidelberg, 2002.
- [Zeu98] Torsten Zeuner, *Entwicklung eines Spurdetektors für das Experiment HERA-B*, Ph.D. thesis, University of Siegen, 1998.
- [Zeu01a] Torsten Zeuner, Private Communication, May 2001.
- [Zeu01b] Torsten Zeuner, Private Communication, March 2001.
- [Zie98] Marcus Ziegler, *Untersuchungen von Detektorprototypen für das innere Spurkammersystem des HERA-B Experiments*, Diploma thesis, University of Heidelberg, March 1998.

Acknowledgements

I am very grateful to my supervisor, Prof. F. Eisele for giving me the opportunity to work with the Inner Tracker group at HERA-*B*. His advice and suggestions were always helpful and valuable.

Also, I'd like to thank Prof. J. Stachel for her prompt willingness to be the second referee of this thesis.

Special thanks go to all present and former colleagues working with the Inner Tracker group from Heidelberg, Siegen, Zürich, Moscow, and Tbilisi, for creating an exceptionally agreeable and fruitful working atmosphere. Ueli Straumann, who taught me a lot about electronics and how to run a test beam experiment, and Sebastian Hausmann, who taught me the art of doing things properly the first time. I should also like to extend a big 'thank you' to 'my' diploma students, Martin Gerlowski and Verena Buchholz.

I also wish to thank Bernhard Schwingenheuer of the MPI Heidelberg for his support and help in setting up and debugging the readout system.

Martin Feuerstack-Raible and Harald Deppe of the ASIC laboratory always were open for questions about the idiosyncrasies of the latest Helix version. Without their advice, working with this beast would have been much harder.

The electronics workshop of the Institute of Physics in Heidelberg was always very cooperative. I'd like to thank especially P. von Walter, A. Rausch and R. Rusnyak, who were always open to new ideas and helped to get them quickly into shape.

I profited much from fruitful and interesting discussions about Drell-Yan physics with Ulrich Husemann of Uni Dortmund and Gerhard Bohm of DESY-Zeuthen.

Many people read parts of the manuscript at various stages and gave helpful comments and suggestions. Thank you, Carsten, Sonja, Thomas, and Ulrich.

I'd like to thank my parents for all their support during the course of my studies and their interest in all this strange physics.

Last, but not least, my special thanks go to Sonja, for her love, and her patience with me during the last few months.